Deciphering the mechanisms of permanent forearc deformation based on marine terraces

---

Roland Freisleben

Kumulative Dissertation

zur Erlangung des akademischen Grades
"doctor rerum naturalium"
(Dr. rer. nat.)
in der Wissenschaftsdisziplin Geologie

eingereicht an der
Mathematisch-Naturwissenschaftlichen Fakultät
Institut für Geowissenschaften
der Universität Potsdam

Ort und Tag der Disputation: Potsdam, 28.09.2023

Hauptbetreuer:	Prof. Manfred R. Strecker, PhD
Betreuer:	Prof. Dr. Peter van der Beek
	Prof. Dr. Julius Jara-Muñoz
Gutachter:	Prof. Dr. Jack Loveless
	Ass. Prof. Vincent Regard

Published online on the
Publication Server of the University of Potsdam:
https://doi.org/10.25932/publishup-61035
https://nbn-resolving.org/urn:nbn:de:kobv:517-opus4-610359

Abstract

The Andes reflect Cenozoic deformation and uplift along the South American margin in the context of regional shortening associated with the interaction between the subducting Nazca plate and the overriding continental South American plate. Simultaneously, multiple levels of uplifted marine terraces constitute laterally continuous geomorphic features related to the accumulation of permanent forearc deformation in the coastal realm. However, the mechanisms responsible for permanent coastal uplift and the persistency of current/decadal deformation patterns over millennial timescales are still not fully understood. This dissertation presents a continental-scale database of last interglacial terrace elevations and uplift rates along the South American coast that provides the basis for an analysis of a variety of mechanisms that are possibly responsible for the accumulation of permanent coastal uplift. Regional-scale mapping and analysis of multiple, late Pleistocene terrace levels in central Chile furthermore provide valuable insights regarding the persistency of current seismic asperities, the role of upper-plate faulting, and the impact of bathymetric ridges on permanent forearc deformation.

The database of last interglacial terrace elevations reveals an almost continuous signal of background-uplift rates along the South American coast at ~0.22 mm/yr that is modified by various short- to long-wavelength changes. Spatial correlations with crustal faults and subducted bathymetric ridges suggest long-term deformation to be affected by these features, while the latitudinal variability of climate forcing factors has a profound impact on the generation and preservation of marine terraces. Systematic wavelength analyses and comparisons of the terrace-uplift rate signal with different tectonic parameters reveal short-wavelength deformation to result from crustal faulting, while intermediate- to long-wavelength deformation might indicate various extents of long-term seismotectonic segments on the megathrust, which are at least partially controlled by the subduction of bathymetric anomalies. The observed signal of background-uplift rate is likely accumulated by moderate earthquakes

near the Moho, suggesting multiple, spatiotemporally distinct phases of uplift that manifest as a continuous uplift signal over millennial timescales.

Various levels of late Pleistocene marine terraces in the 2015 M8.3 Illapel-earthquake area reveal a range of uplift rates between 0.1 and 0.6 mm/yr and indicate decreasing uplift rates since ~400 ka. These glacial-cycle uplift rates do not correlate with current or decadal estimates of coastal deformation suggesting seismic asperities not to be persistent features on the megathrust that control the accumulation of permanent forearc deformation over long timescales of 10^5 years. Trench-parallel, crustal normal faults modulate the characteristics of permanent forearc-deformation; upper-plate extension likely represents a second-order phenomenon resulting from subduction erosion and subsequent underplating that lead to regional tectonic uplift and local gravitational collapse of the forearc. In addition, variable activity with respect to the subduction of the Juan Fernández Ridge can be detected in the upper plate over the course of multiple interglacial periods, emphasizing the role of bathymetric anomalies in causing local increases in terrace-uplift rate. This thesis therefore provides new insights into the current understanding of subduction-zone processes and the dynamics of coastal forearc deformation, whose different interacting forcing factors impact the topographic and geomorphic evolution of the western South American coast.

Kurzfassung

Die känozoischen Anden resultieren aus der regionalen Verkürzung und Hebung der kontinentalen Kruste entlang des südamerikanischen Kontinentalrandes infolge der Interaktion zwischen der subduzierenden Nazca-Platte und der südamerikanischen Platte. Zahlreiche, durch tektonische Prozesse angehobene marine Abrasionsplattformen entlang der Küsten am westlichen Kontinentalrand Südamerikas bilden lateral kontinuierliche Stufen, welche die Akkumulation dauerhafter Deformation im küstennahen Forearc-Bereich widerspiegeln. Die Mechanismen, welche für die dauerhafte Hebung der Küste und die Beständigkeit derzeitiger/dekadischer Deformationsmuster auch über Jahrtausende hinweg verantwortlich sind, sind jedoch noch nicht vollständig geklärt. Vor diesem Hintergrund wird in dieser Dissertation zunächst eine kontinentale Datenbank der gehobenen marinen Terrassen des letzten Interglazials (125,000 Jahre), ihrer Höhenverteilung sowie der daraus abgeleiteten Hebungsraten für die Westküste von Südamerika vorgestellt. Diese Datenbank bildet die Grundlage für die Analyse einer Vielzahl von Mechanismen, welche möglicherweise für die Akkumulation dauerhafter Küstenhebung und Deformation verantwortlich sind. In einem weiteren Schritt wurden zusätzlich spätpleistozäne Terrassenniveaus in Zentralchile regionalmaßstäblich kartiert und hinsichtlich ihrer räumlich-zeitlichen Entwicklung analysiert. Diese Informationen liefern wertvolle Erkenntnisse über die Beständigkeit von seismischen Asperitäten, den Einfluss bathymetrischer Rücken auf die dauerhafte Deformation der Oberplatte sowie die Rolle von krustalen Störungen hinsichtlich der lokalen topographischen Differenzierung seismotektonischer Segmente.

Die Datenbank der im letzten Interglazial entstandenen marinen Terrassen und der abgeleiteten Hebungsraten zeigt ein nahezu kontinuierliches Signal von Hintergrund-Hebungsraten entlang der südamerikanischen Küste von ~0,22 mm/Jahr, das durch verschiedene kurz- bis langwellige Modifikationen gekennzeichnet ist. Räumliche Übereinstimmungen mit krustalen Störungen

und subduzierten bathymetrischen Rücken deuten darauf hin, dass die langfristige Deformation von diesen Parametern beeinflusst wird, während die breitengradabhängige Variabilität von Klimafaktoren tiefgreifende Auswirkungen auf die Entstehung und Erhaltung von marinen Terrassen hat. Systematische Wellenlängenanalysen und Vergleiche des Signals der Terrassenhebungsrate mit verschiedenen tektonischen Parametern zeigen, dass Deformation im kurzwelligen Bereich auf krustale Störungen zurückzuführen ist. Die Deformation im mittel- bis langwelligen Bereich könnte hingegen auf verschiedene Ausdehnungen langfristig aktiver seismotektonischer Segmente der Subduktionszone hindeuten, die zumindest teilweise durch die Subduktion bathymetrischer Anomalien kontrolliert werden. Das beobachtete Signal der Hintergrund-Hebungsrate wird wahrscheinlich durch Erdbeben mittlerer Magnituden in der Nähe der Moho generiert, was auf mehrere, räumlich und zeitlich getrennte Hebungsphasen hindeutet, die sich über Jahrtausende hinweg als kontinuierliches Hebungssignal manifestieren.

Gehobene spätpleistozäne marine Terrassen im Illapel-Erdbebengebiet von 2015 weisen eine Hebungsrate zwischen 0,1 und 0,6 mm/Jahr auf und deuten insgesamt auf abnehmende tektonische Hebungsraten seit ~400,000 Jahren hin. Diese langfristigen Hebungsraten auf glazialen Zeitskalen korrelieren nicht mit den Hebungsraten auf kurzen Zeitskalen, was darauf schließen lässt, dass seismische Asperitäten im Bereich der Subduktionszone keine dauerhaften Merkmale sind, welche die Deformation und Hebung der Forearc-Regionen über lange Zeiträume von mehreren 10^5 Jahren steuern. Wie auch an anderen aktiven konvergenten Plattenrändern existieren in Zentralchile krustale Abschiebungen parallel zum Plattenrand, die das Erscheinungsbild dauerhafter Forearc-Deformation stark beeinflussen. Die Extensionsprozesse der Oberplatte sind dabei wahrscheinlich ein Phänomen zweiter Ordnung, welches durch Subduktionserosion und anschließende Akkretion hervorgerufen wird und sich in regionaler tektonischer Hebung sowie einem gravitativen Kollaps der Forearc-Region äußert. Darüber hinaus lassen sich über verschiedene Glazial- und Interglazialzyklen hinweg Änderungen in der Bedeutung des Juan-Fernández-Rückens hinsichtlich der Deformationsprozesse in der Oberplatte nachweisen; dies unterstreicht die transiente Rolle bathymetrischer Anomalien bei der Beeinflussung lokaler Änderungen der Terrassenhebungsrate. Die vorgelegte Arbeit liefert daher neue Einblicke für ein besseres Verständnis der Deformationsprozesse in Subduktionszonen und den küstennahen Forearc-Regionen sowie ihrer unterschiedlich interagierenden Antriebsfaktoren, welche die topographische und geomorphologische Entwicklung der westlichen südamerikanischen Küste beeinflussen.

Declaration of author contributions

This cumulative dissertation comprises one published paper (Chapter 2), one manuscript accepted for review (Chapter 3), and one additional manuscript (Chapter 4), in all of which Roland Freisleben is the first author. I adjusted the numbering of the figures, tables and equations as well as the orthography to fit the style of the thesis. The supplementary material of Chapter 4 is included in the Appendix and the references of all manuscripts are compiled at the end of the dissertation.

Chapter 2 was published by Freisleben et al. (2021) in EGU's *Earth System Science Data* under the title *'Marine terraces of the last interglacial period along the Pacific coast of South America (1° N–40° S)'*, https://doi.org/10.5194/essd-13-2487-2021. Co-authors were Julius Jara-Muñoz, Daniel Melnick, José Miguel Martínez, and Manfred R. Strecker. The main compilers of the database were RF, JMM, and JJM. The paper was written by RF with significant input from JJ, DM, and MRS regarding interpretation and further improvements of graphical data representation. All co-authors reviewed and edited the manuscript. Constructive reviews by Vincent Regard and Paula Marques Figueiredo helped to improve the paper.

Chapter 3 comprises the manuscript *'Deciphering permanent uplift along the Pacific coast of South America through signal analysis of various tectonic processes'*, which was submitted to AGU's *Tectonics* and co-authored by Julius Jara-Muñoz, Daniel Melnick, Diego Molina Ormazabal, Andrés Tassara, Peter van der Beek, and Manfred R. Strecker. RF carried out the wavelength analysis, interpreted the data and wrote the manuscript under the supervision of and with significant input from JJ, DM, and MRS. DMO provided valuable analysis of tectonic parameters and helped regarding their interpretation. PvdB and AT contributed with improvements on data analysis and their graphical display. All co-authors reviewed and edited the manuscript.

Chapter 4 consists of the manuscript *'Structural and temporal characteristics of marine terraces in the 2015 M8.3 Illapel earthquake area'*, which is currently in preparation for submission and co-authored by Julius Jara-Muñoz, Daniel Melnick, Dominik Brill, Manfred R. Strecker, Christian Creixell Torres, and Ismael Murillo. RF did the terrace mapping and analysis, sediment sampling, and writing of the manuscript under supervision of and with significant input from JJ, DM, MRS. DB dated the samples and helped regarding their interpretation. CCT and IM assisted during the field work and provided useful aspects during the discussion. JJ, DM and MRS reviewed and edited the manuscript.

Contents

List of Figures

List of Tables

Chapter 1: Introduction

Tectonically active coasts at subduction margins constitute highly dynamic geomorphic environments that are repeatedly affected by megathrust earthquakes, associated surface deformation and a variety of cascading effects, such as tsunamis and mass movements (e.g., Lajoie, 1986; Beck et al., 1998; Bilek, 2010; Bletery et al., 2016; Philibosian & Meltzner, 2020). At the same time, many of these coastal zones host densely populated centers with large economic assets and critical infrastructure that are exposed to pronounced hazards and increasing risk (e.g., Melet et al., 2020). There is growing concern in coastal communities about the effects of these phenomena, because they are often associated with high death tolls and staggering financial loss that may even impact global supply chains.

Destructive earthquakes in the Apennines of Italy and the large 2011 Tohoku-Oki M_W 9.0 event in Japan demonstrate some of these issues, even in some of the best-studied areas in the world (Walters et al., 2009; Sawai et al., 2012). Furthermore, on February 27th 2010, Chile experienced the strongest earthquake worldwide since 2004 (M_W8.8), resulting in surprisingly little loss of life or damage to infrastructure, while the M_W7.0 Haiti earthquake a few weeks earlier caused the death of more than 300,000 people (DesRoches et al., 2011). Although different in magnitude and plate-tectonic setting, the partly global economic and political reverberations of these events illustrate, how the geophysical and geological settings are acutely coupled with the human realm and that different levels of knowledge exist regarding the spatial and temporal character of seismicity, especially concerning its recurrence. Central to this issue is our understanding of the seismic cycle and the behavior of the crust in coastal areas, primarily on centennial timescales. Numerous studies concerning the seismic cycle have been conducted along the subduction margin of South America, especially in Chile (Chlieh et al., 2004; Jara-Muñoz et al., 2015; Wesson et al., 2015; Melnick et al., 2017; Saillard et al., 2017).

The seismic cycle of great subduction-zone earthquakes along the Chilean margin and elsewhere has been described as a repetitive sequence of crustal deformation phenomena along the plate interface and neighboring faults, constituting three main steps: strain accumulation during the interseismic period, release of strain by an earthquake during the coseismic stage, and the postseismic period, characterized by complex transient processes in the years to decades following the earthquake (Thatcher, 1990; Wang et al., 2007; Loveless et al., 2010; Barbot et al., 2012). The cumulative, permanent deformation, which is ultimately expressed in mountain building, integrates this cycle over long timescales. It has been proposed that forearc regions are differentiated into seismotectonic segments. Such segments may reflect the long-term structural and topographic expression of numerous earthquake cycles, thus forming geomorphic entities that sustain their style and rate of deformation over long timescales (Kley et al., 1999; Philibosian & Meltzner, 2020; Molina et al., 2021). This notion is partly based on the observation that the slip distribution of some great (M_W8) to giant (M_W9) earthquakes occurs in distinct sectors. However, despite these advances in understanding the mechanics of slip distribution and how strain is accrued during repeated large earthquakes, the correlations between coseismic slip and the sustained long-term segmentation of forearcs, its geomorphic expression in the landscape, and its modification by subsequent tectonic processes as well as the role of bathymetric anomalies and crustal heterogeneities in the upper plate remain poorly understood.

Therefore, profound knowledge of the processes at subduction zones and the dynamics related to the deformation of the coastline and forearc are of utter importance to evaluate the possible impacts of earthquake scenarios and associated tsunami hazards. In order to ultimately reduce risks and to address the impacts of different hazards it is not only important to understand the size and return periods of large earthquakes on decadal timescales, but it is also central to decipher the evolution of tectonic landforms and the characteristics of plate-boundary tectonism on millennial timescales, which provide further insights regarding the temporal variations of the responsible processes.

1.1 The South American margin

The subduction of the oceanic Nazca plate beneath the South American continent constitutes the main driver for shortening and uplift of the Andean orogen and its present seismotectonic framework (Darwin, 1846; Barazangi & Isacks, 1976; Jordan et al., 1983). The South American subduction margin is characterized by varying angles of the subducting plate with relatively steep subduction segments (25°–30°) and two flat-slab segments (5°–10°) beneath central Peru and central Chile (Barazangi & Isacks, 1976; Jordan et al., 1983; Hayes et al., 2018). This segmentation is thought to control volcanic activity, forearc architecture, and the distribution of upper-plate deformation, including the different tectonic styles in the foreland regions of the Andean orogen (Jordan et al., 1983; Kay et al., 1987; Ramos & Folguera, 2009; Margirier et al., 2023; Rodriguez Piceda et al., 2023). Elevated bathymetric features on the seafloor of the subducting plate mark the boundaries between these segments and furthermore influence the degree of interplate coupling and the associated seismic hazard (Wang & Bilek, 2011; Bassett & Watts, 2015; Collot et al., 2017). The most prominent bathymetric anomalies of the Nazca plate comprise the Carnegie, Nazca, Juan Fernández, and Iquique ridges, which consist of seamounts related to hot-spot volcanism (Gutscher et al., 1999; Hampel, 2002).

The ~8000-km-long Andean orogen can be divided by the Arica and Huancabamba oroclinal bends into first-order segments with distinctive geomorphic and tectonic characteristics (Jaillard et al., 2000). The NNE–SSW-trending Ecuadorian segment of the Andes is characterized by a wide coastal plain at elevations of less than 300 m that adjoins the Western Cordillera. Separated by the Dolores–Guayaquil megashear, the Peruvian segment comprises the NW–SE-trending Coastal Cordillera and a narrow coastal area that widens in northern and southern Peru (Suárez et al., 1983; Jaillard et al., 2000). South of the Arica bend (18°S), the N–S-trending Chilean Andes can be structurally divided into the Coastal Cordillera and the Central Depression that separates it from the Main Cordillera in the steep-slab subduction segments (Jordan et al., 1983).

While the Andes are the manifestation of Cenozoic deformation and uplift along the plate boundary, in the coastal realm, within the immediate proximity to the subduction zone, numerous levels of uplifted marine terraces constitute laterally continuous geomorphic features that reflect the accumulation of permanent forearc deformation. Terrace elevation and age increase with elevation in these environments (Lajoie, 1986). Marine terraces are formed

primarily during interglacial and interstadial relative sea-level highstands through the erosional force of waves that cause the carving of abrasion platforms and the retreat of coastal cliffs, a process, which is superposed on the tectonically rising coastline. If tectonic uplift is sufficiently high and sustained over millennial timescales, a sea-level highstand during globally warmer climatic conditions will lead to the formation of a lower, younger terrace level, exposing the older marine terrace in a higher position and eventually creating a staircase morphology of multiple terraces (e.g., Lajoie, 1986). These coastal landforms are therefore at the center of this tectono-geomorphic study of the western South American margin, because they are valuable strain markers that have been used frequently to estimate coastal uplift rates (Pedoja et al., 2006; Saillard et al., 2009; Saillard et al., 2011; Jara-Muñoz et al., 2015; Martinod et al., 2016; Melnick, 2016). In addition, they equally provide an excellent means to identify different sectors of the forearc that are characterized by varying levels of tectonic activity (Melnick et al., 2009; Victor et al., 2011; Jara-Muñoz et al., 2015; Martinod et al., 2016).

1.2 Current state of knowledge and research questions

The South American convergent margin is subjected to giant subduction earthquakes ($\geq M_W8$) that exhibit recurrent patterns in distinct seismotectonic segments of the forearc (Lomnitz, 2004; Philibosian & Meltzner, 2020; Molina et al., 2021). Crustal motion during such megathrust earthquakes is usually distributed heterogeneously and includes regions of pronounced slip, which are commonly known as asperities (Lay & Kanamori, 1981; Kanamori, 1986). Areas characterized by pronounced interplate coupling have been interpreted as asperities that ultimately rupture during future events (Moreno et al., 2010; Schurr et al., 2014; Tilmann et al., 2016). Megathrust earthquakes, such as the 2010 Maule ($M_W8.8$), 2015 Illapel ($M_W8.3$), and 2014 Iquique ($M_W8.2$) earthquakes are recent examples for this type of seismogenic behavior (e.g., Moreno et al., 2010; Métois et al., 2016). During a megathrust earthquake large quantities of elastic strain are suddenly released following long interseismic periods of elastic strain accumulation (Reid, 1910; Savage, 1983; Wang et al., 2003). However, the seismic cycle is not completely elastic and to a certain degree, the accumulated strain might be stored anelastically in the crust in the form of permanent deformation (Briggs et al., 2008; Jara-Muñoz et al., 2015; Wesson et al., 2015). Despite many advances have been made regarding the short-term characteristics of seismic asperities and the distribution of megathrust

earthquakes based on decadal geodetic measurements and historical records, the observational time span is often insufficient to determine the persistency of asperities over multiple seismic cycles as well as the long-term deformation (10^2–10^5-year scale) and segmentation of the forearc. We must therefore aim for a better understanding of the spatiotemporal distribution of seismic asperities, patterns of permanent deformation, and the mechanisms responsible for strain accumulation, since these aspects may ultimately control the magnitude and rupture extent of future megathrust earthquakes.

Previously proposed mechanisms that might be responsible for the accumulation of permanent deformation in the forearc comprise the subduction of bathymetric ridges (Taylor et al., 1987; Hsu, 1992; Pedoja et al., 2006; Saillard et al., 2011; Martinod et al., 2016), basal accretion of subducted trench sediments (Glodny et al., 2005; Melnick & Echtler, 2006; Clift & Hartley, 2007; Bangs et al., 2020; Menant et al., 2020), upper-plate deformation (Armijo & Thiele, 1990; Adam & Reuther, 2000; Armijo et al., 2015), and the motion of forearc slivers (Melnick et al., 2009; Jara-Muñoz et al., 2015). Furthermore, it is still a matter of debate, whether the successive occurrence of earthquakes causes permanent coastal uplift (Melnick et al., 2006; Melnick, 2016; González-Alfaro et al., 2018) or whether coastal uplift rather results from interseismic deformation (Allmendinger & González, 2010; Jolivet et al., 2020; Madella & Ehlers, 2021). In all likelihood, the accumulation of permanent coastal uplift represents a combination of multiple processes. However, the relative significance of individual mechanisms as well as their complex spatiotemporal interactions still require further analysis.

In particular, the analysis of deformation patterns of marine terraces on glacial timescales has not yet been carried out on large regional spatial scales, primarily because studies on terrace sequences have been primarily concentrated on specific areas, where the uplift signal and terrace morphology are best preserved. Discontinuous terrace measurements and the application of different methodological approaches have furthermore prevented regional comparisons and lateral correlations of uplift rates and spatial trends in deformation, which resulted in ambiguous and inconclusive interpretations regarding tectonic and climatic forcing mechanisms that contribute to the formation and degradation of marine terraces (Hsu et al., 1989; Ortlieb & Macharé, 1990; Hsu, 1992; Macharé & Ortlieb, 1992; Pedoja et al., 2006; Saillard et al., 2009; Saillard et al., 2011; Rodríguez et al., 2013). Furthermore, a long-term continental-scale approach on deformation patterns would open up the possibly to study the aforementioned issues concerning the persistency of current seismic asperities and the mechanisms driving

permanent coastal uplift in subduction zones. The well-preserved and almost continuous marine terraces that were generated during the last interglacial sea-level highstand ~125 ka ago (e.g., Siddall et al., 2006; Pedoja et al., 2011), provide this excellent opportunity along the South American convergent margin. As in other coastal regions worldwide, the higher, protracted sea-level during the last interglacial has generated wide, well-defined abrasion platforms along clastic coasts (Lajoie, 1986) that are very useful for a regional analysis of deformation.

In light of these problems and available data sets with respect to further systematic assessments of coastal deformation, one of the principal objectives of this dissertation is the compilation of a continental-scale database of last interglacial marine terrace elevations for the western South American margin, which will be used to understand regional differences in coastal deformation and uplift. This database will ultimately provide information needed to answer the following research questions:

(1) What mechanisms do control the accumulation of permanent coastal uplift and the deformation of the forearc?

(2) When does permanent deformation accumulate?

(3) What is the role of seismic asperities in the accumulation of permanent deformation and how persistent are they over long timescales of 10^5 years?

Resolving these questions is fundamental to our understanding of the processes governing tectonically active coastal regions in South America. In addition, a synoptic view of terrace-uplift patterns will provide relevant insights regarding the mechanisms driving permanent deformation and the longevity of deformation patterns along subduction margins globally over a wide range of timescales, ranging from decades to several millennia.

1.3 Organization of the thesis

After the introductory **Chapter 1**, the data-based parts of this thesis start with **Chapter 2** comprising a regional-scale mapping effort that identified last interglacial marine terraces along the western South American coast using quantitatively replicable approaches that are constrained by published terrace-age estimates. Terrace elevations and resulting uplift rates are

ultimately compared to tectonic and climatic parameters to evaluate the mechanisms controlling their formation and preservation as well as regional trends in crustal deformation patterns along the active margin of South America. This chapter was published by Freisleben et al. (2021) in EGU's *Earth System Science Data*.

Chapter 3 provides the unique opportunity to use the newly established continental-scale database to elucidate the processes driving permanent coastal uplift and surface deformation at subduction margins by applying a novel signal-analysis approach. Algorithms for wavelength analysis are utilized on the uplift-rate signal and signals of tectonic processes and subduction parameters associated with the accumulation of permanent deformation in order to detect possible links and spatiotemporal characteristics. This chapter is currently in review as a second first-author manuscript with AGU's journal *Tectonics*.

In **Chapter 4**, I evaluate the significance of upper-plate structures in the context of megathrust earthquakes on permanent forearc deformation on a more regional scale in the realm of the 2015 Illapel earthquake based on the distribution of different levels of late Pleistocene marine terraces and a derivation of regional uplift rates. The estimations of long-term terrace-uplift rates are further compared to present-day deformation patterns to assess the persistency of seismic asperities over timescales of 10^5 years. This chapter is currently in preparation as a third first-author contribution.

Chapter 5 discusses the results of the previous chapters of this thesis, puts them into an overall context regarding the current state of knowledge and reviews the main arguments how the obtained results contribute to the answering of the principal research questions outlined at the beginning of the text. As such this chapter provides a comprehensive overview on how a continental-scale analysis of marine terraces aids in deciphering mechanisms that control the accumulation of permanent coastal uplift and surface deformation of the forearc along subduction margins.

Finally, **Chapter 6** briefly summarizes the main findings of this dissertation.

Chapter 2: Marine terraces of the last interglacial period along the Pacific coast of South America (1° N–40° S)

2.1 Abstract

Tectonically active coasts are dynamic environments characterized by the presence of multiple marine terraces formed by the combined effects of wave-erosion, tectonic uplift, and sea-level oscillations at glacial-cycle timescales. Well-preserved erosional terraces from the last interglacial sea-level highstand are ideal marker horizons for reconstructing past sea-level positions and calculating vertical displacement rates. We carried out an almost continuous mapping of the last interglacial marine terrace along ~5000 km of the western coast of South America between 1° N and 40° S. We used quantitatively replicable approaches constrained by published terrace-age estimates to ultimately compare elevations and patterns of uplifted terraces with tectonic and climatic parameters in order to evaluate the controlling mechanisms for the formation and preservation of marine terraces, and crustal deformation. Uncertainties were estimated on the basis of measurement errors and the distance from referencing points. Overall, our results indicate a median elevation of 30.1 m, which would imply a median uplift rate of 0.22 mm/yr averaged over the past ~125 kyr. The patterns of terrace elevation and uplift rate display high-amplitude (~100–200 m) and long-wavelength (~10^2 km) structures at the Manta Peninsula (Ecuador), the San Juan de Marcona area (central Peru), and the Arauco Peninsula (south-central Chile). Medium-wavelength structures occur at the Mejillones Peninsula and Topocalma in Chile, while short-wavelength (< 10 km) features are for instance located near Los Vilos, Valparaíso, and Carranza, Chile. We interpret the long-wavelength deformation to be controlled by deep-seated processes at the plate interface such as the subduction of major bathymetric anomalies like the Nazca and Carnegie ridges. In contrast, short-wavelength deformation may be primarily controlled by sources in the upper plate such

as crustal faulting, which, however, may also be associated with the subduction of topographically less pronounced bathymetric anomalies. Latitudinal differences in climate additionally control the formation and preservation of marine terraces. Based on our synopsis we propose that increasing wave height and tidal range result in enhanced erosion and morphologically well-defined marine terraces in south-central Chile. Our study emphasizes the importance of using systematic measurements and uniform, quantitative methodologies to characterize and correctly interpret marine terraces at regional scales, especially if they are used to unravel tectonic and climatic forcing mechanisms of their formation. This database is an integral part of the World Atlas of Last Interglacial Shorelines (WALIS), published online at http://doi.org/10.5281/zenodo.4309748 (Freisleben et al., 2020).

2.2 Introduction

Tectonically active coasts are highly dynamic geomorphic environments and they host densely populated centers and associated infrastructure (Melet et al., 2020). Coastal areas have been episodically affected by the effects of sea-level changes at glacial timescales, modifying the landscape and leaving behind fossil geomorphic markers, such as former paleo-shorelines, and marine terraces (Lajoie, 1986). One of the most prominent coastal landforms are marine terraces that were generated during the protracted last interglacial sea-level highstand that occurred ~125 ka ago (Siddall et al., 2006; Hearty et al., 2007; Pedoja et al., 2011). These terraces are characterized by a higher preservation potential, which facilitates their recognition, mapping, and lateral correlation. Furthermore, because of their high degree of preservation and relatively young age, they have been used to estimate vertical deformation rates at local and regional scales. The relative abundance and geomorphic characteristics of the last interglacial marine terraces make them ideal geomorphic markers with which to reconstruct past sea-level positions and to enable comparisons between distant sites under different climatic and tectonic settings.

The western South American Coast (WSAC) is a tectonically active region that has been repeatedly affected by megathrust earthquakes and associated surface deformation (Beck et al., 1998; Melnick et al., 2006; Bilek, 2010; Baker et al., 2013). Interestingly, previous studies have shown that despite the broad spectrum of latitudinal climatic conditions and erosional regimes along the WSAC, marine terraces are scattered, but omnipresent along the coast (Ota et al.,

1995; Regard et al., 2010; Rehak et al., 2010; Bernhardt et al., 2016; Melnick, 2016; Bernhardt et al., 2017). However, only a few studies on interglacial marine terraces have been conducted along the WSAC, primarily in specific areas where they are best expressed; this has resulted in disparate and inconclusive marine terrace measurements based on different methodological approaches and ambiguous interpretations concerning their origin in a tectonic and climatic context (Hsu et al., 1989; Ortlieb & Macharé, 1990; Hsu, 1992; Macharé & Ortlieb, 1992; Pedoja et al., 2006; Saillard et al., 2009; Pedoja et al., 2011; Saillard et al., 2011; Rodríguez et al., 2013). This lack of reliable data points has revealed a need to re-examine the last interglacial marine terraces along the WSAC based on standardized methodologies in order to obtain a systematic and continuous record of marine terrace elevations along the coast. This information is crucial in order to increase our knowledge of the climatic and tectonic forcing mechanisms that contributed to the formation and degradation of marine terraces in this region.

Marine terrace sequences at tectonically active coasts are landforms formed by wave erosion and/or accumulation of sediments resulting from the interaction between tectonic uplift and superposed oscillating sea-level changes (Lajoie, 1986; Anderson et al., 1999; Jara-Muñoz et al., 2015). Typically, marine terrace elevations are estimated based on the shoreline angle. The marine terrace morphology comprises a gently inclined erosional or depositional paleo-platform that terminates landward at a steeply sloping paleo-cliff surface. The intersection point between both surfaces represents the approximate sea-level position during the formation of the marine terrace, also known as shoreline angle; if coastal uplift is rapid, such uplifting abrasion or depositional surfaces may be preserved in the landscape and remain unaltered by the effects of subsequent sea-level oscillations (Lajoie, 1986).

The analysis of elevation patterns based on shoreline-angle measurements at subduction margins has been largely used to estimate vertical deformation rates and the mechanisms controlling deformation, including the interaction of the upper plate with bathymetric anomalies, the activity of crustal faults in the upper plate, and deep-seated processes such as basal accretion of subducted trench sediments (Taylor et al., 1987; Hsu, 1992; Macharé & Ortlieb, 1992; Ota et al., 1995; Pedoja et al., 2011; Saillard et al., 2011; Jara-Muñoz et al., 2015; Melnick, 2016). The shoreline angle represents a 1D descriptor of the marine terrace elevation, whose measurements are reproducible when using quantitative morphometric approaches (Jara-Muñoz et al., 2016). Furthermore, the estimation of the marine terrace elevations based on

shoreline angles can be further improved by quantifying their relationship with the paleo-sea level, also known as the indicative meaning (Lorscheid & Rovere, 2019).

In this continental-scale compilation of marine terrace elevations along the WSAC, we present systematically mapped shoreline angles of marine terraces of the last (Eemian–Sangamonian) interglacial obtained along 5000 km of coastline between 1° N and 40° S. In this synthesis we rely on chronological constraints from previous regional studies and compilations (Pedoja et al., 2011). For the first time we are able to introduce an almost continuous pattern of terrace elevation and coastal uplift rates at a spatial scale of 10^3 km along the WSAC. Furthermore, in our database we compare tectonic and climatic parameters to elucidate the mechanisms controlling the formation and preservation of marine terraces, and patterns of crustal deformation along the coast. This study was thus primarily intended to provide a comprehensive, standardized database and description of last interglacial marine terrace elevations along the tectonically active coast of South America. This database therefore warrants future research into coastal environments to decipher potential tectonic forcings with regard to the deformation and seismotectonic segmentation of the forearc; as such this database will ultimately help to decipher the relationship between upper-plate deformation, vertical motion, and bathymetric anomalies and aid in the identification of regional fault motions along pre-existing anisotropies in the South American continental plate. Finally, our database includes information on climate-driving forcing mechanisms that may influence the formation, modification, and/or destruction of marine terraces in different climatic sectors along the South American convergent margin. This new database is part of the World Atlas of Last Interglacial Shorelines (WALIS), published online at http://doi.org/10.5281/zenodo.4309748 (Freisleben et al., 2020).

2.3 Geologic and geomorphic setting of the WSAC

2.3.1 Tectonic and seismotectonic characteristics

2.3.1.1 Subduction geometry and bathymetric features

The tectonic setting of the convergent margin of South America is controlled by subduction of the oceanic Nazca plate beneath the South American continental plate. The convergence rate

varies between 66 mm/yr in the north (8° S latitude) and 74 mm/yr in the south (27° S latitude) (Fig. 2.1). The convergence azimuth changes slightly from 81.7° N toward 77.5° N from north to south (DeMets et al., 2010). The South American subduction zone is divided into four major segments with variable subduction angles inferred from the spatial distribution of Benioff seismicity (Fig. 2.1; Barazangi & Isacks, 1976; Jordan et al., 1983). The segments beneath northern and central Peru (2°–15° S) and beneath central Chile (27°–33° S) are characterized by a gentle dip of the subducting plate between 5° and 10° at depths of ~100 km (Hayes et al., 2018), whereas the segments beneath southern Peru and northern Chile (15°–27° S), and beneath southern Chile (33°–45° S) have steeper dips of 25° to 30°. Spatial distributions of earthquakes furthermore indicate a steep-slab subduction segment in Ecuador and southern Colombia (2° S to 5° N) and a flat-slab segment in NW Colombia (north of 5° N; Pilger, 1981; Cahill & Isacks, 1992; Gutscher et al., 2000; Ramos & Folguera, 2009). Processes that have been inferred to be responsible for the shallowing of the subduction slab include the subduction of large buoyant ridges or plateaus (Espurt et al., 2008), as well as the combination of the trenchward motion of thick, buoyant continental lithosphere accompanied by trench retreat (Sobolev & Babeyko, 2005; Manea et al., 2012). Volcanic activity as well as the forearc architecture and distribution of upper-plate deformation, further emphasizes the location of flat-slab subduction segments (Jordan et al., 1983; Kay et al., 1987; Ramos & Folguera, 2009).

Several high bathymetric features have been recognized on the subducting Nazca plate. The two most prominent bathymetric features being subducted beneath South America are the Carnegie and Nazca aseismic ridges at 0° and 15° S, respectively; they consist of seamounts related to hot-spot volcanism (Gutscher et al., 1999; Hampel, 2002). The 300-km-wide and ~2-km-high Carnegie Ridge subducts roughly parallel to the convergence direction and its geometry should have remained relatively stable beneath the continental plate (Angermann et al., 1999; Gutscher et al., 1999; DeMets et al., 2010; Martinod et al., 2016). In contrast, the obliquity of the 200-km-wide and 1.5-km-high Nazca Ridge with respect to the convergence direction resulted in 500 km SE-directed migration of its locus of ridge subduction during the last 10 Ma (Hampel, 2002; Saillard et al., 2011; Martinod et al., 2016). Similarly, smaller aseismic ridges such as the Juan Fernández Ridge and the Iquique Ridge subduct beneath the South American continent at 32° S and 21° S, respectively. The intercepts between these bathymetric anomalies and the upper plate are thought to influence the characteristics of interplate coupling and seismic rupture (Bilek et al., 2003; Wang & Bilek, 2011; Geersen et al.,

2015; Collot et al., 2017), mark the boundaries between flat and steep subduction segments as well as the changes between subduction erosion and accretion (Fig. 2.1; Jordan et al., 1983; von Huene et al., 1997; Ramos & Folguera, 2009).

In addition to bathymetric anomalies, several studies have shown that variations in the volume of sediments in the trench may control the subduction regime from an erosional mode to an accretionary mode (von Huene and Scholl, 1991; Bangs and Cande, 1997). In addition, the volume of sediment in the trench has also been hypothesized to influence the style of interplate seismicity (Lamb & Davis, 2003). At the southern Chilean margin, thick trench-sediment sequences and a steeper subduction angle correlate primarily with subduction accretion, although the area of the intercept of the continental plate with the Chile Rise spreading center locally exhibits the opposite case (von Huene & Scholl, 1991; Bangs & Cande, 1997). Subduction erosion characterizes the region north of the southern volcanic zone from central and northern Chile to southern Peru (33°–15° S) due to decreasing sediment supply to the trench, especially within the flat-slab subduction segments (Stern, 1991; von Huene & Scholl, 1991; Bangs & Cande, 1997; Clift & Vannucchi, 2004). Clift and Hartley (2007) and Lohrmann et al. (2003) argued for an alternate style of slow tectonic erosion leading to underplating of subducted material below the base of the crustal forearc, which is synchronous with tectonic erosion beneath the trenchward part of the forearc. For the northern Andes, several authors also classify the subduction zone as an erosional type (Clift & Vannucchi, 2004; Scholl & von Huene, 2007; Marcaillou et al., 2016).

2.3.1.2 Major continental fault systems in the coastal realm

The South American convergent margin comprises several fault systems with different kinematics, whose presence is closely linked to oblique subduction and the motion and deformation of forearc slivers. Here we summarize the main structures that affect the Pacific coastal areas. North of the Talara bend (5° S), active thrusting and dextral strike-slip faulting dominate the coastal lowlands of Ecuador (e.g., Mache, Bahía, Jipijapa faults), although normal faulting also occurs at Punta Galera (Cumilínche fault) and the Manta Peninsula (Río Salado fault; Fig. 2.1). Farther south, normal faulting is active in the Gulf of Guayaquil (Posorja fault) and dextral strike-slip faulting occurs at the Santa Elena Peninsula (La Cruz fault; Veloza et al., 2012; Costa et al., 2020). The most prominent dextral fault in this region is the 2000-km-long, northeast-striking Dolores–Guayaquil megashear (DGM), which starts in the Gulf of Guayaquil and terminates in the Colombian hinterland east of the range-bounding thrust faults of the

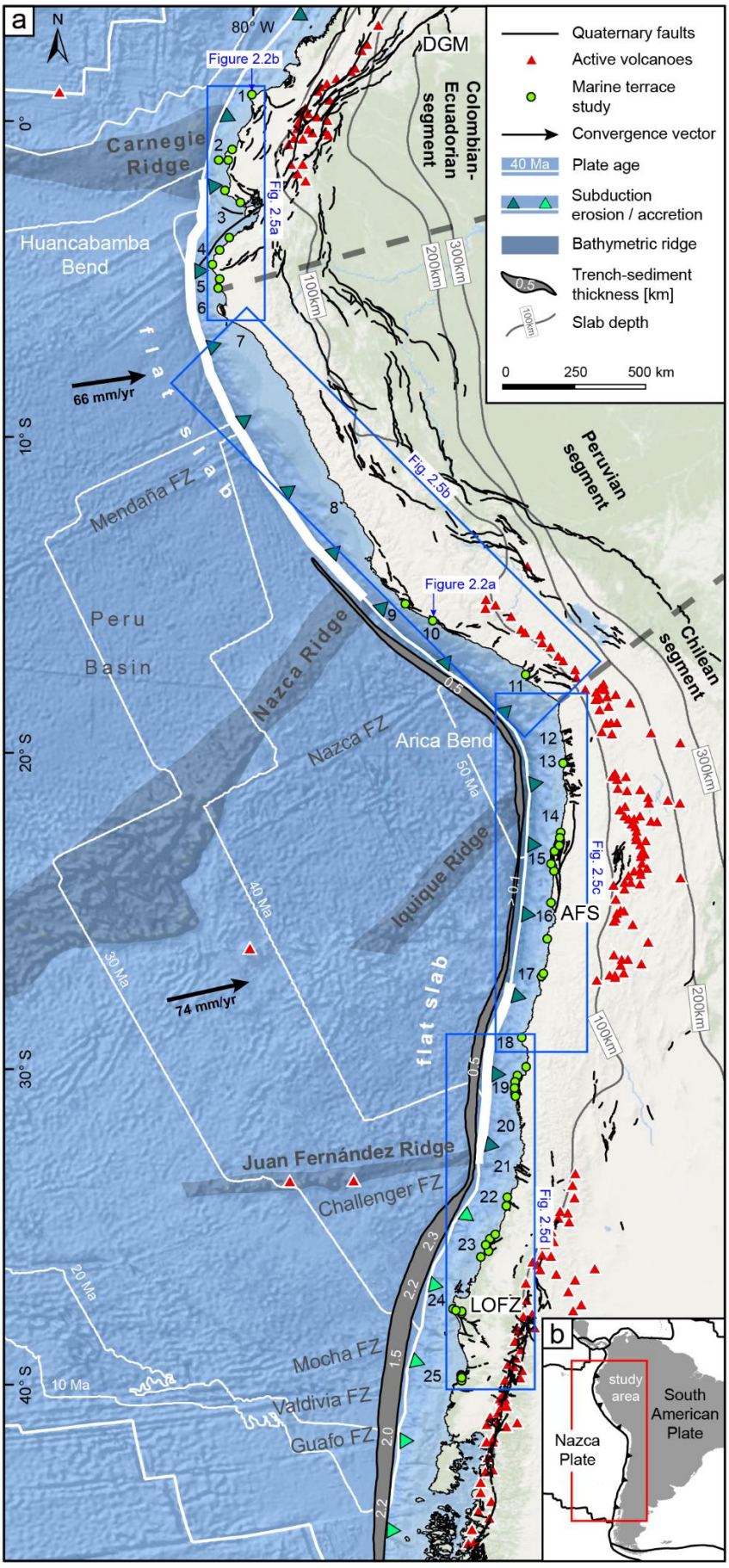

Figure 2.1: (a) Morphotectonic setting of the western South American margin showing major fault systems and crustal faults (Costa et al., 2000; Veloza et al., 2012; Maldonado et al., 2021), slab depth (Hayes et al., 2018), flat-slab subduction segments, active volcanos (Venzke, 2013), bathymetric features of the subducting plate, trench-sediment thickness (Bangs & Cande, 1997), segments of subduction erosion and accretion (Clift & Vannucchi, 2004), plate age (Müller et al., 2008), convergence vectors (DeMets et al., 2010), and marine terrace ages used for lateral correlation. DGM: Dolores–Guayaquil megashear; AFS: Atacama fault system; LOFZ: Liquiñe–Ofqui fault zone; FZ: fracture zone; 1: Punta Galera; 2: Manta Pen.; 3: Gulf of Guayaquil, Santa Elena Pen.; 4: Tablazo Lobitos; 5: Paita Pen.; 6: Illescas Pen.; 7: Chiclayo; 8: Lima; 9: San Juan de Marcona; 10: Chala Bay; 11: Pampa del Palo; 12: Pisagua; 13: Iquique; 14: Tocopilla; 15: Mejillones Pen.; 16: Taltal; 17: Caldera; 18: Punta Choros; 19: Altos de Talinay; 20: Los Vilos; 21: Valparaíso; 22: Topocalma; 23: Carranza; 24: Arauco Pen.; 25: Valdivia (World Ocean Basemap: Esri, Garmin, GEBCO, NOAA NGDC, and other contributors). (b) Location of the study area.

Colombian Andes (Fig. 2.1; Veloza et al., 2012; Villegas-Lanza et al., 2016; Costa et al., 2020). Normal faults have been described along the coast of Peru at the Illescas Peninsula in the north (6° S), within the El Huevo–Lomas fault system in the San Juan de Marcona area (14.5°–16° S), and within the Incapuquio fault system farther south (17°–18° S; Veloza et al., 2012; Villegas-Lanza et al., 2016; Costa et al., 2020). The main fault zones of the Chilean convergent margin comprise the Atacama fault system (AFS) in the Coastal Cordillera extending from Iquique to La Serena (29.75° S; Fig. 2.1), with predominantly north–south-striking normal faults, which result in the relative uplift of their western side (e.g., Mejillones fault, Salar del Carmen fault; Naranjo, 1987; González & Carrizo, 2003; Cembrano et al., 2007). Coastal fault systems farther south are located in the Altos de Talinay area (30.5° S, Puerto Aldea fault), near Valparaíso (33° S, Quintay and Valparaíso faults), near the Arauco Peninsula (36°–39° S, Santa María and Lanalhue faults), and in between these areas (Topocalma, Pichilemu, Carranza, and Pelluhue faults; Fig. 2.1; Ota et al., 1995; Melnick et al., 2009; Santibáñez et al., 2019; Maldonado et al., 2021). However, there is still limited knowledge regarding Quaternary slip rates and kinematics and, most importantly, the location of active faults along the forearc region of South America (Jara-Muñoz et al., 2018; Melnick et al., 2019).

2.3.2 Climate and geomorphic setting

2.3.2.1 Geomorphology

The 8000-km-long Andean orogen is a major, hemisphere-scale feature that can be divided into segments with distinctive geomorphic and tectonic characteristics. The principal segments comprise the NNE–SSW-trending Colombian–Ecuadorian segment (12° N–5° S), the NW–SE-oriented Peruvian segment (5°–18° S), and the north–south-trending Chilean segment (18°–56° S; Fig. 2.1; Jaillard et al., 2000). Two major breaks separate these segments; these are the Huancabamba bend in northern Peru and the Arica bend at the Peru–Chile border. The distance of the trench from the WSAC averages 118 km and ranges between 44 and 217 km. The depth of the trench varies between 2920 and 8177 m (GEBCO Bathymetric Compilation Group, 2020), and the continental shelf has an average width of 28 km (Paris et al., 2016).

In the 50 to 180-km-wide coastal area of the Ecuadorian Andes, where the Western Cordillera is flanked by a structural depression, relief is relatively low (< 300 m a.s.l.). The Gulf of Guayaquil (3° S) and the Dolores–Guayaquil megashear separate the northern from the southern forearc units. The coast-trench distance along the Huancabamba bend is quite small

(~55–90 km), except for the Gulf of Guayaquil, and the trench east of the Carnegie Ridge is at a relatively shallow depth of ~3.5 km. Farther south, the Peruvian forearc comprises the up to 160-km-wide Coastal Plains in the north and the narrow, 3000-m-high Western Cordillera. While the Coastal plains in north-central Peru are relatively narrow (< 40 km), they widen in southern Peru, and the elevation of the Western Cordillera increases to more than 5000 m (Suárez et al., 1983; Jaillard et al., 2000). The region between the coast and the trench in central Peru (up to 220 km) narrows towards the San Juan de Marcona area (~75 km) near the intercept with the Nazca Ridge, and the relatively deep trench (~6.5 km) becomes shallower (< 5 km; GEBCO Bathymetric Compilation Group, 2020). Between 18° S and 28° S, the Chilean forearc comprises the 50-km-wide and up to 2700-m-high Coastal Cordillera, which is separated from the Precordillera by the Central Depression. In the flat-slab subduction segment between 27° S and 33° S there is neither a morphotectonic region characterized by a central depression nor active volcanism in the high Andean cordillera (Fig. 2.1; Jordan et al., 1983). The Chilean forearc comprises the Coastal Cordillera, which varies in altitude from up to 2000 m at 33° S to 500 m at 46° S, and the Central Depression that separates the forearc from the Main Cordillera. From the Arica bend, where the coast-trench distance is up to 170 km and the trench ~8 km deep, a slight increase in coast-trench distance can be observed in Chile towards the south (~80–130 km), as can a decrease in trench depth to ~4.5 km.

2.3.2.2 Marine terraces and coastal uplift rates

Wave erosion generates wave-cut terrace levels, while the accumulation of shallow marine sediments during sea-level highstands forms wave-built terraces. Another type of terrace is known as ‘rasa’ and refers to wide shore platforms formed under slow-uplift conditions (< 0.2 mm/yr), and the repeated reoccupation of this surface by high sea levels (Regard et al., 2010; Rodríguez et al., 2013; Melnick, 2016). Other studies indicate a stronger influence of climate and rock resistance to erosion compared to marine wave action (Prémaillon et al., 2018). Typically, the formation of Pleistocene marine terraces in the study area occurred during interglacial and interstadial relative sea-level highstands that were superposed on the uplifting coastal areas; according to the Quaternary oxygen-isotope curve defining warm and cold periods, high Quaternary sea levels have been correlated with warm periods and are denoted with the odd-numbered Marine Isotope Stages (MISs; Lajoie, 1986; Shackleton et al., 2003).

Along the WSAC, staircase-like sequences of multiple marine terraces are preserved nearly continuously along the coast. These terraces comprise primarily wave-cut surfaces that are

frequently covered by beach ridges of siliciclastic sediments and local accumulations of carbonate bioclastic materials (Ota et al., 1995; Saillard et al., 2009; Rodríguez et al., 2013; Martinod et al., 2016). Rasa surfaces exist in the regions of southern Peru and northern Chile (Regard et al., 2010; Rodríguez et al., 2013; Melnick, 2016). Particularly the well-preserved MIS 5e terrace level has been largely used as a strain marker in the correlation of uplifted coastal sectors due to its lateral continuity and high potential for preservation. Global observations of sea-level fluctuations during MIS 5 allow us to differentiate between three second-order highstands at 80 ka (5a), 105 ka (5c), and 128 to 116 ka (5e) with paleo-sea levels of -20 m for both of the younger and +3 ± 3 m for the oldest highstand (Stirling et al., 1998; Siddall et al., 2006; Hearty et al., 2007; Rohling et al., 2009; Pedoja et al., 2011), although glacio-isostatic adjustments (GIAs) can cause local differences of up to 30 m (Simms et al., 2016; Creveling et al., 2017). The database generated in this study is based exclusively on the last interglacial marine terraces exposed along the WSAC between Ecuador and southern Chile (1° S to 40° S). In the following section we present a brief review of previously studied marine terrace sites in this area.

Paleo-shoreline elevations of the last interglacial (MIS 5e) in Ecuador are found at elevations of around 45 ± 2 m a.s.l. in Punta Galera (Esmeraldas area), 43–57 ± 2 m on the Manta Peninsula and La Plata Island, and 15 ± 5 m a.s.l. on the Santa Elena Peninsula (Pedoja et al., 2006; Pedoja et al., 2006). In northern Peru, MIS 5e terraces have been described at elevations of 18–31 m a.s.l. for the Tablazo Lobitos (Cancas and Mancora areas), at 25 ± 5 m a.s.l. on the Paita Peninsula, and at 18 ± 3 m a.s.l. on the Illescas Peninsula and the Bay of Bayovar (Pedoja et al., 2006). Farther south, MIS 5e terraces are exceptionally high in the San Juan de Marcona area immediately south of the subducting Nazca Ridge, with maximum elevations of 80 m at the Cerro Trés Hermanas and 105 m at the Cerro El Huevo (Hsu et al., 1989; Ortlieb & Macharé, 1990; Saillard et al., 2011). The Pampa del Palo region in southern Peru exhibits relatively thick vertical stacks of shallow marine terrace deposits related to MIS 7, 5e (~20 m), and 5c that may indicate a different geodynamic behavior compared to adjacent regions (Ortlieb et al., 1996). In central and northern Chile, Pleistocene to probably Pliocene marine terraces occur at 250–400, 150–240, 80–130, and 30–40 m and in southern Chile at 170–200, 70, 20–38, and 8–10 m (Fuenzalida et al., 1965). Specifically, between 24° S and 32° S, paleo-shoreline elevations of the last interglacial (MIS 5e) range between 25 and 45 m (Ota et al., 1995; Saillard et al., 2009; Martinod et al., 2016). Shore platforms are higher in the Altos de Talinay area (30.3°–31.3° S),

but are small, poorly preserved, and terminate at a high coastal scarp between 26.75° S and 24° S (Martinod et al., 2016). Shoreline-angle elevations between 34° and 38° S (along the Maule seismotectonic segment) vary from high altitudes in the Arauco and Topocalma areas (200 m) to moderate elevations near Carranza (110 m) and to very low elevations in between (15 m) (Melnick et al., 2009; Jara-Muñoz et al., 2015).

Coastal uplift-rate estimates along the WSAC mainly comprise calculations for the Talara Arc, the San Juan de Marcona area, the Mejillones Peninsula, the Altos de Talinay area, and several regions in south-central Chile. Along the Talara Arc (6.5° S to 1° N), marine terraces of the Manta Peninsula and La Plata Island in central Ecuador indicate the most pronounced uplift rates of 0.31 to 0.42 mm/yr since MIS 5e, while similar uplift rates are documented to the north in the Esmeraldas area (0.34 mm/yr), and lower ones to the south at the Santa Elena Peninsula (0.1 mm/yr). In northern Peru, last interglacial uplift rates are relative low, ranging from 0.17–0.21 mm/yr for the Tablazo Lobitos and 0.16 mm/yr for the Paita Peninsula, to 0.12 mm/yr for the Bay of Bayovar and the Illescas Peninsula (Pedoja et al., 2006; Pedoja et al., 2006). Marine terraces on the continental plate above the subducting Nazca Ridge (13.5°–15.6° S) record variations in uplift rate where the coastal forearc above the northern flank of the ridge is either stable or has undergone net subsidence (Macharé & Ortlieb, 1992). The coast above the ridge crest has been rising at about 0.3 mm/yr and the coast above the southern flank (San Juan de Marcona) has been uplifting at a rate of 0.5 mm/yr (Hsu, 1992) or even 0.7 mm/yr (Ortlieb & Macharé, 1990) for at least the last 125 kyr. Saillard et al. (2011) state that long-term regional uplift in the San Juan de Marcona area has increased since about 800 ka related to the southward migration of the Nazca Ridge, and ranges from 0.44 to 0.87 mm/yr. The Pampa del Palo area in southern Peru rose more slowly or was even down-faulted and had subsided with respect to the adjacent coastal regions (Ortlieb et al., 1996). These movements ceased after the highstand during the MIS 5e and slow-uplift rates of approximately 0.16 mm/yr have characterized the region since 100 ka (Ortlieb et al., 1996). In northern Chile (24°–32° S), uplift rates for the Late Pleistocene average around 0.28 ± 0.15 mm/yr (Martinod et al., 2016), except for the Altos de Talinay area, where pulses of rapid uplift occurred during the Middle Pleistocene (Ota et al., 1995; Saillard et al., 2009; Martinod et al., 2016). The central Andean rasa (15°–33° S) and Lower to Middle Pleistocene shore platforms – which are also generally wider – indicate a period of tectonic stability or subsidence followed by accelerated and spatially continuous uplift after ~400 ka (MIS 11; Regard et al., 2010; Rodríguez et al., 2013; Martinod et al., 2016).

However, according to Melnick (2016), the central Andean rasa has experienced slow and steady long-term uplift with a rate of 0.13 ± 0.04 mm/yr during the Quaternary, predominantly accumulating strain through deep earthquakes at the crust–mantle boundary (Moho) below the locked portion of the plate interface. The lowest uplift rates occur at the Arica bend and increase gradually southward; the highest values are attained along geomorphologically distinct peninsulas (Melnick, 2016). In the Maule segment (34°-38° S), the mean uplift rate for the MIS 5 terrace level is 0.5 mm/yr, exceeded only in the areas of Topocalma, Carranza, and Arauco, where it amounts to 1.6 mm/yr (Melnick et al., 2009; Jara-Muñoz et al., 2015). Although there are several studies of marine terraces along the WSAC, these are isolated and based on different methodological approaches, mapping and leveling resolutions, and dating techniques, which make regional comparisons and correlations difficult in the context of the data presented here.

2.3.2.3 Climate

Apart from latitudinal temperature changes, the present-day morphotectonic provinces along the South American margin have a pronounced impact on the precipitation gradients on the west coast of South America. Since mountain ranges are oriented approximately perpendicular to moisture-bearing winds, they affect both flanks of the orogen (Strecker et al., 2007). The regional-scale pattern of wind circulation is dominated by westerly winds at subtropical and extratropical latitudes primarily up to about 27° S (Garreaud, 2009). However, anticyclones over the South Pacific result in winds blowing from the south along the coast between 35° S and 10° S (Garreaud, 2009). The moisture in the equatorial Andes (Ecuador and Colombia) and in the areas farther south (27° S) is fed by winds from the Amazon basin and the Gulf of Panama, resulting in rainfall mainly on the eastern flanks of the mountain range (Bendix et al., 2006; Bookhagen & Strecker, 2008; Garreaud, 2009). The Andes of southern Ecuador, Peru, and northern Chile are dominated by a rain-shadow effect that causes aridity within the Andean Plateau (Altiplano-Puna), the Western Cordillera, and the coastal region (Houston & Hartley, 2003; Strecker et al., 2007; Garreaud, 2009). Furthermore, the aridity is exacerbated by the effects of the cold Humboldt current, which prevents humidity from the Pacific from penetrating inland (Houston & Hartley, 2003; Garreaud, 2009; Coudurier-Curveur et al., 2015). The precipitation gradient reverses between 27° S and 35° S where the Southern Hemisphere westerlies cause abundant rainfall on the western flanks of the Coastal and Main cordilleras (Garreaud, 2009). Martinod et al. (2016) proposed that latitudinal differences in climate largely influence coastal morphology, specifically the formation of high coastal scarps that prevent the

development of extensive marine terrace sequences. However, the details of this relationship have not been conclusively studied along the full extent of the Pacific coast of South America.

2.4 Methods

We combined – and describe in detail below – bibliographic information, different topographic data sets, and uniform morphometric and statistical approaches to assess the elevation of marine terraces and accompanying vertical deformation rates along the western South American margin.

2.4.1 Mapping of marine terraces

Marine terraces are primarily described based on their elevation, which is essential for determining vertical deformation rates. The measurements of the marine terrace elevations of the last interglacial were performed using TanDEM-X topography (12 and 30 m horizontal resolution; German Aerospace Center, 2018) and digital terrain models from lidar (1, 2.5, and 5 m horizontal resolution). The digital elevation models (DEMs) were converted to orthometric heights by subtracting the EGM2008 geoid and projected in the universal transverse mercator (UTM) coordinate system using the World Geodetic System (WGS1984) using zone 19S for Chile, zone 18S for southern and central Peru, and zone 17S for northern Peru and Ecuador.

To trace the MIS 5 shoreline, we mapped its inner edge along the west coast of South America based on slope changes in TanDEM-X topography at the foot of paleo-cliffs (Fig. 2.2a, b; Jara-Muñoz et al., 2016). To facilitate mapping, we used slope and hillshade maps. We correlated the results of the inner-edge mapping with the marine terraces catalog of Pedoja et al. (2011) and references therein (section 0, Table 2.1). Further references used to validate MIS 5e terrace heights include Victor et al. (2011) for the Pampa de Mejillones, Martinod et al. (2016) for northern Chile, and Jara-Muñoz et al. (2015) for the area between 34° and 38° S. We define the term ‘referencing point’ for these previously published terrace heights and age constraints. The referencing point with the shortest distance to the location of our measurements served as a topographical and chronological benchmark for mapping the MIS 5 terrace in the respective areas. In addition, this distance is used to assign a quality rating (QR) to our measurements.

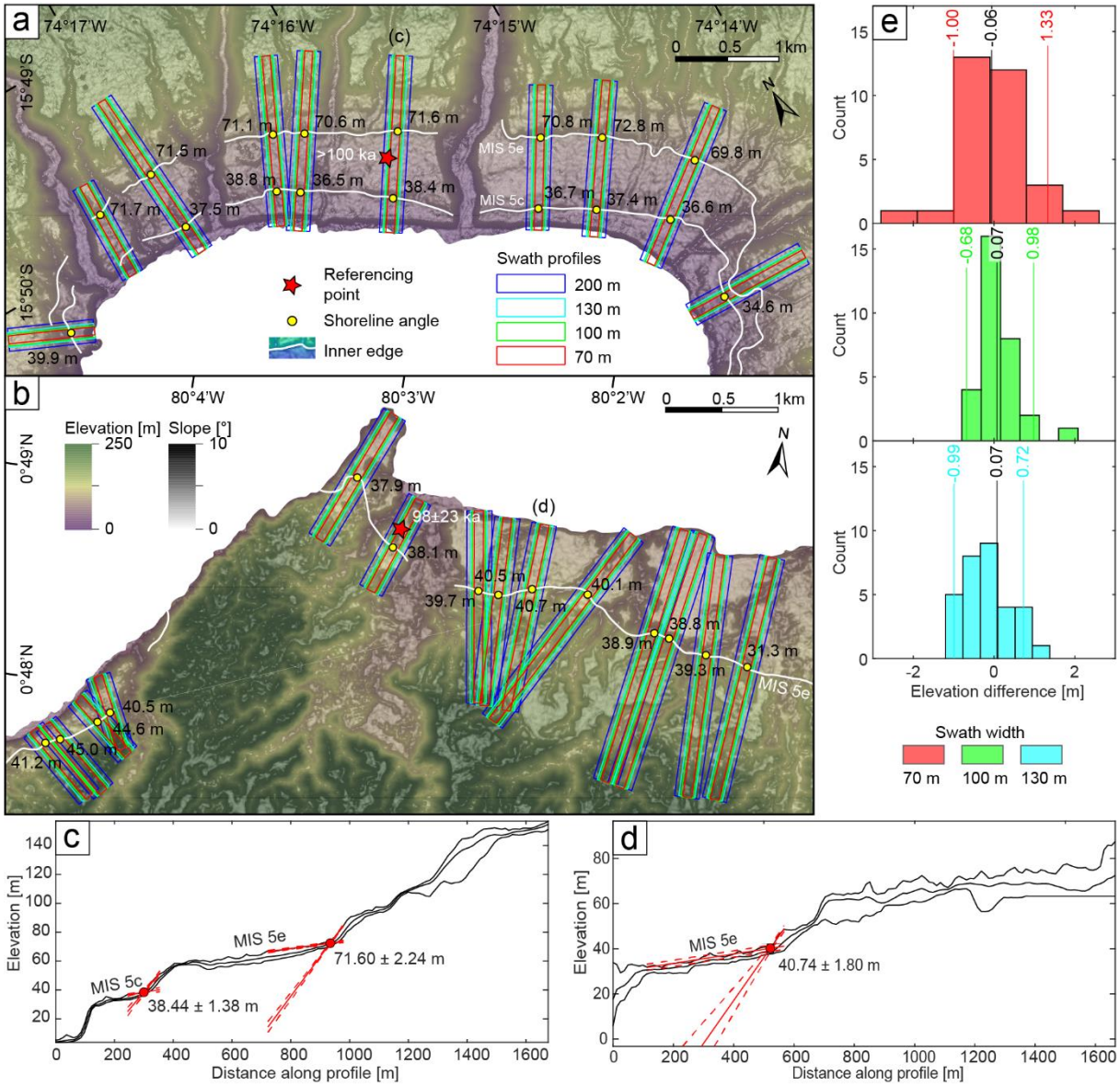

Figure 2.2: Orthometrically corrected TanDEM-X and slope maps of (a) Chala Bay in south-central Peru and (b) Punta Galera in northern Ecuador with mapped inner shoreline edges of the MIS 5e and 5c terrace levels. Colored rectangles represent swath-profile boxes of various widths that were placed perpendicular to the inner edges for the subsequent estimation of terrace elevation in TerraceM. The red star indicates the referencing point with the age constraint for the respective area (Pedoja et al., 2006; Saillard, 2008). Panels (c) and (d) show the estimation of shoreline-angle elevations in TerraceM by intersecting linear-regression fits of the paleo-cliff and paleo-platform (200-m-wide swath profiles). (e) Histograms of elevation differences measured in both areas for various swath widths (70 m, 100 m, and 130 m) with respect to the 200-m-wide reference swath profile (blue). Vertical lines indicate median values and standard deviations (2σ).

In addition to MIS 5e, we also mapped MIS 5c in areas with high uplift rates such as at the Manta Peninsula, San Juan de Marcona, Topocalma, Carranza, and Arauco. Although we observed a terrace level correlated to MIS 5a in the Marcona area, we excluded this level from the database due to its limited preservation at other locations and lack of chronological constraints. Our assignment of mapped terrace levels to MIS 5c is primarily based on age

constraints by Saillard et al. (2011) for the Marcona area and Jara-Muñoz et al. (2015) for the area between 34° and 38° S. However, in order to evaluate the possibility that our correlation with MIS 5c is flawed, we estimated uplift rates for the lower terraces by assigning them tentatively to either MIS 5a or MIS 5c. We interpolated the uplift rates derived from the MIS 5e level at the sites of the lower terraces and compared the differences (Fig. 2.3a). If we infer that uplift rates were constant in time at each site throughout the three MIS 5 substages, the comparison suggests these lower terrace levels correspond to MIS 5c because of the smaller difference in uplift rate rather than to MIS 5a (Fig. 2.3b).

Table 2.1: Age constraints used for mapping of the inner edge of MIS 5 and for verifying our terrace-elevation measurements. This compilation is mainly based on the terrace catalog of Pedoja et al. (2011); added references include Victor et al. (2011) for Pampa de Mejillones, Martinod et al. (2016) for northern Chile, and Jara-Muñoz et al. (2015) for south-central Chile. Absolute ages refer to MIS 5e marine terraces, unless otherwise specified; inferred ages refer to their associated MIS. IRSL: infrared-stimulated luminescence, AAR: amino-acid racemization, CRN: cosmogenic radionuclides, ESR: electron-spin resonance.

Country	Location	Lat.	Long.	Dating method	Confid-ence	Reference	Age [ka]
Ecuador	Galera	0.81	-80.03	IRSL	5	Pedoja et al., 2006b	98±23
Ecuador	Manta	-0.93	-80.66	IRSL, U/Th	5	Pedoja et al., 2006b	76±18, 85±1
Ecuador	La Plata	-1.26	-81.07	U/Th	5	Pedoja et al., 2006b	104±2
Ecuador	Manta	-1.27	-80.78	IRSL	5	Pedoja et al., 2006b	115±23
Ecuador	Santa Elena	-2.21	-80.88	U/Th	5	Pedoja et al., 2006b	136±4, 112±2
Ecuador	Puna	-2.60	-80.40	U/Th	5	Pedoja et al., 2006b	98±3, 95±0
Peru	Cancas	-3.72	-80.75	Morpho-stratigraphy	5	Pedoja et al., 2006b	~125
Peru	Mancora/ Lobitos	-4.10	-81.05	Morpho-stratigraphy	5	Pedoja et al., 2006b	~125
Peru	Talara	-4.56	-81.28	Morpho-stratigraphy	5	Pedoja et al., 2006b	~125
Peru	Paita	-5.03	-81.06	Morpho-stratigraphy	5	Pedoja et al., 2006b	~125
Peru	Bayovar/ Illescas	-5.31	-81.10	IRSL	5	Pedoja et al., 2006b	111±6
Peru	Cerro Huevo	-15.31	-75.17	CRN	5	Saillard et al., 2011	228±28 (7e)
Peru	Chala Bay	-15.85	-74.31	CRN	5	Saillard, 2008	> 100
Peru	Ilo	-17.55	-71.37	AAR	5	Ortlieb et al., 1996b; Hsu et al., 1989	~125, ~105
Chile	Punta Lobos	-20.35	-70.18	U/Th, ESR	5	Radtke, 1989	~125
Chile	Cobija	-22.55	-70.26	Morpho-stratigraphy	4	Ortlieb et al., 1995	~125, ~105
Chile	Michilla	-22.71	-70.28	AAR	3	Leonard & Wehmiller, 1991	~125

Chile	Hornitos	-22.85	-70.30	U/Th	5	Ortlieb et al., 1996	108±1, 118±6
Chile	Chacaya	-22.95	-70.30	AAR	5	Ortlieb et al., 1996a	~125
Chile	Pampa Mejillones	-23.14	-70.45	U/Th	5	Victor et al., 2011	124±3
Chile	Mejillones/ Punta Jorge	-23.54	-70.55	U/Th, ESR	3	Radtke, 1989	~125
Chile	Coloso	-23.76	-70.46	ESR	3	Schellmann & Radtke, 1997	106±3
Chile	Punta Piedras	-24.76	-70.55	CRN	5	Martinod et al., 2016b	138±15
Chile	Esmeralda	-25.91	-70.67	CRN	5	Martinod et al., 2016b	79±9
Chile	Caldera	-27.01	-70.81	U/Th, ESR	5	Marquardt et al., 2004	~125
Chile	Bahia Inglesa	-27.10	-70.85	U/Th, ESR	5	Marquardt et al., 2004	~125
Chile	Caleta Chanaral	-29.03	-71.49	CRN	5	Martinod et al., 2016b	138±0
Chile	Coquimbo	-29.96	-71.34	AAR	5	Leonard & Wehmiller, 1992; Hsu et al., 1989	~125
Chile	Punta Lengua de Vaca	-30.24	-71.63	U/Th	5	Saillard et al., 2012	95±2 (5c)
Chile	Punta Lengua de Vaca	-30.30	-71.61	U/Th	5	Saillard et al., 2012	386±124 (11)
Chile	Quebrada Palo Cortado	-30.44	-71.69	CRN	5	Saillard et al., 2009	149±10
Chile	Rio Limari	-30.63	-71.71	CRN	5	Saillard et al., 2009	318±30 (9c)
Chile	Quebrada de la Mula	-30.79	-71.70	CRN	5	Saillard et al., 2009	225±17 (7e)
Chile	Quebrada del Teniente	-30.89	-71.68	CRN	5	Saillard et al., 2009	678±51 (17)
Chile	Puertecillo	-34.09	-71.94	IRSL	5	Jara-Munoz et al., 2015	87±7 (5c)
Chile	Pichilemu	-34.38	-71.97	IRSL	5	Jara-Munoz et al., 2015	106±9 (5c)
Chile	Putu	-35.16	-72.25	IRSL	5	Jara-Munoz et al., 2015	85±8 (5c)
Chile	Constitución	-35.40	-72.49	IRSL	5	Jara-Munoz et al., 2015	105±8 (5c)
Chile	Constitución	-35.44	-72.47	IRSL	5	Jara-Munoz et al., 2015	124±11
Chile	Carranza	-35.58	-72.61	IRSL	5	Jara-Munoz et al., 2015	67±6 (5c)
Chile	Carranza	-35.64	-72.54	IRSL	5	Jara-Munoz et al., 2015	104±9
Chile	Pelluhue	-35.80	-72.54	IRSL	5	Jara-Munoz et al., 2015	112±10
Chile	Pelluhue	-35.80	-72.55	IRSL	5	Jara-Munoz et al., 2015	102±9 (5c)
Chile	Curanipe	-35.97	-72.78	IRSL	5	Jara-Munoz et al., 2015	265±29
Chile	Arauco	-37.62	-73.67	IRSL	5	Jara-Munoz et al., 2015	89±9 (5c)
Chile	Arauco	-37.68	-73.57	CRN	5	Melnick et al., 2009	127±13
Chile	Arauco	-37.71	-73.39	CRN	5	Melnick et al., 2009	133±14
Chile	Arauco	-37.76	-73.38	CRN	5	Melnick et al., 2009	130±13
Chile	Cerro Caleta Curiñanco	-39.72	-73.40	Tephro-chronology	4	Pino et al., 2002	~125
Chile	South Curiñanco	-39.76	-73.39	Tephro-chronology	4	Pino et al., 2002	~125

Chile	Valdivia	-39.80	-73.39	Tephro-chronology	4	Pino et al., 2002	~125
Chile	Camping Bellavista	-39.85	-73.40	Tephro-chronology	4	Pino et al., 2002	~125
Chile	Mancera	-39.89	-73.39	Tephro-chronology	5	Silva, 2005	~125

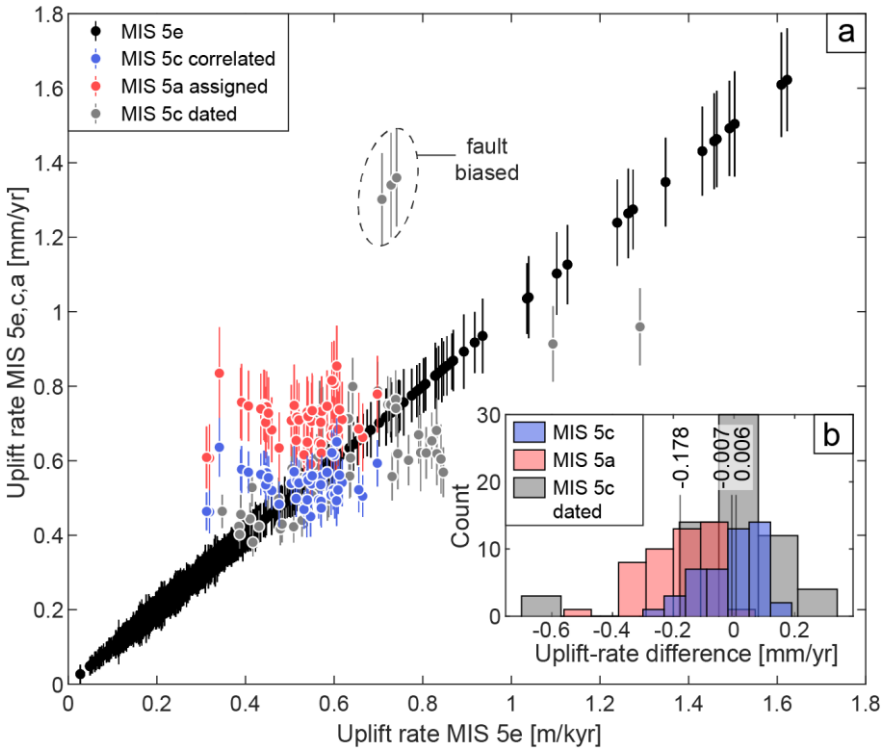

Figure 2.3: Comparison of MIS 5 uplift-rate estimates. (a) Uplift rates derived by correlating mapped terrace occurrences located immediately below the MIS 5e level to either MIS 5c (blue) or MIS 5a (red) with respect to MIS 5e uplift rates. Marine terraces correlated to MIS 5c by an age constraint are plotted in gray color. (b) Histograms of differences between MIS 5a or MIS 5c uplift rates and MIS 5e uplift rates. Vertical lines show median uplift-rate differences. See section 2.3.2.2. for relative sea-level elevations of MIS 5a, 5c, and 5e.

A rigorous assessment of marine terrace elevations is crucial for determining accurate vertical deformation rates. Since fluvial degradation and hillslope processes subsequent to the abandonment of marine terraces may alter terrace morphology (Anderson et al., 1999; Jara-Muñoz et al., 2015), direct measurements of terrace elevations at the inner edge (foot of the paleo-cliff) may result in overestimation of the terrace elevations and vertical deformation rates (Jara-Muñoz et al., 2015). To precisely measure the shoreline-angle elevations of the MIS 5 terrace level, we used a profile-based approach in TerraceM, a graphical user interface in MATLAB® (Jara-Muñoz et al., 2016); www.terracem.com (last access: 6 May 2021). We placed swath profiles of variable width perpendicular to the previously mapped inner edge, which were used by the TerraceM algorithm to extract maximum elevations to avoid areas of fluvial incision (Fig. 2.2a, b). For the placement of the swath profiles we tried to capture a local

representation of marine terrace topography with a sufficiently long, planar paleo-platform, and a sufficiently high paleo-cliff, simultaneously avoiding topographic disturbances, such as colluvial wedges or areas affected by incision. North of Caleta Chañaral (29° S), we used swath profiles of 200 m width, although we occasionally used 100-m-wide profiles for narrow terrace remnants. South of 29° S, we used swath widths of 130 and 70 m. The width was chosen based on fluvial drainage densities that are associated with precipitation gradients.

Sensitivity tests comparing shoreline-angle measurements from different swath widths in the Chala Bay and at Punta Galera show only minimal vertical deviations of less than 0.5 m (Fig. 2.2e). The sections of these profiles, which represent the undisturbed paleo-platform and paleo-cliff areas, were picked manually and fitted by linear regression. The extrapolated intersection between both regression lines ultimately allowed us to determine the buried shoreline-angle elevation and associated uncertainty, which is derived from the 95 % confidence interval (2σ) of both regressions (Fig. 2.2c, d). In total, we measured 1843 MIS 5e and 110 MIS 5c shoreline-angle elevations. To quantify the paleo-position of the relative sea-level elevation and the involved uncertainty for the WALIS database, we calculated the indicative meaning for each marine terrace measurement using the IMCalc software from Lorscheid and Rovere (2019). The indicative meaning comprises the range between the lower and upper limits of sea-level formation – the indicative range – as well as its mathematically averaged position, which corresponds to the reference water level (Lorscheid & Rovere, 2019). Table 2.2 documents the medians and standard deviations of these values for four extensive regions along the WSAC.

Table 2.2: Median values and standard deviations (2σ) representing the indicative meaning along the WSAC. The four sectors were chosen based on their main geomorphic characteristics (see results section).

	Upper limit of modern analog [m]	Lower limit of modern analog [m]	Reference water level [m]	Indicative range [m]
Ecuador and northern Peru	2.89 ± 0.16	-1.78 ± 0.47	0.54 ± 0.21	4.66 ± 0.65
Central and southern Peru	2.98 ± 0.31	-3.05 ± 0.52	-0.03 ± 0.11	6.06 ± 0.90
Northern Chile	3.01 ± 0.15	-2.89 ± 0.30	0.06 ± 0.08	5.90 ± 0.51
Central Chile	3.21 ± 0.19	-3.03 ± 0.38	0.07 ± 0.11	6.25 ± 0.60

To quantify the reliability and consistency of our shoreline-angle measurements, we developed a quality rating from low (1) to high (5) confidence. Equation 2.1 illustrates how we calculated the individual parameters and the overall quality rating:

$$QR = 1 + 2.4 * \left(\frac{C_{RP}}{\max(C_{RP})} * \left(1 - \frac{D_{RP}}{\max(D_{RP})}\right)\right)^{e} + 1.2 * \left(1 - \frac{E_T}{\max(E_T)}\right) + 0.4 * 1.2 * \left(1 - \frac{R}{\max(R)}\right)$$

(Eq. 2.1)

The four parameters included in our quality rating (QR) comprise a) the distance to the nearest referencing point (D_{RP}), b) the confidence of the referencing point based on the dating method used by previous studies (C_{RP}) (Pedoja et al., 2011), c) the measurement error in TerraceM (E_T), and (d) the pixel-scale resolution of the topographic data set (R; Fig. 2.4). We did not include the error that results from the usage of different swath widths since the calculated elevation difference with respect to the most frequently used 200 m swath width is very low (< 0.5 m) (Fig. 2.2e). From the reference points we only used data points with a confidence value of 3 or greater (1 – poor, 5 – very good) based on the previous qualification of Pedoja et al. (2011). The confidence depends mainly on the reliability of the dating method, but can be increased by good age constraints of adjacent terrace levels or detailed morphostratigraphic correlations, such as in Chala Bay (Fig. 2.2a; Goy et al., 1992; Saillard, 2008). We further used this confidence value to quantify the quality of the age constraints in the WALIS template.

To account for the different uncertainties of the individual parameters in the QR, we combined and weighted the parameters D_{RP} and C_{RP} in a first equation claiming 60 % of the final QR, E_T in a second and R in a third equation weighted 30 % and 10 %, respectively. We justify these percentages by the fact that the distance and confidence to the nearest referencing point is of utmost importance for identifying the MIS 5e terrace level. The measurement error represents how well the mapping of the paleo-platform and paleo-cliff resulted in the shoreline-angle measurement, while the topographic resolution of the underlying DEM only influences the precise representation of the actual topography and has little impact on the measurement itself. The coefficient assigned to the topographic resolution is multiplied by a factor of 1.2 in order to maintain the possibility of a maximum QR for a DEM resolution of 5 m. Furthermore, we added an exponent to the first part of the equation to reinforce low confidence and/or high distance of the referencing point for low-quality ratings. The exponent adjusts the QR according to the distribution of distances from referencing points, which follows an exponential relationship (Fig. 2.4d).

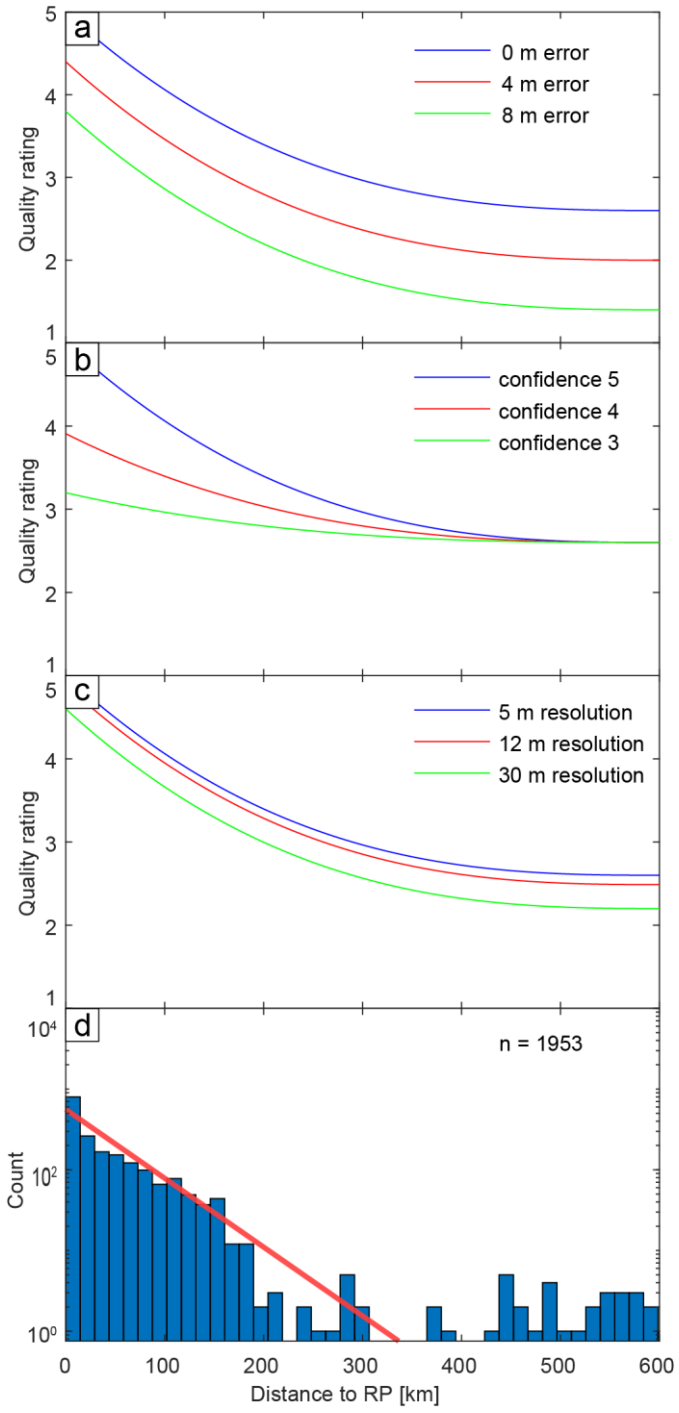

Figure 2.4: Influence of the parameters on the quality rating. The x-axis is the distance to reference point (RP), the y-axis is the quality rating, the color lines represent different values of quality-rating parameters. While one parameter is being tested, the remaining parameters are set to their best values. That is why the QR does not reach values of 1 in the graphs displayed here. (a) Shoreline-angle elevation error. (b) Confidence value of the referencing point. (c) Topographic resolution of the DEM used for terrace-elevation estimation. (d) Histogram displaying the distribution of distances between each shoreline-angle measurement and its nearest RP (n: number of measurements). The red line is an exponential fit.

The influence of each parameter to the quality rating can be observed in Fig. 2.4. We observe that for high D_{RP} values the QR becomes constant; likewise, the influence of QR parameters becomes significant for QR values higher than 3. We justify the constancy of the QR for high D_{RP} values (> 300 km) by the fact that most terrace measurements have D_{RP} values below 200 km (Fig. 2.4d). The quality rating is then used as a descriptor of the confidence of marine terrace-elevation measurements.

2.4.2 Estimating coastal uplift rates

Uplift-rate estimates from marine terraces *(u)* were calculated using equations 2.2 and 2.3:

$$\Delta H = H_T - H_{SL} \quad \text{(Eq. 2.2)}$$

$$u = \frac{H_T - H_{SL}}{T} \quad \text{(Eq. 2.3)}$$

where ΔH is the relative sea level, H_{SL} is the sea-level altitude of the interglacial maximum, H_T is the shoreline-angle elevation of the marine terrace, and T is its associated age (Lajoie, 1986).

We calculated the standard error *SE(u)* using equation 2.4 from Gallen et al. (2014):

$$SE(u)^2 = u^2 \left(\left(\frac{\sigma_{\Delta H}^2}{\Delta H^2} \right) + \left(\frac{\sigma_T^2}{T^2} \right) \right) \quad \text{(Eq. 2.3)}$$

where $\sigma_{\Delta H}^2$, the error in relative sea level, equals $(\sigma_{H_T}^2 + \sigma_{H_{SL}}^2)$. The standard-error estimates comprise the uncertainty in shoreline-angle elevations from TerraceM (σ_{H_T}), error estimates in absolute sea level $(\sigma_{H_{SL}})$ from Rohling et al. (2009), and an arbitrary range of 10 kyr for the duration of the highstand (σ_T).

Vertical displacement rates and relative sea level are influenced by flexural rebound associated with loading and unloading of ice sheets during glacio-isostatic adjustments (GIAs; Stewart et al., 2000; Shepherd & Wingham, 2007). The amplitude and wavelength of GIAs is mostly determined by the flexural rigidity of the lithosphere (Turcotte & Schubert, 1982) and should therefore not severely influence vertical deformation along non-glaciated coastal regions (Rabassa & Clapperton, 1990) that are located in the forearc of active subduction zones. This is supported by Creveling et al. (2017) who showed no significant GIA along the WSAC between 1° N and 40° S since MIS 5a. Current GIA models use an oversimplified lithospheric structure defined by horizontal layers of homogeneous rheology (Creveling et al., 2017), which might be appropriate for cratons and ocean basins, but not necessarily for the forearcs of subduction margins. Therefore, we did not account for the GIA effect on terrace elevations and uplift rates.

2.4.3 Tectonic parameters of the South American convergent margin

We compared the deformation patterns of marine terraces along the coast of South America with proxies that included crustal faults, bathymetric anomalies, trench-sediment thickness, and distance to the trench. To evaluate the possible control of climatic parameters in the morphology of marine terraces, we compared our data set with wave heights, tidal range, mean annual precipitation rate, and the azimuth of the coastline (Fig. 2.1; Schweller et al., 1981; Bangs & Cande, 1997; von Huene et al., 1997; Collot et al., 2002; Ceccherini et al., 2015; Hayes et al., 2018; Santibáñez et al., 2019; GEBCO Bathymetric Compilation Group, 2020).

To evaluate the potential correlations between tectonic parameters and marine terraces, we analyzed the latitudinal variability of these parameters projected along a curved 'simple profile' and a 300-km-wide 'swath profile' following the trace of the trench. We used simple profiles for visualizing 2D data sets; for instance, to compare crustal faults along the forearc area of the margin (Veloza et al., 2012; Maldonado et al., 2021), we projected the seaward tip of each fault. For the trench-sediment thickness, we projected discrete thickness estimates based on measurements from seismic reflection profiles of Bangs and Cande (1997), Collot et al. (2002), von Huene et al. (1996), and Schweller et al. (1981). Finally, we projected the discrete trench distances from the point locations of our marine terrace measurements along a simple profile. To compare bathymetric features on the oceanic plate, we used a compilation of bathymetric measurements at 450 m resolution (GEBCO Bathymetric Compilation Group, 2020). The data set was projected along a curved, 300-km-wide swath profile using TopoToolbox (Schwanghart & Kuhn, 2010).

Finally, to elucidate the influence of climatic factors on marine terrace morphology, we compared the elevation, but also the number of measurements as a proxy for the preservation and exposure of marine terraces. We calculated wave heights, tidal ranges, and reference water levels at the point locations of our marine terrace measurements using the indicative meaning calculator (IMCalc) from Lorscheid and Rovere (2019). We used the maximum values of the hourly significant wave height, and for the tidal range we calculated the difference between the highest and lowest astronomical tide. The reference water level represents the averaged position of the paleo-sea level with respect to the shoreline-angle elevation and, together with the indicative range (uncertainty), quantifies the indicative meaning (Lorscheid & Rovere, 2019). We furthermore used the high-resolution data set of Ceccherini et al. (2015) for mean annual

precipitation, and we compared the azimuth of the coast in order to evaluate its exposure to wind and waves. To facilitate these comparisons, we extracted the values of all these parameters at the point locations of our marine terrace measurements and projected them along a simple profile. Calculations and outputs were processed and elaborated using MATLAB® 2020b.

2.5 Results

2.5.1 Marine terrace geomorphology and shoreline-angle elevations

In the following sections we describe our synthesized database of last interglacial marine terrace elevations along the WSAC. Marine terraces of the last interglacial are generally well preserved and almost continuously exposed along the WSAC, allowing the estimation of elevations with a high spatial density. To facilitate the descriptions of marine terrace-elevation patterns, we divided the coastline into four sectors based on their main geomorphic characteristics (Fig. 2.5): 1) the Talara bend in northern Peru and Ecuador, 2) southern and central Peru, 3) northern Chile, and 4) central and south-central Chile. In total we carried out 1843 MIS 5e terrace measurements with a median elevation of 30.1 m a.s.l. and 110 MIS 5c terrace measurements with a median of 38.6 m. The regions with exceptionally high marine terrace elevations (≥ 100 m) comprise the Manta Peninsula in Ecuador, the San Juan de Marcona area in south-central Peru, and three regions in south-central Chile (Topocalma, Carranza, and Arauco). Marine terraces at high altitudes (≥ 60 m) can also be found in Chile on the Mejillones Peninsula, south of Los Vilos, near Valparaíso, in Tirúa, and near Valdivia, while terrace levels only slightly above the median elevation are located at Punta Galera in Ecuador, south of Puerto Flamenco, at Caldera and Bahía Inglesa, near Caleta Chañaral, and near the Quebrada El Moray in the Altos de Talinay area in Chile. In the following sections we describe the characteristics of each site in detail; the names of the sites are written in brackets following the same nomenclature as in the WALIS database (i.e., Pe – Peru, Ec – Ecuador, Ch – Chile).

2.5.1.1 Ecuador and northern Peru (1° N–6.5° S)

The MIS 5e terrace levels in Ecuador and northern Peru [sites Ec1 to Ec4 and Pe1] are discontinuously preserved along the coast (Fig. 2.6). They often occur at low elevations (between 12 m and 30 m) and show abrupt local changes in elevation, reaching a maximum at

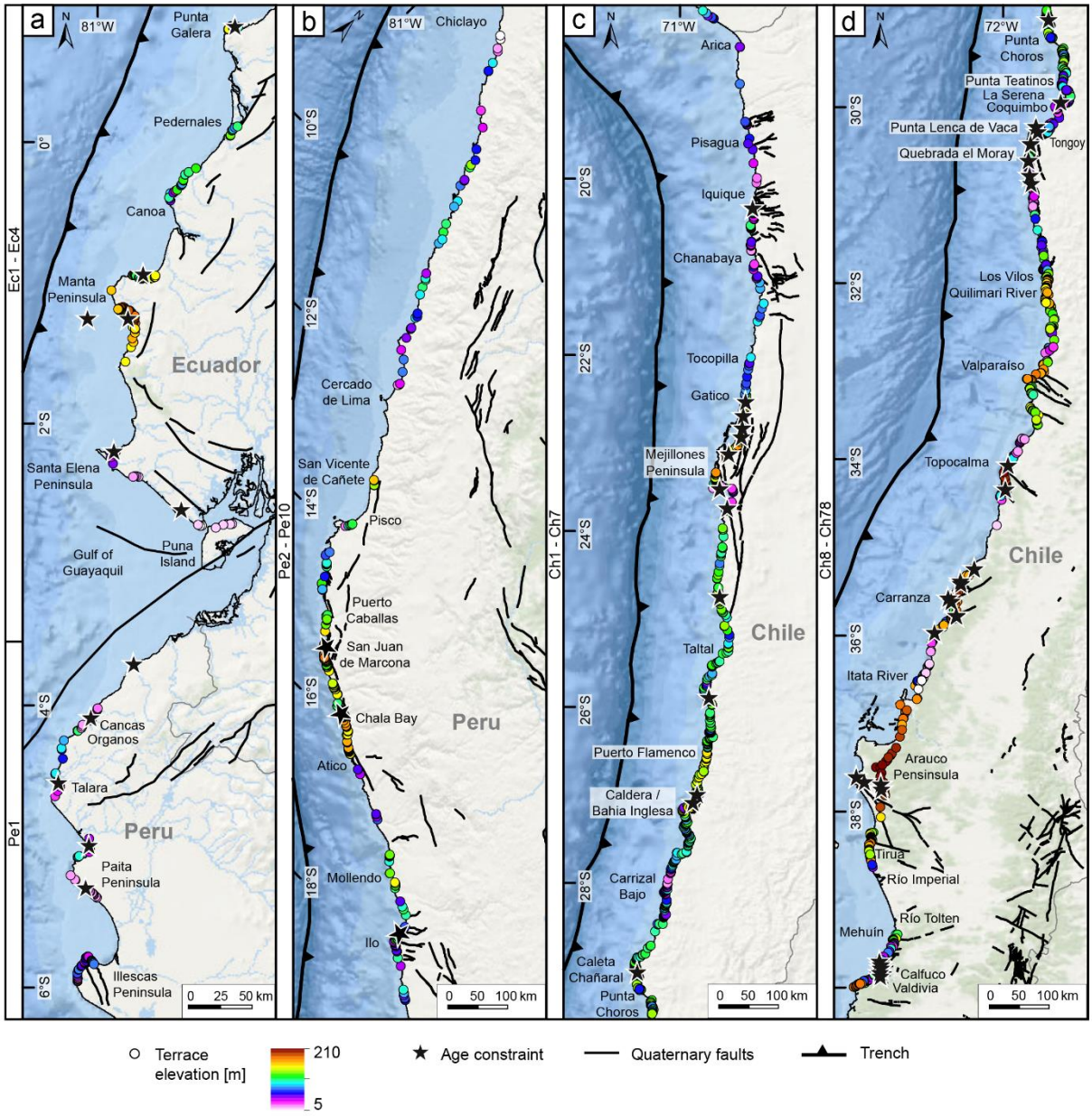

Figure 2.5: Shoreline-angle elevation measurements (colored points), referencing points (black stars), Quaternary faults (bold black lines; Veloza et al., 2012; Maldonado et al., 2021), and locations mentioned in the text for the four main geomorphic segments (for location see Fig. 2.1a; World Ocean Basemap: Esri, Garmin, GEBCO, NOAA NGDC, and other contributors). Site names referring to the entries in the WALIS database are on the left margin of each panel (Pe – Peru, Ec – Ecuador, Ch – Chile). (a) Talara bend in Ecuador and northern Peru. (b) Central and southern Peru. (c) Northern Chile. (d) Central and south-central Chile.

the Manta Peninsula. Punta Galera in northern Ecuador displays relatively broad and well-preserved marine terraces ranging between 40 and 45 m elevation that rapidly decrease eastward to about 30 m a.s.l. across the Cumilínche fault [Ec1]. Farther south, between Pedernales and Canoa [Ec1], narrow terraces occur at lower altitudes of 22–34 m a.s.l. A long-wavelength (~120 km) pattern in terrace-elevation change can be observed across the Manta

Peninsula with the highest MIS 5e terraces peaking at ~100 m a.s.l. at its southern coast [Ec2]. This terrace level is hardly visible in its highest areas with platform widths smaller than 100 m due to deeply incised and narrowly spaced river valleys. We observe lower and variable elevations between 30 and 50 m across the Rio Salado fault in the San Mateo paleo-gulf in the north, while the terrace elevations increase gradually from ~40 m in the Pile paleo-gulf in the south [Ec3] toward the center of the peninsula (El Aromo dome) and the Montecristi fault [Ec3]. A lower terrace level correlated to MIS 5c displays similar elevation patterns as MIS 5e within the Pile paleo-gulf and areas to the north. Near the Gulf of Guayaquil and the Dolores–Guayaquil megashear, the lowest terrace elevations occur at the Santa Elena Peninsula ranging between 17 and 24 m a.s.l., even lower altitudes in its southern part, and between 11 and 16 m a.s.l. on the Puna Island [Ec4]. In northern Peru [Pe1], we observe dismembered MIS 5e terraces in the coastal area between Cancas and Talara below the prominent Mancora Tablazo. 'Tablazo' is a local descriptive name used in northern Peru (~3.5–6.5° S) for marine terraces that cover a particularly wide surface area (Pedoja et al., 2006). South of Cancas, MIS 5e terrace elevations range between 17 and 20 m a.s.l., reaching 32 m near Organos, and vary between 20 and 29 m in the vicinity of Talara. In the southward continuation of the Talara harbor, the Talara Tablazo

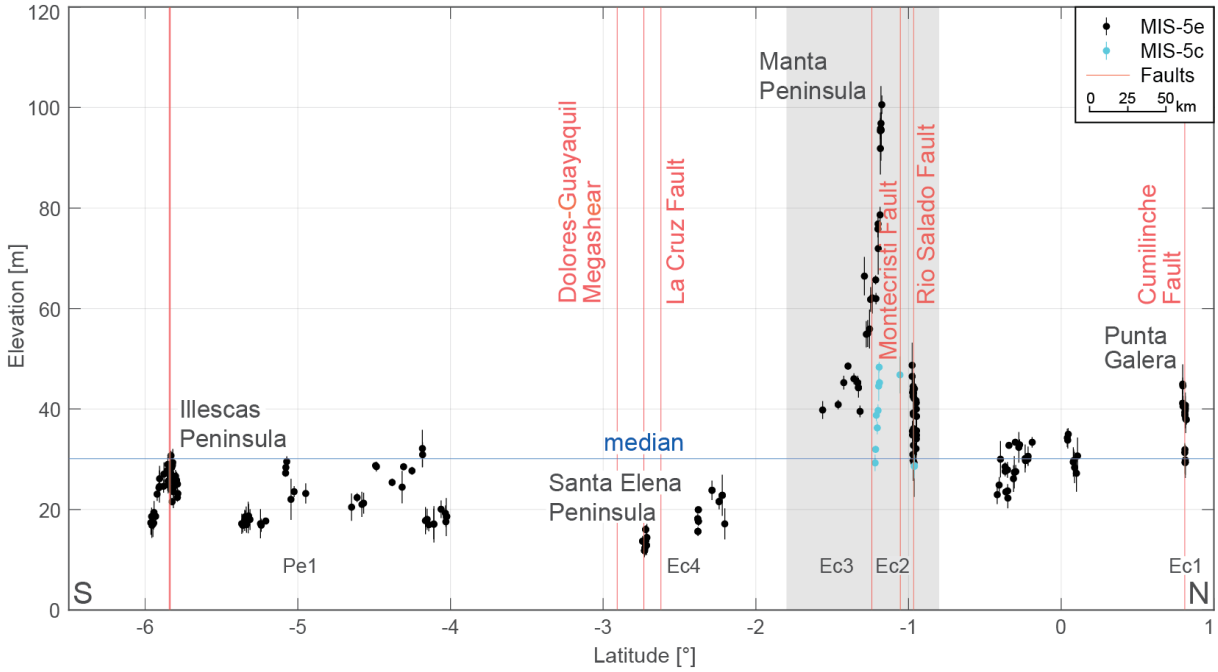

Figure 2.6: Measured shoreline-angle elevations of MIS 5e and 5c terraces in Ecuador (Ec) and northern Peru (Pe). A high and inferred long-wavelength change in terrace elevation occurs at the Manta Peninsula (gray area) and at low elevations farther south at the Santa Elena Peninsula. Several terrace-elevation changes over short distances coincide with faulting at Punta Galera and on the Illescas Peninsula. Median elevation: 30.1 m. For location see Fig. 2.5a.

widens, with a lower marine terrace at about 23 m a.s.l. immediately north of Paita Peninsula reaching 30 m a.s.l. in the northern part of the peninsula. The last occurrence of well-preserved MIS 5e terraces in this sector exists at the Illescas Peninsula, where terrace elevations decrease from around 30 m to 17 m a.s.l. southward.

2.5.1.2 Central and southern Peru (6.5°–18.3° S)

This segment comprises marine terraces at relatively low and constant elevations, but which are rather discontinuous [sites Pe2 to Pe10], except in the San Juan de Marcona area, where the terraces increase in elevation drastically (Fig. 2.7). The coast in north-central Peru exhibits poor records of MIS 5e marine terraces characterized by mostly narrow and discontinuous remnants that are sparsely distributed along the margin with limited age constraints. Marine terraces increase in elevation from 11 to 35 m a.s.l. south of Chiclayo [Pe2] and decrease to 17 m a.s.l. near Cercado de Lima [Pe3, Pe4], forming a long-wavelength (~600 km), small amplitude (~20 m) upwarped structure. The MIS 5e terrace levels are better expressed in the south-central and southern part of Peru at elevations between 35 and 47 m a.s.l. in San Vicente de Cañete, decreasing to approximately 30 m a.s.l. in the vicinity of Pisco [Pe5]. South of Pisco, the coastal area becomes narrow with terrace elevations ranging between 25 and 34 m a.s.l. [Pe6] and increasing abruptly to 74–79 m near Puerto Caballas and the Río Grande delta. MIS 5e terrace elevations are highest within the San Juan de Marcona area, reaching 93–109 m at Cerro Huevo and 56–87 m at Cerro Trés Hermanas [Pe7]. These higher terrace elevations coincide with a wider coastal area, a better-preserved terrace sequence, and several crustal faults, such as the San Juan and El Huevo faults.

Terrace heights west of Yauca indicate a further decrease to 50–58 m before a renewed increase to 70–72 m can be observed in the Chala embayment [Pe8]. We observe a similar trend in elevation changes for the shoreline angles attributed to the MIS 5c interglacial within the previously described high-elevation area: 31–39 m near the Río Grande delta, 58–62 m below the Cerro Huevo peak, 27–64 m below the Cerro Trés Hermanas peak [Pe7], 36–40 m near Yauca, and 34–40 m within the Chala embayment [Pe8]. Besides various changes in between, terrace elevations decrease slowly from 54 m south of the Chala region to 38 m near Atico [Pe8]. The overall decrease south of the San Juan de Marcona area therefore contrasts strikingly with the sharper decrease to the north. These high-elevation marine terraces, which extend ~250 km along the coast from north of the San Juan de Marcona area to south of Chala Bay, constitute one of the longest wavelength structures of the WSAC. Southeast of Atico, less well-preserved

marine terraces appear again in the form of small remnants in a narrower coastal area. Starting with elevations as low as 24 m, MIS 5e terrace altitudes increase southeastward to up to 40 m near Mollendo [Pe9] before they slightly decrease again. The broader and quite well-preserved terraces of the adjacent Ilo area resulted in a smooth increase from values greater than 25 m to 33 m and a sudden decrease to as low as 22 m across the Chololo fault [Pe9]. North of the Arica bend, shoreline-angle measurements yielded estimates of 24–29 m in altitude [Pe10].

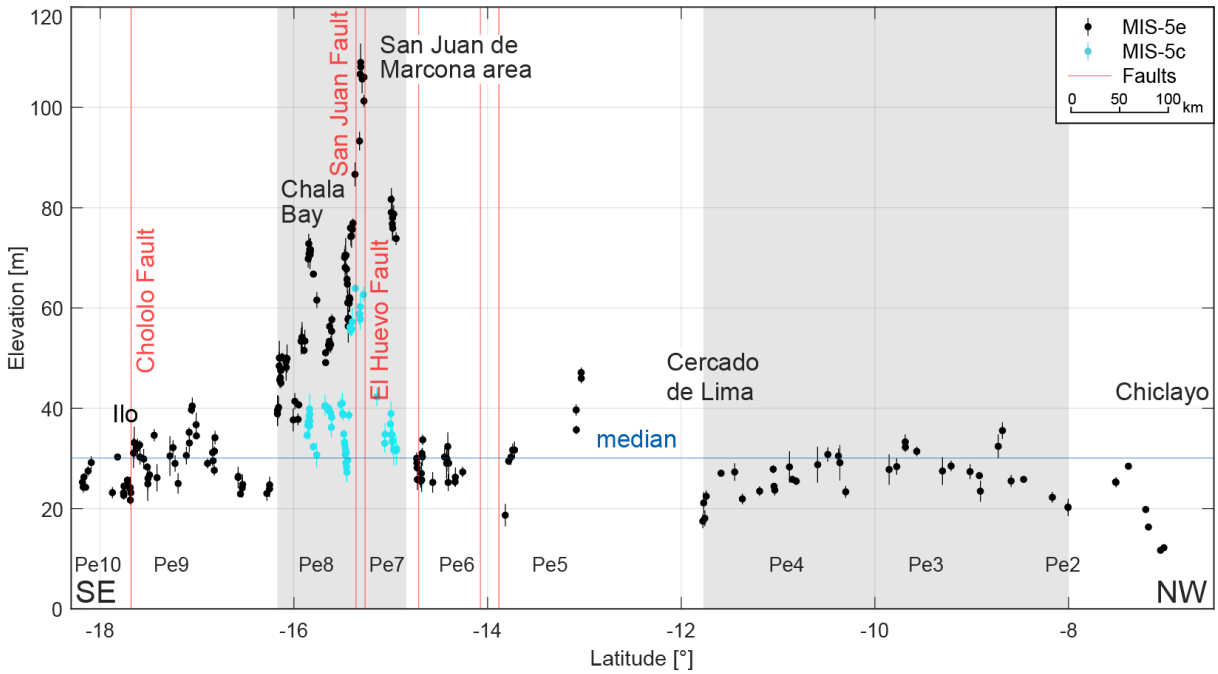

Figure 2.7: Measured shoreline-angle elevations of MIS 5e and 5c terraces in central and southern Peru (Pe). While only sparsely preserved terraces below the median (30.1 m) occur in central Peru between Chiclayo and Lima, a relatively broad and asymmetric distribution of marine terraces characterizes the area of San Juan de Marcona. For location see Fig. 2.5b.

2.5.1.3 Northern Chile (18.3°–29.3° S)

Along the northern Chilean coast, marine terraces of the MIS 5e are characterized by a variable elevation pattern and the occurrence of numerous crustal faults associated with the Atacama fault system, although the changes in terrace elevation are not as pronounced as in the northern segments (Fig. 2.8) [sites Ch1 to Ch7]. The local widening of the coastal area near the Arica bend narrows southward with MIS 5e terraces at elevations of between 24 and 28 m a.s.l. in northernmost Chile [Ch1]. Just north of Pisagua, we measured shoreline-angle elevations of well-preserved marine terraces between 19 and 26 m across the Atajana fault [Ch1]. An areally limited zigzag pattern starting with shoreline-angle elevation values of 32 m south of Iquique and south of the Zofri and Cavancha faults decreases rapidly to approximately 22 m but increases again to similar altitudes and drops as low as 18 m toward Chanabaya south of the

Barranco Alto fault [Ch1]. A gentle, steady rise in terrace elevations can be observed south of Tocopilla where altitudes of 25 m are attained. South of Gatico, terrace markers of the MIS 5e highstand increase and continue northward for much of the Mejillones Peninsula within an approximate elevation range of 32–50 m a.s.l. before reaching a maximum of 62 m a.s.l. at the Pampa de Mejillones [Ch2]. With its ~100 km latitudinal extent, we consider this terrace-elevation change to be a medium-wavelength structure. Although no MIS 5e terrace levels have been preserved at the Morro Mejillones Horst (Binnie et al., 2016), we measured shoreline-angle elevations at the elevated southwestern part of the peninsula that decrease sharply from 55 to 17 m a.s.l. in the vicinity of the Mejillones fault system [Ch2]. After a short interruption of the MIS 5e terrace level at Pampa Aeropuerto, elevations remain relatively low between 19 and 25 m farther south [Ch2]. Along the ~300-km coastal stretch south of Mejillones, marine terraces are scattered along the narrow coastal area ranging between 25 and 37 m a.s.l. [Ch3]. South of Puerto Flamenco, MIS 5e terrace elevations range between 40 and 45 m a.s.l. until Caldera and Bahía Inglesa [Ch4]. The MIS 5e marine terrace elevations decrease abruptly south of the Caldera fault and the Morro Copiapó (Morro Copiapó fault) to between 25 and 33 m a.s.l., reaching 20 m a.s.l. north of Carrizal Bajo [Ch4]. In the southernmost part of the northern

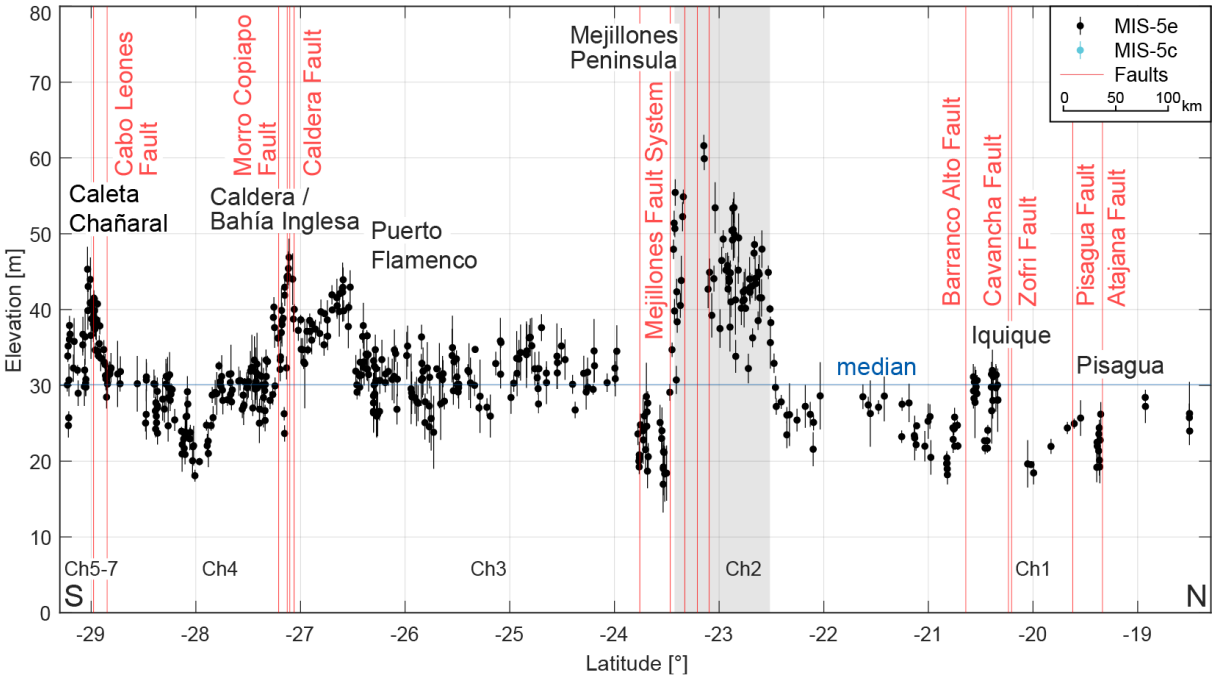

Figure 2.8: Measured shoreline-angle elevations of MIS 5e and 5c terraces in northern Chile (Ch). Faults and asymmetrically uplifted marine terraces of up to 60 m elevation characterize the Mejillones Peninsula, reaching values below 20 m at the southern margin. Terrace elevations attain peak values south of Puerto Flamenco, at Caldera and Bahía Inglesa, and north of Caleta Chañaral, while in between minimum elevations below 20 m prevail (north of Carrizal Bajo). Median elevation: 30.1 m. For location see Fig. 2.5c.

Chilean sector, the MIS 5e terraces rise from around 30 m a.s.l. to a maximum of 45 m a.s.l. near the Cabo Leones fault [Ch4], before decreasing in elevation abruptly near Caleta Chañaral and Punta Choros [Ch5, Ch6, Ch7].

2.5.1.4 Central Chile (29.3°–40° S)

Marine terraces along central Chile display variable, high-amplitude terrace-elevation patterns associated with numerous crustal faults, and include a broad-scale change in terrace altitudes with the highest MIS 5e marine terrace elevations of the entire South American margin on the Arauco Peninsula (Fig. 2.9) [sites Ch8 to Ch78]. South of Punta Choros, marine terrace elevations decrease from values close to 40 to 22 m a.s.l. north of Punta Teatinos [Ch8, Ch9]. A maximum elevation of 40 m is reached by the terraces just south of this area [Ch10] whereas north of La Serena, a sharp decrease leads to values between 20 and 30 m for marine terraces south of Coquimbo Bay and in the Tongoy Bay area [Ch11, Ch12]. South of Punta Lengua de Vaca, our measurements of the exceptionally well-preserved staircase morphology of the terraces are within the same elevation range between 20 and 30 m, increasing slowly to 40 m near the Quebrada el Moray [Ch13]. Although we could not observe a significant change in terrace elevation across the Puerto Aldea fault, we measured an offset of ~7 m across the Quebrada Palo Cortado fault. MIS 5e terrace levels decrease thereafter and vary between 20 and 30 m in altitude until north of Los Vilos [Ch14–Ch18] where they increase in elevation [Ch19], reaching 60 m near the Quilimari River [Ch20]. The marine terraces become wider in this area and are associated with scattered sea stacks. Decreasing farther south to only 20 m a.s.l. [Ch21–Ch25], the coastal area narrows and has terrace heights of up to 64 m near Valparaíso in an area that is cut by numerous faults (e.g., Valparaíso and Quintay faults) [Ch26–Ch32]. Another low-elevation area follows southward, with values as low as 17 m [Ch33–Ch35]. Farther south, between 34° S and 38° S, broad (~200 km at Arauco), medium (~45 km at Topocalma), and narrow (Carranza) upwarped zones occur that are manifested by variable terrace elevations. These include prominent high-terrace elevations at Topocalma with a maximum of 180 m [Ch36–Ch39], slightly lower levels of 110 m at Carranza [Ch42–Ch47], exceptionally low values near the Itata River (< 10 m) [Ch48–Ch64, Ch66], and the most extensive and highest shoreline-angle elevations on the Arauco Peninsula with elevations in excess of 200 m [Ch67–Ch73]. Additionally, we measured MIS 5c terrace elevations in the three higher exposed areas with a range of 20–55 m at Carranza, and a few locations at Topocalma (76–81 m) and Arauco (117–123 m). The medium-wavelength structure of

Topocalma is bounded by the Pichilemu and Topocalma faults, and near Carranza several fault offsets (e.g., Pelluhue and Carranza faults) are responsible for the short-wavelength changes in terrace elevation. In contrast, crustal faulting is nearly absent in the high-elevation and long-wavelength structure at Arauco. MIS 5e terrace elevations are highly variable within a small area south of the Arauco Peninsula near the Tirúa fault, increasing rapidly from 27 m to 78 m and decreasing thereafter to approximately 20 m [Ch74, Ch75]. The continuity of terraces is interrupted by the absence of terrace levels between the Imperial and Toltén rivers but resumes afterwards with a highly frequent zigzag pattern and multiple faults (e.g., Estero Ralicura and Curinanco faults) from as low as 18 m to a maximum of 40 m [Ch76, Ch77]. In this area locations with the highest terrace levels comprise the terraces near Mehuín and Calfuco. A final increase in shoreline-angle elevations from about 20–30 m up to 76 m near Valdivia coincides with the southern terminus of our terrace-elevation measurements [Ch78].

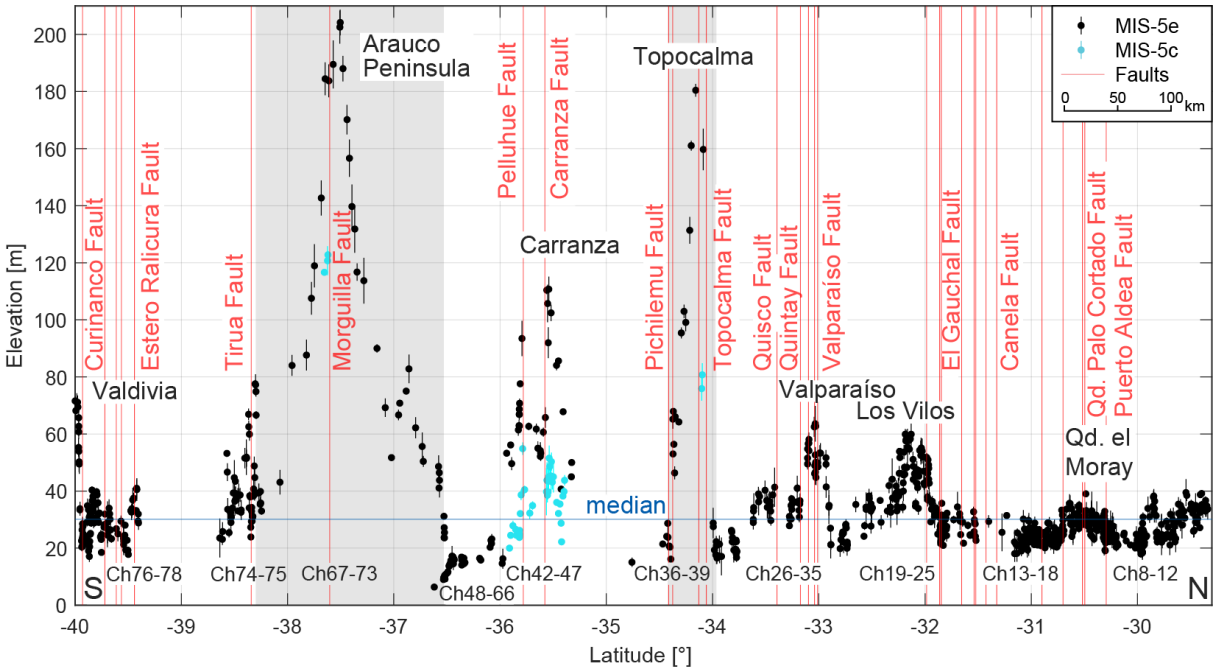

Figure 2.9: Measured shoreline-angle elevations of MIS 5e and 5c terraces in central Chile (Ch). Extensive faulting coincides with various high-terrace elevations of the last interglacial highstand north of Los Vilos, near Valparaíso, at Topocalma, Carranza, and near Valdivia. The most pronounced long-wavelength change in terrace elevation occurs on the Arauco Peninsula with maximum elevations over 200 m and minimum elevations below 10 m north of Concepción. Qd. – Quebrada. Median elevation: 30.1 m. For location see Fig. 2.5d.

2.5.2 Statistical analysis

Our statistical analysis of mapped shoreline-angle elevations resulted in a maximum kernel density at 28.96 m with a 95 % confidence interval from 18.59 m to 67.85 m (2σ) for the MIS

5e terrace level (Fig. 2.10a). The MIS 5c terrace yielded a maximum kernel density at a higher elevation of 37.20 m with 2σ ranging from 24.50 m to 63.92 m. It is important to note that the number of MIS 5c measurements is neither as high nor as continuous as compared to that of the MIS 5e level. MIS 5c data points were measured almost exclusively at sites where MIS 5e reaches high elevations (e.g., San Juan de Marcona with MIS 5e elevations between 40 and 110 m).

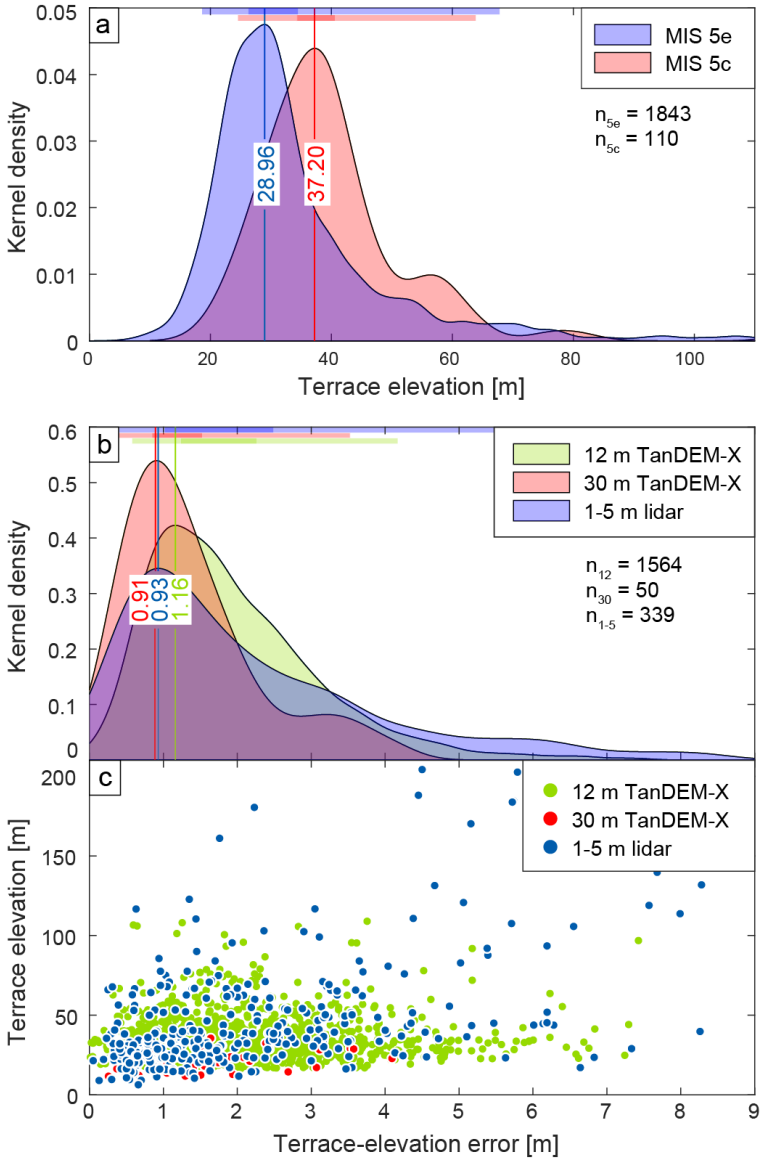

Figure 2.10: Statistical analysis of measured shoreline-angle elevations. (a) Kernel-density plot of MIS 5e and 5c terrace elevations with maximum likelihood probabilities (MLPs) at 28.96 m elevation for MIS 5e and 37.20 m elevation for MIS 5c (*n*: number of measurements). Colored bars on top highlight the standard deviations σ and 2σ. (b) Kernel densities and their associated standard-deviation (σ and 2σ) calculations of terrace-elevation errors for source DEMs of various resolutions. The measurements on the most abundant DEM, 12 m TanDEM-X, have an MLP error of 1.16 m, while the 30 m TanDEM-X and the 1–5 m LIDAR produce slightly lower errors of 0.91 m and 0.93 m, respectively. (c) Terrace-elevation errors plotted against terrace elevation for the individual source DEMs. Although the point density for high terrace elevations is low, a weak correlation of high errors with high terrace elevations can be observed.

The distribution of measurement errors was studied using probability kernel-density plots for each topographic resolution (1–5 m lidar, 12 m TanDEM-X, and 30 m TanDEM-X). The three data sets display similar distributions and maximum likelihood probabilities (MLPs); for instance, lidar data show an MLP of 0.93 m, the 12 m TanDEM-X an MLP of 1.16 m, and 30 m TanDEM-X an MLP of 0.91 m (Fig. 2.10b). We observe the lowest errors from the 30 m

TanDEM-X, slightly higher errors from the 1–5 m lidar data, and the highest errors from the 12 m TanDEM-X. This observation is counterintuitive as we would expect lower errors for topographic data sets with higher resolution (1–5 m lidar). The reason for these errors is probably related to the higher number of measurements using the 12 m TanDEM-X (1564) in comparison with the measurements using 30 m TanDEM-X (50), which result in a higher dispersion and a more realistic representation of the measurement errors (Fig. 2.10b). In addition, the relation between terrace elevations and error estimates shows that comparatively higher errors are associated with higher terrace elevations, although the sparse point density of high terrace-elevation measurements prevents the recognition of a clear correlation (Fig. 2.10c).

2.5.3 Coastal uplift-rate estimates

We calculated uplift rates from 1953 terrace-elevation measurements of MIS 5e (1843) and MIS 5c (110) along the WSAC with a median uplift rate of approximately 0.22 mm/yr (Fig. 2.11). As with the distribution of terrace elevations, we similarly observed several small-scale and large-scale, high-amplitude changes in uplift rate along the coast. The most pronounced long-wavelength highs (≥ 1° latitude) in uplift rate are located on the Manta Peninsula (0.79 mm/yr), in the San Juan de Marcona area (0.85 mm/yr), and on the Arauco Peninsula (1.62 mm/yr). Medium-wavelength structures include the Mejillones Peninsula (0.47 mm/yr) and Topocalma (1.43 mm/yr), while shorter wavelength structures that are characterized by exceptionally high uplift rates seem to be limited to the central Chilean part of the coastline, especially between 31.5° and 40° S. The most striking example includes Carranza with an uplift rate of up to 0.87 mm/yr since the formation of the oldest MIS 5 terrace levels. Lower, but still quite high, uplift rates were calculated for areas north of Los Vilos (0.46 mm/yr), near Valparaíso (0.49 mm/yr), and near Valdivia (0.59 mm/yr). The lowest uplift rates along the South American margin occur at Penco immediately north of Concepción (0.03 mm/yr), south of Chiclayo in northern Peru (0.07 mm/yr), and on the southern Santa Elena Peninsula in Ecuador (0.07 mm/yr).

2.6 Discussion

2.6.1 Advantages and limitations of the database of last interglacial marine terrace elevations along the WSAC

In this study we generated a systematic database of last interglacial marine terrace elevations with unprecedented resolution based on an almost continuous mapping of ~2000 measurements along 5000 km of the WSAC. This opens up several possibilities for future applications in which this database can be used; for example, marine terraces are excellent strain markers that can be used in studies on deformation processes at regional scale, and thus the synthesis allows for comparisons between deformation rates at different temporal scales in different sectors of the margin or analyses linking specific climate-driven and tectonic coastal processes, and landscape evolution. However, there are a number of limitations and potential uncertainties that can limit the use of this database in such studies without taking several caveats into consideration.

One of the most critical limitations of using the database is associated with the referencing points used to tie our marine terrace measurements, which are in turn based on the results and chronological constraints provided by previous studies. The referencing points are heterogeneously distributed along the WSAC, resulting in some cases with distances of up to 600 km to the nearest constrained point, such as in Central Peru [e.g., Pe2]. This may have a strong influence on the confidence in the measurement of the marine terrace elevation at these sites. In addition, the geochronological control of some of the referencing points may be based on dating methods with pronounced uncertainties (e.g., amino-acid racemization, electron-spin resonance, terrestrial cosmogenic radionuclides), which may result in equivocal interpretations and chronologies of marine terrace levels. In order to address these potential factors of uncertainty we defined a quality rating (see section 2.4.1) which allows us to classify our mapping results based on their confidence and reliability. Therefore, by considering measurements above a defined quality it is possible to increase the level of confidence for future studies using this database; however, this might result in a decrease in the number of measurements available for analysis and comparison.

2.6.2 Tectonic and climatic controls on the elevation and morphology of marine terraces along the WSAC

In this section we provide a brief synthesis of our data set and its implications for coastal processes and overall landscape evolution influenced by a combination of tectonic and climatic forcing factors. This synthesis emphasizes the significance of our comprehensive data set for a variety of coastal research problems that were briefly introduced in section 2.6.1. Our detailed measurements of marine terraces along the WSAC reveal variable elevations and a heterogeneous distribution of uplift rates associated with patterns of short, medium, and long wavelengths. In addition, we observe different degrees of development of marine terraces along the margin expressed in variable shoreline-angle densities. There are several possible causes for this variability, which we explore by comparing terrace-elevation patterns with different climatic and tectonic parameters.

2.6.2.1 Tectonic controls on coastal uplift rates

The spatial distribution of the MIS 5 marine terrace elevations along the convergent South American margin has revealed several high-amplitude and long-wavelength changes with respect to tectonically controlled topography. Long-wavelength patterns in terrace elevation (~10^2 km) are observed at the Manta Peninsula in Ecuador, central Peru between Chiclayo and Lima, San Juan de Marcona (Peru), and on the Arauco Peninsula in Chile, while medium-wavelength structures occur at Mejillones Peninsula and Topocalma (Chile). Instead, short-wavelength patterns in MIS 5 terrace elevations are observed, for instance, near Los Vilos, Valparaíso, and Carranza in Chile.

The subduction of bathymetric anomalies has been shown to exert a substantial influence on upper-plate deformation (Fryer & Smoot, 1985; Taylor et al., 1987; Macharé & Ortlieb, 1992; Cloos & Shreve, 1996; Gardner et al., 2013; Wang & Bilek, 2014; Ruh et al., 2016), resulting in temporally and spatially variable fault activity, kinematics, and deformation rates (Mann et al., 1998; Saillard et al., 2011; Morgan & Bangs, 2017; Melnick et al., 2019). When comparing the uplift pattern of MIS 5 marine terraces and the bathymetry of the oceanic plate, we observe that the two long-wavelength structures in this area, on the Manta Peninsula and at San Juan de Marcona, both coincide with the location of the subducting Nazca and Carnegie ridges, respectively (Fig. 2.11a, b); this was also previously observed by other authors (Macharé &

Ortlieb, 1992; Gutscher et al., 1999; Pedoja et al., 2006; Saillard et al., 2011). In summary, long-wavelength structures in coastal areas of the upper plate may be associated with deep-seated processes (Melosh & Raefsky, 1980; Watts & Daly, 1981) possibly related to changes in the mechanical behavior of the plate interface. In this context it is interesting that the high uplift rates on the Arauco Peninsula do not correlate with bathymetric anomalies, which may suggest a different deformation mechanism. The scarcity of crustal faults described in the Arauco area rather suggests that shallow structures associated with crustal bending and splay faults occasionally breaching through the upper crust (Melnick et al., 2012; Jara-Muñoz et al., 2015; Jara-Muñoz et al., 2017; Melnick et al., 2019) may cause long-wavelength warping and uplift there (Fig. 2.11a).

In contrast, small-scale bathymetric anomalies correlate in part with the presence of crustal faults perpendicular to the coastal margin near, for instance, the Juan Fernández, Taltal, and Copiapó ridges (Fig. 2.11b); this results in short-wavelength structures and a more localized altitudinal differentiation of uplifted terraces. This emphasizes also the importance of last interglacial marine terraces as strain markers with respect to currently active faults, which might be compared in the future with short-term deformation estimates from GPS or the earthquake catalog. In summary, short-wavelength structures in the coastal realms of western South America may be associated with faults that root at shallow depths within the continental crust (Jara-Muñoz et al., 2015; Jara-Muñoz et al., 2017; Melnick et al., 2019).

The thickness of sediment in the trench is an additional controlling factor on forearc architecture that may determine which areas of the continental margin are subjected to subduction erosion or accretion (Hilde, 1983; Cloos & Shreve, 1988; Menant et al., 2020). Our data show that the accretionary part of the WSAC (south of the intersection with the Juan Fernández Ridge at 32.9° S) displays faster median uplift rates of 0.26 mm/yr than in the rest of the WSAC (Fig. 2.11b, c). However, no clear correlation is observed between trench fill, uplift rates, and the different structural patterns in the erosive part of the margin. On the other hand, we observe lower uplift rates for greater distances from the trench at the Arica bend, in central Peru, and in the Gulf of Guayaquil, while higher uplift rates occur in areas closer to the trench, such as near the Nazca and Carnegie ridges and the Mejillones Peninsula.

2.6.2.2 Climatic controls on the formation and preservation of last interglacial marine terraces

The latitudinal climate differences that characterize the western margin of South America may also control coastal morphology and the generation and preservation of marine terraces (Martinod et al., 2016). In order to evaluate the influence of climate in the generation and/or degradation of marine terraces, we compared the number of marine terrace measurements, which is a proxy for the degree of marine terrace preservation, and climatically controlled parameters such as wave height, tidal range, coastline orientation, and the amount of precipitation.

The maximum wave height along the WSAC decreases northward from ~8 to ~2 m (see section 2.4.3, Fig. 2.11d). Similarly, the tidal range decreases progressively northward from 2 to 1 m between Valdivia and San Juan de Marcona, followed by a rapid increase to 4 m between San Juan de Marcona and the Manta Peninsula. We observe an apparent correlation between the number of measurements and the tidal range in the north, between Illescas and Manta (Fig. 2.11f). Likewise, the increasing trend in the number of measurements southward matches with the increase in wave height (Fig. 2.11d). An increase in wave height and tidal range may lead to enhanced erosion and morphologically well-expressed marine terraces (Anderson et al., 1999; Trenhaile, 2002), which is consequently reflected in a higher number of measurements that can be carried out. Furthermore, we observe low values for the reference water level (< 0.7 m) resulting from tide and wave-height estimations in IMCalc (Lorscheid & Rovere, 2019), which are used to correct our shoreline-angle measurements in the WALIS database (see section 2.4.3).

The control of wave-erosion processes on the morphological expression of marine terraces may be counteracted by erosional processes such as river incision. We note that the high number of preserved marine terraces between Mejillones and Valparaíso decreases southward, which coincides with a sharp increase in mean annual precipitation from 10 to 1000 mm/yr (Fig. 2.11e, f) and fluvial dissection. However, in the area with a high number of measurements between the Illescas Peninsula and Manta we observe an opposite correlation: higher rainfall associated with an increase of marine terrace preservation (Fig. 2.11e). This suggests that the interplay between marine terrace generation and degradation processes apparently buffer each other, resulting in different responses under different climatic conditions and coastal settings.

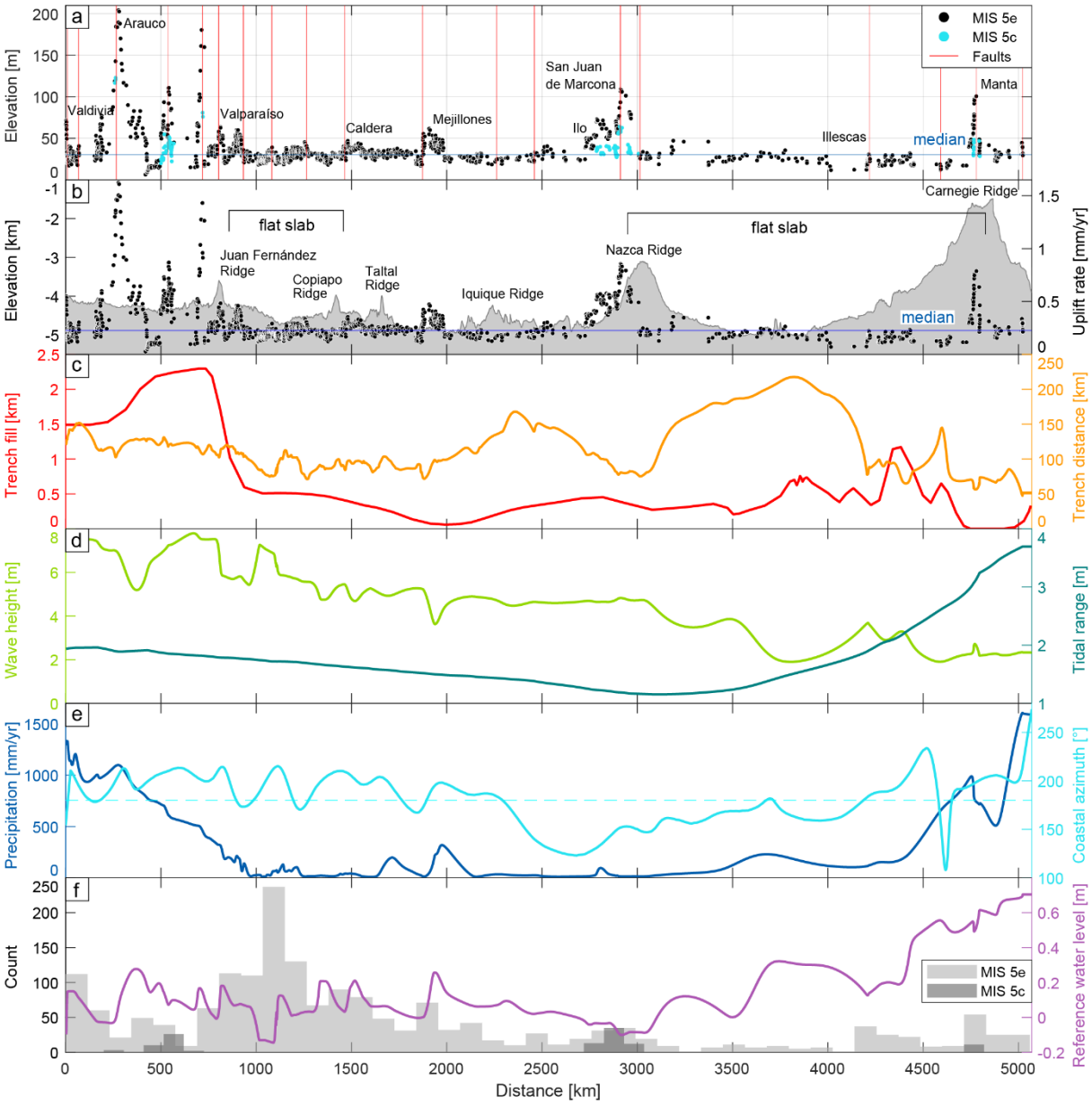

Figure 2.11: Terrace-elevation and uplift-rate estimates plotted in comparison with various parameters (i.e., bathymetry, trench fill, trench distance, wave height, tidal range, precipitation, and coastal azimuth) that might influence the disparate characteristics of the marine terrace distribution revealed by our data set. We projected these parameters, elevations, and uplift rates with respect to a north–south-oriented polyline that represents the trench. (a) Terrace-elevation measurements and the most important crustal faults (Veloza et al., 2012; Maldonado et al., 2021). This shows the range of altitudes in different regions along the coast and possible relationships between terrace elevation and crustal faulting. The blue horizontal line indicates the median elevation (30.1 m). (b) Coastal uplift rates and mean bathymetry (GEBCO Bathymetric Compilation Group, 2020) of a 150-km swath profile west of the trench. The blue horizontal line indicates the median uplift rate (0.22 mm/yr). (c) Sediment thickness of trench-fill deposits (red; Bangs & Cande, 1997) and the distance of the trench from our terrace measurements (orange). Flat-slab segments of the subducting Nazca plate are indicated for central Chile and Peru. (d) Maximum wave heights along the WSAC (light green) and the tidal range (dark green) between highest and lowest astronomical tides (Lorscheid & Rovere, 2019). (e) Precipitation (blue) along the WSAC (Ceccherini et al., 2015) and azimuthal orientation of the coastline (cyan). (f) Histogram of terrace-elevation measurements along the WSAC.

The greater number of marine terraces between Mejillones and Valparaíso and north of Illescas corresponds with a SSW–NNE orientation of the coastline (azimuth between 200 and 220°). In contrast, NW–SE- to N–S-oriented coastlines (azimuth between 125 and 180°), such as between the Arica and Huancabamba bends, correlate with a lower number of marine terrace measurements (Fig. 2.11e, f). This observation appears, however, implausible considering that NW–SE-oriented coastlines may be exposed more directly to the erosive effect of storm waves associated with winds approaching from the south. We interpret the orientation of the coastline therefore to be of secondary importance at regional scale for the formation of marine terraces compared to other parameters, such as wave height, tidal range, or rainfall.

2.7 Conclusions

We measured 1953 shoreline-angle elevations as proxies for paleo-sea levels of the MIS 5e and 5c terraces along ~5000 km of the WSAC between Ecuador and southern Chile. Our measurements are based on a systematic methodology and the resulting data have been standardized within the framework of the WALIS database. Our mapping was tied using referencing points based on previously published terrace-elevation estimates and age constraints that are summarized in the compilation of Pedoja et al. (2011). The limitations of this database are associated with the temporal accuracy and spatial distribution of the referencing points, which we attempt to consider by providing a quality-rating value to each measurement. The marine terrace elevations display a median value of 30.1 m for the MIS 5e level and a median uplift rate of 0.22 mm/yr for MIS 5e and 5c. The lowest terrace elevations and uplift rates along the entire WSAC occur immediately north of Concepción in Chile (6 m, 0.03 mm/yr), south of Chiclayo in northern Peru, and on the Santa Elena Peninsula in Ecuador (both 12 m, 0.07 mm/yr). The regions with exceptionally high marine terrace elevations (≥ 100 m) comprise the Manta Peninsula in Ecuador, the San Juan de Marcona area in south-central Peru, and three regions in south-central Chile (Topocalma, Carranza, and Arauco).

The pattern of terrace elevations displays short-, medium- and long-wavelength structures controlled by a combination of various mechanisms. Long-wavelength structures may be controlled by deep-seated processes at the plate interface, such as the subduction of major bathymetric anomalies (e.g., Manta Peninsula and San Juan de Marcona region). In contrast,

short- and medium-wavelength deformation patterns may be controlled by crustal faults rooted within the upper plate (e.g., between Mejillones and Valparaíso).

Latitudinal climate characteristics along the WSAC may influence the generation and preservation of marine terraces. An increase in wave height and tidal range generally results in enhanced erosion and morphologically well-expressed, sharply defined marine terraces, which correlates with the southward increase in the number of our marine terrace measurements. Conversely, river incision and lateral scouring in areas with high precipitation may degrade marine terraces, thus decreasing the number of potential marine terrace measurements, such as observed south of Valparaíso.

Chapter 3: Deciphering permanent uplift along the Pacific coast of South America through signal analysis of various tectonic parameters

3.1 Abstract

The tectonically active South American margin is characterized by the accumulation of deformation contributing to the uplift of the Andean forearc at millennial timescales. However, the mechanisms responsible for permanent coastal uplift are still debated, mainly because continental-scale analyses of uplifted terraces have not yet been carried out. Uplifted marine terraces are generally used to infer permanent coastal deformation and uplift; we used almost 2000 measurements of last interglacial marine terraces to calculate an uplift-rate signal and to perform a wavelength analysis. The same spectral analysis was applied to tectonic processes and subduction parameters associated with the accumulation of permanent deformation to detect possible links with the uplift rate. The uplift-rate signal displays a constant background rate along the margin, disturbed by changes of variable wavelengths. Similarities between its wavelength spectrum and the spectra of tectonic features suggest potential correlations pointing towards several underlying processes. For example, crustal faulting is mainly responsible for short-wavelength deformation; intermediate- to long-wavelength tectonic features indicate various extents of locked areas on the megathrust that relate to its long-term seismotectonic segmentation. We suggest that moderate, long-term background uplift is caused by modest, deep earthquakes near the Moho. Since the occurrence of these earthquakes is not continuous along the coast, we infer accumulation of permanent deformation over millennial timescales through multiple, distinct uplift phases that are spatially and temporally distributed. Our study highlights the application and utility of a novel signal-analysis approach to elucidate the mechanisms driving surface deformation in subduction zones at a continental scale.

3.2 Introduction

Multiple marine terraces and strandlines along the tectonically active coast of western South America record the accumulation of deformation that contributes to uplift of the Andean forearc at a variety of timescales (Darwin, 1846; Hsu, 1992; Regard et al., 2010; Saillard et al., 2011; Pedoja et al., 2014; Jara-Muñoz et al., 2015; Wesson et al., 2015; Melnick, 2016). The processes proposed to explain forearc deformation in this geodynamic setting include the subduction of bathymetric anomalies (Hsu, 1992; Pedoja et al., 2006; Saillard et al., 2011; Martinod et al., 2016), upper-plate deformation (Armijo & Thiele, 1990; Adam & Reuther, 2000; Armijo et al., 2015), underplating of subducted trench sediments (Glodny et al., 2005; Melnick & Echtler, 2006; Clift & Hartley, 2007; Bangs et al., 2020; Menant et al., 2020), and the motion of forearc slivers (Melnick et al., 2009; Jara-Muñoz et al., 2015). Importantly, while some authors propose successive earthquakes as a possible cause for coastal uplift (Melnick et al., 2006; Melnick, 2016; González-Alfaro et al., 2018), others suggest that uplift is achieved through interseismic deformation (Allmendinger & González, 2010; Jolivet et al., 2020; Madella & Ehlers, 2021). The different processes addressed here are not mutually restrictive, and in all likelihood a combination of different factors may be responsible for deformation and uplift of coastal areas. However, the relative significance of different individual mechanisms for long-term coastal uplift is still debated, and analyses of continental-scale deformation patterns along the South American convergent margin are lacking, thus leaving two open fundamental questions: (1) What mechanisms control the accumulation of permanent deformation in the forearc? (2) When does permanent deformation accumulate? These two questions are fundamental to our understanding of tectonically active coastal regions, not only in South America but also on a global scale. Clarification of these issues is therefore central both to the assessment of coastal tectonic landforms and their use in deciphering the characteristics of long-term plate-boundary tectonism, but also to seismogenesis and associated hazards on much shorter timescales that include, for example, the earthquake cycle.

Along tectonically active clastic coasts, the signal of permanent deformation at 10^4–10^6 year timescales is preserved in the morphology of marine terraces that have evolved through the interplay between wave erosion and coastal retreat, tectonic uplift/subsidence, and climate-controlled, glacial-cycle sea-level oscillations (e.g., Lajoie, 1986). Marine terraces formed during the last interglacial ~125 ka ago are some of the most prominent and widely distributed

coastal landforms (Siddall et al., 2006; Pedoja et al., 2011), which have been used extensively to estimate long-term coastal uplift rates (Pedoja et al., 2011; Saillard et al., 2011; Muhs et al., 2014; Jara-Muñoz et al., 2015). However, along the western coast of South America varying methodological approaches to measure terrace elevation, coupled with discontinuous surveys focused primarily on locations with good terrace preservation, have largely prevented regional comparisons and lateral correlations of uplifted terraces. In this regard, the recently published database of Freisleben et al. (2021), which includes almost 2000 elevation measurements of the last interglacial terrace level in western South America, affords an opportunity to detect potential correlations between coastal deformation and the underlying tectonic mechanisms on a continental scale.

In this study, we performed spectral analysis to test for possible links between the uplift-rate signal of marine terraces along the western South American coast and various tectonic processes that have been proposed to be responsible for the accumulation of permanent deformation in the Andean forearc. To analyze spectral similarities between the individual signals, we carried out multiple signal analyses using Fast Fourier Transformations (FFTs). Spectral correlations between uplift rate and multiple tectonic features revealed several potential mechanisms responsible for different wavelengths of permanent deformation. With respect to the mechanisms being responsible for the continuous background signal of uplift rate along the western South American margin, we tested the hypothesis of Melnick (2016) and compared it to predictions of coastal uplift patterns by Jolivet et al. (2020). Melnick (2016) proposed moderate, domain-C earthquakes (M7–M8, ~35–55 km depth) down-dip of the interseismically locked megathrust to accumulate anelastic and therefore permanent deformation. While this hypothesis argues for coastal deformation not being associated with the seismic cycle of mega-earthquakes, Jolivet et al. (2020) suggested that a small portion of geodetically derived interseismic uplift rates translate into permanent deformation. Both hypotheses thus make contrary predictions as to when permanent deformation accumulates; we addressed this problem by comparing long-term uplift rates with cumulative vertical displacements of moderate, deep earthquakes as well as interseismic uplift rates. Our study features new methodological approaches and perspectives to further elucidate the role of tectonic processes with respect to the evolution of active continental margins at glacial-cycle timescales.

3.3 Geologic and tectonic setting

3.3.1 Coastal geomorphology and marine terraces along the western South American coast

The approximately 8000-km-long Andean orogen constitutes the major physiographic feature along the western portion of the South American continent. It is divided by the Huancabamba and Arica bends into distinctive geomorphic segments with different tectonic characteristics (Fig. 3.1a; Jaillard et al., 2000). From north to south along the western South American coast, the relatively wide (50 to 180 km) coastal area of the NNE–SSW-trending Ecuadorian Andes is characterized by a relatively low relief (< 300 m a.s.l.) and separated from the southern forearc by the Dolores–Guayaquil megashear. The NW–SE-oriented Peruvian segment comprises wide coastal plains of up to 160 km in the north that narrow to less than 40 km and slightly widen again in the south (Suárez et al., 1983). The N–S-trending Chilean segment of the coastal region includes the up to 2700-m-high Coastal Cordillera that decreases in altitude to 500 m at 46° S (Jordan et al., 1983).

Multiple marine coastal terraces at successively higher elevations in the forearc are formed at glacial-cycle timescales through the combined effects of wave erosion, tectonic uplift, and climate-driven sea-level oscillations. Interglacial and interstadial relative sea-level highstands during Pleistocene warm periods were responsible for the carving of abrasion platforms and the retreat of coastal cliffs, which were subsequently exposed due to continued uplift and a falling sea level during cold periods. If the coastal uplift rate in such a scenario is high enough, the abrasion platforms will remain subaerially exposed and during the following relative sea-level highstand a new abrasion platform will be sculpted into the rocks of the forearc at a lower position, thus leading to a staircase morphology (e.g., Lajoie, 1986). The resulting terrace sequences are assigned to odd-numbered Marine Isotope Stages (MIS; Shackleton et al., 2003). Multiple marine terrace levels can be observed along almost the entire western coast of South America. Based on global observations of sea-level fluctuations the surface of the last-interglacial marine terrace (MIS 5) is associated with three second-order highstands; these comprise MIS 5a at 80 ka, 5c at 105 ka, and 5e at ~125 ka (from 128 to 116 ka) with paleo-sea level heights at -20 ± 5 m for both of the younger and +3 ± 3 m for the oldest highstand (Stirling et al., 1998; Siddall et al., 2006; Hearty et al., 2007; Rohling et al., 2009; Pedoja et al., 2011).

The best-preserved and laterally most continuous terrace level was formed during MIS 5e and has been used frequently as a geomorphic strain marker for the estimation of coastal deformation and uplift rates (Fig. 3.1; Muhs et al., 2002; Dumas et al., 2006; Saillard et al., 2011; Muhs et al., 2014; Jara-Muñoz et al., 2015; Matsu'ura et al., 2019; Simms et al., 2020; Freisleben et al., 2021; Tam & Yokoyama, 2021).

3.3.2 Subduction geometry and bathymetry of the subducting plate

At the convergent margin of South America, the oceanic Nazca plate subducts beneath the South American continent with fairly constant convergence rates, varying between 59 mm/yr in the north (8° S) and 63 mm/yr in the south (27° S), and convergence azimuths, varying from 84.1° N to 80.7° N towards the south (Fig. 3.1; Kendrick et al., 2003). The subduction zone in South America can be divided into four major segments based on spatial distributions of Benioff-zone seismicity, which delineate varying angles of the subducting slab. Relatively steep segments of the subducting plate, dipping 25° to 30° at depths of ~100 km, are interrupted by two major flat-slab subduction segments, dipping only 5° to 10°, beneath central Peru (2°–15° S) and beneath central Chile (27°–33° S; Jordan et al., 1983; Hayes et al., 2018).

Several bathymetric anomalies characterize the seafloor of the subducting plate, the two most prominent ones are the Carnegie and Nazca aseismic ridges at 0° and 15° S, respectively. The 300-km-wide and ~2-km-high Carnegie Ridge subducts roughly parallel to the convergence direction, while the obliquity of the 200-km-wide and 1.5-km-high Nazca Ridge has caused its intersection with the trench to be shifted 500 km towards the SE during the last 10 Ma (Gutscher et al., 1999; Hampel, 2002; Kendrick et al., 2003). Additional smaller bathymetric anomalies include the Juan Fernández, Copiapó, Taltal, and Iquique ridges as well as several fracture zones (e.g., Mendaña and Nazca fracture zones; Fig. 3.1). The subduction of these bathymetric anomalies influences the degree of interplate coupling and the associated seismic hazard by creating fracture networks that promote small earthquakes and aseismic creep (Wang & Bilek, 2011; Bassett & Watts, 2015; Collot et al., 2017).

3.3.3 Major coastal fault systems and seismicity

The main structures affecting the convergent margin of the western South American coast comprise multiple fault systems with varying kinematics; their occurrence is closely connected

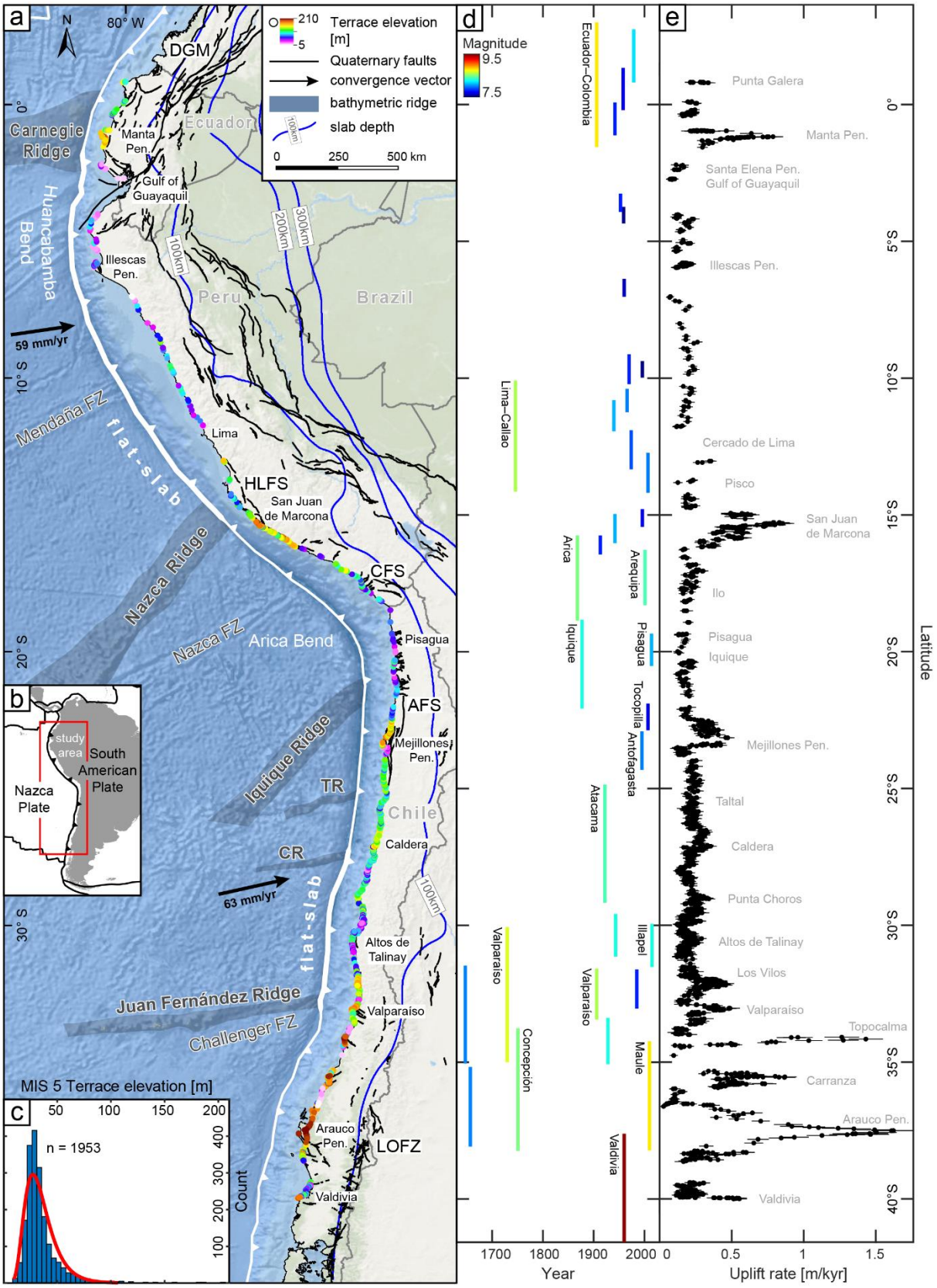
a
N
80° W
DGM
Terrace elevation [m]
210
-5
Quaternary faults
convergence vector
bathymetric ridge
slab depth
0
250
500 km
Carnegie Ridge
Manta Pen.
Gulf of Guayaquil
Ecuador
Huancabamba Bend
Illescas Pen.
Peru
Brazil
100km
200km
300km
59 mm/yr
10° S
Mendaña FZ
flat-slab
Lima
HLFS
San Juan de Marcona
CFS
Nazca Ridge
Nazca FZ
Arica Bend
20° S
Pisagua
AFS
Mejillones Pen.
Iquique Ridge
TR
Chile
Caldera
CR
63 mm/yr
30° S
Altos de Talinay
Juan Fernández Ridge
Challenger FZ
Valparaiso
Arauco Pen.
LOFZ
Valdivia
b
study area
South American Plate
Nazca Plate
MIS 5 Terrace elevation [m]
c
50
100
150
200
n = 1953
Count
100
200
300
400
d
Magnitude
9.5
7.5
Ecuador–Colombia
Lima–Callao
Arica
Iquique
Arequipa
Pisagua
Tocopilla
Antofagasta
Atacama
Valparaiso
Concepción
Illapel
Maule
Valdivia
1700
1800
1900
2000
Year
e
Punta Galera
Manta Pen.
Santa Elena Pen.
Gulf of Guayaquil
Illescas Pen.
Cercado de Lima
Pisco
San Juan de Marcona
Ilo
Pisagua
Iquique
Mejillones Pen.
Taltal
Caldera
Punta Choros
Altos de Talinay
Los Vilos
Valparaiso
Topocalma
Carranza
Arauco Pen.
Valdivia
0°
5°S
10°S
15°S
20°S
25°S
30°S
35°S
40°S
Latitude
0
0.5
1
1.5
Uplift rate [m/kyr]

Figure 3.1: (a) Tectonic setting of the western South American plate margin showing the major crustal fault systems (Costa et al., 2000; Veloza et al., 2012; Maldonado et al., 2021), slab depth (Hayes et al., 2018) and flat-slab subduction segments, bathymetric features of the subducting plate, convergence vectors (Kendrick et al., 2003), and elevations of last interglacial marine terraces (Freisleben et al., 2021). DGM: Dolores–Guayaquil megashear; HLFS: El Huevo–Lomas fault system; CFS: Chololo fault system; AFS: Atacama fault system; LOFZ: Liquiñe–Ofqui fault zone; FZ: fracture zone; TR: Taltal Ridge; CR: Copiapó Ridge (World Ocean Basemap: Esri, Garmin, GEBCO, NOAA, NGDC, and other contributors). (b) Location of the study area. (c) Histogram of last interglacial marine terrace elevations from the database of Freisleben et al. (2021). The count of terrace elevations follows a log-normal distribution with a median of 30 m. MIS 5: Marine Isotopic Stage 5. (d) Latitudinal extent of great subduction earthquakes (≥ M7.5) along the western South American coast between 1647 and 2015 colored by magnitude (Udias et al., 2012; Villegas-Lanza et al., 2016). (e) Uplift rates of last interglacial marine terraces (MIS 5e and 5c) calculated using terrace elevations of Freisleben et al. (2021).

with the subducting Nazca plate and inherited heterogeneities in the South American continental plate (e.g., Armijo & Thiele, 1990; Audin et al., 2008; Wang & Bilek, 2014). North of the Huancabamba Bend, dextral strike-slip and thrust faulting occurs in the coastal areas of Ecuador, although normal faulting has been observed at some locations such as Punta Galera or at the Manta Peninsula (Fig. 3.1). The largest structure in this region is the 2000-km-long, dextral and NE-striking Dolores–Guayaquil megashear (DGM), which separates the northern from the southern forearc units and is associated with normal faulting in the Gulf of Guayaquil as well as dextral strike-slip faulting on the Santa Elena Peninsula and regions to the north (Baize et al., 2015; Alvarado et al., 2016; Margirier et al., 2023). In the coastal regions of Peru, normal faulting occurs primarily on the Illescas Peninsula, within the El Huevo–Lomas fault system (San Juan de Marcona area), and within the Chololo fault system (CFS) farther south (Audin et al., 2008; Veloza et al., 2012; Costa et al., 2020). The principal coastal faults that have been described along the northern Chilean convergent margin are part of the Atacama fault system (AFS), which extends from Iquique to La Serena (30° S) with predominantly N–S-striking normal faults (Fig. 3.1; Naranjo, 1987; Santibáñez et al., 2019). Smaller and more disconnected fault systems occur farther south in the Altos de Talinay area (e.g., Puerto Aldea fault) near Valparaiso, Topocalma, and Carranza, and on the Arauco Peninsula (Fig. 3.1; Maldonado et al., 2021).

Most great (≥ M_W7.5) earthquakes along the tectonically active western margin of South America are associated with the subduction of the Nazca plate beneath the South American continent, although some correspond to normal-faulting events within the down-going slab (Beck et al., 1998). Figure 3.1d shows the spatial and temporal distribution of those earthquakes that display patterns of recurrent great events in distinct seismotectonic segments of the forearc (Lomnitz, 2004; Saillard et al., 2017; Molina et al., 2021).

3.4 Methods and data

Our approach to analyze the terrace signal and potential processes controlling the spatial distribution of uplift rates comprises the decomposition of the signals themselves and a comparison of their frequency spectra. The calculations and outputs were processed and elaborated using MATLAB®. We used uplift rates calculated from the terrace-elevation database of Freisleben et al. (2021), which show a log-normal distribution (Fig. 3.1c) with a relatively constant background signal of uplift rates and several increases of varying wavelength and amplitude along the western South American coast (Fig. 3.1e). We are aware that some terrace-elevation measurements within the database vary qualitatively based on several factors, most notably the distance to the nearest age estimate. However, the continuous distribution and generally good quality rating of the measurements (Freisleben et al., 2021) provide the unique opportunity to thoroughly analyze this database for the first time on a continent-wide scale with potential parameters and associated mechanisms that may influence permanent forearc deformation.

3.4.1 Input signals

For the marine terrace signal, we calculated uplift rates using MIS 5e and 5c shoreline-angle elevations of last interglacial marine terraces (Freisleben et al., 2021) as well as associated sea-level altitudes and terrace-age estimates. We analyzed and compared the wavelength(s) of the marine terrace signal to those of the signals of residual gravity anomaly, interseismic uplift rate, effective basal friction, coseismic land-level change, bathymetric anomaly, distance to the trench, and background seismicity (Fig. 3.3). To allow for a better comparison with terrace-uplift rates, we calculated all signals except bathymetric anomaly and background seismicity at the terrace locations and projected them along the trench.

The signal of residual gravity anomaly was obtained by applying the principal component analysis method described in Molina et al. (2021) for the Chilean margin to the Free-Air gravity anomaly grid from Sandwell et al. (2014) for the entire western coast of South America (Fig. A.1a). In a second step, we calculated the mean value along trench-perpendicular profiles from the terrace location to the trench, which provides an indirect measure of the effective normal stress across the entire accretionary wedge since the residual gravity anomaly is associated with variations in forearc density and thus vertical stresses acting on the megathrust (Molina et al.,

2021). To attain estimates of interseismic uplift rate, we created a block model of South America similar to Graham et al. (2018), which decomposes interseismic GPS velocities to slip deficit on block-bounding faults, coupling on triangular dislocation elements (Fig. A.1b), and plate rotations. We then calculated interseismic uplift rates at the terrace locations using the results of the block model and a built-in forward-model function. For the signal related to great subduction earthquakes, we used Okada models of 12 great earthquakes ($\geq M_W7.5$) since 1995 that were generated from finite fault models by Hayes (2017). From these models we extracted the cumulative vertical displacement at the location of each marine terrace measurement to create a signal of coseismic land-level changes along the South American coast. To obtain the signal related to bathymetric anomalies, we generated a 150-km-wide, trench-parallel swath profile west of the trench, on which we subsequently applied a high-pass Butterworth filter (Fig. A.6). With this filter we generated a signal of bathymetric irregularities instead of bathymetric depth by enhancing high-frequency parts of the bathymetry signal, but also maintaining the long wavelengths. We estimated the distance to the trench by projecting the points of the marine terrace measurements perpendicular to the trench and using the obtained projection distance.

Another parameter included in our analysis was the coefficient of effective basal friction (μ_b^{eff}). Assuming the forearc to act like a non-cohesive critical Coulomb wedge, the critical taper angle can be described by its coefficients of internal and basal friction (μ_i and μ_b) as well as its internal and basal Hubbert-Rubey fluid-pressure ratios (λ_i and λ_b; Dahlen, 1984). To calculate μ_b^{eff}, we used a combination of the solution for a non-cohesive critical Coulomb wedge by Dahlen (1984) generalized with a Mohr's construction by Lehner (1986), which was established by Cubas et al. (2013):

$$\mu_b{}^{eff} = (1 - \lambda_b)\,\mu_b, \qquad \text{(Eq. 3.1)}$$

The critical taper angle $(\alpha + \beta)_{crit.}$ is calculated using the angles between the maximum principal stress and the base and the top of the wedge (ψ_b and ψ_0):

$$(\alpha + \beta)_{crit.} = \psi_b - \psi_0, \qquad \text{(Eq. 3.2)}$$

where the two angles ψ_b and ψ_0 are a function of the internal and basal angles of friction (ϕ_i and ϕ_b):

$$\psi_b = \frac{1}{2}\arcsin\left(\frac{sin\,\phi_b'}{sin\,\phi_b}\right) - \frac{1}{2}\phi_b' \text{ with } \mu_b = tan\,\varphi_b \text{ and} \qquad \text{(Eq. 3.3)}$$

$$\psi_0 = \frac{1}{2}\arcsin\left(\frac{sin\ \alpha'}{sin\ \phi_i}\right) - \frac{1}{2}\alpha' \quad \text{with } \mu_i = tan\ \varphi_i. \qquad \text{(Eq. 3.4)}$$

The angles α' and ϕ'_b additionally take into account pore-fluid pressure through internal and basal Hubbert-Rubey fluid-pressure ratios:

$$tan\ \phi'_b = \left(\frac{1-\lambda_b}{1-\lambda_i}\right)\tan\phi_b, \qquad \text{(Eq. 3.5)}$$

$$\alpha' = \arctan\left[\left(\frac{1-\frac{\rho_w}{\rho}}{1-\lambda_i}\right) tan\ \alpha\right]. \qquad \text{(Eq. 3.6)}$$

To calculate the topographic slope (α), we divided the height difference between the trench and terrace location by their distance using the GEBCO 2020 bathymetric and topographic grid (GEBCO Bathymetric Compilation Group, 2020). The dip of the subducting plate (β) results from the slab depth at the terrace location using the Slab2.0 model of Hayes et al. (2018) and the distance to the trench. For the remaining coefficients we chose $\mu_i = 0.6$, $\lambda_i = \lambda_b = 0.85$, $\rho = 2.7$ g/cm^3, $\rho_w = 1$ g/cm^3, where ρ and ρ_w are the densities of the wedge material and the pore fluid (water). The chosen values for μ_i and λ_i are commonly used values for the coefficient of internal friction in South America and the pore-fluid pressure ratio according to Byerlee's law (Dahlen, 1984; Cubas et al., 2013).

Background seismicity constitutes the last continuous signal that we analyzed and compared with the uplift rate. We extracted background seismicity along the western South American coast following the approach of Madella and Ehlers (2021), using all earthquakes that occurred since 1973 between the trench and the 60-km depth contour from the USGS earthquake catalog; prior to 1973, the records are incomplete (https://earthquake.usgs.gov/earthquakes/search/, downloaded on 17.09.2021). Additional filters include a reduction of the magnitude range (M4.3–M6) based on a Gutenberg-Richter plot. In addition to using all of the described seismic events in one analysis (Fig. A.2), in a separate analysis (Fig. A.3) we excluded earthquakes more than 10 km away from the subducting slab. To retrieve the background seismicity, we excluded great earthquakes with multiple postseismic events by carrying out a cluster analysis using the 'DBSCAN' algorithm in MATLAB® based on spatial and temporal cluster characteristics. We then counted all earthquakes within 20-km-wide bins from the subduction trench to the 60-km depth contour to obtain a signal for background seismicity (Fig. A.2, A.3).

3.4.2 Signal analysis

The signal analysis involved several steps to estimate the contribution of each process influencing the observed signal of cumulative permanent coastal uplift. In the first step, we interpolated the signals using a step size of 10 km to ensure equal point density along the entire length of the trench (see Fig. A.8 for point spacing before interpolation). To assess the role of the step size for the interpolation of the input signals, we carried out a sensitivity test, which resulted in no significant change of the output wavelength spectrum for step sizes ≤ 30 km (Fig. A.4). In the second step, we carried out a Fast Fourier Transformation (FFT) and calculated the power spectral density (PSD) of the frequency range for each signal, which we reciprocated to obtain wavelength values (Fig. 3.3). By the application of an inverse FFT and a power-spectrum threshold below the major peaks we were able to accurately reproduce the input signals.

Spectral comparison of uplift rates and tectonic features via signal analysis focuses on the distribution of wavelengths but neglects the equally important aspect of spatial coherence between individual signals. However, we propose that this kind of analysis accounts for spatiotemporal changes in tectonic processes over millennial timescales that might otherwise be overlooked.

Apart from these continuous signals along the margin, we also analyzed wavelengths related to discrete processes such as crustal faulting, which, although not suitable for FFT, might still control parts of the uplift-rate spectrum. We analyzed crustal faulting using Okada models (Okada, 1992) of 33 faults near the coast with the input fault geometry and fault parameters of the CHAF database of active faults in Chile (Fig. A.1c; Maldonado et al., 2021). Since the depth, dip, slip rate, and rake are not well known for most of the analyzed faults, we iterated several dislocation models by arbitrarily varying these parameters within defined ranges based on well-studied faults in South America of similar kinematics (Table 3.1).

Table 3.1: Fault parameters used for elastic modeling of crustal faults. Up-dip depth, down-dip depth or fault-dip change after three model runs, during which three different slip rates are tested.

Model run	Up-dip depth [km]	Down-dip depth [km]	Dip	Slip rate [mm/yr]	Rake
1–3	0	25	60	0.2; 1; 2	90
4–6	2	25	60	0.2; 1; 2	90
7–9	0	15	60	0.2; 1; 2	90
10–12	0	25	90	0.2; 1; 2	90

We used a down-dip depth of 25 km for the elastic models, which is typical for crustal faults in the forearc (e.g., El Yolki fault in Melnick et al. (2019)), changing this parameter only for three model runs to a depth of 15 km (e.g., Santa María fault in Jara-Muñoz et al. (2017)). From the Okada models, we extracted displacement profiles of 200 km length perpendicular to the fault strike and calculated the distance between -10 and +10 cm displacement (Fig. A.5). The resulting lengths are ultimately displayed in a histogram and are fitted to a kernel density function (Fig. 3.4).

3.4.3 Estimation of spectral correlation

We quantified correlations between uplift rate and the analyzed tectonic features using the resulting wavelength spectra. To ensure equal point spacing and similar maximum amplitudes, we interpolated (step size: 10 km) and normalized all wavelength signals. Since most of the analyzed features are restricted to certain wavelength ranges, we calculated the product of normalized PSDs of tectonic features and uplift rate for each wavelength point to quantify and locate high correlation with respect to the uplift-rate spectrum (Fig. 3.5, A.9–A.16). The linear correlation coefficients between the entire spectra were also included in our calculations.

3.5 Results

For the description of the wavelength analysis, we defined three categories of peaks depending on their amplitude relative to the maximum amplitude of the wavelength spectrum. Wavelength peaks are considered small, medium, or large if they reach < 30 %, 30–60 %, or > 60 % of the maximum amplitude, respectively.

3.5.1 Uplift-rate signal

At the scale of the western coast of South America, long-term coastal uplift rates estimated over the past ~125 kyr display a relatively constant background signal (median: 0.22 mm/yr) with at least ten short-wavelength (e.g., near Los Vilos, Valparaíso, Carranza) and five long-wavelength peaks (e.g., on the Manta and Arauco peninsulas or San-Juan de Marcona; Fig. 3.3a). To test the reliability of the background signal, we randomly removed an increasing number of uplift-rate estimates from the terrace database while calculating the median of the

remaining values. We iterated this procedure 50 times to eliminate any statistical artefacts for the randomly removed points; however, we only observed a significant variation of the median uplift rate (deviating more than the median error of uplift rate) when more than 90 % of the points were removed (Fig. 3.2). We therefore consider the background signal of uplift rate to be significant at the scale of the South American margin.

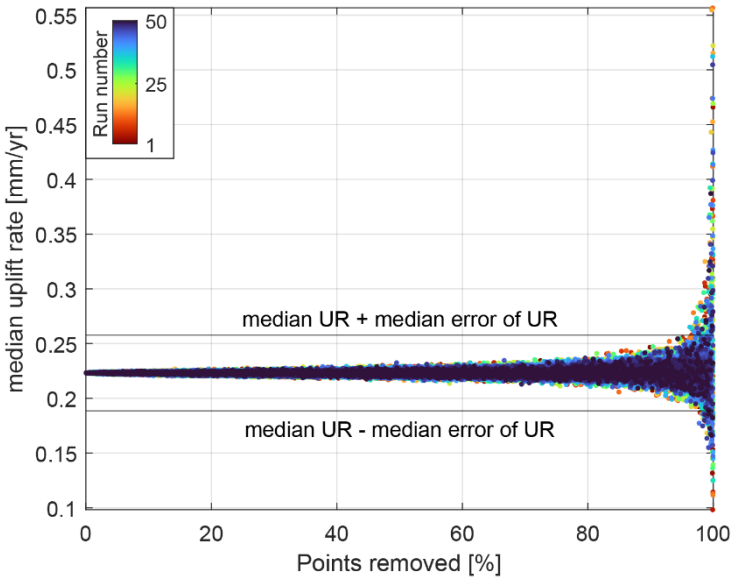

Figure 3.2: Reliability test of the continuous background signal of uplift rates. Median uplift rates (y-axis) stay relatively constant when an increasing number of terrace measurements is removed (x-axis). The different colors display the individual runs of random point removal (n = 50), and the black horizontal lines represent the median uplift rate plus or minus the median error of uplift rate.

The wavelength spectrum of the uplift-rate signal resulting from the FFT analysis shows several small peaks at wavelengths between 20 and 180 km, medium peaks within the range of 190 and 360 km, a broad large peak between 400 and 600 km wavelength, and another large peak at 835 km (Fig. 3.3b).

3.5.2 Residual gravity anomaly and distance to the trench

The residual gravity anomaly along the western coast of South America varies between -100 and 100 mgal, showing a relatively long-wavelength signal (Fig. 3.3c). The wavelength spectrum indicates only a few small peaks below 400 km. The main part of the signal is characterized by a broad medium-sized peak between 430 and 650 km wavelength and a major peak at 835 km (Fig. 3.3d). Only two smaller peaks appear at wavelengths of 280 and 310 km.

The distances from our terrace-measurement locations to the trench vary between 50 and 150 km but show large and very long-wavelength increases (> 1000 km) at the Arica Bend and in central Peru (Fig. 3.3e). Shorter-wavelength changes in distance to the trench are represented

in the wavelength spectrum by two large peaks at 280 km and between 580 and 750 km wavelength (Fig. 3.3f).

3.5.3 Coseismic land-level changes and interseismic uplift rate

Coseismic vertical displacements show an even distribution of subsidence and uplift along the coast (Fig. 3.3g, A.7), with most significant land-level changes resulting from the Illapel (2015), Maule (2010), Arequipa (2001), and Antofagasta (1995) earthquakes. The wavelength spectrum displays three small peaks (at 125, 195 and 240 km), five medium peaks (at 150, 295, 385, 500, and 780 km), and one large peak (at 335 km) representing mainly intermediate to long-wavelength signals (Fig. 3.3h).

The signal of interseismic vertical velocities is characterized by medium to long wavelengths, indicating subsidence in Chile/southern Peru and uplift in northern Peru/Ecuador (Fig. 3.3i). The wavelengths might result partially from the model resolution, which is constrained by a triangular-element raster with side lengths between ~60 and 100 km (Graham et al., 2018). We observe multiple small peaks in the spectrum below 500 km wavelength, while one medium peak appears at 560 km wavelength and one large peak can be observed at 835 km (Fig. 3.3j).

3.5.4 Basal friction and bathymetric anomalies

Along the western coast of South America, the coefficient of effective basal friction varies in a long-wavelength pattern from ~0 to 0.2, with higher values being characteristic for Peru and south-central Chile (Fig. 3.3k). Analysis of this signal reveals two small peaks around 200 and one at 390 km, a medium peak at 280 km wavelength, and two large peaks at 630 and 835 km (Fig. 3.3l).

The filtered and detrended bathymetry signal that represents bathymetric anomalies shows changes of ±500 m, with the most significant anomalies at the Nazca, Carnegie, Juan Fernández, Copiapo, and Taltal ridges (Fig. 3.3m). This signal results in a power spectrum with three small peaks from 165 to 265 km wavelengths and at 845 km, two medium peaks at 440 and 560 km, and one large peak at 360 km wavelength (Fig. 3.3n).

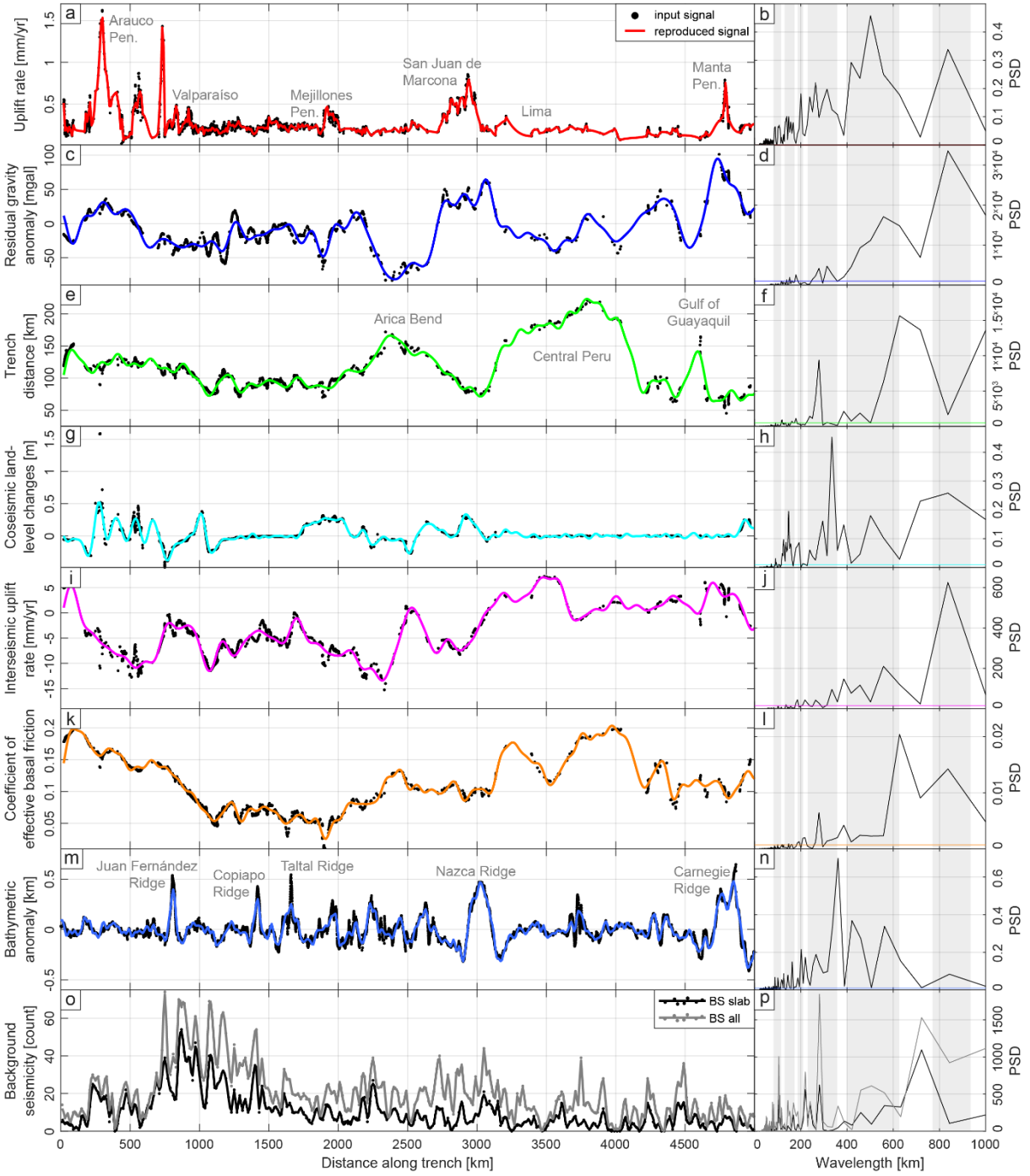

Figure 3.3: Comparison of the uplift-rate signal (a) and its corresponding wavelength spectrum (b) with the signals and analysis of various tectonic features such as residual gravity anomaly (c, d), distance to the trench (e, f), coseismic land-level changes (g, h), interseismic uplift rate (i, j), effective basal friction (k, l), bathymetric anomaly (m, n), and background seismicity (o, p). Vertical gray bars in the wavelength spectra indicate the most prominent peaks in the uplift-rate spectrum. Orientation: south-north.

3.5.5 Background seismicity and crustal faulting

The signal of background seismicity shows relatively high variability with seismicity increasing broadly (hundreds of km width) in the vicinity of the Juan Fernández Ridge (Fig. 3.3o). Accordingly, the wavelength spectrum shows several small peaks below 240 km and two medium peaks at 105 and 220 km (Fig. 3.3p). We further observe a medium to large peak at 280 km, a broad medium-sized peak from 450 to 600 km (only for the entire background-seismicity signal), and another large peak at 720 km wavelength.

We performed 120 elastic Okada models on 33 crustal faults along the western South American coast, which show absolute vertical displacements (> 10 cm) in areas of maximum 22.5 to 66.2 km extent measured perpendicular to the fault trace (Fig. 3.4, S5). The kernel-fitted density function of this wavelength distribution shows an asymmetric peak at smaller wavelengths with a median at 36.1 km (Fig. 3.4).

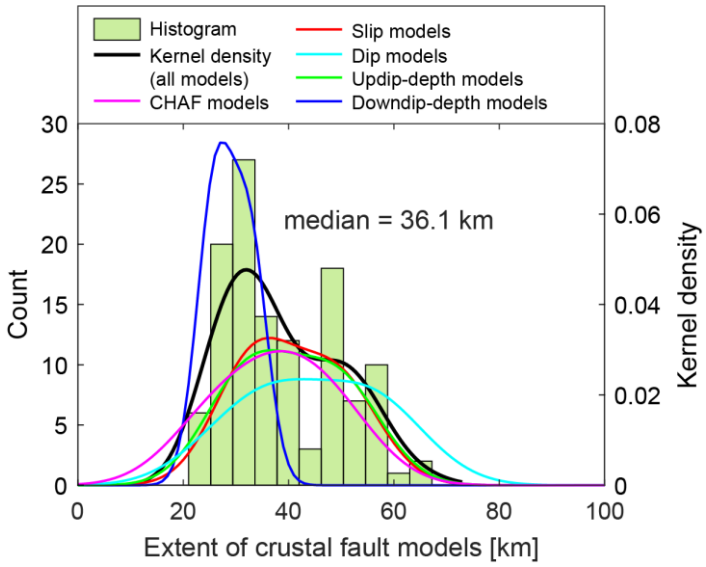

Figure 3.4: Histogram of the extent of fault displacement resulting from all elastic Okada models using either CHAF parameters or varying fault parameters for less well-studied crustal faults. Colored graphs represent kernel-density functions of the individual fault models, where the specified parameter changes according to Table 3.1; bold black line represents the kernel fit for all Okada models.

3.6 Discussion

3.6.1 Processes controlling various wavelengths of deformation

The mechanisms contributing to the accumulation of permanent deformation along tectonically active forearcs are currently a matter of debate, primarily because they have not yet been analyzed on a continental scale (Mann et al., 1998; Melnick, 2016; Jolivet et al., 2020; Menant et al., 2020). We attempt to contribute to this ongoing debate by analyzing and comparing the

wavelength signal of terrace-uplift rates with the wavelength signals of a selection of tectonic processes and parameters thought to be associated with permanent forearc uplift. For better comparability, we divided the uplift-rate spectrum in ranges of short- (< 100 km), intermediate- (100–450 km), and long-wavelength (> 450 km) deformation. Although our analysis reveals multiple mechanisms and parameters correlating to certain ranges of wavelength in the uplift-rate spectrum, we infer that a specific set of processes associated with the seismotectonic segmentation of the megathrust is responsible for these signals (Fig. 3.5).

Linear correlations between the entire wavelength spectra of coastal uplift rate and potential driving mechanisms are highest for the residual gravity anomaly, followed by the interseismic uplift rate, coseismic land-level changes, and bathymetric anomalies, suggesting that these phenomena are characterized by similar wavelengths compared to the long-term uplift-rate pattern (Fig. 3.5). In contrast, the negative correlations of background seismicity, trench distance, and crustal faulting are attributed to the dominance of certain wavelengths in these spectra that are not present or not as pronounced in the long-term uplift-rate signal.

Quantifying and localizing correlations at specific wavelengths suggest that short wavelengths (< 100 km) in the uplift-rate signal are mainly caused by crustal faulting. The absence of a significant overall correlation between uplift rate and crustal faulting is attributed to the low power of short-wavelength signals in the uplift-rate spectrum. However, we consider wavelengths between 22.5 and 66.2 km to be a reasonable maximum estimate for crustal faults (Fig. 3.4), taking into account that small faults may be underrepresented in our analysis and that complete rupture of large faults is rare. Intermediate-wavelength (100–450 km) variations in terrace-uplift rate coincide in the spectrum primarily with (1) coseismic vertical displacements related to great earthquakes (M7.5–M8), (2) medium bathymetric anomalies (e.g., Taltal or Copiapo ridges), and (3) high-frequency changes in background seismicity (Fig. 3.5). The correlating shorter wavelengths of these features may indicate the locked areas on the megathrust, which rupture either during multiple, small cascading events (background seismicity) or during great earthquakes (Schurr et al., 2014; Métois et al., 2016; Remy et al., 2016; Madella & Ehlers, 2021). The respective longer wavelengths (megathrust earthquakes > M8, long-wavelength background seismicity, large bathymetric anomalies) are similarly correlated with the uplift-rate spectrum in the long-wavelength range (> 450 km) and might represent the upper extent of locked megathrust patches (Fig. 3.5). The remaining parameters primarily show correlations with the uplift-rate spectrum at long wavelengths, namely

interseismic uplift rates, basal friction, residual gravity anomaly, and trench distance (Fig. 3.5). In this context, we have to note that the distance to the trench is included in the calculation of effective basal friction and is therefore not independent from this parameter. The related processes might influence the long-term seismotectonic segmentation of the megathrust on 10^2-km scales and affect the physical behavior of the megathrust. This may apply, for instance, to lateral density variations in the forearc that change the vertical loading on faults and thus the effective normal stresses (Cubas et al., 2013; Molina et al., 2021).

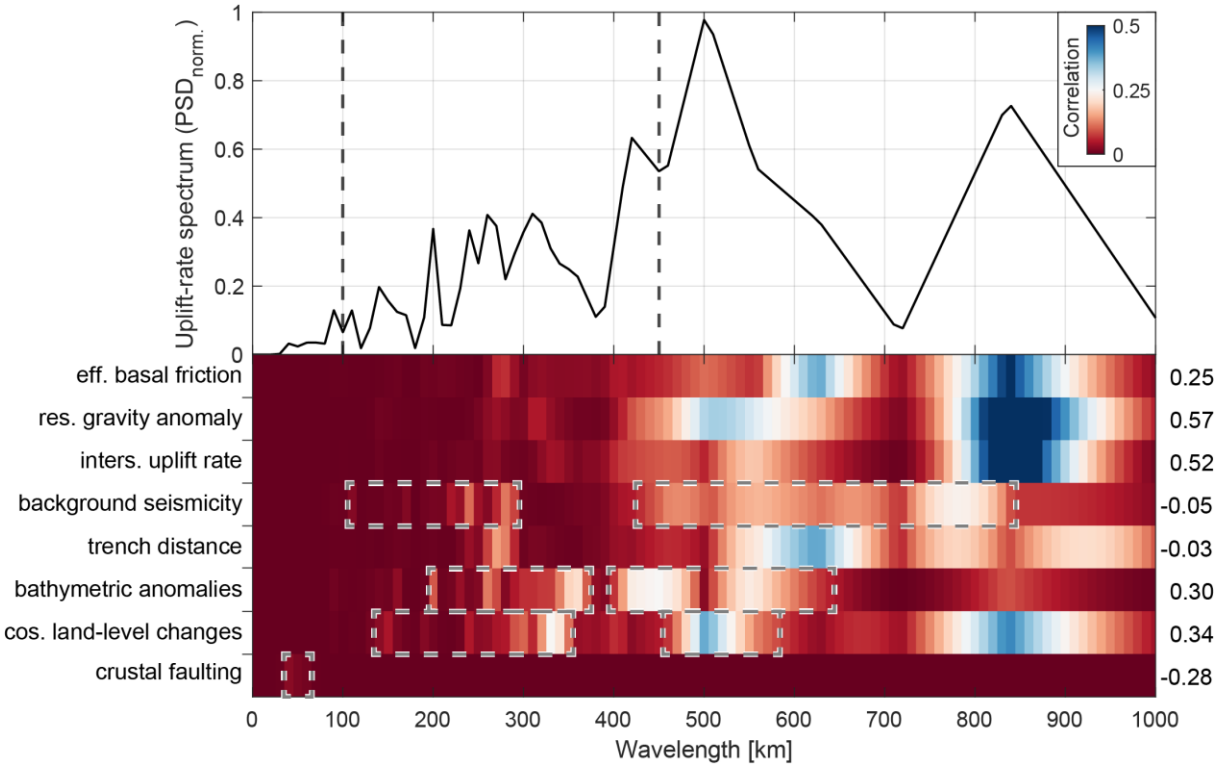

Figure 3.5: Normalized wavelength spectrum resulting from the analysis of the uplift-rate signal (top). Dashed black lines indicate ranges of short- (< 100 km), intermediate- (100–450 km), and long-wavelength (> 450 km) deformation. Color scales below quantify and localize the correlation (0–red to 0.5–blue) between the wavelength spectra of various tectonic features and the uplift rate. Gray dashed boxes indicate several correlations described in the text, and the numbers on the right quantify the linear correlation between the full spectra.

Our signal-analysis approach supports the notion that mechanisms such as the subduction of bathymetric anomalies and coseismic slip are related to various wavelengths of permanent deformation and the seismotectonic segmentation of the megathrust, as had been proposed in previous studies (Singh et al., 2011; Philibosian & Meltzner, 2020; Molina et al., 2021). In light of this, we emphasize the significant correlations between terrace-uplift rates and coseismic land-level changes in both, long- and intermediate-wavelength ranges, suggesting primarily coseismic accumulation of permanent coastal uplift (Fig. 3.5; Melnick, 2016; González-Alfaro

et al., 2018). Our analysis furthermore confirms that short-wavelength deformation in the forearc is controlled by crustal faults in the upper plate (Kelsey et al., 1996; Jara-Muñoz et al., 2015; Matsu'ura, 2015), while long-wavelength parameters such as basal friction or residual gravity anomalies might influence the larger-scale segmentation of the megathrust (Molina et al., 2021).

3.6.2 The continuous uplift-rate signal along the western coast of South America

Besides the previously described and interpreted deformation patterns with wavelengths of up to 850 km, we observe a fairly continuous background signal of uplift rates along the entire western South American margin (Fig. 3.1e, 3.2), which may be explained by two scenarios. In the first scenario, the background uplift could originate from a single, low-magnitude mechanism acting continuously along the entire margin. The second scenario involves one single or multiple, spatially distributed processes that temporarily change location and/or magnitude and accrue over millennial timescales towards a continuous and permanent signal of background-uplift rate. In search for the mechanism(s) being responsible for the observed background-uplift signal, we exclude processes that have a localized and high-amplitude impact on the comparatively low-amplitude, continuous signal of background-uplift rate. These include phenomena attributed to the subduction of bathymetric anomalies, such as high-uplift areas where the Nazca and Carnegie ridges intercept the forearc (Hsu, 1992; Pedoja et al., 2006) as well as the Topocalma and Carranza regions or the Arauco and Mejillones peninsulas, which represent coastal sectors with pronounced crustal faulting, and the motion of forearc slivers (Melnick et al., 2009; Jara-Muñoz et al., 2015). Such processes have also been associated with short- to intermediate wavelengths of upper-plate deformation at other subduction zones (Kelsey et al., 1996; Sak et al., 2004; Gardner et al., 2013; Matsu'ura, 2015; McKenzie et al., 2022) and are viewed as unlikely to accommodate a rather continuous low-magnitude background-uplift rate as observed by us.

With respect to the first scenario, the low-magnitude mechanisms and parameters generally seem to lack the spatial continuity along the entire continental margin that would be required to explain the observations. Background seismicity (Fig. 3.3o) could be considered for this scenario, since Madella and Ehlers (2021) show a possible correlation with long-term uplift rates in northern Japan and central South America. However, high-frequency changes in our

signal of background seismicity and the relatively short time interval of ~50 years analyzed in comparison with the duration of a seismic cycle (~100 to 300 years; Comte & Pardo, 1991; Cisternas et al., 2005) prevent further interpretations regarding the role of this mechanism.

As described for the second scenario, the virtually continuous background signal of uplift rates might result from a single or various mechanisms of different wavelength, timing, and location that overlap and accumulate over millennial timescales. We used the results of our analysis to test the mechanism proposed by Jolivet et al. (2020) where a small portion of interseismic uplift translates into permanent deformation. We furthermore tested the hypothesis by Melnick (2016) who suggested moderate, domain-C earthquakes (~35–55 km depth) to be responsible for permanent coastal uplift signals.

The mechanism proposed by Jolivet et al. (2020) was tested by plotting interseismic uplift rates directly against terrace-uplift rates. Interestingly, interseismic uplift displays no direct correlation with terrace-uplift rates, neither when points near active faults are removed (Fig. 3.6a), nor when points in the vicinity of crustal faults are plotted (Fig. 3.6b). The selection of fault-influenced points was created using a 10-km-wide buffer around each coastal fault from the CHAF and GEM databases (Styron & Pagani, 2020; Maldonado et al., 2021). Furthermore, interseismic velocities indicate almost exclusively subsidence for southern Peru and Chile, representing approximately 60 % of the analyzed margin (Fig. 3.3i). On the other hand, testing such a relationship at a continental scale cannot rule out local correlations between interseismic and long-term coastal uplift. We therefore suggest either a very small fraction of interseismic slip is being accumulated as permanent deformation or a local confinement to specific areas.

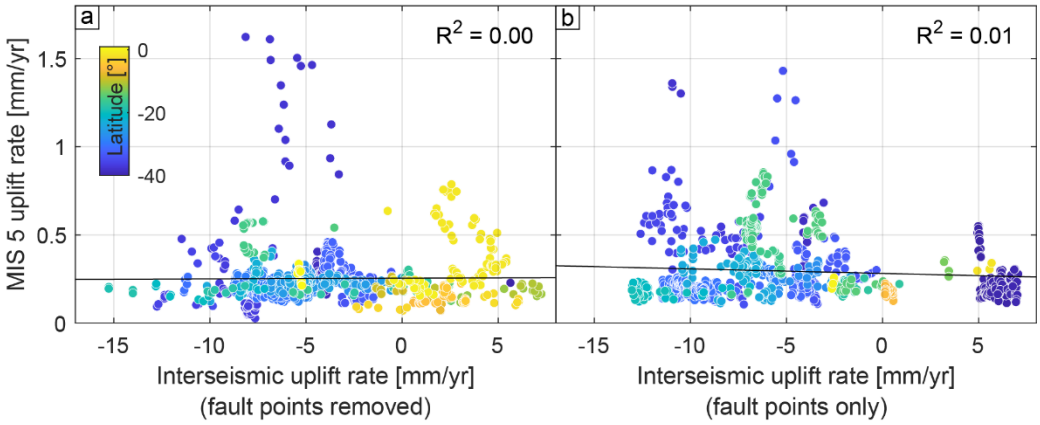

Figure 3.6: Interseismic uplift rates derived from the block model show no correlation with long-term uplift-rate estimates of marine terraces. (a) Points > 10 km away from active faults and (b) points ≤ 10 km away from active faults based on the CHAF and GEM databases (Styron & Pagani, 2020; Maldonado et al., 2021). All points are colored by latitude.

Since the occurrence of great earthquakes (M > 7.5) exhibits an equal degree of coseismic coastal subsidence and uplift (Fig. 3.3g, A.7; Ocola, 2008; Gusman et al., 2015; Melnick, 2016), we interpret no generally applicable and immediate causality between coseismic vertical displacements and terrace-uplift rates. Apparently not all earthquakes are responsible for permanent coastal uplift, but moderate earthquakes near the Moho (M7–M8, ~35–55 km depth) that have recently caused several decimeters of coastal uplift (Fig. 3.7a, b) might explain the observed background-uplift rates. The well-correlated wavelength spectra of terrace-uplift rate and coseismic coastal uplift resulting from such events (Fig. 3.7c) indicate the relationship between both features. In conjunction with moderate coseismic uplift resulting from modest domain-C earthquakes we propose that spatiotemporal variations of such events could produce a continuous signal of background uplift over millennial timescales. This would support the hypothesis proposed by Melnick (2016) that accumulation of anelastic deformation occurs down-dip of the interseismically locked megathrust. Maximum coseismic displacements along the coast vary between 309 and 386 mm for the considered earthquakes (Fig. 3.7a). A recurrence time of 86.5 years of domain-C earthquakes would therefore be needed to account for a background-uplift rate of 0.22 mm/yr during the last 125 kyr (using a median coseismic uplift of 318 mm). Although the occurrence of such moderate and deep earthquakes has not yet been recorded continuously along the western South American coast, we consider the calculated recurrence time to be reasonable due to similar recurrence times of 82.4 to 123 years for M7.7–M8 earthquakes based on Gutenberg-Richter distributions in northern Chile (Sippl et al., 2019). However, the discontinuous nature of domain-C earthquakes along the western South American margin makes further validation of this hypothesis necessary.

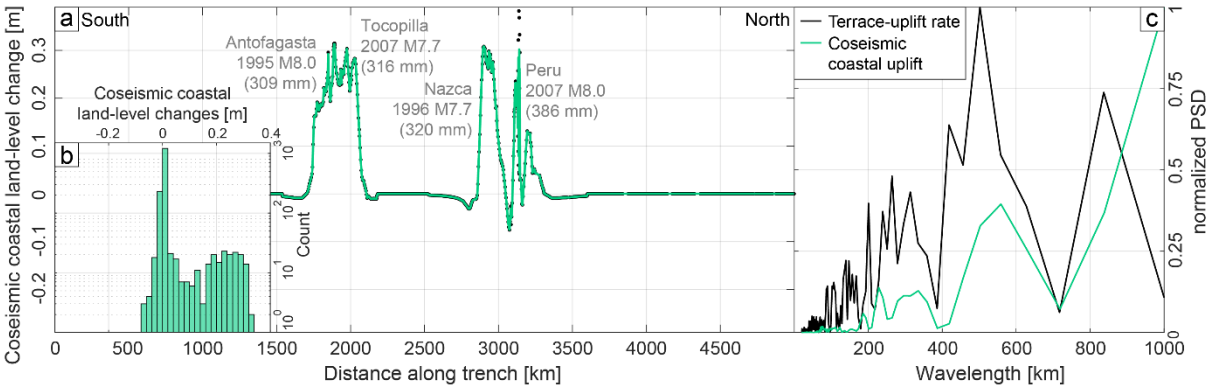

Figure 3.7: Cumulative vertical displacements of moderate domain-C earthquakes extracted at the coastline and projected along the trench (a), primarily showing coseismic uplift when plotted in a histogram (b). Maximum coseismic displacement at the coast is stated in parentheses below each earthquake. (c) Wavelength spectrum of coseismic coastal land-level changes demonstrating a significant correlation with the spectrum of terrace-uplift rate.

3.7 Conclusions

In this study, we tested the impact of various tectonic mechanisms and related parameters with respect to the accumulation of permanent forearc deformation along the western South American coast. Our previously compiled database of nearly 2000 elevation measurements of uplifted marine terraces affords a unique opportunity to analyze long-term coastal deformation since the last interglacial (at ~125 ka) at a continental scale. Spectral analysis of the uplift-rate signal and selected tectonic features provided new insights into possible contributions of tectonic processes that act on different spatial and temporal scales. The available database also allowed us to test various mechanisms that might explain the continuous background uplift that characterizes the coast of western South America. Our findings are as follows:

1. The uplift-rate signal along the western South American coast is characterized by a constant background signal (median: 0.22 mm/yr), which is disturbed by short- (~20 km) to long-wavelength (~850 km) variations.

2. Similarities between the wavelength spectra of uplift rate and those of several tectonic signals suggest potential correlations: Short-wavelength signals in uplift rate are primarily caused by the effects of local crustal faulting (22.5–66.2 km). Intermediate- to long-wavelength variations in uplift rate correlate with tectonic features, indicating various extents of locked areas on the megathrust that are likely related to the long-term seismotectonic segmentation of the megathrust. The spectral correlation of terrace-uplift rates with cumulative coseismic displacements suggests coseismic accumulation of permanent deformation, especially for modest earthquakes with focal depths near the Moho.

3. With respect to the continuous background signal of uplift revealed in our analysis, we did not find a direct link between interseismic and long-term coastal uplift at continental scale, not even when crustal faulting is taken into account. However, coastal uplift resulting from moderate earthquakes near the Moho (M7–M8, ~35–55 km depth) might explain the accumulation of anelastic deformation as suggested by good spectral correlation regarding terrace-uplift rates and moderate uplift, indicating similar recurrence times for the last interglacial period compared to current Gutenberg-Richter distributions.

4. Since domain-C earthquakes do not affect coastal regions continuously, we propose that accumulation of permanent deformation arises from multiple, spatially distributed and temporally distinct phases of uplift that add up over millennial timescales.

5. The application of this novel signal-analysis approach provides a useful tool to elucidate the mechanisms driving surface deformation in subduction zones at continental scale, with potential application to tectonic environments elsewhere.

Chapter 4: Structural and temporal characteristics of marine terraces in the 2015 M8.3 Illapel earthquake area

4.1 Abstract

Uplifted Pleistocene marine terraces record glacial-cycle accumulation of permanent deformation along the tectonically active South American coast. Especially within the Altos de Talinay area of central Chile, changes in terrace elevation accompanied by normal faulting highlight the importance of upper-plate structures with respect to the permanent deformation and modulation of uplift in the forearc region. However, little is known about the fault-related mechanisms driving permanent coastal uplift and about the persistency of current uplift-rate patterns over time. To address these issues, we carried out a continuous mapping of late Pleistocene marine terraces in the area of the 2015 M_W8.3 Illapel earthquake to study upper-plate faults as a mechanism for variations in uplift rate. We furthermore compared terrace-derived uplift rates with decadal GPS velocities, associated interseismic locking, and coseismic slip during the Illapel earthquake to analyze the persistency of seismic asperities over time. Our results show uplift rates ranging from 0.1 to 0.6 mm/yr with higher uplift rates generally observed for older terraces as well as pronounced changes in uplift rate accompanied by crustal normal faults, which indicates varying tectonic activity through time. Upper-plate normal faulting might be the result of local gravitational collapse, a second-order phenomenon overprinting regional tectonic uplift that might result from subduction erosion and subsequent underplating. We propose that crustal fault slip is a responsible mechanism for such short-wavelength changes in uplift rate but its relation with the earthquake cycle still remains unclear. The lack of correlations between current asperities and long-term uplift rates furthermore suggests that decadal-scale estimates of coastal deformation are not representative with respect to millennial-scale permanent deformation of the forearc.

4.2 Introduction

Multiple late Pleistocene marine terraces along tectonically active plate margins are the vestiges of a complex interplay between coastal abrasion during relative sea-level highstands and vertical tectonic motion (e.g., Darwin, 1846; Hsu, 1992; Pedoja et al., 2014; Shikakura, 2014; Matsu'ura, 2015; Muhs, 2022). These terraces record anelastic deformation and topographic change in coastal areas that have been associated with the cumulative effects of plate-boundary slip during and between earthquakes (Sawai et al., 2004; Bookhagen et al., 2006; Melnick et al., 2006; Briggs et al., 2008; Baker et al., 2013; Hasegawa & Yoshida, 2015; Wesson et al., 2015; Melnick, 2016). Identifying, mapping and explaining the spatiotemporal distribution of coastal terraces and strandlines is therefore an important task and it has been used in global efforts to elucidate the mechanisms and forcing factors that impact the tectonic evolution and inherent seismic hazards of forearcs and their shoreline environments (e.g., Jara-Muñoz et al., 2015; Matsu'ura, 2015; Freisleben et al., 2021; McKenzie et al., 2022). Knowledge of regional terrace and shoreline elevation may ultimately enable the deduction of the deformation history, an assessment of the rate of vertical motions, and the spatial characterization of coastal deformation. Consequently, if these parameters can be quantified, they may provide valuable information about differential tectonic behavior and tectonic segmentation as well as the history of repeatedly active earthquake-rupture zones along forearcs, which are necessary for earthquake hazard and risk assessments (e.g., Melet et al., 2020).

The western continental margin of South America is characterized by numerous sites with the typical staircase morphology of multiple marine terraces that increase in age with elevation and distance from the present-day shoreline; these landforms thus constitute valuable strain markers of Quaternary vertical movements that document strain accumulation spanning several thousand kilometers and reflecting landscape-evolution processes on timescales of up to several 10^5 years (Pedoja et al., 2006; Saillard et al., 2011; Jara-Muñoz et al., 2015). Particularly well-preserved, differentially uplifted sequences of marine terraces occur in the Altos de Talinay area of central Chile between approximately 30° and 31° S (Fig. 4.1). Despite being located at a margin where forearc uplift and mountain building farther inland are ongoing, this region is also characterized by ubiquitous Quaternary normal faults in the forearc that have influenced the spatial distribution and local deformation patterns of these terrace sequences on longer timescales beyond the earthquake cycle (Ota et al., 1995; Saillard et al., 2009). Next to the

uplifted Quaternary terrace sequences within the different seismotectonic blocks of the forearc, Quaternary normal-fault scarps highlight the importance of upper-plate structures with respect to the modification of permanent deformation features and topographic evolution as well as their role in modifying expected regional seismogenic hazards (Armijo & Thiele, 1990; Adam & Reuther, 2000; Farías et al., 2011; Aron et al., 2013; Toda & Tsutsumi, 2013; Armijo et al., 2015; Melnick et al., 2019).

While the existence of normal faults straddling the coast of Chile and other subduction margins worldwide has been known for some time, the ultimate cause for trench-parallel extensional faulting and its spatiotemporal relationship with uplift and contractional deformation associated with megathrust earthquakes is not very clear. It has been suggested that normal-faulting is intimately linked and possibly triggered by megathrust earthquakes that rupture the forearc over a length of several hundreds of kilometers (e.g., Clarke & Carver, 1992; Farías et al., 2011; Toda & Tsutsumi, 2013; Gomberg & Sherrod, 2014; Melnick et al., 2019; Jara-Muñoz et al., 2022). Such a close link between the occurrence of megathrust earthquakes and normal faulting in the forearc of Chile has been suggested by several authors. This comprises recent seismicity and extensional faulting triggered by the 2010 Maule earthquake (Farías et al., 2011; Aron et al., 2013) as well as Holocene activity of currently inactive normal faults (Melnick et al., 2019). The well-preserved Pleistocene marine terraces in the Altos de Talinay area in central Chile and trench-parallel normal faults cutting these landforms afford an excellent opportunity to assess the relationships between coastal uplift in a wide seismotectonic segment and the effects of an overprint by localized extensional faulting. Since the compressional tectonic regime is responsible for permanent coastal uplift as well as thrust faulting and mountain building farther inland, crustal normal faults seem to be a second-order feature modifying coastal morphology on a short-wavelength scale. In this context, we address the following questions in this study. First, to what extent do crustal normal faults affect the uplift rate in the central Chilean Altos de Talinay region and what could be the associated mechanisms, also with respect to the permanent deformation of the forearc? Second, how persistent and representative are present-day uplift-rate patterns over time, especially when uplift is extrapolated and assessed on timescales of several 10^4 to 10^5 years? Answering the first question will not only furnish further insights into the activity of crustal faulting in this area, but might also improve our understanding as to what mechanisms determine the characteristics of permanent coastal uplift along active convergent margins. Answering the second question will help to unravel the

relationship between asperities revealed by decadal GPS velocities as well as interseismic locking and millennial-scale uplift-rate patterns inferred from marine terraces.

In this study we extend the marine-terrace mapping of Freisleben et al. (2021) to the well-preserved terrace levels that are older than the last interglacial period within the area that was affected by the 2015 M_W8.3 Illapel earthquake. We exploit the versatility of the TerraceM software in MATLAB® (Jara-Muñoz et al., 2019) in providing a consistent methodological approach for a continuous mapping of terrace elevations and a reliable comparison between the different levels, particularly with respect to the local influence of crustal faulting. We further support published age constraints used for terrace-level assignment with detailed stratigraphic sections and age determinations to calculate laterally continuous uplift rates. We observed the impact of numerous crustal faults on modifying terrace elevations and associated uplift rate along the forearc, which allowed us to draw further conclusions regarding the activity of these structures through time. Additional mapping of drowned marine terraces in the northern sector of the study area near Coquimbo allowed for the first time uplift-rate estimates of even younger Pleistocene terrace sequences.

4.3 Tectonic and geomorphic setting

4.3.1 Tectonic setting

At the South American convergent plate margin, the oceanic Nazca plate subducts beneath the South American continent at a convergence rate of 63.3 mm/yr (at 30° S) and with a convergence azimuth of 80.7° N (Kendrick et al., 2003). Spatial distributions of Benioff-zone seismicity delineate varying angles of the subducting slab allowing the subduction zone to be divided into segments. Comparably steep segments of the subducting plate dipping 25° to 30° at depths of ~100 km, are interrupted by two major flat-slab subduction segments, dipping only 5° to 10°, beneath central Peru (2°–15° S) and beneath central Chile (27°–33° S; Jordan et al., 1983; Hayes et al., 2018). Our study area is located in the central Chilean flat-slab subduction segment, which has generated several megathrust earthquakes during the last 150 years (Beck et al., 1998; Lomnitz, 2004; Ruiz & Madariaga, 2018) and which is characterized by multiple Pleistocene marine terraces (e.g., Ota et al., 1995; Saillard et al., 2009).

The seafloor of the subducting plate is characterized by several high bathymetric anomalies; for example, the Juan Fernández and Copiapó ridges delimit the southern and northern terminations of the Chilean flat-slab subduction segment (Fig. 4.1c). According to various authors (Wang & Bilek, 2011; Bassett & Watts, 2015; Collot et al., 2017), subduction of such bathymetric anomalies influences locking of the megathrust and the associated seismic hazard.

4.3.2 Major coastal fault systems and seismicity

The subduction of the Nazca plate is closely linked with the occurrence of multiple fault systems of different kinematics that affect the western South American coast. The main structures along the north-central Chilean convergent margin belong to the Atacama fault system (AFS), which extends from Iquique to La Serena, characterized by predominantly N–S-striking normal faults (Fig. 4.1c; Naranjo, 1987; Santibáñez et al., 2019). The Altos de Talinay area and regions farther south (30.2°–32° S) are mainly characterized by N–S-striking normal faults offsetting older terrace levels (Fig. 4.1b; e.g., Puerto Aldea, El Fraile, Los Loros, Quebrada del Teniente faults; Ota et al., 1995; Maldonado et al., 2021).

Great earthquakes (≥ M_W7.5) along the South American margin are related to the subduction of the Nazca plate beneath the South American continent, apart from few normal-faulting events within the subducting slab (Beck et al., 1998). The spatial and temporal distribution of seismicity displays patterns of recurrent mega-earthquakes in distinct seismotectonic segments of the forearc (Thatcher, 1990; Lomnitz, 2004; Saillard et al., 2017; Molina et al., 2021). Great earthquakes along the central Chilean margin comprise the 1922 M8.4 Atacama event, the area of which constitutes a major seismic gap ever since. Farther south is the Illapel segment, which ruptured during M8.3 events in 1943 and 2015, and the Valparaíso segment that ruptured in 1906 (M8.4) and 1985 (Beck et al., 1998; Lomnitz, 2004; Barnhart et al., 2016).

4.3.3 Coastal geomorphology

The western portion of the South American continent is mainly characterized by the major physiographic feature of the Andean orogen that can be divided into distinct morphotectonic segments (Jaillard et al., 2000). In the N–S-trending Chilean Andes (south of 18° S), the forearc comprises the 50-km-wide and up to 2700-m-high Coastal Cordillera, which is separated from the Precordillera by the Central Depression (Jordan et al., 1983). In the flat-slab subduction

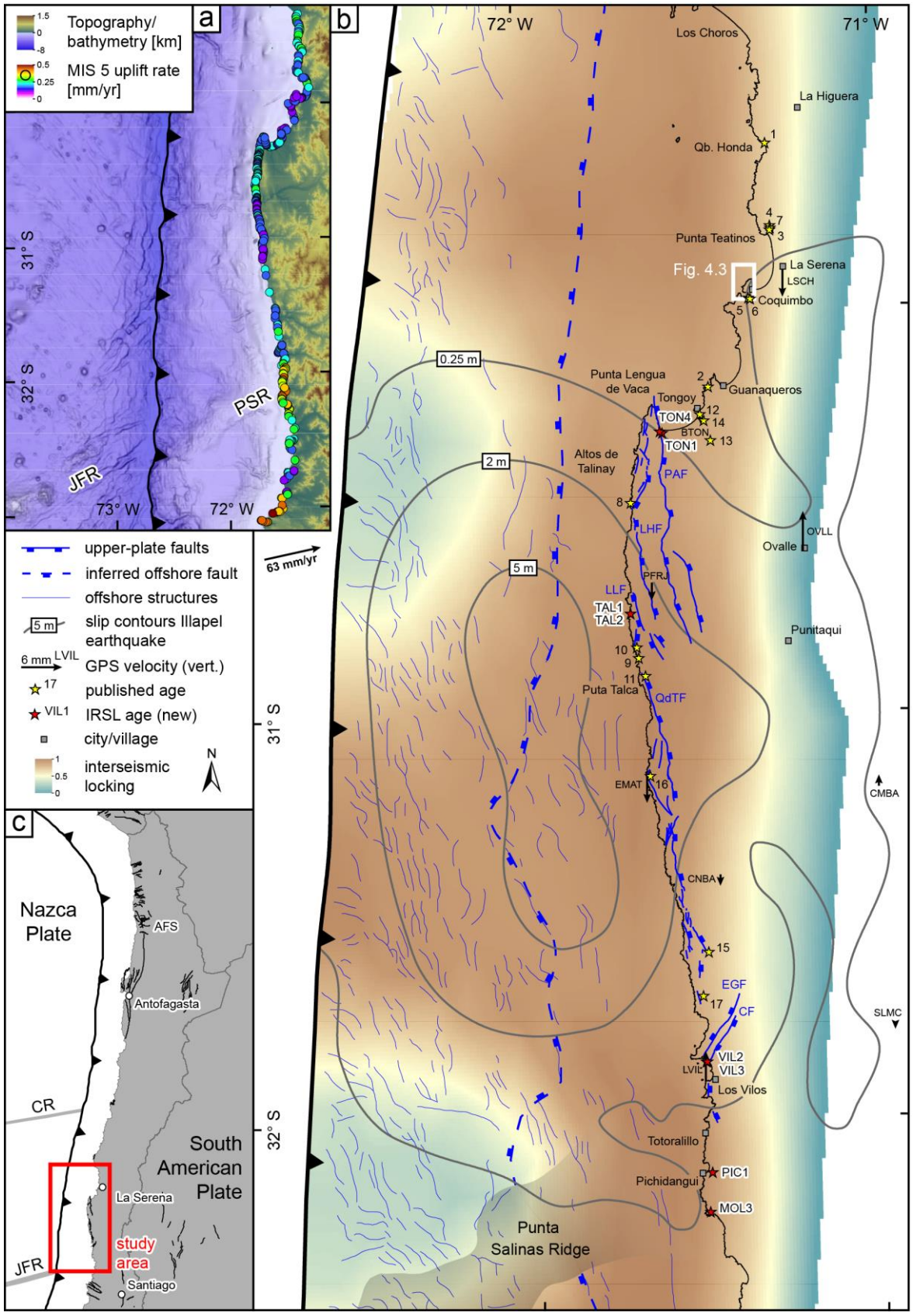
a
Topography/ bathymetry [km]
MIS 5 uplift rate [mm/yr]
31° S
32° S
73° W
72° W
PSR
JFR
b
72° W
71° W
Los Choros
La Higuera
Qb. Honda
Punta Teatinos
Fig. 4.3
La Serena
LSCH
Coquimbo
0.25 m
Punta Lengua de Vaca
Guanaqueros
Tongoy
TON4
BTON
TON1
2 m
Altos de Talinay
PAF
LHF
Ovalle
OVLL
5 m
PFRJ
LLF
TAL1
TAL2
Punitaqui
Puta Talca
QdTF
EMAT
CMBA
CNBA
EGF
CF
SLMC
VIL2
VIL3
LVIL
Los Vilos
Totoralillo
Pichidangui
PIC1
MOL3
Punta Salinas Ridge
63 mm/yr
upper-plate faults
inferred offshore fault
offshore structures
slip contours Illapel earthquake
GPS velocity (vert.)
published age
IRSL age (new)
city/village
interseismic locking
N
c
Nazca Plate
AFS
Antofagasta
CR
South American Plate
La Serena
study area
JFR
Santiago

Figure 4.1: (a) Topographic and bathymetric map with MIS 5 uplift rates (Freisleben et al., 2021). (b) Raster of interseismic locking and GPS velocities before the Illapel earthquake (2010–2015, both from Melnick et al. (2017)), contours of coseismic slip of the Illapel earthquake (Tilmann et al., 2016), crustal faults (Saillard et al., 2009; Maldonado et al., 2021), offshore structures (Becerra et al., 2017), location of published age estimates and new sampling sites for luminescence dating. (c) Geodynamic setting and location of the study area. Abbreviations: AFS – Atacama fault system, CR – Copiapó Ridge, JFR – Juan Fernández Ridge, PAF – Puerto Aldea fault, QPCF – Quebrada Palo Cortado fault, LHF – Los Huiros fault, LLF – Los Loros fault, QdTF – Quebrada del Teniente fault.

segment between 27° S and 33° S there is neither a central depression nor active volcanism in the high Andes, and south of this segment, the Coastal Cordillera decreases to 500 m at 46° S.

In the coastal realm, marine terraces are formed at glacial-cycle timescales by the combined effects of wave-erosion, tectonic uplift, and sea-level oscillations. Interglacial and interstadial relative sea-level highstands during the Pleistocene are associated with the formation of marine terraces and are denoted according to odd-numbered Marine Isotope Stages (MIS) that were characterized by relative sea-level highstands (Shackleton et al., 2003). Staircase-like sequences of multiple marine terrace levels can be observed along almost the entire western South American coast (Pedoja et al., 2006; Jara-Muñoz et al., 2015; Freisleben et al., 2021). The best-preserved and laterally most continuous terrace level along the coast of western South America and elsewhere was formed during the last interglacial sea-level highstand and is attributed to MIS 5e based on global observations of sea-level fluctuations and our detailed mapping of terrace surfaces. The temporal range of this highstand that formed wide abrasion platforms that are now mostly uplifted, extends from 119 to 130 ka with a paleo-sea level height of +3 ± 3 m (Stirling et al., 1998; Siddall et al., 2006; Hearty et al., 2007). This terrace level has been used frequently as a geomorphic marker for the estimation of coastal uplift rates (Ota et al., 1995; Saillard et al., 2009; Rodríguez et al., 2013; Jara-Muñoz et al., 2015; Martinod et al., 2016; Melnick, 2016; Freisleben et al., 2021). Additional Pleistocene sea-level highstands and their associated paleo-sea level elevations are summarized in Table 4.1.

Table 4.1: Age ranges of Pleistocene sea-level highstands and their corresponding paleo-sea level elevations. The fourth column shows the terrace age and the duration of the highstand used for the calculation of uplift rate and uplift-rate error. References: 1 – Hearty et al. (2007); 2 – Siddall et al. (2006); 3 – Rohling et al. (2009).

Marine Isotope Stage	Paleo-sea level [m]	Age range [ka]	Age [ka], duration of the highstand [kyr]	References
MIS 5e	3 ± 3	119–130	125; 11	1; 2; 3
MIS 7	-10 ± 5	190–235	210; 45	2; 3
MIS 9c	2 ± 5	318–324	320; 6	2; 3
MIS 11	0 ± 10	395–415	400; 20	2; 3

Previously published ages of marine terraces in the study area (Table 4.2) were estimated using various dating techniques. They comprise U/Th dating of marine shells (Radtke, 1987, 1989; Saillard et al., 2012) as well as mollusk aminostratigraphy (AAR) and electron-spin resonance (ESR; Leonard & Wehmiller, 1992). These techniques are primarily applied to terrace levels of the last or penultimate interglacial (MIS 5 or MIS 7) in the northern part of the study area from Los Choros to Tongoy. Ages of older terrace levels are scarce, primarily constrained by cosmogenic nuclide dating in the Altos de Talinay area and farther south (Saillard et al., 2009; Saillard et al., 2012; Rodríguez et al., 2013; Martinod et al., 2016).

Table 4.2: Published age constraints of marine terrace levels in the study area. Numbers refer to the age constraints shown in Fig. 4.1b. ESR: electron-spin resonance; AAR: amino-acid racemization (aminostratigraphy).

Nr.	Location	Latitude [° S]	Longitude [° W]	Technique	MIS	Age [ka]	Reference
1	Quebrada Honda	29.6	71.29	U/Th, ESR	5c	100.1	Radtke (1987)
2	Guanaqueros	30.2	71.47	U/Th, ESR	5c	100	Radtke (1987)
3	Punta Teatinos	29.81	71.28	U/Th, ESR	5e	124.8	Radtke (1989)
4	Punta Teatinos	29.8	71.28	U/Th, ESR	9	315	Radtke (1989)
5	Herradura	29.98	71.35	U/Th, ESR, AAR	5e	128.7	Radtke (1989); Leonard and Wehmiller (1992)
6	Coquimbo	29.98	71.34	U/Th, ESR, AAR	≥ 7	251.5	Radtke (1989); Leonard and Wehmiller (1992)
7	Punta Teatinos	29.81	71.28	AAR	≥ 7	242.3	Leonard and Wehmiller (1992)
8	Altos de Talinay	30.48	71.69	10Be	5	142.4	Saillard et al. (2009)
9	Altos de Talinay	30.86	71.68	10Be	7	214	Saillard et al. (2009)
10	Altos de Talinay	30.84	71.69	10Be	9-11	303.8	Saillard et al. (2009)
11	Altos de Talinay	30.91	71.66	10Be	≥ 15	653	Saillard et al. (2009)
12	Tongoy	30.26	71.49	U/Th	5c	94.5	Saillard et al. (2012)
13	Tongoy	30.33	71.46	U/Th	11	361	Saillard et al. (2012)
14	Tongoy	30.28	71.48	U/Th	11	386	Saillard et al. (2012)
15	Choapa River	31.59	71.5	10Be	11	419.6	Rodríguez et al. (2013)
16	Caleta Maiten	31.15	71.66	10Be	≥ 13	531.9	Rodríguez et al. (2013)
17	Chigualoco	31.7	71.52	10Be	≥ 11	-	Martinod et al. (2016)

4.4 Methods

4.4.1 Mapping of marine terrace elevations

At tectonically active coasts, erosional marine terraces can be used to estimate tectonic uplift rates from their elevations, if past sea-level oscillations are taken into account. The

topographical data to carry out elevation measurements comprised TanDEM-X topography of 12 m horizontal resolution (German Aerospace Center, 2018), which was converted to orthometric heights using the EGM2008 geoid and projected in UTM zone 19S. Similarly to the procedure described in Freisleben et al. (2021) for the MIS 5 terrace level, we mapped the inner edge of shorelines of three additional, higher terrace levels based on slope changes at the foot of the paleo-cliffs (Jara-Muñoz et al., 2016). However, the shoreline angle constitutes the most accurate representation of terrace height, usually disturbed after the abandonment of the marine terrace by fluvial degradation and hillslope processes (Anderson et al., 1999; Jara-Muñoz et al., 2015). Elevation measurements were therefore conducted using a profile-based approach in TerraceM, which extrapolates the intersection of linear regression lines that were picked manually along undisturbed sections of the paleo-cliff and paleo-platform (Fig. 4.3a and 4.3b; Jara-Muñoz et al., 2016). TerraceM extracts maximum elevations from the swath profile and calculates the uncertainty of each measurement from the 95 % confidence intervals of both regressions. We placed the associated swath profiles in a perpendicular position with respect to the inner edge at locations characterized by sufficiently well-developed paleo-platforms and minimal topographic disturbances such as colluvial wedges, paleo-deltas, or areas of high river incision. Due to differences in platform width and river spacing, we used swath-profile widths of 200 m for the highest terrace level and 100 m for both lower levels.

4.4.2 Luminescence dating of marine terrace deposits

Sediments covering wave-cut marine terraces usually consist of regressive sequences deposited immediately after a sea-level highstand (Bradley, 1957; Jara-Muñoz et al., 2015), which can therefore be used to approximate minimum ages for such landforms (Choi et al., 2003; Bianca et al., 2011; Jara-Muñoz et al., 2015; McKenzie et al., 2022). In this study, we describe and analyze stratigraphic sections of marine terrace deposits (Fig. 4.2) that presumably belong to MIS 5 based on lateral correlations. The interpreted stratigraphy as well as accompanying ages of samples within the sedimentary sequences support the lateral assignment of last interglacial marine terraces.

We dated eight sediment samples from marine terrace deposits (Fig. 4.2) using the post-infrared infrared-stimulated luminescence (post-IR IRSL) signal of K-feldspar. The sediments consist of sand material from either alluvial or marine depositional environments that were sampled between 1.2 and 5.5 m depth at five different locations within the study area (Fig. 4.1, 4.2, Table

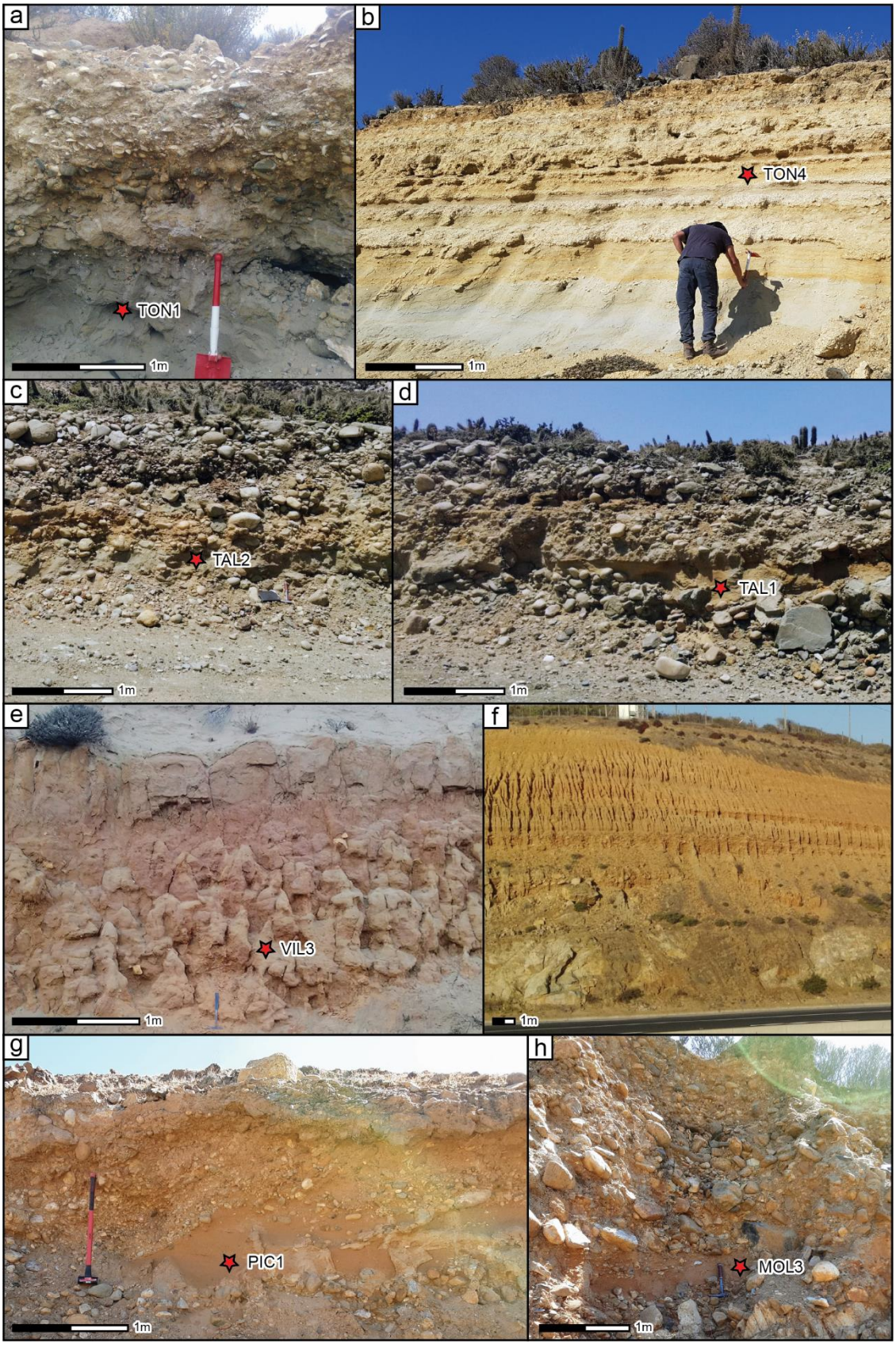

Figure 4.2: Field views of sedimentary sequences and sampling sites of the deposits dated using post-IR IRSL. Panel f shows the sedimentary sequence from which VIL2 was sampled, although the actual sampling location is not included in the photo.

4.3). The measurements were conducted on coarse-grained K-feldspar (150–200 μm) after pre-processing under red-light conditions that included drying at 50 °C, sieving to the envisaged grain size, and chemical treatment to remove carbonates, organic material, and clay minerals as well as density separation for K-feldspar.

All samples were measured with a standard post-IR IRSL protocol with first stimulation temperature at 50 °C and second stimulation temperature at 225 °C ($pIRIR_{225}$; Buylaert et al., 2009). Both signals were stimulated with infrared LEDs for 200 sec. during the multi-grain measurements or with an infrared laser for 2 sec. during the single-grain measurements, and detected through a LOT interference filter. The preheating was set to 250 °C (60 sec.) throughout the protocol and each measurement cycle was ended by a hotbleach at 270 °C (100 sec). The suitability of the applied $pIRIR_{225}$ protocol for our samples was checked by means of dose recovery tests and residual dose measurements, which included resetting of the natural signal in a solar simulator for 24 h. Dose recovery ratios are within 10 % of the uncertainties of all samples and the laboratory residual doses remain at insignificant levels (< 5 %) of all burial doses. For the calculation of burial doses, only aliquots were considered that showed (1) IRSL signals > 3 times above background, (2) recycling ratios between 0.9 and 1.1, and (3) were not in saturation. Excluding these, between 5 and 6 equivalent doses (D_e) were measured on 1 mm aliquots to calculate a mean burial dose for each sample using the central age model of Galbraith et al. (1999) (Table 4.3). Additional single-grain measurements for samples TON1 and TON4 with D_e measurements on 55 and 78 grains, respectively, show a large scatter of overdispersion (39–46 %) and are therefore based on the minimum age model (Table 4.3; Galbraith et al., 1999). Luminescence ages were ultimately calculated by combining burial doses and dose rates using the DRAC software (Table 4.3; Durcan et al., 2015). The necessity to correct for anomalous fading was evaluated through fading measurements on three 8 mm aliquots for each sample according to the procedure of Auclair et al. (2003). The associated g-values (1.2–1.8 % per decade) were assumed to be insignificant (Buylaert et al., 2012) and not used for correcting $pIRIR_{225}$ ages.

Environmental dose rates of the surrounding sediments are based on radionuclide analysis (U, Th, K) by means of high-resolution gamma spectrometry (Table 4.3). The radiation attenuation by pore water was considered by using water contents of 5 ± 5 % and alpha efficiency was assumed to be 11 ± 2 % according to Kreutzer et al. (2014). Internal dose rates are based on the empirical potassium content of K-feldspar (12.5 ± 0.5 %; Huntley & Baril, 1997) and the

determination of cosmic dose rates followed the approach of Prescott and Hutton (1994) using sampling depth, sediment density, geographical position, and altitude above sea level.

Table 4.3: Infrared-stimulated luminescence (IRSL) ages and key parameters for their calculation. Elev – sample elevation, Depth – sample depth, Size – aliquot size, SG – single-grain measurement, N – number of accepted aliquots, OD – overdispersion, Dose – burial dose, 2xD0 – characteristic dose (89 % of saturation), *based on 2xD0.

Sample	Long [° W]	Lat [° S]	Elev [m]	Depth [m]	Dose [Gy]	Size [mm]	N	OD [%]	2xD0 [Gy]	U [ppm]	Th [ppm]	K [%]	Age [ka]
TON1	71.60	30.31	18.1	2.2	766±84 437±62	1 SG	6 55	27±8 46±5	532	1.62± 0.04	6.85± 0.16	2.08± 0.03	> 144* 119±18
TON4	71.61	30.30	15.1	1.5	734±90 305±37	1 SG	6 78	30±9 39±4	504	3.8± 0.06	3.79± 0.14	1.42± 0.07	> 150* 89±12
TAL1	71.70	30.75	13.9	2	278±30	1	6	26±8	600	0.93± 0.07	3.79± 0.27	2.16± 0.06	84±10
TAL2	71.70	30.75	13.9	1.5	292±44	1	6	37± 10	700	1.55± 0.11	10.28 ±0.71	1.67± 0.04	82±13
VIL2	71.51	31.86	36.2	4.5	369±23	1	5	13±5	560	2.18± 0.15	7.65± 0.53	1.74± 0.04	104±8
VIL3	71.51	31.86	43.2	5.5	460±47	1	6	24±7	560	2.16± 0.15	8.63± 0.6	1.84± 0.05	124±14
PIC1	71.50	32.13	27.9	1.2	473±24	1	6	10±4	620	1.21± 0.09	6.62± 0.47	2.45± 0.06	117±8
MOL3	71.51	32.23	18.9	2.8	377±28	1	5	16±5	650	1.63± 0.11	9.11± 0.63	2.88± 0.07	80±7

4.4.3 Terrace-level assignment and calculation of uplift rates

Mapping of marine terrace elevations in the study area was carried out for the three most continuous terrace levels above the position of the last interglacial terraces associated with MIS 5. Our assignment to odd-numbered MIS is based on previously published age constraints (Table 4.2), newly dated luminescence ages (Table 4.3), and lateral tracking of the same terrace levels in areas with limited age estimates. Consequently, we attributed the three newly mapped terrace levels to MIS 7, MIS 9 and MIS 11 (from lowest to highest). This decision, as well as existing conflicts with previously published terrace assignments, will be discussed below.

To calculate uplift rates for the various levels of marine terraces, we first subtracted paleo sea-level altitudes of the respective interglacial maximum from the measured shoreline-angle elevations and subsequently divided this relative sea level (ΔH) by the associated terrace age (T). Paleo-sea level and terrace age are listed in Table 4.1 for the most recent interglacial

maxima of the Pleistocene. The standard error of uplift rates SE(u) was calculated using Eq. 1 from Gallen et al. (2014):

$$SE(u)^2 = u^2 \left(\left(\frac{\sigma_{\Delta H}^2}{\Delta H^2} \right) + \left(\frac{\sigma_T^2}{T^2} \right) \right) \quad \text{(Eq. 4.1)}$$

where σ_T is the duration of the highstand and $\sigma_{\Delta H}^2$ equals $\sigma_{H_T}^2 + \sigma_{H_{SL}}^2$, which sums the uncertainty in shoreline-angle elevation from TerraceM (σ_{H_T}) and error estimates in absolute sea level ($\sigma_{H_{SL}}$) (Table 4.1; Siddall et al., 2006; Hearty et al., 2007; Martinod et al., 2016).

4.4.4 High-resolution bathymetry and mapping of drowned marine terraces

High-resolution bathymetry allowed the mapping of drowned submarine terraces in a small area (11x13 km) off the coast of Coquimbo (Fig. 4.3). Bathymetric point data was provided with 5 m horizontal resolution by the Servicio Hidrográfico y Oceanográfico de la Armada de Chile (SHOA). The survey was carried out using single- and multi-beam echosounders (Kongsberg EA400 and EM3002) with real time kinematic positioning systems. The raw data were processed at SHOA using CARIS HIPS & SIPS software, and corrections were made for inaccuracies regarding GPS, tides, sound velocity, and vessel motion. We subsequently calculated a bathymetric grid using the point data in a triangulation-based natural neighbor interpolation ('griddata' function in MATLAB® version 2022b). Similar to the uplifted onshore marine terraces, we then mapped the inner edge of the paleo-shoreline (Fig. 4.3a) and estimated the shoreline-angle elevations in TerraceM using swath profiles of 200 m width (Fig. 4.3a, 4.3b).

4.4.5 Landscape-evolution model

In absence of robust terrace-age constraints, the application of a landscape-evolution model (LEM) has been proven useful to decipher the timing and uplift rates of marine terrace sequences (Melnick, 2016; Jara-Muñoz et al., 2017; Racano et al., 2020). We therefore applied the LEM included in TerraceM (Jara-Muñoz et al., 2019) to estimate the age of the terrace levels where age constraints were limited. The LEM is based on the wave erosion and energy-dissipation model previously developed by Sunamura (1992) and Anderson et al. (1999). For

the modeling itself we used the sea-level curve of Rohling et al. (2009) and a constant uplift rate varying between the individual models from 0.05 to 0.5 mm/yr (step size: 0.05 mm/yr) as well as a variable uplift rate for the last model (constant at 0.5 mm/yr, decreasing at 30 ka linearly to 0.05 mm/yr). Additional parameters comprised an initial slope of 5° based on the geometry of the swath profiles (Fig. 4.4), a wave height of 5 m, which is typical for central Chile (Lorscheid & Rovere, 2019; Freisleben et al., 2021), and an initial erosion rate of 0.3 m/yr, which usually shows a weak dependence on the model results (Jara-Muñoz et al., 2017). We truncated the sea-level curve at the Last Glacial Maximum (LGM), since the modeled marine terraces locate below the current sea level and would be deleted in the model by the Holocene sea-level rise.

4.4.6 Interseismic GPS velocities, interseismic locking, and coseismic slip

To estimate the influence of recent interseismic and coseismic displacements on long-term coastal uplift, we compared uplift rates of marine terraces with interseismic GPS velocities, the associated degree of locking on the megathrust, and coseismic slip during the Illapel earthquake. We used decadal, vertical GPS velocities from Melnick et al. (2017) derived from trajectory models of the time series and referring to a stable South American reference frame. The time series and the resulting GPS velocities were separated by the 2010 M_W8.8 Maule and the 2015 M_W8.3 Illapel earthquakes into two interseismic intervals (subsequently named pre-2010 and 2010–2015). Accordingly, the degree of interseismic plate locking was estimated for both time periods and expressed as a fraction of plate-convergence rate (Melnick et al., 2017). Apart from interseismic GPS velocities and plate locking, we further used coseismic slip occurring during the 2015 Illapel earthquake from Tilmann et al. (2016) for the comparison with terrace-uplift rates. GPS vertical velocities were displayed as vectors of variable lengths (Fig. 4.6d); we extracted values of interseismic locking (Fig. 4.6d) and coseismic slip (Fig. 4.6a) along a swath profile extending 10 km inland of a simplified coastline. To test for direct correlations between these parameters, we extracted the values of interseismic locking (both interseismic periods) as well as the values of coseismic slip at the locations of our terrace measurements and visualized these as scatter plots (Fig. 4.7). We chose to apply this procedure only for the two most continuously preserved terrace levels of MIS 5 and MIS 11.

4.5 Results

4.5.1 Depths and uplift rates of drowned marine terraces

Mapping of high-resolution bathymetry allowed us to measure the depths of one less-well preserved and two rather pronounced levels of drowned marine terraces in a narrowly defined area offshore Coquimbo (Fig. 4.3a, 4.3b). The lowermost and best-preserved terrace level displays shoreline-angle elevations from 80 to 92.9 m below sea level, with generally lower

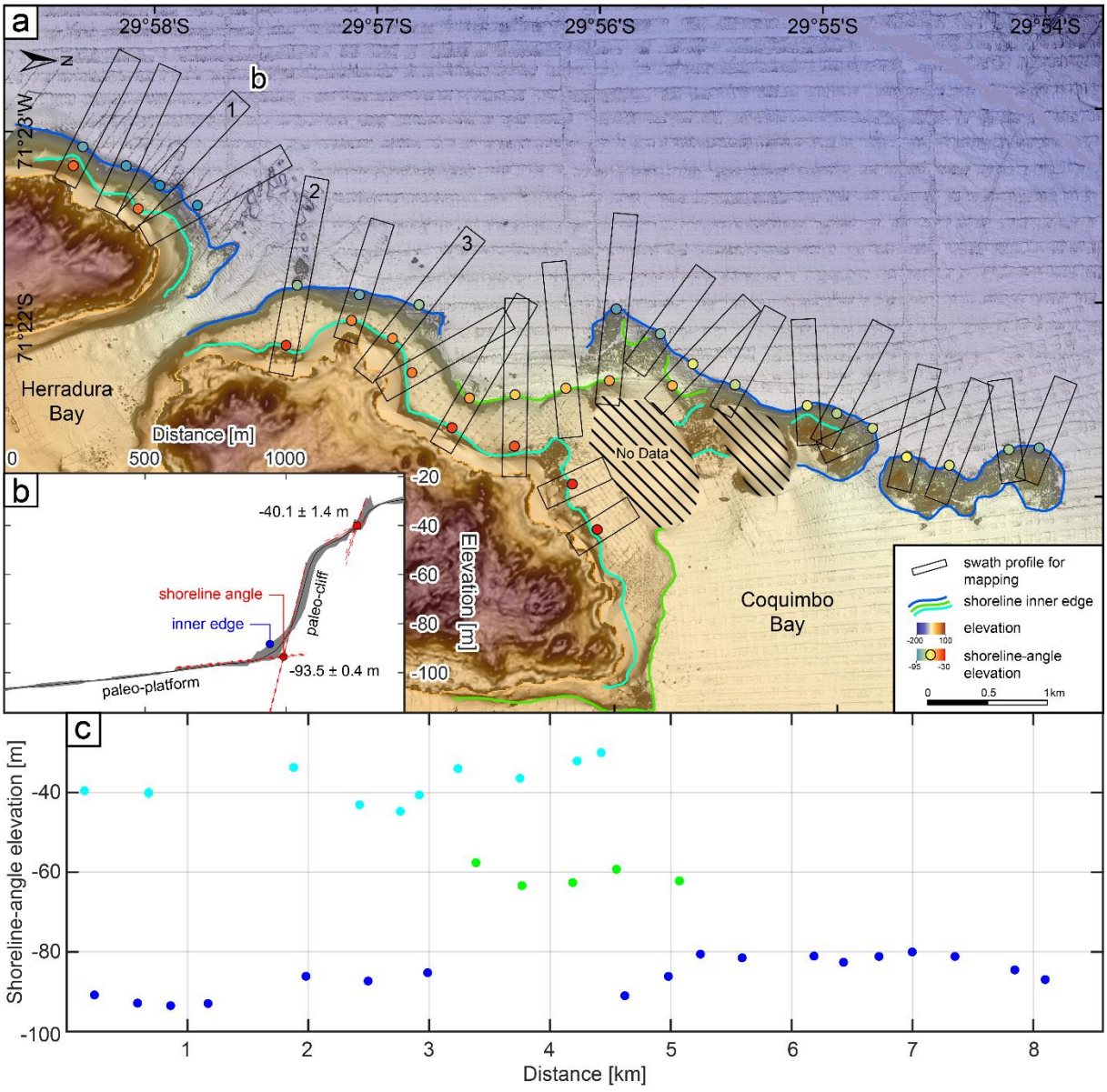

Figure 4.3: (a) High-resolution bathymetry offshore Coquimbo with mapped inner edges of shorelines of drowned marine terraces and locations of swath profiles and their resulting shoreline-angle measurements. (b) Example of a swath profile used in TerraceM to measure shoreline-angle elevations (location specified in a). (c) Depths of shoreline-angle measurements indicating two pronounced, and one less-well preserved terrace level.

depths in the northern Coquimbo Bay region (Fig. 4.3c). The uppermost terrace level varies between 30 and 44.7 m depth showing greater depths generally south of Herradura Bay. The terrace level between the previously described terraces only appears in the central part of the mapped bathymetric area with elevations of ~60 m below sea level.

To estimate uplift rates associated with the measured shoreline-angle depths, we applied a LEM testing a variety of constant uplift rates (0.05–0.5 mm/yr) as well as a variable uplift rate that decreases linearly from 0.5 mm/yr at 30 ka to 0.05 mm/yr. The LEMs show a clear development of two terrace levels below the current sea level that are related to the highstand of MIS 3 and the lowstand of MIS 2 (LGM; Fig. 4.4). With respect to the greater depths measured for the swath profiles in the south (profile 1), low uplift rates (0–0.1 mm/yr) agree with the depth of the MIS 2 terrace, and higher uplift rates (0.4 mm/yr) correlate with the position of the MIS 3 terrace. Farther north, swath profiles documenting more moderate shoreline-angle depths (profile 2 and 3) might indicate higher uplift rates. For instance, profile 2 correlates with uplift rates of 0.1–0.2 mm/yr for MIS 2 and 0.5 mm/yr for MIS 3, while profile 3 agrees with uplift rates of 0.2–0.3 mm/yr for MIS 2 and 0.4 for MIS 3. Since the disparity between both drowned terrace levels might indicate a changing uplift rate between MIS 3 and MIS 2, we also calculated a LEM using a variable uplift rate. With a constant uplift rate of 0.5 mm/yr that decreases at 30 ka linearly to 0.05 mm/yr, we were able to reproduce the terrace morphology that is characteristic for the central and southern part of the examined bathymetric patch. This LEM

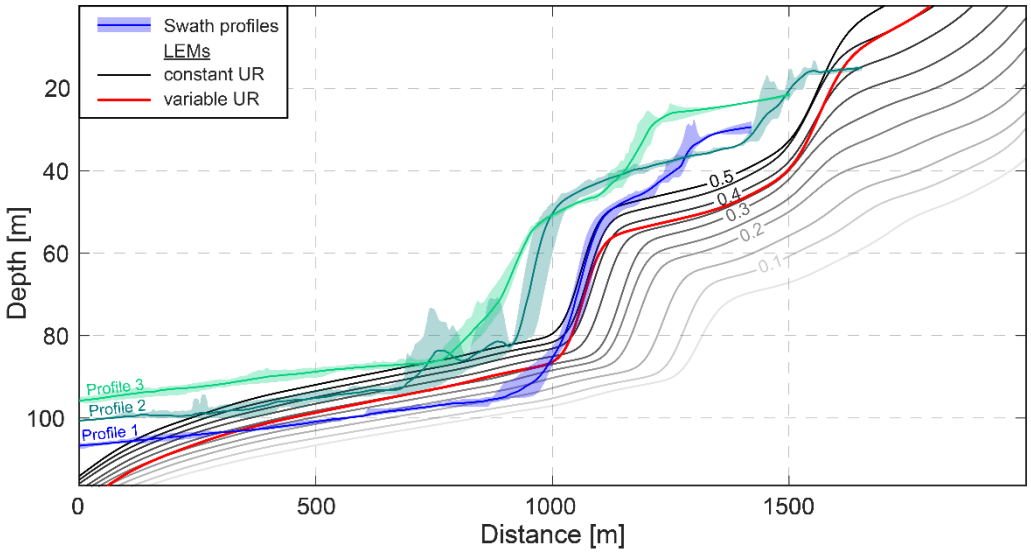

Figure 4.4: Swath profiles extracted from the high-resolution bathymetry (locations in Fig. 4.3) in comparison with landscape-evolution models (LEMs) using constant uplift rates (UR) or a varying uplift rate (constant at 0.5 mm/yr until 30 ka, decreasing linearly to 0.05 mm/yr subsequently).

results in a lower terrace at 86 m depth that is related to MIS 2 and a higher terrace at 40 m depth that is related to MIS 3.

4.5.2 Stratigraphy and luminescence ages of selected MIS 5 terrace sites

To support the assignment of last interglacial marine terraces in our study area, we dated several sedimentary deposits using post-IR IRSL. In the following paragraphs, we describe the sedimentary sequences, interpret the stratigraphy regarding their depositional environments and assign the terrace deposits to a MIS based on the results of the luminescence dating.

The sedimentary sequence sampled SW of Tongoy (Fig. 4.2a, 4.5a) starts with a carbonate crust on top that is separated from a matrix-supported conglomerate below by a sharp undulating contact. The conglomerate consists of a fossil-rich upper part containing bivalves, gastropods and crustaceans (e.g., Austromegabalanus psittacus) as well as a brown, clayey matrix with fossil fragments. Towards its lower part, the layer becomes increasingly supported by well-rounded, poorly sorted, and polymictic clasts. The adjacent layer consists of fine to medium sand characterized by incipient leaching of carbonate and small inclined fractures. Luminescence dating of TON1 sampled within this layer resulted in an age of 118 ± 18 ka indicating burial at the end of MIS 5e (119–130 ka; Hearty et al., 2007). The exposed sedimentary facies suggests an upper-shoreface marine environment, which presumably existed right after the last interglacial sea-level highstand and which is in good agreement with the provided age estimate.

Another sedimentary sequence (Fig. 4.2b, 4.5b) in the Tongoy area is located only ~100 m from the PAF, where we sampled brown, solidified medium sand that characterizes the uppermost layers (TON4). The dm- to m-sized layers underneath comprise clay-rich lithified sand of various color shades ranging from beige to brown and gray that contain small gastropod and bivalve fossils. The lowermost deposit consists of light brown and occasionally gray lithified silt and clay that includes thin calcareous layers. TON4 provided a luminescence age of 89 ± 12 ka, which indicates deposition either during MIS 5a or 5c. Considering the depositional environments of the various layers, we interpret the sampled material to be related to an upper-shoreface environment or a transition to beach berms.

The next two samples TAL1 and TAL2 were collected at a small roadcut immediately north of Quebrada Los Loros in the Altos de Talinay area. Until 1 m depth, the uppermost layers consist

of well-sorted, clast-supported, but unlithified conglomerates with a downward decrease in clast size (Fig. 4.2c, 4.2d, 4.5c). The adjacent deposits below comprise a poorly sorted, matrix-supported conglomerate with subangular to rounded clasts and layers of brown to gray sand, where both geochronology samples were taken. The resulting luminescence ages are within a narrow time interval ranging from 81.9 ± 13 ka for the upper sample TAL2 and 83.6 ± 9.9 ka for the lower TAL1, suggesting deposition during MIS 5a. The depositional environment at this site is interpreted to have been characterized by alluvial deposition of the matrix-supported conglomerate on top of the metamorphic basement, which was superseded by a fluvial environment that deposited the clast-supported conglomerates above.

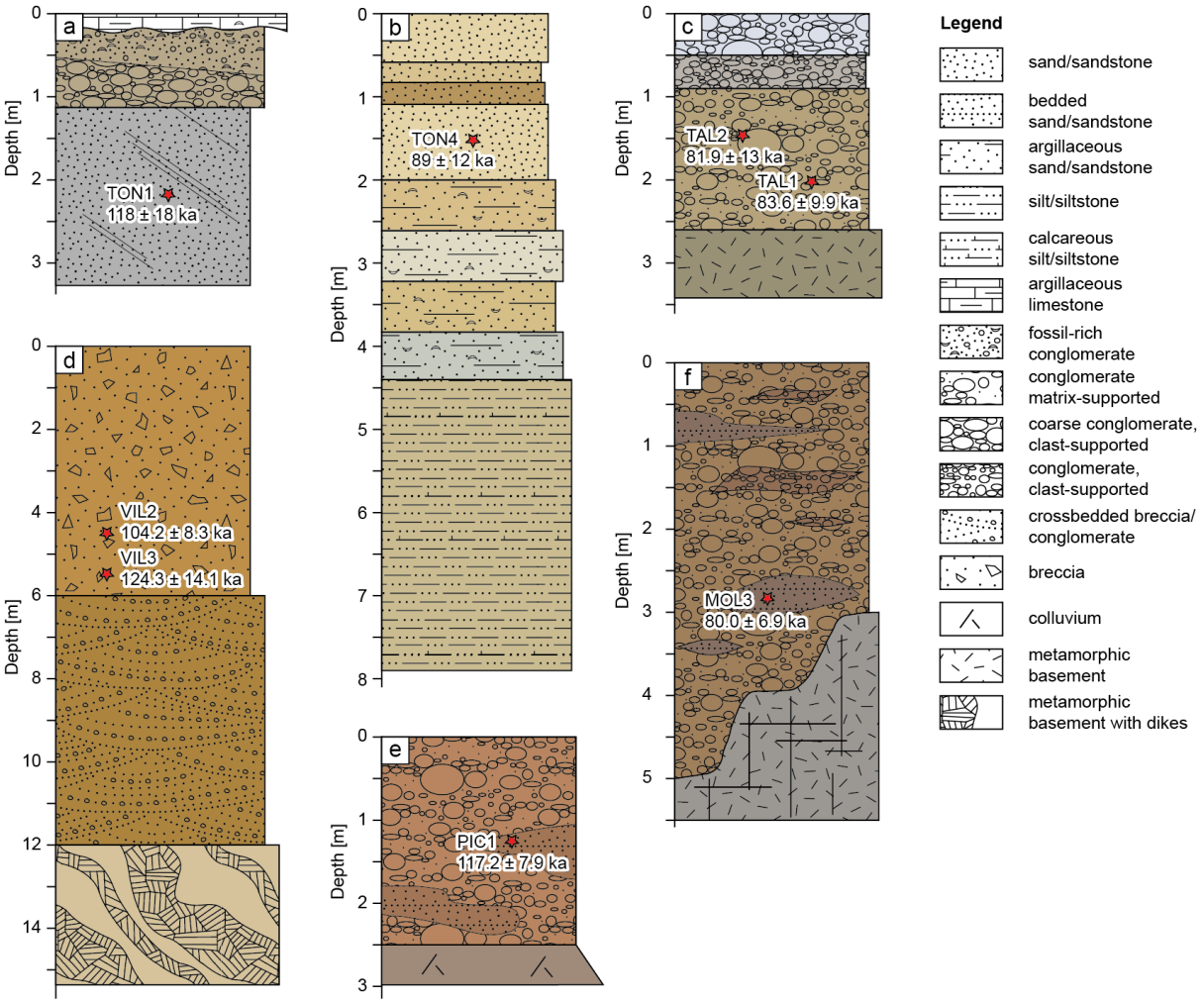

Figure 4.5: Stratigraphic sections of geochronology sampling sites described and interpreted in the text. The red star indicates the sampling position of the dated sedimentary deposits using post-IR IRSL. The location of these outcrops is indicated in Fig. 4.1 and field views are shown in Fig. 4.2.

We furthermore collected two samples at a large roadcut of the Panamericana Norte highway north of Los Vilos. The stratigraphic section exposes metamorphic basement rocks at the base,

which are overlain by a thick layer of cross-bedded, matrix-supported, sub-angular conglomerates with medium to coarse sand, and intercalated coarser conglomerate layers with less matrix (Fig. 4.2e, 4.2f, 4.5d). The cross-bedded texture disappears in the uppermost layer, which is characterized by a similar thickness and also comprises a matrix-supported conglomerate with sub-angular clasts and medium to coarse sand. Luminescence samples within this layer record deposition during MIS 5c or MIS 5e for VIL2 (104.2 ± 8.3 ka) or VIL3 (124.3 ± 14.1), respectively. The sedimentary sequence suggests multiple alluvial-fan deposition, which in some cases was interrupted by paleosol formation.

Between Pichidangui and Quilimari, marine terrace-platform deposits are locally exposed along a railroad track, which enabled sampling (Fig. 4.2g, 4.5e). The sequence comprises a poorly sorted, matrix-supported conglomerate with angular to well-rounded clasts and lenses of fine to medium sand, which occasionally contain clay. Sample PIC1 was taken from the sand lenses and luminescence dating resulted in an age of 117 ± 8 ka, suggesting burial during a late stage of MIS 5e. We interpret these deposits as alluvial sediments that were deposited after terrace abandonment.

The southernmost sedimentary sequence that we sampled with MOL3 (Fig. 4.2h, 4.5f) is located in the north of Los Molles at the northwestern flank of Quebrada Coiles. Above the exposed bedrock, the deposits comprise a poorly sorted, matrix-supported conglomerate with cm- to dm-sized clasts of up to 70 cm in diameter and a matrix of medium to coarse sand. Occasionally, we observed wide lenses of clast-supported well-rounded conglomerates and lenses of fine to medium brown sand, where MOL3 was sampled. This sequence constitutes alluvial and colluvial sediments deposited after terrace abandonment; the luminescence age of 80 ± 7 ka corresponds to MIS 5a.

Based on the new luminescence ages, we assign the lowermost terrace level to the last interglacial sea-level highstand (MIS 5e), despite several sediments being deposited as early as MIS 5a or MIS 5c. In the case of VIL2, thick layers of sediment underneath the sample suggest a significant temporal gap between terrace abandonment and deposition of the sampled material. In contrast, the younger MIS 5a ages of TON4, TAL1, TAL2, and MOL3 might be either related to the partial reoccupation of the outermost part of the terrace platform during this latest substage of MIS 5 or to the delay of fluvial and alluvial processes causing their deposition.

4.5.3 Elevations and uplift rates of onshore marine terraces

Shoreline-angle elevations of the last interglacial marine terraces (MIS 5e) decrease slowly from 40 m above sea level (a.s.l.) at Los Choros to 20 m a.s.l. at Punta Teatinos with locally higher elevations north of Quebrada (Qb.) Honda (Fig. 4.6a). The subsequent subtle increase to more than 30 m a.s.l. follows the strike of the Puerto Aldea fault (PAF) southward and is suddenly interrupted by a local decrease in elevation at the Los Loros fault (LLF), but continues thereafter towards Los Vilos. Farther south, MIS 5e terrace elevations rise to almost 60 m a.s.l. near Totoralillo and Pichidangui before decreasing again to approximately 35 m. Associated uplift rates of the last interglacial marine terraces are characterized by the same distribution of higher or lower uplift rates, respectively. Accordingly, values mostly range between 0.1 and 0.3 mm/yr, but increase to maximum rates of 0.46 mm/yr in the southern part near Pichidangui (Fig. 4.6c).

Marine terraces of MIS 7 are less well preserved, only occurring from Los Choros to Punta Teatinos, from Coquimbo to Punta Lengua de Vaca, south of the Limarí river, and north of the Choapa river. Similar to MIS 5e, terraces elevations of MIS 7 decrease in the northern section (Los Choros to Punta Teatinos) from 75 to 52 m a.s.l., but subsequently maintain an elevation between 40 and 55 m a.s.l. near Punta Lengua de Vaca and south of the Limarí river (Fig. 4.6a). Especially at the latter location, a steady increase in elevation (from 40 to 50 m a.s.l.) can be observed, coinciding again with the southward continuation of the LLF. Few measurement points on both sides of the PAF furthermore indicate a slight offset, although not as clearly as observed at the LLF. Very locally, higher elevations of almost 70 m are reached north of the Choapa river. Uplift rates of the MIS 7 terrace level are generally higher than MIS 5e terrace-uplift rates. According to the terrace-height distribution, uplift rates decrease in the northern part from about 0.4 to 0.3 mm/yr and vary between 0.25 and 0.3 mm/yr farther south, only being close to 0.4 mm/yr north of the Choapa river (Fig. 4.6c).

The next higher terrace level assigned to MIS 9 is characterized by a generally better preservation as well as more pronounced changes in terrace elevation and uplift rate. It similarly starts with a decrease in elevation from 150 m a.s.l. in the northern part (Los Choros) to just above 70 m near Tongoy (Fig. 4.6a). Slightly increasing terrace elevations (90 to 100 m a.s.l.) were observed in the southward continuation of the PAF after a sudden increase immediately at its northernmost tip. The MIS 9 terrace level is seen again a bit south of the coastal

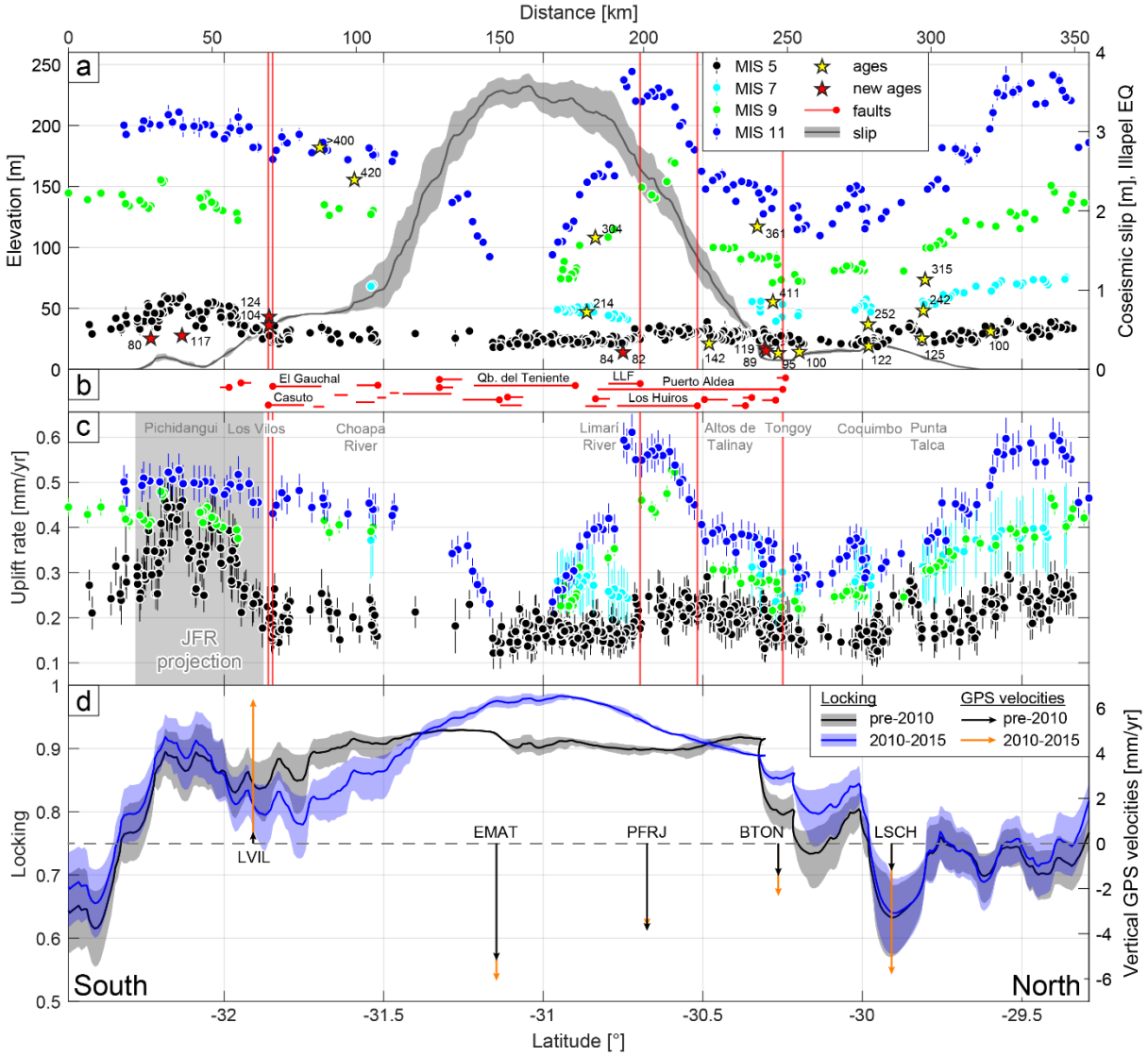

Figure 4.6: (a) Shoreline-angle elevations of terrace levels assigned to MIS 5, 7, 9, and 11 with yellow stars indicating previously published age constraints and red stars indicating luminescence ages presented in this study. The gray curve displays coseismic slip during the Illapel earthquake (Tilmann et al., 2016) along a 5-km-wide swath profile inland from the coast. (b) Extent of crustal faults near the coast (Maldonado et al., 2021) with the red point marking the intersection with the coast or its closed point. Vertical red lines in (a) and (c) mark the onsets of the most important faults mentioned in the text. (c) Uplift-rate estimates resulting from the terrace-elevation measurements. Note the higher MIS 5 uplift rates at the projection of the Juan Fernández Ridge (JFR, gray box). (d) Locking and vertical velocities of coastal GPS stations for the interseismic intervals before the 2010 Maule and 2015 Illapel earthquakes (Melnick et al., 2017).

intersection of the Los Huiros fault (LHF) at approximately 170 m a.s.l. after a small gap south of 30.5° S, which then decreases to around 150 m. We observed another sharp decrease to 115 m that corresponds with the onset of the LLF, followed by a slower decline before the terraces of MIS 9 disappear near Punta Talca. The terraces of MIS 9 reappear north of the Choapa river and seem to slightly increase in elevation from 130 to 140 m a.s.l. towards the southern termination of our study area, despite their preservation being less continuous. Associated uplift

rates of this terrace level decrease from 0.45 mm/yr in the north to almost 0.2 mm/yr and subsequently increase to 0.3 mm/yr near the onset of the LHF (~30.5° S) showing similar values compared to terrace-uplift rates of MIS 7. In contrast, the following rapid decrease from more than 0.5 to ~0.2 mm/yr (at 31° S) does not match MIS 7 terrace-uplift rates in the area south of the LLF, which is characterized by an increasing uplift rate. North of the Choapa river, both terrace levels show similar uplift rates of 0.4 mm/yr and the preservation of MIS 9 terrace levels allows to infer a slow increase in uplift rate to 0.45 mm/yr farther south.

In comparison with the MIS 9 terrace levels, marine terraces generated during MIS 11 show a similar distribution of higher and lower shoreline-angle elevations, respectively. Despite an initial increase from 180 to almost 250 m a.s.l. south of Los Choros, terrace elevations follow the same decreasing trend towards Coquimbo as the previously described terrace levels (Fig. 4.6a). Locally higher elevations of 150 m are reached south of Coquimbo before they increase slowly to 160 m a.s.l. with the southward continuation of the PAF and even faster to 230 m south of the LHF. Terrace elevations of MIS 11 subsequently decrease with the onset of the LLF and southward to values as low as 95 m before vanishing at around 31° S. A short section farther south apparently indicates a similarly steep increase in terrace elevation to ~140 m, although the age assignment in this area could not be verified through lateral correlation, lower terrace levels or rigorous age constraints. After another gap in terrace preservation, elevations of the MIS 11 terrace level rise more slowly from 175 m a.s.l. to elevations in excess of 200 m, slightly decreasing again below this value at the southern end of our study area. We furthermore observed another local decrease in terrace elevation near the El Gauchal fault (EGF) and the Casuto fault (CF), north of Los Vilos. Estimations of uplift rate are accordingly highly variable for MIS 11 and in general exceed those for the lower terrace levels. The decrease in uplift rate from 0.6 to 0.3 mm/yr in the north is followed by increases south of the PAF and the LHF to 0.6 mm/yr and by another decrease to 0.2 mm/yr south of the LLF at 31° S (Fig. 4.6c). Less frequently preserved terraces between 31° and 31.5° S indicate a steep increase and flatten southward with uplift rates of approximately 0.5 mm/yr.

4.5.4 Distribution of interseismic locking, GPS velocities, and coseismic slip

Locking of the megathrust during the interseismic phase of the seismic cycle as well as decadal GPS velocities have been correlated with long-term uplift-rate estimates of marine terraces

indicating interseismic accumulation of permanent deformation (Jolivet et al., 2020; Madella & Ehlers, 2021). The central part of our study area (30.3°–31.4° S) is characterized by very high values of interseismic locking (≥ 0.9) at the coast (Fig. 4.6d). Farther south, locking still remains relatively high (0.8 to 0.9), but decreases to values as low as 0.6 rather fast between 32.25° and 32.5° S. Locking also decreases north of Tongoy, varying between 0.6 and 0.8. Absolute changes of interseismic locking also depend on the distance to the trench, which can be observed especially north of Altos de Talinay. Changes between both interseismic phases, i.e., before the Maule (pre-2010) and before the Illapel earthquakes (2010–2015), primarily occur between 30° and 32° S. We observed an increase in locking before the Illapel (and after the Maule) earthquake from 30° to 31.4° S and a decrease towards the south until 32° S. When plotting interseismic locking directly versus terrace-uplift rates (Fig. 4.7a, 4.7b), no correlation is observable.

Interseismic rates of vertical displacement from decadal GPS measurements primarily indicate coastal subsidence, except for the area of Los Vilos (LVIL), which exhibits coastal uplift (Fig. 4.6d). Before the 2010 Maule earthquake, subsidence increased from north to south (-1.2 to -5.2 mm/yr) and uplift near Los Vilos was relatively low (+0.5 mm/yr). The subsequent interseismic phase prior to the Illapel earthquake indicates significant changes for the northernmost station of LSCH with increasing subsidence to -5.8 mm/yr as well as the southernmost station of LVIL increasing uplift to +6.4 mm/yr. The remaining coastal stations (EMAT, PFRJ, BTON) show similar values as during the previous interseismic phase before the Maule earthquake. Comparing the vertical GPS velocities with the long-term uplift-rate estimates of marine terraces, we could not observe any correlation. Subsidence indicated by decadal GPS measurements occurs in areas of high long-term uplift (station PFRJ) and in areas of low long-term uplift (EMAT), while short-term uplift coincides with an area of moderate to high long-term uplift (LVIL). Additionally, both interseismic periods (pre-Maule and pre-Illapel) show at least two stations (LSCH and LVIL) characterized by significant changes in vertical displacement rates, which makes correlations with long-term coastal deformation difficult.

Virtually the entire study area experienced coseismic slip during the 2015 M_W8.3 Illapel earthquake. When projected to the coastline, the curve of slip distribution resembles a Gaussian shape and centers at 31° S, reaching maximum values of 3.7 m (Fig. 4.6a). Coseismic slip decreased symmetrically from this point toward the north and the south, but was still greater

than 1 m between 30.5° and 31.5° S. The subsequent decrease of coseismic slip north of 30.3° S and south of 31.7° S appears to be less steep, while significant amounts of slip cannot be observed anymore north of 29.7° S and south of 32.25° S. The distribution of coseismic slip coincides with those areas, where interseismic locking was most pronounced between both interseismic phases (i.e., pre-2010 and 2010–2015, 30° to 32° S), which is highlighted by the black and blue lines in Fig. 4.6d. Interestingly, the coastal regions that experienced the highest amounts of coseismic slip show either comparably low terrace elevations and uplift rates or no terrace preservation at all (Fig. 4.6a). Similar to the trends in interseismic locking, we did not observe a direct correlation between terrace-uplift rate and coseismic slip (Fig. 4.7c).

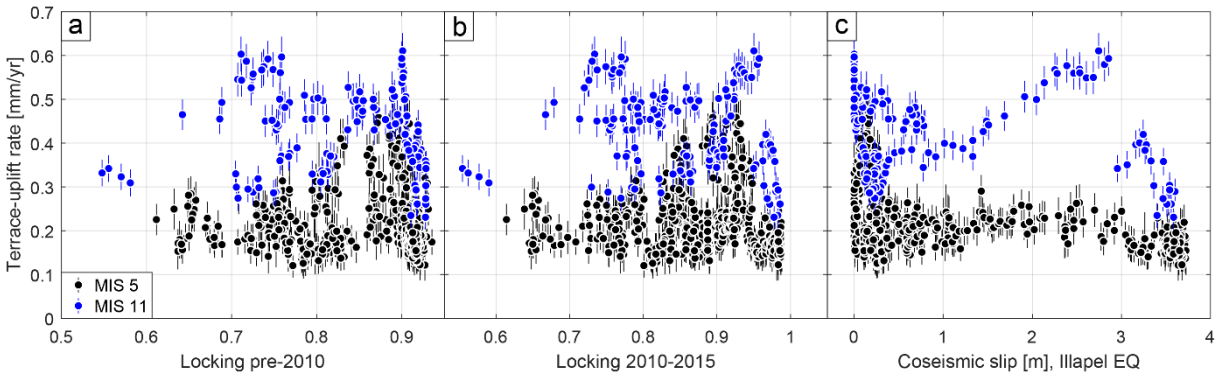

Figure 4.7: Scatter plots of MIS 5 and MIS 11 terrace-uplift rate versus interseismic locking before the 2010 Maule (a) and 2015 Illapel earthquakes (b), and versus coseismic slip during the Illapel earthquake (c). All values were extracted at the locations of the terrace measurements. Note lack of significant correlations.

4.6 Discussion

4.6.1 Age assignment of terrace levels

We primarily based our terrace-level assignment on previously published age estimates and IRSL-dated samples of the investigated marine terraces (Tables 4.2 and 4.3), on the tracking of continuously preserved terraces along the coast, and similar elevations of terrace sequences in other areas. However, our interpretation of the newly mapped terrace levels (i.e., older than MIS 5) should be viewed with caution, since several age estimates either rely on older dating techniques with large errors (AAR, ESR), might be impacted by the subsequent addition of matter that changes their true age, or contain unquantified corrections. For instance, U/Th dating of bivalves (e.g., Saillard et al., 2012) might be compromised by a long-known *post mortem*-

exchange of uranium from sea water (Flint, 1971) leading to altered initial concentrations and thus unreliable age estimations. Furthermore, with respect to surface-exposure dating using cosmogenic radionuclides, broad ranges of erosion-rate values have been used to explain highly dispersed ^{10}Be chronologies (Rodríguez et al., 2013; Martinod et al., 2016). The cosmogenic nuclide ages listed in Table 4.2 refer to zero erosion and should therefore be considered as minimum ages; this especially applies to older terrace levels (MIS 11 or older; Saillard et al., 2009; Rodríguez et al., 2013; Martinod et al., 2016), where such an assumption may not be true.

Despite our terrace-level assignment being based on previously published age constraints and new IRSL data, we favor a different interpretation for the Altos de Talinay area compared to Saillard et al. (2009). They attribute the ~170-m-high terrace level to MIS 9 (Fig. 4.6a, blue points) and the 55 m level to MIS 7 (cyan); however, we observed another terrace level in between both terraces (green). This can be reconciled by the assumption of higher erosion rates as reported by Martinod et al. (2016) that could result in an older cosmogenic nuclide age or a sampling position in the intermediate terrace level that we attributed to MIS 9. Based on our assignment of the mapped terrace levels to MIS 5e, 7, 9, and 11 (with increasing elevation), we generally observed higher uplift rates for the older terraces suggesting a gradual uplift-rate decrease since MIS 11 (400 ka; Saillard et al., 2009).

In the Coquimbo region, the application of our LEM clearly showed the drowned terrace levels at ~40 m and ~86 m depth to be assigned to MIS 3 and MIS 2, respectively. The intermediate terrace level at ~60 m depth could represent a less dominant highstand during one of the MIS 3 substages, but since the LEM did not reproduce any scenario with three terrace levels at the observed depths, we rather interpret the intermediate depths to result from submarine mass movements. This interpretation is supported by the observation that below this only very locally occurring level usually no sharp shoreline angle of the MIS 2 terrace is preserved. The applied LEM further indicates comparably high uplift rates of 0.4 to 0.5 mm/yr since MIS 3, which likely diminished to 0.05 mm/yr for the period since the LGM (MIS 2). This definitely highlights the variable nature of uplift rates between the individual interglacials and might additionally prove the decrease of uplift rates over time that we observed for the onshore terraces based on the terrace-level assignments to MIS 5, 7, 9, and 11.

4.6.2 Correlation of short- and long-term estimates of forearc deformation

Viewing the two consecutive interseismic periods prior to the Maule and Illapel earthquakes highlights significant changes in vertical displacement rates (Fig. 4.6d) within a relatively short period of time with respect to the thousands of years required to uplift the marine terraces analyzed in this study. Furthermore, we did not observe a direct correlation between terrace-uplift rates and interseismic locking or coseismic slip during the Illapel earthquake (Fig. 4.7). We therefore consider decadal-scale estimates of interseismic and coseismic deformation related to megathrust earthquakes to be not representative with respect to permanent uplift rates of marine terraces that are estimated over millennial timescales. This might change however, when observation periods become longer and more profound knowledge about interseismic and coseismic coastal uplift will be ultimately available.

Similar to our observation of fault-related changes in uplift rate, previously proposed mechanisms to explain permanent forearc deformation also highlight the importance of upper-plate structures (Armijo & Thiele, 1990; Adam & Reuther, 2000; Armijo et al., 2015). We therefore will take a closer look particularly at the impact of upper-plate normal faults with respect to the long-term uplift of coastal landforms.

4.6.3 Impact of crustal faulting on permanent coastal uplift

Our observations of variability in marine terrace elevations in the forearc of central Chile and co-varying uplift rates show that these changes are tied to the occurrence of trench-parallel normal faults (e.g., Ota et al., 1995; Saillard et al., 2009). Gradual southward increases in terrace-uplift rates are observed in the continuation of the PAF and abruptly decreasing uplift rates are seen across the LLF for all terrace levels (MIS 5 to MIS 11), which underscores the long-term impact that these structures have on the topographic evolution of coastal areas. Despite being recorded only for the MIS 9 and 11 terrace levels, the LHF seems to cause quite a rapid southward increase in uplift rates. We did not observe well-defined latitudinal changes in uplift rate for the Quebrada del Teniente fault (QdTF) due to its coast-parallel orientation and shoreline-angle elevations being measured on both sides of the fault. However, offset wave-cut platforms of terraces older than MIS 9 could be observed at various locations along the fault trace. Farther south, the EGF and the CF displace MIS 5 and 11 terrace levels. These examples

highlight the importance of crustal faulting with respect to the accumulation of permanent deformation and in particular the role of the investigated faults to cause 100-km-wavelength changes in uplift rate when oriented approximately parallel to the coastline. Changes in uplift rate associated with individual faults as well as the absence of fault displacements on specific terrace levels further enable us to estimate the activity of these faults. The Puerto Aldea, Los Loros, El Gauchal and Casuto faults seem to have been active for the entire time interval since MIS 11, despite exhibiting different characteristics of uplift-rate changes along the coast that are either gradual or abrupt. On the other hand, fault activity decreased or even ceased on the Quebrada del Teniente, Los Huiros, and Quebrada Palo Cortado faults (QPCF) since MIS 5, while an estimation of their activity during MIS 7 is difficult due to the discontinuous preservation of this terrace level. The variable activity of upper-plate faults might be related to variations in coseismic slip distributions and different recurrence intervals between megathrust earthquakes that trigger slip on these structures (Melnick et al., 2019).

Importantly, these observations in Chile are relevant for other subduction margins as well, since upper-plate faults have been associated with triggered slip following megathrust earthquakes at various subduction zones around the world (Clarke & Carver, 1992; Farías et al., 2011; Aron et al., 2013; Toda & Tsutsumi, 2013; Gomberg & Sherrod, 2014; Melnick et al., 2019). For instance, triggered slip on upper-plate faults was observed after recent megathrust earthquakes such as the 2011 Tohoku-oki, 2004 Sumatra, and 1964 Alaska events (Toda & Tsutsumi, 2013; Gomberg & Sherrod, 2014). The relevance of these faults mainly lies in their potential to nucleate very hazardous events due to their proximal occurrence in the upper plate with respect to population centers (Gomberg & Sherrod, 2014).

Similar to the central part of our study area, upper-plate normal faults along other segments of the western South American margin appear to be a common phenomenon (e.g., Farías et al., 2011; Aron et al., 2013). The extensional regime responsible for large-scale normal faulting in the Atacama region has been related to co/postseismic elastic rebound and subduction-erosion processes as well as interseismic flexure of the margin (von Huene & Ranero, 2003; Allmendinger & González, 2010; Loveless et al., 2010; Baker et al., 2013). Armijo and Thiele (1990) argued that the extensional structures might indicate ramp stacking at the subduction interface that contributes to the uplift of the forearc. In addition, the occurrence of seismically-induced, extensional surface cracks in the Antofagasta area underlines the relationship between megathrust earthquakes and extensional processes in the forearc (Loveless et al., 2016; Scott et

al., 2016). The unique preservation of cracks in the hyperarid Atacama environment indicates reopening of pre-existing cracks with a deviating orientation, but nevertheless seems to represent the most common slip pattern in the northern Chilean seismotectonic segment (Loveless et al., 2016).

According to Carrasco et al. (2019), shallow intraplate seismicity associated with the Illapel earthquake only shows few normal faulting and strike-slip events that are either related to offshore structures or a southward extension of the AFS and not necessarily to the upper-plate normal faults along the coast. In any case, the analysis of Illapel-earthquake aftershocks seems to suggest subduction erosion and subsequent underplating to be responsible for the extensional tectonic regime (Comte et al., 2019), which was similarly proposed for the Atacama segment in northern Chile (e.g., von Huene & Ranero, 2003; Allmendinger & González, 2010). Trenchward-dipping, offshore normal faults furthermore represent geomorphic expressions of gravitational collapse associated with upper crustal extension (Contreras-Reyes et al., 2015; Becerra et al., 2017), an argument that is strengthened by the occurrence of seismicity on these structures before and after the Illapel earthquake (Carrasco et al., 2019). We therefore propose for the central part of our study area that the significant variabilities in terrace elevation and uplift rate are related to the extensional (re-)activation of upper-plate normal faults following great subduction earthquakes, such as the 2015 Illapel event. The upwarping patterns of uplift rate that are created by these normal faults and which are especially well-developed for the older terrace levels represent bell-shaped footwall uplift along these structures. The less-pronounced upwarping of the lower terrace levels (e.g., MIS 5) as well as the active offshore structures might indicate outward migration of deformation from the inner wedge in response to gravitational collapse and wedge stabilization following the critical taper theory (Dahlen, 1984). This upper-plate extension might be related to subduction erosion and subsequent underplating causing long-wavelength coastal uplift, but at the same time local gravitational collapse of the forearc wedge through normal faulting (Becerra et al., 2017; Comte et al., 2019).

In the context of plate-interface thrusting, the South American margin is characterized by a compressional tectonic regime (Zoback, 1992; Heidbach et al., 2018) responsible for the relatively continuous uplift of the coast as well as thrust faulting and mountain building farther inland. In such a scenario the coastal normal faults likely constitute a second-order phenomenon that overprint the manifestations of an overall compressional regime with the effects of a local tensional regime, thus modifying uplift rates on a short-wavelength scale.

4.6.4 Other high-uplift-rate regions

The relatively high uplift rates of up to 0.6 mm/yr (MIS 11 terrace level) in the northern and southern part of the study area are not accompanied by crustal faulting and therefore indicate the overall compressional tectonic regime that drives large-scale coastal uplift. Such large-scale deformation of the forearc might result from moderate deep earthquakes (Melnick, 2016), the subduction of bathymetric ridges or the underplating of trench sediments (Pedoja et al., 2006; Bangs et al., 2020).

The northern part of our study area is characterized by a northward-increasing uplift rate for all terrace levels starting at Punta Talca (Fig. 4.6; 29.3°–30.25° S), which indicates a quite uniform change in uplift rate across this area. Conversely, the high uplift rates in the southern part of the study area, in particular south of 31.5° S, depict a similar pattern for the older terrace levels (Fig. 4.6), while uplift rates of MIS 5 terraces are only locally high. These anomalously higher uplift rates are located in the continuation of the Punta Salinas Ridge (Fig. 4.1a), a prominent topographic expression on the upper plate caused by the subduction of the Juan Fernández Ridge (JFR; von Huene et al., 1997). A causal relationship between currently higher coastal uplift rates in this area is supported by clustered aftershock seismicity of the Illapel earthquake related to subducted seamounts of the JFR (Lange et al., 2016). We propose the subduction of seamounts of the JFR and associated varying seismicity to be responsible for a change in uplift rates over a timespan involving several interglacial periods. In this context the observed higher local uplift rates of the MIS 5 terrace might therefore be related to a < 125-kyr-old subducted or currently subducting seamount, while the relatively constant uplift rates reflected by the older terrace levels might indicate a more reduced impact of JFR-subduction prior to this.

4.7 Conclusions

In this study we mapped and analyzed three onshore levels of late Pleistocene marine terraces in the Illapel earthquake area as well as two drowned terrace levels near Coquimbo in central Chile using TerraceM software and a landscape-evolution model. Based on previously published age constraints, eight new IRSL ages, and lateral terrace correlations, we assigned the mapped terraces that are older than the last interglacial level (MIS 5) to MIS 7, 9 and 11.

Our results reveal uplift rates ranging from 0.1 to 0.6 mm/yr with decreasing values in the north (Punta Choros) until Coquimbo, peaking between Altos de Talinay and the Limarí river, and gradually increasing again farther south after a regional decline and absence of marine terraces at ~31° S. Higher uplift rates were generally observed with increasing terrace age, only terraces assigned to MIS 7 and 9 show similar uplift rates. Drowned terraces near Coquimbo are found at depths of ~86 and ~40 m and could be assigned to MIS 2 (LGM) and MIS 3, respectively. The application of a LEM suggests comparably high uplift rates (0.5 mm/yr) that decreased towards the LGM, therefore supporting the notion of an uplift-rate decline during the late Pleistocene.

The comparison of terrace-uplift rates with coseismic slip of the 2015 Illapel earthquake, interseismic GPS velocities and associated interplate locking revealed no correlation. This suggests decadal estimates of coastal deformation not to be representative with respect to millennial-scale permanent deformation of the forearc. In the central part of the study area, pronounced changes in uplift rate of up to 100 km wavelength are accompanied by the activity of crustal normal faults. Gradual southward increases in uplift rate were observed for the PAF, even faster increases for the LHF, whereas an abrupt decline is observed for the LLF. While some faults seem to have been active during the entire time interval since MIS 11 (PAF, LLF, EGF, CF), the activity of other faults decreased or even ceased entirely (LHF, QdTF, QPCF). Illapel-earthquake aftershocks seem to suggest that upper-plate extension is related to subduction erosion and subsequent underplating causing regional tectonic uplift and local gravitational collapse of the forearc through normal faulting, which is further supported by the occurrence of several extensional faults offshore. These second-order features likely overprint the overall compressional tectonic regime that is represented by areas lacking the occurrence of upper-plate faulting and that are the result of various other processes accumulating permanent coastal deformation. For instance, we interpret the local uplift-rate increase seen in MIS 5 terraces in the south (near Pichidangui) to be associated with the subduction of the JFR, which is characterized by Illapel-earthquake aftershocks and topographically expressed as the Punta Salinas Ridge on the submerged sector of the continental plate. Absent uplift-rate changes of older terrace levels in this area might suggest a smaller impact of the JFR-subduction prior to MIS 5.

Chapter 5: Discussion

My main motivation for writing this dissertation was the expansion of our current understanding of deformation processes in forearc regions that act on different wavelengths and timescales. It was hypothesized that deciphering the dynamics, extent and style of forearc deformation would ultimately help to better evaluate future earthquake and deformation scenarios as well as associated hazards, including mass movements and tsunamis. The results of this study clearly show that a rigorous analysis of these problems requires an expansion of the observational time span from instrumental, decadal deformation and historical earthquake records to determine the spatiotemporal evolution of seismic asperities along the forearc, since these features are thought to indicate the magnitude and rupture extent of possible megathrust earthquakes (Moreno, 2010; Schurr et al., 2014; Tilmann et al., 2016). The principal objective of this study was therefore aimed at estimating glacial-cycle deformation patterns and detecting possible mechanisms responsible for accruing deformation over such long timescales. The approach to decipher, characterize, and compare deformation mechanisms and uplift patterns is key in light of frequently observed uplift-rate changes on multiple timescales and associated changes in potential trigger mechanisms. The following research questions, which I posed at the outset of this endeavor (section 1.2), guided me through my research and helped to organize it:

> *(1) What mechanisms do control the accumulation of permanent coastal uplift and the deformation of the forearc?*
>
> *(2) When does permanent deformation accumulate?*
>
> *(3) What is the role of seismic asperities in the accumulation of permanent deformation and how persistent are they over long timescales of 10^5 years?*

Consequently, my first task included the generation of a spatially continuous database of last interglacial marine terrace elevations along the western South American coast to provide a well-

defined strain marker to study glacial-cycle deformation patterns and the processes causing them (Chapter 2). My second task involved applying a novel signal-analysis approach using Fourier transforms to this continental-scale database and a number of selected tectonic features to elucidate the mechanisms driving permanent coastal uplift and surface deformation in subduction zones (Chapter 3). Finally, in my third task I evaluated the importance of upper-plate faults and megathrust earthquakes on modulating permanent coastal uplift patterns in a spatially more limited area using multiple levels of marine terraces, which also allowed a comparison with current deformation patterns and an assessment of the persistency of seismic asperities (Chapter 4).

In this chapter, I discuss the primary outcomes of these analyses that were presented in the previous chapters, how my findings contribute to resolve the principal research questions outlined above, and how the obtained results advance the current state of knowledge.

5.1 Considerations and findings from the database of last interglacial marine terraces

Systematic mapping of last interglacial marine terrace elevations resulted in 1953 measurements along the ~5000-km-long western South American coast (section 2.5, Fig. 2.5). Since marine terraces are excellent strain markers, this spatially virtually continuous signal of terrace elevations provided a unique opportunity to study tectonic processes of forearc deformation at a continental-scale as well as potential climatic forcing mechanisms on the formation and preservation of marine terraces (Fig. 2.11). Limitations of this terrace-elevation database are primarily related to the accuracy of the age constraints and their spatial distribution with respect to the terrace measurements. Among other parameters, I accounted for these limitations and uncertainties by providing a quality-rating value to each measurement, which helped to generate a high-quality database.

Last interglacial terrace elevations revealed a relatively constant signal of background-uplift rate along the entire western South American coast that is, however, disturbed by distinct patterns of various wavelengths (Fig. 2.11). The comparison of the uplift-rate signal with different tectonic and climatic parameters supports several existing theories regarding the

mechanisms driving permanent deformation in the forearc as well as the formation and preservation of marine terraces (section 2.6).

For example, high-amplitude changes in uplift rate of the MIS 5 marine terraces coincide with the location of the subducting Nazca, Carnegie, Juan Fernández, Taltal, and Copiapó ridges (Fig. 2.11b; Macharé & Ortlieb, 1992; Gutscher et al., 1999; Pedoja et al., 2006; Saillard et al., 2011). Large-scale bathymetric anomalies like the Nazca and Carnegie ridges might cause long-wavelength changes in the mechanical behavior of the plate interface and deep-seated processes associated with changes in gravity anomalies (e.g., Watts & Daly, 1981). Small-scale bathymetric anomalies such as the Juan Fernández, Taltal, and Copiapó ridges often coincide with upper-plate faults causing a more localized change in uplift rate. In contrast, the long-wavelength warping and uplift of the Arauco area is probably related to shallow upper-plate structures causing crustal bending and splay faulting (Jara-Muñoz et al., 2015; Jara-Muñoz et al., 2017; Melnick et al., 2019). The amount of subducted trench sediment has been proposed as an additional factor controlling forearc architecture in terms of subduction erosion or accretion (Fig. 2.11c; Cloos & Shreve, 1988; Menant et al., 2020) and my newly generated database reveals generally higher uplift rates in the accretionary part of the South American margin (i.e., south of the Juan Fernández Ridge). However, a clear correlation between the individual uplift-rate patterns and the trench fill does not exist. Furthermore, the amount of sediment that is being subducted might not be related directly with the sediment thickness in the trench, since in some segments sediment is accreted frontally, in others basally and below the frontal wedge, while in others most sediment is subducted straight into the mantle wedge.

Apart from these tectonic forcing mechanisms, latitudinal differences in climate influence the surface processes in western South America and seem to further control the formation, destruction and general degree of preservation of marine terraces. However, none of these climate parameters points towards a direct influence on the uplift rate itself, thus excluding the forcing of a coupled climate-tectonic feedback mechanism on uplift. The climatic influence on marine terraces is expressed in the number of terrace measurements (Fig. 2.11f), which either highlights the processes promoting the formation of marine terraces or inhibit their degradation. Elevated values of wave heights and tidal ranges in areas characterized by morphologically well-preserved marine terraces suggest an influence of these parameters on the generation of marine terraces (Fig. 2.11d; Anderson et al., 1999; Trenhaile, 2002). The formation of marine terraces through wave-erosion processes is apparently counteracted by denudation processes

related to high annual precipitation (Fig. 2.11e), which promotes their overall degradation and fluvial dissection. Consequently, the combination of tectonic uplift and climate-driven processes responsible for the formation and degradation of marine terraces results in different morphological expressions of uplifted terraces along the western coast of South America.

The continuously measured last interglacial terrace elevations provide a continental-scale database of glacial-cycle deformation patterns along the tectonically active South American forearc, which were ultimately used to evaluate tectonic and climatic mechanisms that control the formation and preservation of marine terraces as well as crustal deformation in the coastal realm. The database afforded the opportunity to analyze the spatiotemporal characteristics of the individual mechanisms driving the accumulation of permanent coastal strain and the regional characteristics of forearc deformation. This was especially targeted towards the different wavelength patterns of terrace uplift as well as the spatially continuous signal of background uplift, which will be discussed in the following sections.

5.2 Mechanisms controlling the accumulation of permanent deformation

While the uplift-rate patterns calculated from the database of last interglacial marine terraces already highlighted several tectonic drivers that might be responsible for the accumulation of permanent forearc deformation, the relative significance of these mechanisms on various spatial scales as well as their temporal characteristics needed further analysis. This also required finding an explanation for the continuous uplift-rate signal along the entire western South American coast, which is only interrupted by several uplift-rate changes of variable wavelength (Fig. 3.1e).

5.2.1 High-amplitude changes in uplift rate on various wavelengths

The analysis and comparison of the wavelength spectra of terrace-uplift rates and a selection of tectonic features suggested potential correlations that indicate several, potentially responsible processes (section 3.6.1, Fig. 3.3, 3.5). Short-wavelength changes in coastal uplift rate (< 100 km) are primarily caused by upper-plate faulting as suggested in previous studies and as pointed

out at other subduction margins (e.g., Kelsey et al., 1996; Jara-Muñoz et al., 2015; Matsu'ura, 2015). At various spatial scales, intermediate- (100–450 km) to long-wavelength (> 450 km) variations in uplift rate correlate with the signals of coseismic vertical displacements, bathymetric anomalies, and background seismicity. These might indicate different extents of locked areas on the megathrust that contribute to the accumulation of permanent deformation either through multiple, small consecutive events or through great earthquakes (Schurr et al., 2014; Métois et al., 2016; Remy et al., 2016; Madella & Ehlers, 2021). The causes responsible for this kind of seismotectonic segmentation are probably related to the subduction of bathymetric anomalies (Singh et al., 2011; Philibosian & Meltzner, 2020; Molina et al., 2021). At even greater wavelengths (> 700 km), correlations between the uplift-rate signal and basal friction, interseismic uplift rate, and gravity anomaly (Fig. 3.5) could indicate more extensive segments of the megathrust that originate from changes in the physical properties of the megathrust or lateral density variations in the forearc (Cubas et al., 2013; Molina et al., 2021). This study therefore highlighted the importance of individual mechanisms that were previously proposed to be responsible for permanent coastal uplift as well as the wavelengths on which these processes affect the long-term uplift-rate signal.

5.2.2 Moderate and continuous background uplift

In search for the mechanism(s) being responsible for the low-amplitude and fairly continuous uplift-rate signal along the South American margin (section 3.6.2), I excluded processes such as crustal faulting or the subduction of bathymetric anomalies, which exert a localized and high-amplitude impact on the uplift-rate signal. Such short- to intermediate-wavelength processes have been associated with upper-plate deformation on the western South American coast (Hsu, 1992; Pedoja et al., 2006; Melnick et al., 2009; Jara-Muñoz et al., 2015) and at other subduction zones (Kelsey et al., 1996; Sak et al., 2004; Gardner et al., 2013; Matsu'ura, 2015; McKenzie et al., 2022), but are unlikely to accommodate the observed low-magnitude background uplift in a sustained manner over long timescales. The identified signal of background-uplift rate could originate from a single, low-magnitude mechanism acting continuously along the entire coast; however, the analyzed mechanisms (Fig. 3.3) seem to lack the spatial continuity along the entire continental margin that would be required for such a scenario. Alternatively, the observations may be explained with spatiotemporally changing processes that accumulate towards a continuous and permanent signal of uplift rates over millennial timescales.

The latter scenario could be achieved if small fractions of interseismic uplift translate into permanent deformation (e.g., Jolivet et al., 2020; Madella & Ehlers, 2021) and accumulate a continuous uplift-rate signal over long timescales. However, the absence of a correlation between interseismic uplift rates and terrace-uplift rates (Fig. 3.6) suggests no causal relationship, although such a continental-scale analysis cannot rule out a local confinement of interseismic accumulation of permanent deformation to specific areas. Additionally, the South American margin of Chile and southern Peru is almost exclusively characterized by interseismic coastal subsidence (Fig. 3.3), which further reduces the importance of this mechanism.

Another hypothesis suggests moderate earthquakes near the Moho (M7–M8, ~35–55 km depth) to cause permanent coastal uplift by accumulating anelastic deformation down-dip of the interseismically locked megathrust (Melnick, 2016). The analysis of great earthquakes (M > 7.5) indicates no direct correlation between coseismic vertical displacements and terrace-uplift rates, since they exhibit an equal degree of coseismic coastal subsidence and uplift (Fig. 3.3g, A.7; Ocola, 2008; Gusman et al., 2015; Melnick, 2016). On the other hand, several decimeters of coastal uplift have been observed due to moderate, domain-C earthquakes, such as the 1995 Antofagasta or 2007 Tocopilla events in Chile (Delouis et al., 1997; Schurr et al., 2012). In addition, the wavelength spectra of terrace-uplift rate and coseismic uplift resulting from these events are well correlated (Fig. 3.7). I therefore propose spatiotemporal variations of such earthquakes to result in a continuous signal of background uplift over millennial timescales, supporting the hypothesis of Melnick (2016) involving anelastic deformation downdip of the megathrust. Interestingly, the observed coseismic displacements of moderate, domain-C earthquakes would require a recurrence time of 86.5 years to account for the background-uplift rate of 0.22 mm/yr during the last 125 kyr, which is in agreement with recurrence intervals of 82.4 to 123 years for earthquakes of such magnitudes based on Gutenberg-Richter distributions in northern Chile (Sippl et al., 2019). However, the discontinuous occurrence of these types of earthquakes along the western South American coast make further validation of this hypothesis necessary.

5.2.3 The influence of crustal faulting and bathymetric ridges

Crustal faulting and the subduction of bathymetric ridges were already considered in this study to be among the most important processes to modify glacial-cycle uplift-rate patterns based on

coinciding wavelength spectra (Fig. 3.5). Regional-scale uplift-rate estimates on multiple terrace levels in central Chile (Illapel earthquake area) provided further insight into the temporal variability of crustal normal faulting, ridge subduction, and their responsible mechanisms in the overall compressive tectonic regime of the South American margin (Heidbach et al., 2018; section 4.6).

Generally higher uplift rates of the older terrace levels suggest a progressive uplift-rate decrease since the formation of the terraces assigned to MIS 11 (~400 ka) as previously proposed by Saillard et al. (2009). The continuous terrace measurements further revealed either gradual or abrupt changes in uplift rate that are accompanied by the activity of trench-parallel normal faults (Fig. 4.6; e.g., Ota et al., 1995; Saillard et al., 2009). The differentially uplifted terrace levels record temporally decreasing or even ceased activity for some normal faults (e.g., Los Huiros, Quebrada del Teniente faults), while other structures seem to have been active since the formation of the MIS 11 terrace (e.g., Puerto Aldea, Los Loros faults). One possible explanation might be varying distributions of coseismic slip or changing recurrence intervals between megathrust earthquakes that trigger slip on such upper-plate faults and cause variations in their activity (Melnick et al., 2019). This behavior would not be surprising, since earthquake-induced slip on upper-plate faults has been observed at various subduction zones worldwide (e.g., Clarke & Carver, 1992; Toda & Tsutsumi, 2013; Gomberg & Sherrod, 2014; Melnick et al., 2019). However, in the area of the 2015 Illapel earthquake, shallow intraplate seismicity only shows few normal faulting and strike-slip events that are not necessarily related to the upper-plate normal faults along the coast (Carrasco et al., 2019).

Crustal normal faulting appears to be a common phenomenon along other segments of the western South American margin (e.g., Farías et al., 2011; Aron et al., 2013), where the extensional tectonic regime has been related to co/postseismic elastic rebound and interseismic flexure of the margin (Allmendinger & González, 2010; Loveless et al., 2010; Baker et al., 2013), or subduction erosion and ramp stacking (Armijo & Thiele, 1990; von Huene & Ranero, 2003). The analyses of aftershocks of the Illapel earthquake suggest the extensional regime to be the result of subduction erosion, subsequent underplating and bending of the upper plate (Comte et al., 2019). This might explain regional tectonic uplift as well as gravitational collapse inferred from offshore normal faults (Contreras-Reyes et al., 2015; Becerra et al., 2017), which were associated with recent seismicity before and after the Illapel earthquake (Carrasco et al., 2019). In combination, the recently active offshore structures (Carrasco et al., 2019) and the

less-pronounced fault-related uplift of younger terraces (MIS 5) could furthermore suggest an outward migration of deformation from the inner forearc wedge as a result of wedge stabilization in the context of gravitational collapse, similar to the original models explaining critical taper theory (Dahlen et al., 1984). Normal faulting resulting from the extensional collapse of slightly overcritical wedges has also been observed in other regions of the South American margin and in other subduction zones around the world (e.g., von Huene et al., 1996; Adam & Reuther, 2000; von Huene et al., 2000; Kopp et al., 2006). I therefore interpret trench-parallel, coastal normal faults in the central Chilean study area in the context of a second-order, extensional phenomenon that overprints the manifestations of the overall compressional tectonic regime of the South American margin (Heidbach et al., 2018; section 4.6.3). The significantly modified uplift rates on a short-wavelength scale are a manifestation of this process.

Conversely, the area around Pichidangui (31.9–32.2° S) is characterized by the absence of crustal faults; furthermore, a bell-shaped zone of increased uplift-rate is revealed for the MIS 5 terrace level that cannot be observed for the older terraces (Fig. 4.6). This pattern of an upwarped forearc area is located in the immediate continuation of the Punta Salinas Ridge (Fig. 4.1a), a high topographic sector of the forearc on the upper plate that is related to the subduction of the Juan Fernández Ridge (JFR; von Huene et al., 1997). Clustered aftershock seismicity of the Illapel earthquake around individual JFR-seamounts (Lange et al., 2016) therefore suggests the subduction of these high bathymetric seamounts to be responsible for the observed increase in last interglacial uplift rates. The absence of such a pattern for the older terrace levels might indicate a much more subdued impact of bathymetric anomalies related to the JFR-subduction prior to MIS 5.

5.3 The persistency of seismic asperities

Asperities are regions of pronounced slip during megathrust earthquakes that are characterized by a high degree of interplate coupling during the interseismic phase of the seismic cycle and that ultimately rupture during subsequent events (Lay & Kanamori, 1981; Kanamori, 1986; Moreno et al., 2010; Schurr et al., 2014). Despite the well-documented short-term characteristics of seismic asperities based on historical earthquake records and decadal geodetic

measurements, their persistency over multiple seismic cycles has not been studied on a continental scale or using a variety of continuously mapped terrace levels that represent different glacial-cycle time intervals. Such a detailed analysis would be crucial, however, to assess the potential behavior of future megathrust earthquakes regarding their magnitude and rupture extent.

As described above, various intermediate- to long-wavelength mechanisms and parameters such as coseismic vertical displacements, bathymetric anomalies, background seismicity, and interseismic uplift rate could indicate different extents of locked areas on the megathrust contributing to the accumulation of permanent deformation in the forearc. However, apart from the correlation of their wavelength spectra with the signal of terrace-uplift rates (Fig. 3.5), a direct spatial correlation between the individual signals is missing (e.g., Fig. 3.6), with the exception of bathymetric anomalies (Fig. 2.11, 3.3).

On a more regional scale involving central Chile, a direct correlation between terrace-uplift rates and interseismic locking or coseismic slip during the 2015 Illapel earthquake has not been observed either (Fig. 4.7). Significant changes in vertical, geodetically measured displacement rates over the course of two consecutive interseismic periods (Fig. 4.6d) further highlight their short-term variability in comparison with the thousands of years required to uplift the marine terraces that were analyzed in this study. Thus, the distributions of interseismic locking and coseismic slip of megathrust earthquakes representing seismic asperities are apparently no persistent indicators of millennial-scale permanent forearc deformation expressed by terrace-uplift rates. Permanent deformation of the forearc on glacial-cycle timescales is rather modified by fault-related changes in uplift rate (e.g., Armijo & Thiele, 1990; Adam & Reuther, 2000) and the subduction of bathymetric ridges (e.g., Hsu, 1992; Pedoja et al., 2006; Gardner et al., 2013).

Chapter 6: Conclusions

This dissertation has generated new insights into the current understanding of subduction-zone processes and the dynamics of coastal forearc deformation by analyzing the mechanisms that control the accumulation of permanent coastal uplift, the spatiotemporal evolution of seismic asperities and their impact on the upper plate. Although seismogenic hazards of subduction margins were not the focus of this study, it is expected that the results will help to better evaluate earthquake-related hazards and to minimize the risk and vulnerability of communities, critical infrastructure, and economic assets. The most significant findings of this thesis are summarized below:

Continuous, continental-scale mapping of almost 2000 last interglacial (MIS 5) shoreline-angle elevations of uplifted marine terraces along the western South American coast resulted in a standardized database that is tied to and supported by previously published terrace-age constraints. This database reveals last interglacial terraces at a median elevation of 30.1 m with a median uplift rate of 0.22 mm/yr. In addition, this new database documents that terrace elevations are characterized by various short- to long-wavelength patterns of uplift and deformation. Spatial correlations suggest medium- to long-wavelength patterns to be controlled by the subduction of major bathymetric ridges while short-wavelength deformation appears to be the result of upper-plate faulting. Latitudinal climate variability further controls the generation of marine terraces exerting influence by increasing wave heights and tidal ranges that cause enhanced erosion and morphologically well-expressed terraces. Conversely, the long-term preservation of uplifted terraces is inhibited through high precipitation, which increases marine terrace degradation, river incision and lateral scouring. The database of last interglacial terrace elevations enabled the calculation of long-term uplift rates and the analysis of glacial-cycle deformation patterns as well as the processes causing their topographical differentiation.

Systematic spectral analysis, performed by applying Fourier transforms to the signal of last interglacial uplift rates and to the signals of various tectonic mechanisms and parameters provided new insights into the different spatiotemporal effects of various parameters on the accumulation of permanent coastal uplift and the deformation of the forearc. Correlations between the individual wavelength spectra suggest short-wavelength deformation to result from crustal faulting, while intermediate- to long-wavelength variations in uplift rate might indicate various extents of locked areas on the megathrust that are related to its long-term seismotectonic segmentation. This segmentation is at least partially controlled by the subduction of bathymetric anomalies, but might originate at longer wavelengths from changes in the physical properties of the megathrust and the forearc. The observed continuous signal of background uplift likely results from moderate, domain-C earthquakes (M7–M8, ~35–55 km depth), since such events exhibit a good spectral correlation with terrace-uplift rates, and their uplift estimates indicate similar recurrence times for the last interglacial period compared to current Gutenberg-Richter distributions. Given the spatially discontinuous nature of these moderate-magnitude earthquakes, I propose permanent deformation to accumulate over multiple, spatially distributed and temporally distinct uplift phases that add up to a continuous uplift signal over millennial timescales. This novel signal-analysis approach further highlights its applicability to elucidate the mechanisms driving surface deformation in subduction zones at a continental scale.

Mapping and analysis of multiple levels of late Pleistocene marine terraces revealed several interesting results for the spatially more restricted area of the 2015 M8.3 Illapel-earthquake in central Chile. Terrace-uplift rates assigned to MIS 5, 7, 9, and 11 range from 0.1 to 0.6 mm/yr and are generally higher for the older terraces. These millennial-scale uplift rates do not correlate with current or decadal estimates of coastal deformation represented by coseismic slip during the Illapel earthquake, interseismic vertical GPS velocities, and associated interplate locking. This finding suggests seismic asperities not to be persistent features on the megathrust that control protracted accumulation of permanent deformation over long timescales of 10^5 years.

Pronounced gradual or abrupt changes in uplift rate along the central Chilean coast are, however, accompanied by the occurrence of crustal normal faults that display varying degrees of activity over the course of different interglacial periods. The fault scarps are the morphological expression of upper-plate extension, which is probably related to subduction

erosion and subsequent underplating. The extensional structures may thus reflect regional tectonic uplift and local gravitational collapse of the forearc, an interpretation supported by the characteristics of Illapel-earthquake aftershocks and the occurrence of numerous offshore normal faults. Although reflecting an important process, upper-plate normal faulting likely represents a second-order phenomenon that overprints the overall compressional geodynamic setting of the western South American margin. In addition, the subduction of the Juan Fernández Ridge (JFR) emphasize the role of subducting bathymetric anomalies with respect to local increases in terrace-uplift rates. This is furthermore evidenced by Illapel-earthquake aftershocks in the vicinity of subducted seamounts and the location of the JFR in the continuation of the Punta Salinas Ridge, the expression of a bathymetric anomaly on the upper plate. Importantly, since higher uplift rates are only observed for MIS 5 terraces, I propose a smaller impact of JFR-subduction processes prior to the last interglacial period.

This study highlights that the accumulation of permanent coastal deformation on glacial-cycle timescales is probably not represented by the current distribution of seismic asperities, but rather subject to a combination of various mechanisms. While regional-scale tectonic uplift is likely driven by moderate earthquakes near the Moho, subduction erosion and underplating, local changes in uplift rate are overprinting this continuous signal through upper-plate faulting and the subduction of bathymetric ridges, which further contribute to the seismotectonic segmentation of the forearc.

Appendix

Supporting information for Chapter 3

This supporting information provides additional figures related to the analyzed tectonic features mentioned in the main text (Fig. A1 to A8). It further provides more detailed visualizations regarding the correlation calculations between the uplift-rate spectrum and the spectra of the individual tectonic features (Figures A9 to A16).

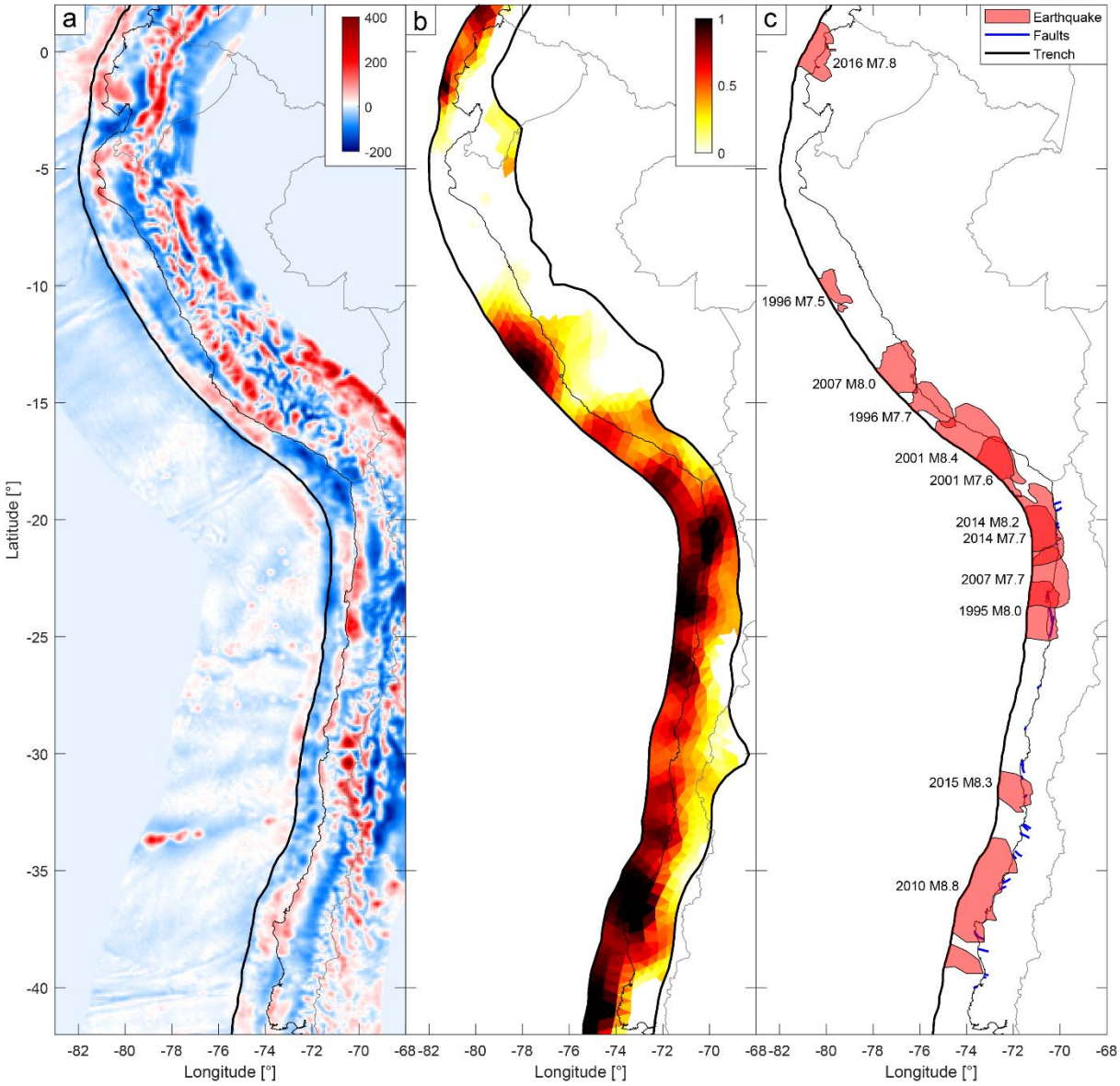

Figure A.1: Maps showing tectonic parameters used for the wavelength analyses. (a) Residual gravity anomaly obtained by applying a principal component analysis (Molina et al., 2021) for the Chilean margin to the Free-Air gravity anomaly grid of Sandwell et al. (2014) for the entire WSAC. (b) Interplate coupling calculated from rates of slip-deficit accumulation, which were modelled based on inverted GPS velocities on triangular dislocation elements in a global block model by Graham et al. (2018). (c) 33 crustal faults near the Chilean coast (blue lines), selected from the CHAF database of active faults in Chile (Maldonado et al., 2021) as well as the extent of vertical displacement areas (≥ 0.3 m) of megathrust earthquakes since 1995 (M ≥ 7.5) compiled from published Okada models (Hayes, 2017).

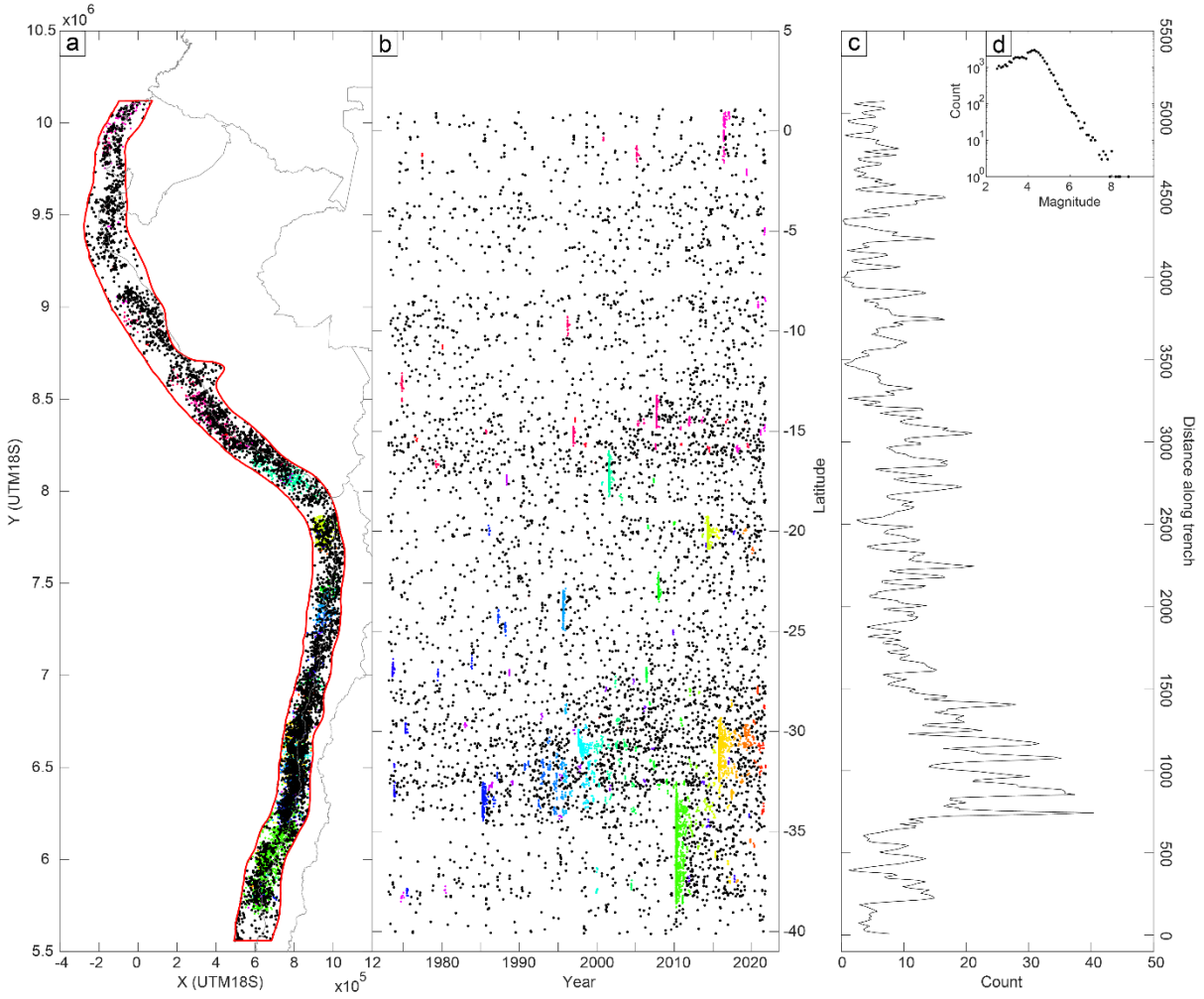

Figure A.2: Estimation of background seismicity with unlimited distance to the subduction slab (method similar to Madella and Ehlers (2021)). (a) Map of earthquakes since 1973 with magnitudes ranging from 4.3 to 6 and located within the 60-km depth contour of the subduction slab. (b) Temporal distribution of the earthquakes in (a). Colored earthquakes represent the removed events to extract the background seismicity using the cluster-analysis algorithm DBSCAN in MATLAB®. (c) Signal of background seismicity used for the wavelength analyses. (d) Gutenberg-Richter plot to estimate the magnitude range for the background seismicity.

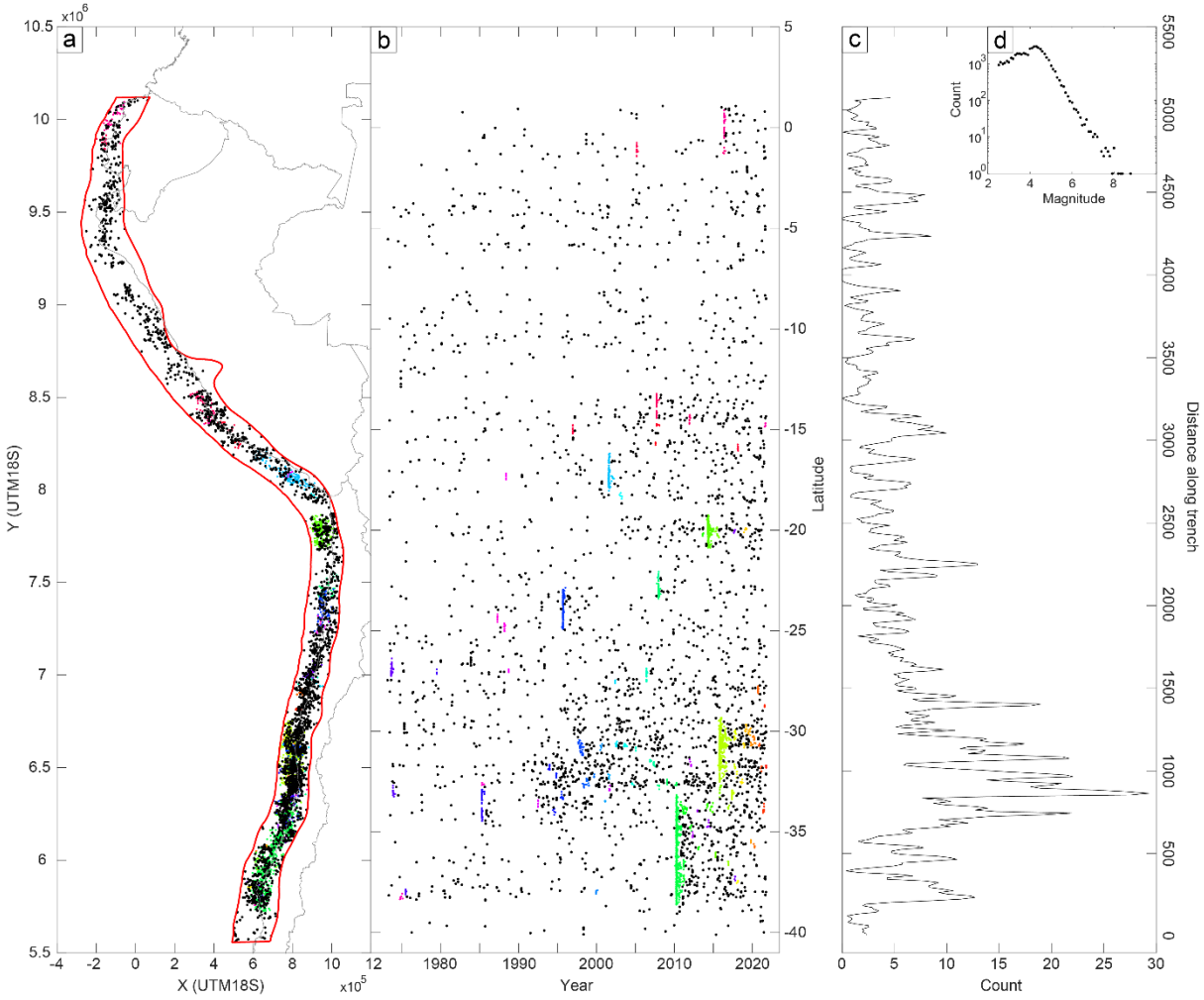

Figure A.3: Estimation of background seismicity with distances to the subduction slab below or equal to 10 km (method similar to Madella and Ehlers (2021)). (a) Map of earthquakes since 1973 with magnitudes ranging from 4.3 to 6 and located within the 60-km depth contour of the subduction slab. (b) Temporal distribution of the earthquakes in (a). Colored earthquakes represent the removed events to extract the background seismicity using the cluster-analysis algorithm DBSCAN in MATLAB®. (c) Signal of background seismicity used for the wavelength analyses. (d) Gutenberg-Richter plot to estimate the magnitude range for the background seismicity.

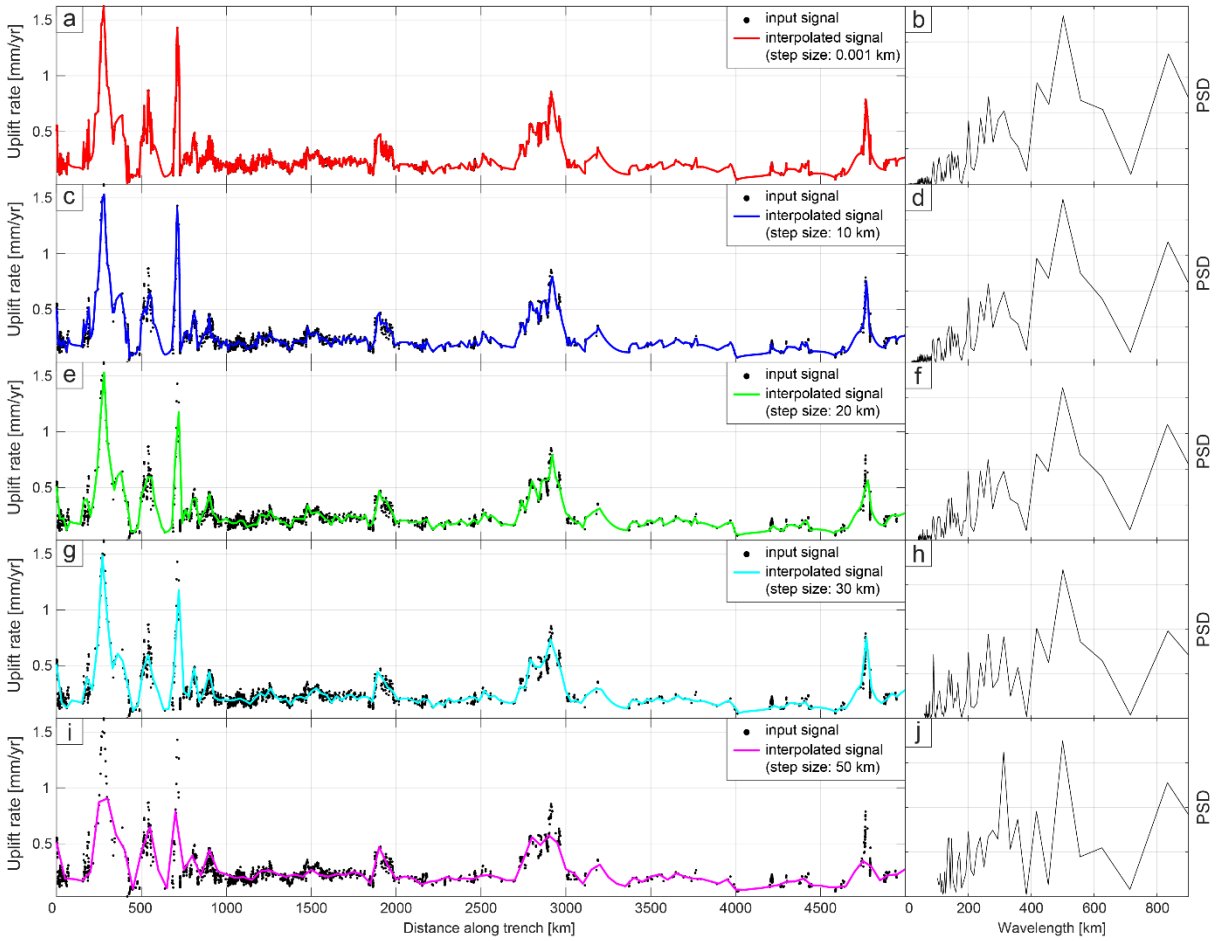

Figure A.4: Sensitivity test for the wavelength analysis of the uplift-rate signal using step sizes of 10^{-3}, 10, 20, 30, and 50 km (from top to bottom) for the interpolation of the input signal.

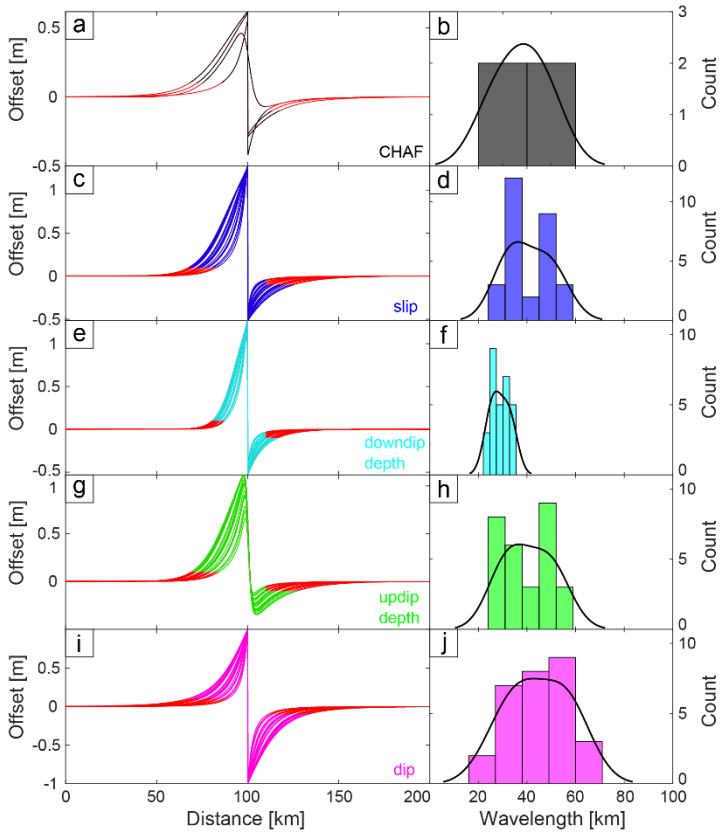

Figure A.5: Displacement profiles (200 km length, fault-perpendicular) of 33 crustal faults near the Chilean coast resulting from elastic Okada modelling (left). Red sections of each line represent cutoffs at absolute vertical displacements < 10 cm. Histograms and kernel density functions delineating associated wavelength of the displacement profiles (right). We used fault parameters and geometry of the CHAF database of active faults in Chile (Maldonado et al., 2021) if they were available (a and b). For the remaining (29) faults we systematically varied the input parameters (fault depth, dip, slip rate, and rake) (c to j) according to Table 3.1.

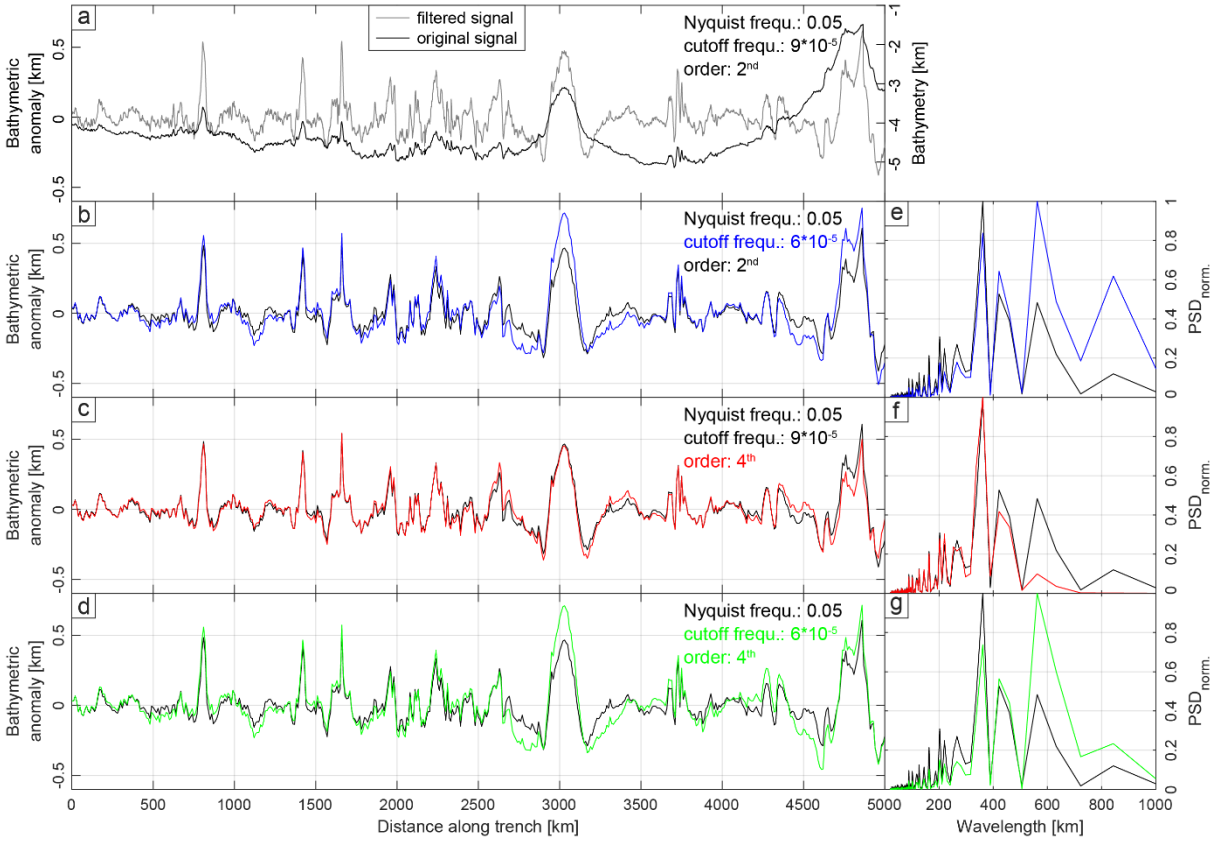

Figure A.6: (a) Bathymetry signal (black) and Butterworth-filtered bathymetry signal (gray) representing bathymetric anomalies. Parameters for the Butterworth filter are shown on the upper right of each subplot. Plots below show variations in the signals (left) and the respective wavelength spectra (right) when the cutoff frequency (b, e), the order of the filter (c, f), or both (d, g) are changed. Black lines in a, b-g represent the Butterworth-filtered signal and wavelength spectrum that we used for our analysis of the bathymetric anomaly.

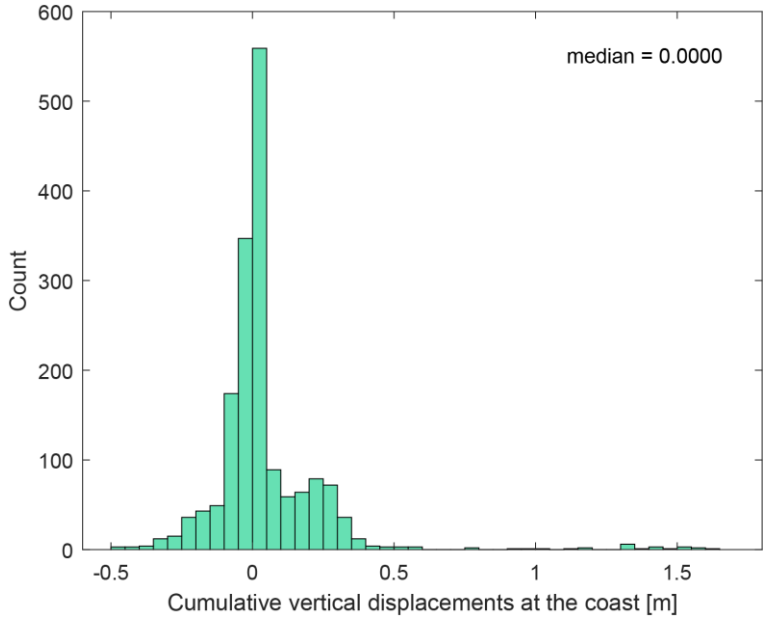

Figure A.7: Cumulative coseismic vertical displacements extracted from Okada models of 12 great-sized subduction earthquakes (Hayes, 2017) at the South American coast. The histogram shows approximately evenly distributed subsidence and uplift with a median of 0 m vertical displacement.

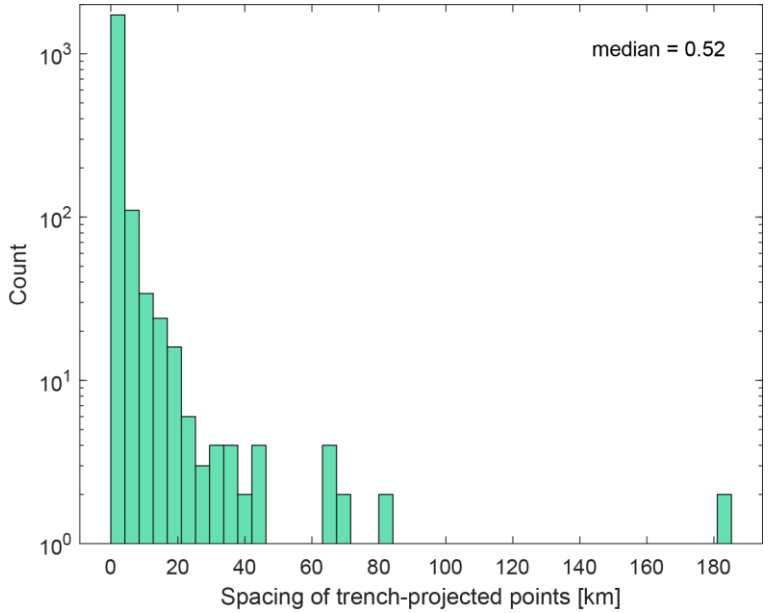

Figure A.8: Histogram of the spacing between trench-projected points (logarithmic y-axis) showing a median value of 0.52 km.

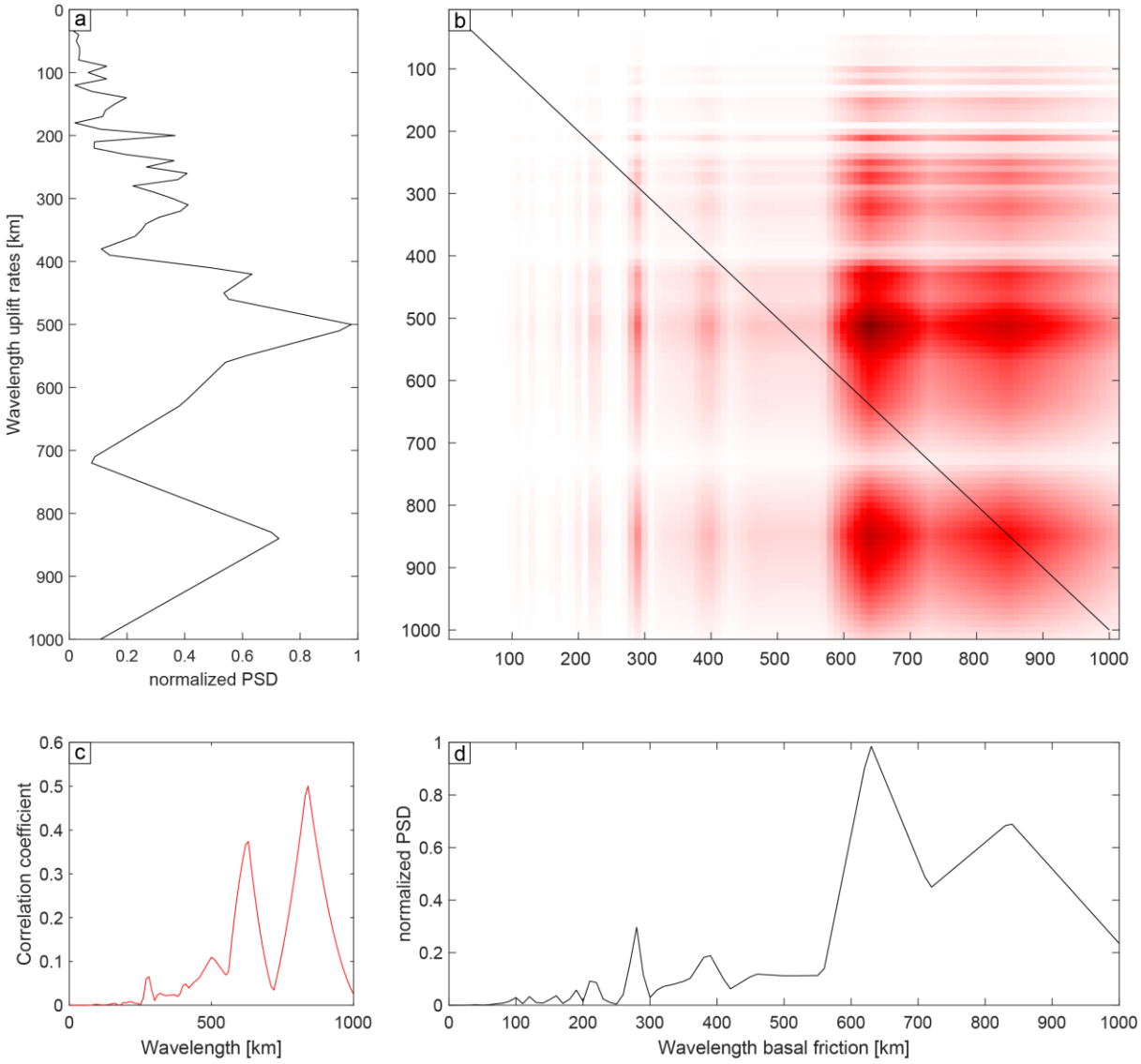

Figure A.9: Calculation of the correlation between the spectra of uplift rate (a) and basal friction (d). Both normalized power-spectral densities (PSDs) are multiplied and the diagonal values (c) of the resulting raster (b) represent the correlation of both spectra at the same wavelength. Colors in b range from zero (white) to one (dark red).

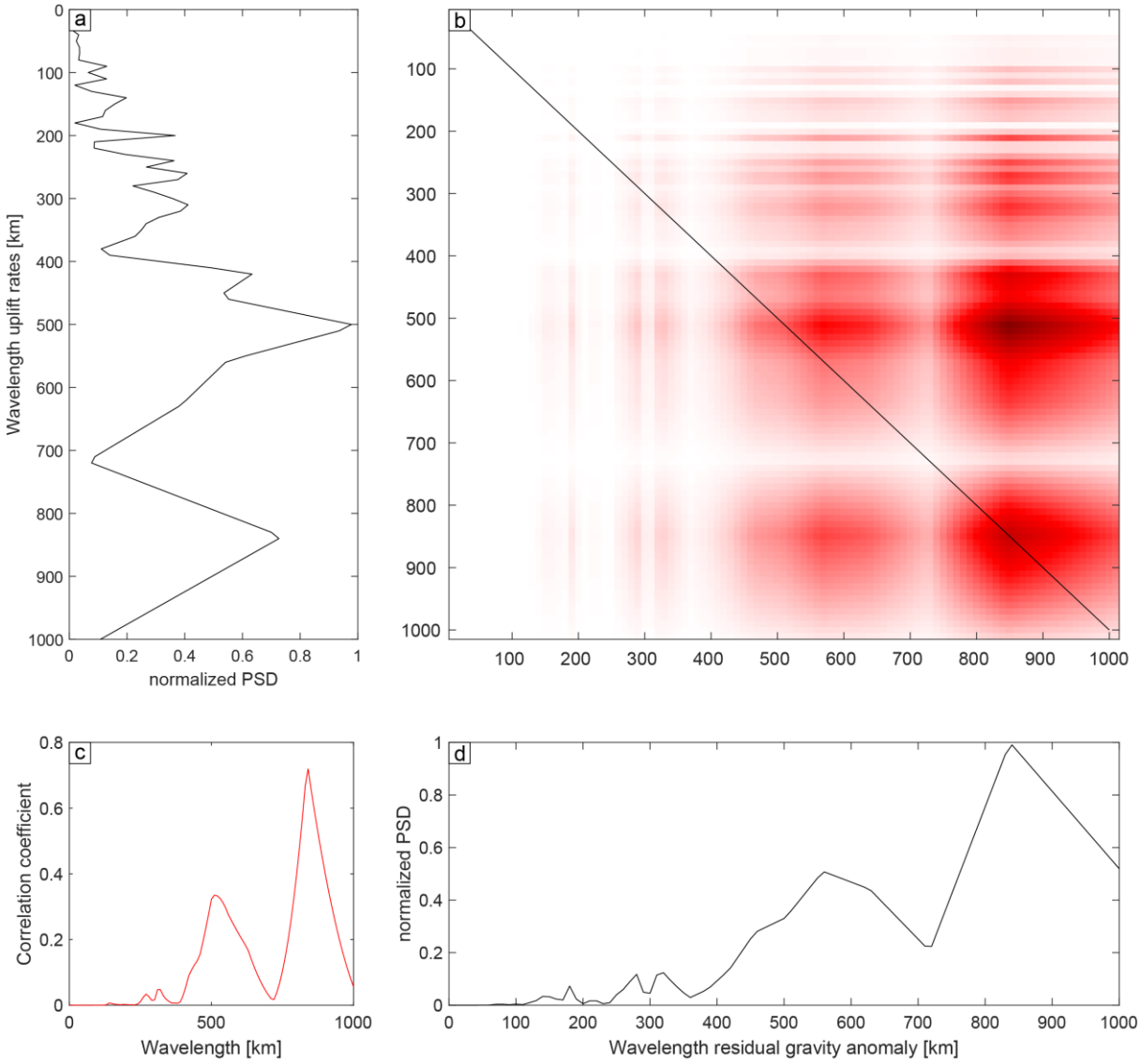

Figure A.10: Calculation of the correlation between the spectra of uplift rate (a) and residual gravity anomaly (d). Both normalized power-spectral densities (PSDs) are multiplied and the diagonal values (c) of the resulting raster (b) represent the correlation of both spectra at the same wavelength. Colors in b range from zero (white) to one (dark red).

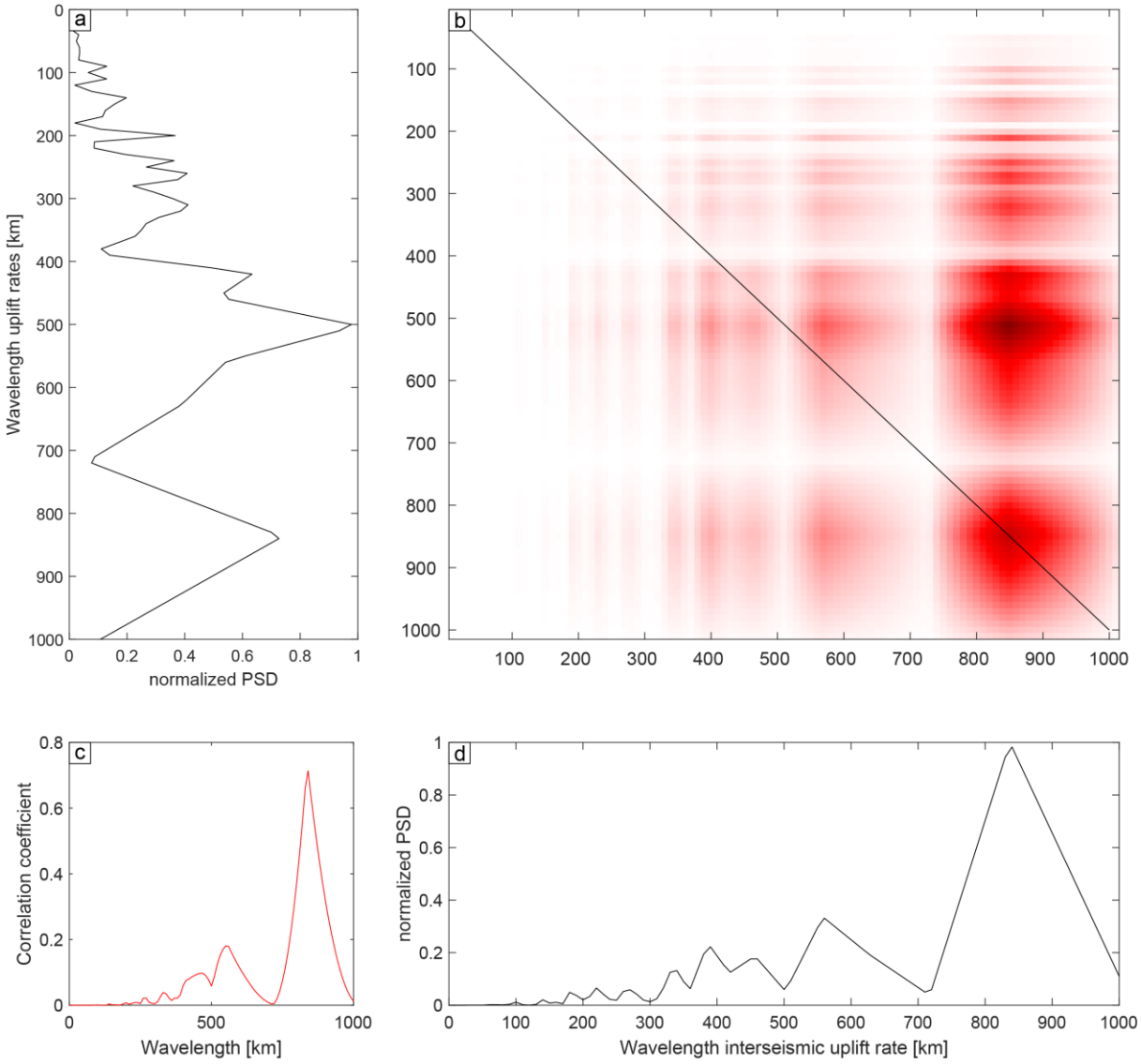

Figure A.11: Calculation of the correlation between the spectra of terrace uplift rate (a) and modeled interseismic uplift rate (d). Both normalized power-spectral densities (PSDs) are multiplied and the diagonal values (c) of the resulting raster (b) represent the correlation of both spectra at the same wavelength. Colors in b range from zero (white) to one (dark red).

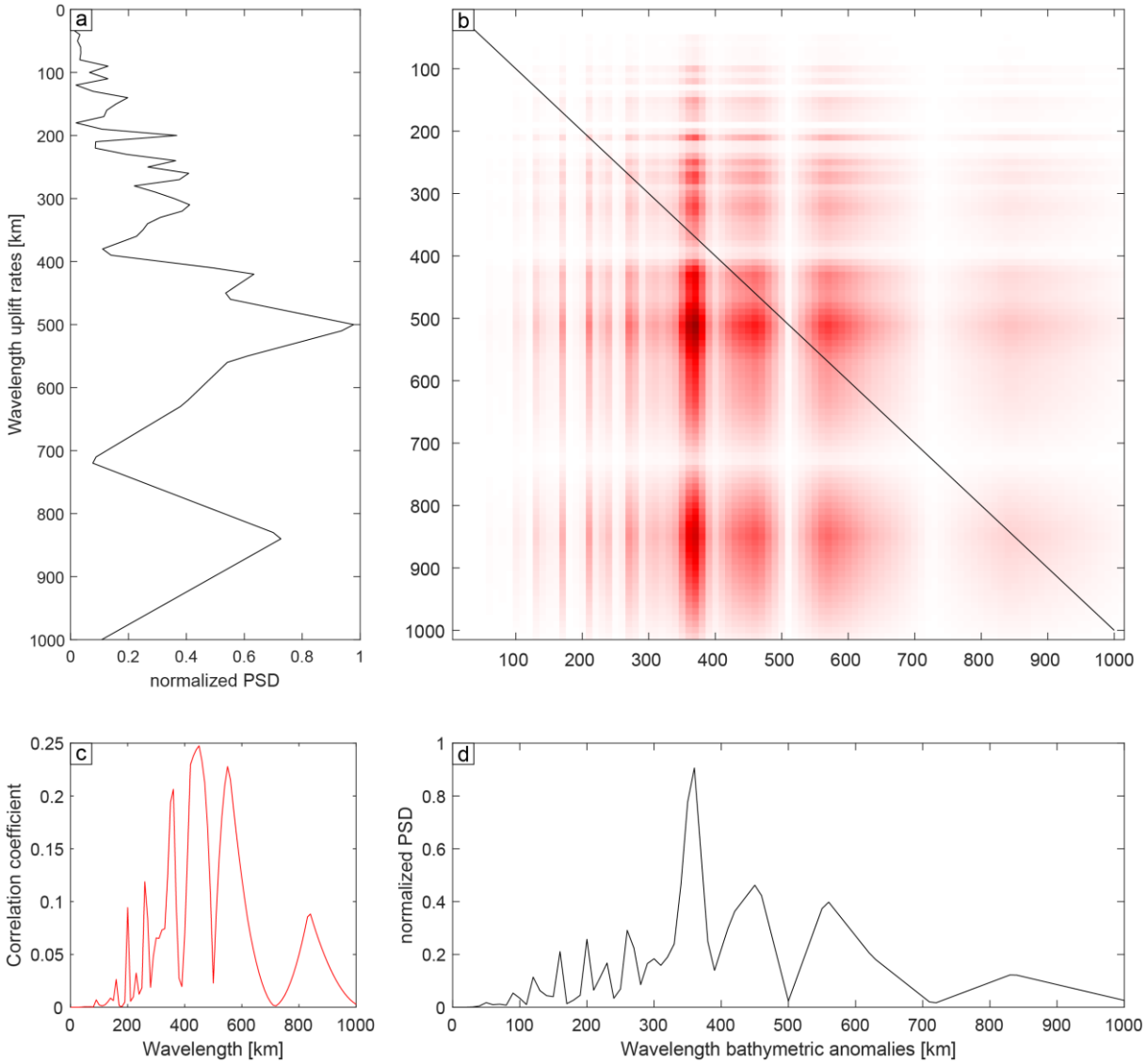

Figure A.12: Calculation of the correlation between the spectra of uplift rate (a) and bathymetric anomalies (d). Both normalized power-spectral densities (PSDs) are multiplied and the diagonal values (c) of the resulting raster (b) represent the correlation of both spectra at the same wavelength. Colors in b range from zero (white) to one (dark red).

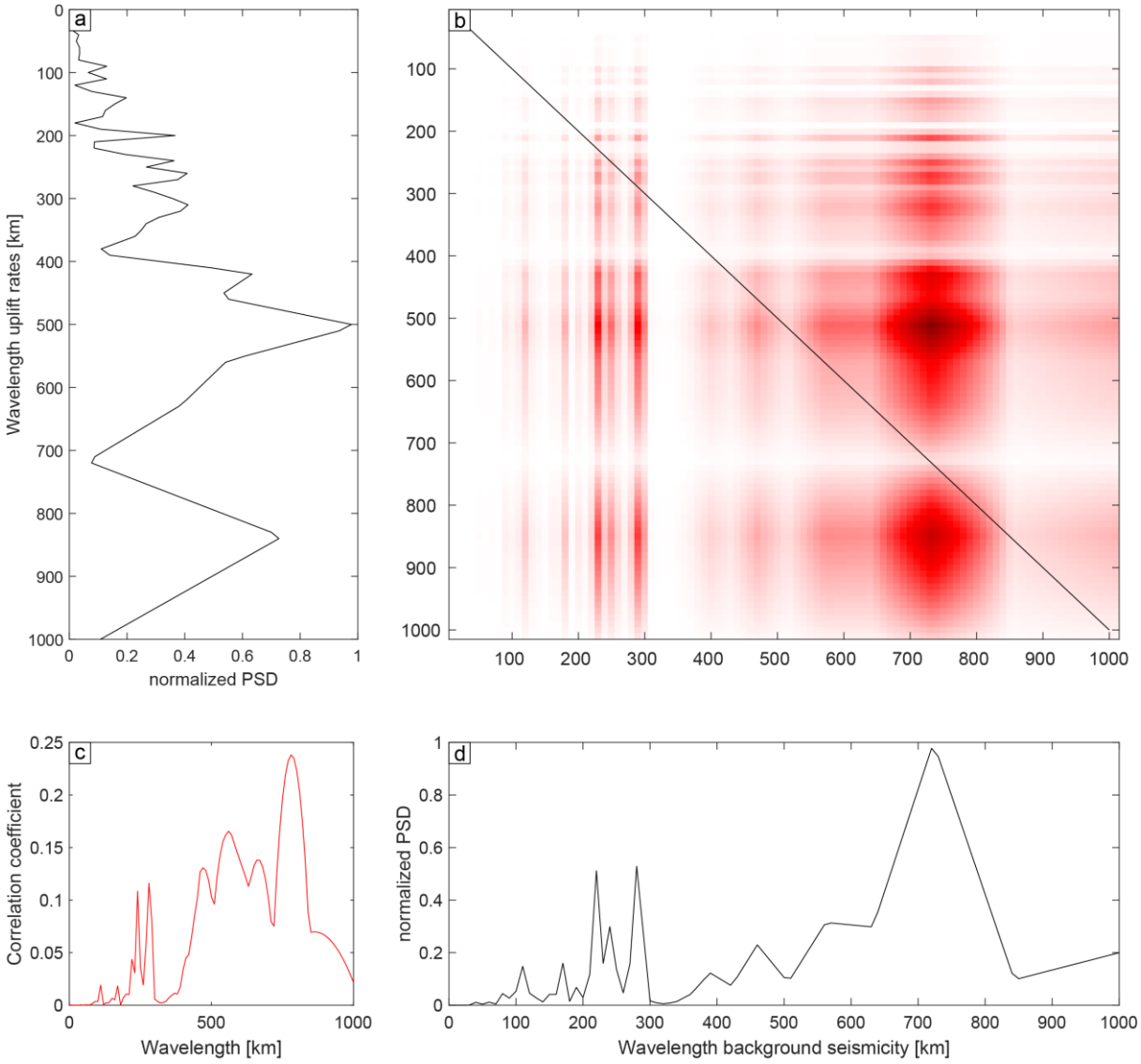

Figure A.13: Calculation of the correlation between the spectra of uplift rate (a) and background seismicity (d). Both normalized power-spectral densities (PSDs) are multiplied and the diagonal values (c) of the resulting raster (b) represent the correlation of both spectra at the same wavelength. Colors in b range from zero (white) to one (dark red).

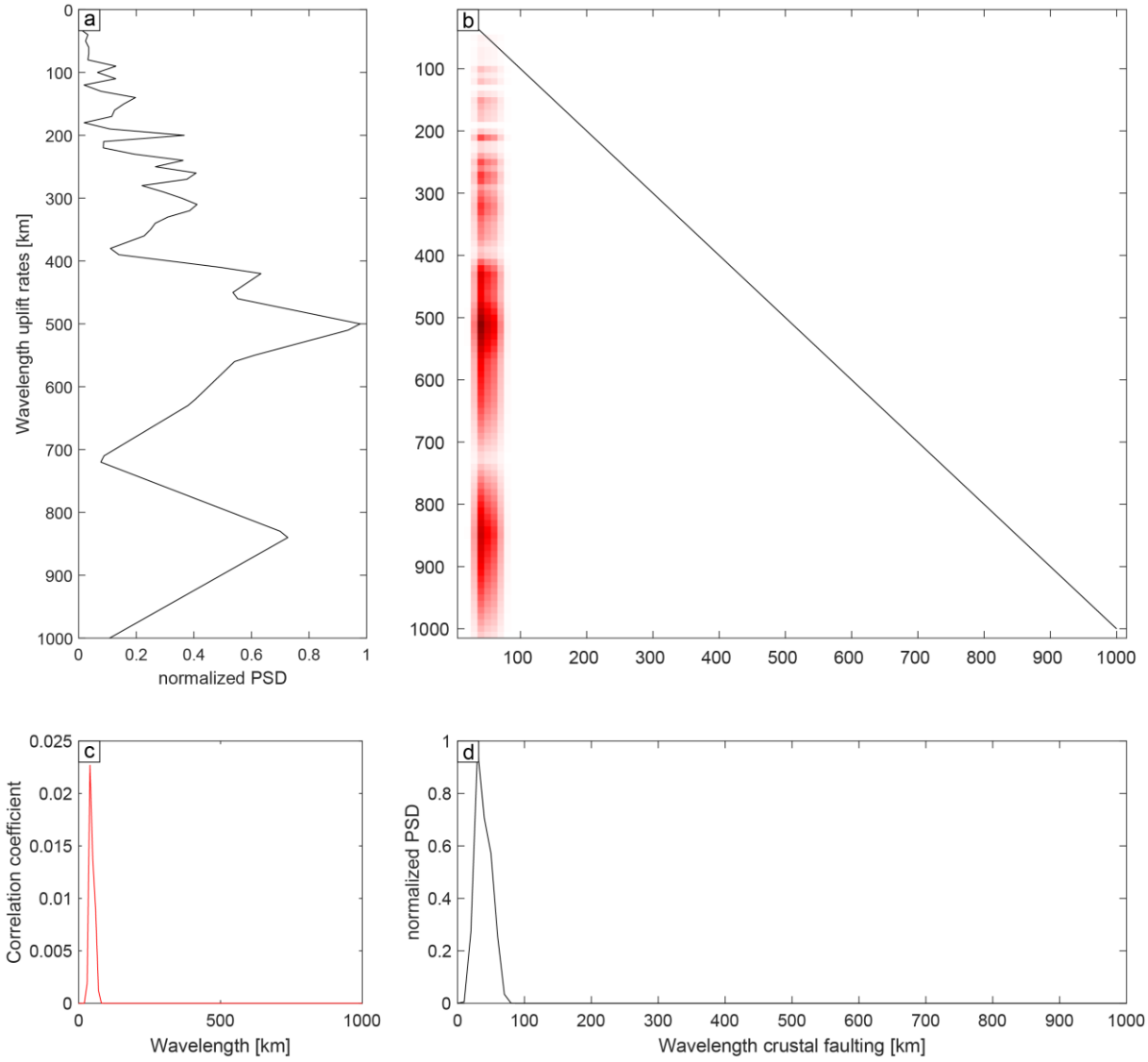

Figure A.14: Calculation of the correlation between the spectra of uplift rate (a) and crustal faulting (d). Both normalized power-spectral densities (PSDs) are multiplied and the diagonal values (c) of the resulting raster (b) represent the correlation of both spectra at the same wavelength. Colors in b range from zero (white) to one (dark red).

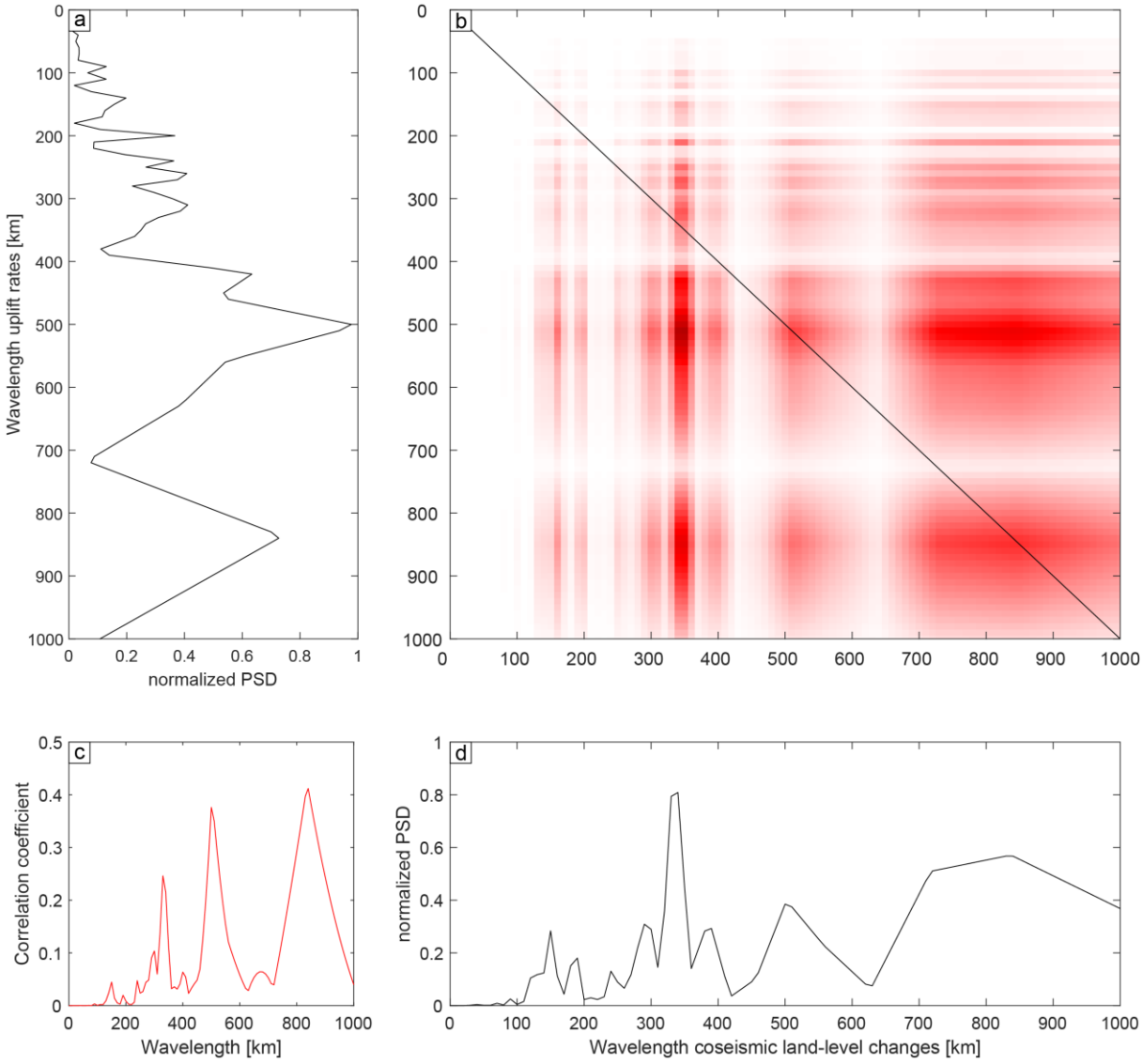

Figure A.15: Calculation of the correlation between the spectra of uplift rate (a) and coseismic land-level changes (d). Both normalized power-spectral densities (PSDs) are multiplied and the diagonal values (c) of the resulting raster (b) represent the correlation of both spectra at the same wavelength. Colors in b range from zero (white) to one (dark red).

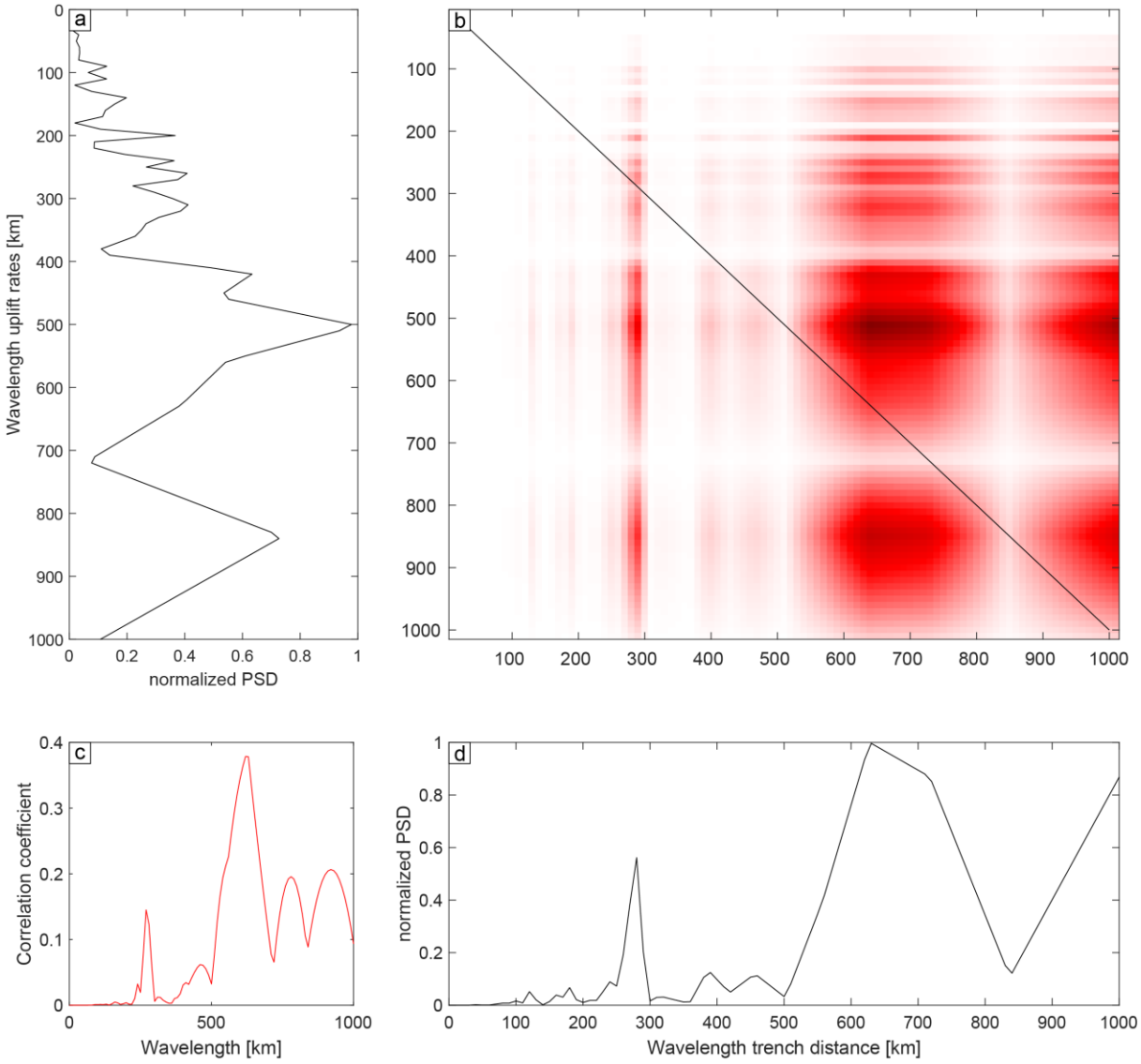

Figure A.16: Calculation of the correlation between the spectra of uplift rate (a) and trench distance (d). Both normalized power-spectral densities (PSDs) are multiplied and the diagonal values (c) of the resulting raster (b) represent the correlation of both spectra at the same wavelength. Colors in b range from zero (white) to one (dark red).

Software and data availability

Topographic calculations and outputs were processed and elaborated in ArcGIS® (ESRI) and MATLAB® (MathWorks Inc.) using TopoToolbox 2 (Schwanghart & Scherler, 2014). Adobe® Illustrator (Adobe Inc.) was used to refine figures and to combine multiple plots. The South American database of last interglacial shoreline-angle elevations (Chapter 2) is available online at https://doi.org/10.5281/zenodo.4309748 (Freisleben et al., 2020).

Acknowledgements

During my time as a doctoral student at the University of Potsdam, I got to know a variety of people who either helped me to advance my dissertation or simply made my time more enjoyable. Therefore, I would like to dedicate some words of gratitude to all those people in the following paragraphs.

This thesis is part of the ARTE project about *'Investigating asperity activity during multiple earthquake cycles'*, which was supported by a research grant of the Deutsche Forschungsgemeinschaft to Manfred R. Strecker (DFG STR373/41-1). My sincere thanks go to all the people in Germany and Chile who granted and secured the funding that made this work possible and who enabled me to go to the field. Those comprise especially Manfred Strecker, Julius Jara-Muñoz, and Daniel Melnick.

To my supervisors Manfred Strecker and Peter van der Beek: it was a great pleasure to work alongside with you. Manfred, thank you very much for providing constructive and valuable feedback at numerous stages of my dissertation. Your profound knowledge on the Andean geology always considered the big picture, which improved interpretations and helped me to stay focused on the most important tasks and not to get lost in the bits and pieces. Many thanks to Peter as well regarding your valuable feedback on the manuscripts, which not only improved their structure and interpretation, but also helped to get rid of methodological flaws. Special thanks go to my mentor Julius Jara-Muñoz who was my main contact person for any kind of problem, new idea, or first review/edit of a new manuscript, especially during the early stages of my thesis. He not only made sure that all my scientific skills and knowledge of relevant literature improved over time, but also enabled contacts to other researchers and made my field work in Chile a lot easier. I am deeply grateful for all your support.

In addition, I would like to thank my colleagues from Chile. It was a great pleasure to work with Daniel Melnick who often provided creative input during discussions, shared valuable data sets with me, and suggested skillful ways to improve weak aspects of our manuscripts. For their assistance in the field, my gratitude goes to Julius and Daniel, his former students Valentina Alarcón and Diego Ignacio, and to Christian Creixell and Ismael Murillo, without whom field work would have been less productive and enjoyable. Furthermore, I would like to thank Dominik Brill who dated our luminescence samples and helped with their interpretation as well as Tanja Klaka-Tauscher who supported me with organizational and bureaucratic tasks at the University of Potsdam. My sincere thanks further go to all my co-authors who dedicated their time to review and edit our manuscripts.

Most certainly, my time at the University would not have been as enjoyable without my long-time office mates Christoph and Valentina as well as my dear colleagues in the SMURF seminar group. Last but not least, I would like to thank my friends, family and especially my girlfriend Jenny. You always encouraged me right from the beginning, made my days brighter in times of setbacks, and supported me in every way I can think of.

Thank you very much!

References

Adam, J., & Reuther, C.-D. (2000). Crustal dynamics and active fault mechanics during subduction erosion. Application of frictional wedge analysis on to the North Chilean Forearc. *Tectonophysics*, *321*(3), 297–325. https://doi.org/10.1016/S0040-1951(00)00074-3

Allmendinger, R. W., & González, G. (2010). Neogene to Quaternary tectonics of the coastal Cordillera, northern Chile. *Tectonophysics*, *495*(1-2), 93–110. https://doi.org/10.1016/j.tecto.2009.04.019

Alvarado, A., Audin, L., Nocquet, J. M., Jaillard, E., Mothes, P., & Jarrín, P., et al. (2016). Partitioning of oblique convergence in the Northern Andes subduction zone: Migration history and the present-day boundary of the North Andean Sliver in Ecuador. *Tectonics*, *35*(5), 1048–1065. https://doi.org/10.1002/2016TC004117

Anderson, R. S., Densmore, A. L., & Ellis, M. A. (1999). The generation and degradation of marine terraces. *Basin Research*, *11*(1), 7–19. https://doi.org/10.1046/j.1365-2117.1999.00085.x

Angermann, D., Klotz, J., & Reigber, C. (1999). Space-geodetic estimation of the Nazca-South America Euler vector. *Earth and Planetary Science Letters*, *171*(3), 329–334. https://doi.org/10.1016/S0012-821X(99)00173-9

Armijo, R., Lacassin, R., Coudurier-Curveur, A., & Carrizo, D. (2015). Coupled tectonic evolution of Andean orogeny and global climate. *Earth-Science Reviews*, *143*, 1–35. https://doi.org/10.1016/j.earscirev.2015.01.005

Armijo, R., & Thiele, R. (1990). Active faulting in northern Chile: ramp stacking and lateral decoupling along a subduction plate boundary? *Earth and Planetary Science Letters*, *98*(1), 40–61. https://doi.org/10.1016/0012-821X(90)90087-E

Aron, F., Allmendinger, R. W., Cembrano, J., González, G., & Yáñez, G. (2013). Permanent fore-arc extension and seismic segmentation: Insights from the 2010 Maule earthquake, Chile. *Journal of Geophysical Research: Solid Earth*, *118*(2), 724–739. https://doi.org/10.1029/2012JB009339

Auclair, M., Lamothe, M., & Huot, S. (2003). Measurement of anomalous fading for feldspar IRSL using SAR. *Radiation Measurements*, *37*(4-5), 487–492. https://doi.org/10.1016/S1350-4487(03)00018-0

Audin, L., Lacan, P., Tavera, H., & Bondoux, F. (2008). Upper plate deformation and seismic barrier in front of Nazca subduction zone: The Chololo Fault System and active tectonics along the Coastal Cordillera, southern Peru. *Tectonophysics*, *459*(1-4), 174–185. https://doi.org/10.1016/j.tecto.2007.11.070

Baize, S., Audin, L., Winter, T., Alvarado, A., Pilatasig Moreno, L., & Taipe, M., et al. (2015). Paleoseismology and tectonic geomorphology of the Pallatanga fault (Central

Ecuador), a major structure of the South-American crust. *Geomorphology*, *237*, 14–28. https://doi.org/10.1016/j.geomorph.2014.02.030

Baker, A., Allmendinger, R. W., Owen, L. A., & Rech, J. A. (2013). Permanent deformation caused by subduction earthquakes in northern Chile. *Nature Geoscience*, *6*(6), 492–496. https://doi.org/10.1038/ngeo1789

Bangs, N. L., & Cande, S. C. (1997). Episodic development of a convergent margin inferred from structures and processes along the southern Chile margin. *Tectonics*, *16*(3), 489–503.

Bangs, N. L., Morgan, J. K., Tréhu, A. M., Contreras-Reyes, E., Arnulf, A. F., & Han, S., et al. (2020). Basal accretion along the South Central Chilean margin and its relationship to great earthquakes. *Journal of Geophysical Research: Solid Earth*, *125*(11), 16. https://doi.org/10.1029/2020JB019861

Barazangi, M., & Isacks, B. L. (1976). Spatial distribution of earthquakes and subduction of the Nazca plate beneath South America. *Geology*, *4*(11), 686. https://doi.org/10.1130/0091-7613(1976)4<686:SDOEAS>2.0.CO;2

Barbot, S., Lapusta, N., & Avouac, J.-P. (2012). Under the hood of the earthquake machine: toward predictive modeling of the seismic cycle. *Science (New York, N.Y.)*, *336*(6082), 707–710. https://doi.org/10.1126/science.1218796

Barnhart, W. D., Murray, J. R., Briggs, R. W., Gomez, F., Miles, C. P. J., & Svarc, J., et al. (2016). Coseismic slip and early afterslip of the 2015 Illapel, Chile, earthquake: Implications for frictional heterogeneity and coastal uplift. *Journal of Geophysical Research: Solid Earth*, *121*(8), 6172–6191. https://doi.org/10.1002/2016JB013124

Bassett, D., & Watts, A. B. (2015). Gravity anomalies, crustal structure, and seismicity at subduction zones: 1. Seafloor roughness and subducting relief. *Geochemistry, Geophysics, Geosystems*, *16*(5), 1508–1540. https://doi.org/10.1002/2014GC005684

Bassett, D., & Watts, A. B. (2015). Gravity anomalies, crustal structure, and seismicity at subduction zones: 2. Interrelationships between fore-arc structure and seismogenic behavior. *Geochemistry, Geophysics, Geosystems*, *16*(5), 1541–1576. https://doi.org/10.1002/2014GC005685

Becerra, J., Arriagada, C., Contreras-Reyes, E., Bascuñan, S., Pascale, G. P. de, & Reichert, C., et al. (2017). Gravitational deformation and inherited structural control on slope morphology in the subduction zone of north-central Chile (ca. 29-33°S). *Basin Research*, *29*(6), 798–815. https://doi.org/10.1111/bre.12205

Beck, S., Barrientos, S., Kausel, E., & Reyes, M. (1998). Source characteristics of historic earthquakes along the central Chile subduction zone. *Journal of South American Earth Sciences*, *11*(2), 115–129. https://doi.org/10.1016/S0895-9811(98)00005-4

Bendix, J., Rollenbeck, R., & Reudenbach, C. (2006). Diurnal patterns of rainfall in a tropical Andean valley of southern Ecuador as seen by a vertically pointing K-band Doppler radar. *International Journal of Climatology*, *26*(6), 829–846. https://doi.org/10.1002/joc.1267

Bernhardt, A., Hebbeln, D., Regenberg, M., Lückge, A., & Strecker, M. R. (2016). Shelfal sediment transport by an undercurrent forces turbidity-current activity during high sea level along the Chile continental margin. *Geology*, *44*(4), 295–298. https://doi.org/10.1130/G37594.1

Bernhardt, A., Schwanghart, W., Hebbeln, D., Stuut, J.-B. W., & Strecker, M. R. (2017). Immediate propagation of deglacial environmental change to deep-marine turbidite systems along the Chile convergent margin. *Earth and Planetary Science Letters*, *473*, 190–204. https://doi.org/10.1016/j.epsl.2017.05.017

Bianca, M., Catalano, S., Guidi, G. de, Gueli, A. M., Monaco, C., & Ristuccia, G. M., et al. (2011). Luminescence chronology of Pleistocene marine terraces of Capo Vaticano

peninsula (Calabria, Southern Italy). *Quaternary International*, *232*(1-2), 114–121. https://doi.org/10.1016/j.quaint.2010.07.013

Bilek, S. L. (2010). Invited review paper: Seismicity along the South American subduction zone: Review of large earthquakes, tsunamis, and subduction zone complexity. *Tectonophysics*, *495*(1-2), 2–14. https://doi.org/10.1016/j.tecto.2009.02.037

Bilek, S. L., Schwartz, S. Y., & DeShon, H. R. (2003). Control of seafloor roughness on earthquake rupture behavior. *Tectonics*, *31*(5), 455. https://doi.org/10.1130/0091-7613(2003)031<0455:COSROE>2.0.CO;2

Binnie, A., Dunai, T. J., Binnie, S. A., Victor, P., González, G., & Bolten, A. (2016). Accelerated late quaternary uplift revealed by 10Be exposure dating of marine terraces, Mejillones Peninsula, northern Chile. *Quaternary Geochronology*, *36*, 12–27. https://doi.org/10.1016/j.quageo.2016.06.005

Bletery, Q., Thomas, A. M., Rempel, A. W., Karlstrom, L., Sladen, A., & Barros, L. de. (2016). Mega-earthquakes rupture flat megathrusts. *Science (New York, N.Y.)*, *354*(6315), 1027–1031. https://doi.org/10.1126/science.aag0482

Bookhagen, B., Echtler, H. P., Melnick, D., Strecker, M. R., & Spencer, J. Q. G. (2006). Using uplifted Holocene beach berms for paleoseismic analysis on the Santa María Island, south-central Chile. *Geophysical Research Letters*, *33*(15), 329. https://doi.org/10.1029/2006GL026734

Bookhagen, B., & Strecker, M. R. (2008). Orographic barriers, high-resolution TRMM rainfall, and relief variations along the eastern Andes. *Geophysical Research Letters*, *35*(6), 139. https://doi.org/10.1029/2007GL032011

Bradley, W. C. (1957). Origin of marine-terrace deposits in the Santa Cruz area, California. *Geological Society of America Bulletin*, *68*(4), 421. https://doi.org/10.1130/0016-7606(1957)68[421:OOMDIT]2.0.CO;2

Briggs, R. W., Sieh, K., Amidon, W. H., Galetzka, J., Prayudi, D., & Suprihanto, I., et al. (2008). Persistent elastic behavior above a megathrust rupture patch: Nias island, West Sumatra. *Journal of Geophysical Research*, *113*(B12), 449. https://doi.org/10.1029/2008JB005684

Buylaert, J. P., Murray, A. S., Thomsen, K. J., & Jain, M. (2009). Testing the potential of an elevated temperature IRSL signal from K-feldspar. *Radiation Measurements*, *44*(5-6), 560–565. https://doi.org/10.1016/j.radmeas.2009.02.007

Buylaert, J.-P., Jain, M., Murray, A. S., Thomsen, K. J., Thiel, C., & Sohbati, R. (2012). A robust feldspar luminescence dating method for Middle and Late Pleistocene sediments. *Boreas*, *41*(3), 435–451. https://doi.org/10.1111/j.1502-3885.2012.00248.x

Cahill, T., & Isacks, B. L. (1992). Seismicity and shape of the subducted Nazca Plate. *Journal of Geophysical Research*, *97*(B12), 17503. https://doi.org/10.1029/92JB00493

Carrasco, S., Ruiz, J. A., Contreras-Reyes, E., & Ortega-Culaciati, F. (2019). Shallow intraplate seismicity related to the Illapel 2015 Mw 8.4 earthquake: Implications from the seismic source. *Tectonophysics*, *766*(5), 205–218. https://doi.org/10.1016/j.tecto.2019.06.011

Ceccherini, G., Ameztoy, I., Hernández, C., & Moreno, C. (2015). High-Resolution Precipitation Datasets in South America and West Africa based on Satellite-Derived Rainfall, Enhanced Vegetation Index and Digital Elevation Model. *Remote Sensing*, *7*(5), 6454–6488. https://doi.org/10.3390/rs70506454

Cembrano, J., Lavenu, A., Yañez, G., Riquelme, R., García, M., González, G., & Hérail, G. (2007). Neotectonics. In T. Moreno & W. Gibbons (Eds.), *The geology of Chile* (pp. 231–261). London: Geological Society.

Chlieh, M., Chabalier, J. B. de, Ruegg, J. C., Armijo, R., Dmowska, R., Campos, J., & Feigl, K. L. (2004). Crustal deformation and fault slip during the seismic cycle in the North Chile subduction zone, from GPS and InSAR observations. *Geophysical Journal International*, *158*(2), 695–711. https://doi.org/10.1111/j.1365-246X.2004.02326.x

Choi, J. H., Murray, A. S., Jain, M., Cheong, C. S., & Chang, H. W. (2003). Luminescence dating of well-sorted marine terrace sediments on the southeastern coast of Korea. *Quaternary Science Reviews*, *22*(2-4), 407–421. https://doi.org/10.1016/S0277-3791(02)00136-1

Cisternas, M., Atwater, B. F., Torrejón, F., Sawai, Y., Machuca, G., & Lagos, M., et al. (2005). Predecessors of the giant 1960 Chile earthquake. *Nature*, *437*(7057), 404–407. https://doi.org/10.1038/nature03943

Clarke, S. H., & Carver, G. A. (1992). Late holocene tectonics and paleoseismicity, southern cascadia subduction zone. *Science (New York, N.Y.)*, *255*(5041), 188–192. https://doi.org/10.1126/science.255.5041.188

Clift, P., & Vannucchi, P. (2004). Controls on tectonic accretion versus erosion in subduction zones: Implications for the origin and recycling of the continental crust. *Reviews of Geophysics*, *42*(2), 19. https://doi.org/10.1029/2003RG000127

Clift, P. D., & Hartley, A. J. (2007). Slow rates of subduction erosion and coastal underplating along the Andean margin of Chile and Peru. *Geology*, *35*(6), 503. https://doi.org/10.1130/G23584A.1

Cloos, M., & Shreve, R. L. (1988). Subduction-channel model of prism accretion, melange formation, sediment subduction, and subduction erosion at convergent plate margins: 1. Background and description. *Pure and Applied Geophysics*, *128*(3-4), 455–500. https://doi.org/10.1007/BF00874548

Cloos, M., & Shreve, R. L. (1996). Shear-zone thickness and the seismicity of Chilean- and Marianas-type subduction zones. *Geology*, *24*(2), 107. https://doi.org/10.1130/0091-7613(1996)024<0107:SZTATS>2.3.CO;2

Collot, J.-Y., Charvis, P., Gutscher, M.-A., & Operto, S. (2002). Exploring the Ecuador-Colombia Active Margin and Interplate Seismogenic Zone. *Eos, Transactions, American Geophysical Union*, *83*(17), 185. https://doi.org/10.1029/2002EO000120

Collot, J.-Y., Sanclemente, E., Nocquet, J.-M., Leprêtre, A., Ribodetti, A., & Jarrin, P., et al. (2017). Subducted oceanic relief locks the shallow megathrust in central Ecuador. *Journal of Geophysical Research: Solid Earth*, *122*(5), 3286–3305. https://doi.org/10.1002/2016JB013849

Comte, D., Farias, M., Roecker, S., & Russo, R. (2019). The nature of the subduction wedge in an erosive margin: Insights from the analysis of aftershocks of the 2015 Mw 8.3 Illapel earthquake beneath the Chilean Coastal Range. *Earth and Planetary Science Letters*, *520*(1–2), 50–62. https://doi.org/10.1016/j.epsl.2019.05.033

Comte, D., & Pardo, M. (1991). Reappraisal of great historical earthquakes in the northern Chile and southern Peru seismic gaps. *Natural Hazards*, *4*(1), 23–44. https://doi.org/10.1007/BF00126557

Contreras-Reyes, E., Ruiz, J. A., Becerra, J., Kopp, H., Reichert, C., Maksymowicz, A., & Arriagada, C. (2015). Structure and tectonics of the central Chilean margin (31°–33°S): implications for subduction erosion and shallow crustal seismicity. *Geophysical Journal International*, *203*(2), 776–791. https://doi.org/10.1093/gji/ggv309

Costa, C., Alvarado, A., Audemard, F., Audin, L., Benavente, C., & Bezerra, F. H., et al. (2020). Hazardous faults of South America; compilation and overview. *Journal of South American Earth Sciences*, *104*(1), 102837. https://doi.org/10.1016/j.jsames.2020.102837

Costa, C., Machette, M. N., Dart, R. L., Bastias, H. E., Paredes, J. D., & Perucca, L. P., et al. (2000). *Map and database of Quaternary faults and folds in Argentina* (Open-File Report): US Geological Survey. Retrieved from http://dx.doi.org/10.3133/ofr00108

Coudurier-Curveur, A., Lacassin, R., & Armijo, R. (2015). Andean growth and monsoon winds drive landscape evolution at SW margin of South America. *Earth and Planetary Science Letters*, *414*, 87–99. https://doi.org/10.1016/j.epsl.2014.12.047

Creveling, J. R., Mitrovica, J. X., Clark, P. U., Waelbroeck, C., & Pico, T. (2017). Predicted bounds on peak global mean sea level during marine isotope stages 5a and 5c. *Quaternary Science Reviews*, *163*(6), 193–208. https://doi.org/10.1016/j.quascirev.2017.03.003

Cubas, N., Avouac, J.-P., Souloumiac, P., & Leroy, Y. (2013). Megathrust friction determined from mechanical analysis of the forearc in the Maule earthquake area. *Earth and Planetary Science Letters*, *381*, 92–103. https://doi.org/10.1016/j.epsl.2013.07.037

Dahlen, F. A. (1984). Noncohesive critical Coulomb wedges: An exact solution. *Journal of Geophysical Research*, *89*(B12), 10125–10133. https://doi.org/10.1029/JB089iB12p10125

Dahlen, F. A., Suppe, J., & Davis, D. (1984). Mechanics of fold-and-thrust belts and accretionary wedges: Cohesive Coulomb Theory. *Journal of Geophysical Research*, *89*(B12), 10087–10101. https://doi.org/10.1029/JB089iB12p10087

Darwin, C. R. (1846). *Geological observations on South America. Being the third part of the geology of the voyage of the Beagle, under the command of Capt. Fitzroy, R.N. during the years 1832 to 1836.* London: Smith Elder and Co.

Delouis, B., Monfret, T., Dorbath, L., Pardo, M., Rivera, L., & Comte, D., et al. (1997). The Mw = 8.0 Antofagasta (northern Chile) earthquake of 30 July 1995: A precursor to the end of the large 1877 gap. *Bulletin of the Seismological Society of America*, *87*(2), 427–445. https://doi.org/10.1785/BSSA0870020427

DeMets, C., Gordon, R. G., & Argus, D. F. (2010). Geologically current plate motions. *Geophysical Journal International*, *181*(1), 1–80. https://doi.org/10.1111/j.1365-246X.2009.04491.x

DesRoches, R., Comerio, M., Eberhard, M., Mooney, W., & Rix, G. J. (2011). Overview of the 2010 Haiti Earthquake. *Earthquake Spectra*, *27*(1_suppl1), 1–21. https://doi.org/10.1193/1.3630129

Dumas, B., Hoang, C. T., & Raffy, J. (2006). Record of MIS 5 sea-level highstands based on U/Th dated coral terraces of Haiti. *Quaternary International*, *145-146*, 106–118. https://doi.org/10.1016/j.quaint.2005.07.010

Durcan, J. A., King, G. E., & Duller, G. A.T. (2015). DRAC: Dose Rate and Age Calculator for trapped charge dating. *Quaternary Geochronology*, *28*(2), 54–61. https://doi.org/10.1016/j.quageo.2015.03.012

Espurt, N., Funiciello, F., Martinod, J., Guillaume, B., Regard, V., Faccenna, C., & Brusset, S. (2008). Flat subduction dynamics and deformation of the South American plate: Insights from analog modeling. *Tectonics*, *27*(3), n/a-n/a. https://doi.org/10.1029/2007TC002175

Farías, M., Comte, D., Roecker, S., Carrizo, D., & Pardo, M. (2011). Crustal extensional faulting triggered by the 2010 Chilean earthquake: The Pichilemu seismic sequence. *Tectonics*, *30*(6). https://doi.org/10.1029/2011TC002888

Flint, R. F. (1971). *Glacial and quaternary geology*. New York: John Wiley and Sons.

Freisleben, R., Jara-Muñoz, J., Melnick, D., Martínez, J. M., & Strecker, M. (2020). Marine terraces of the last interglacial period along the Pacific coast of South America (1°N-40°S). *Zenodo.* Advance online publication. https://doi.org/10.5281/ZENODO.4309748

Freisleben, R., Jara-Muñoz, J., Melnick, D., Martínez, J. M., & Strecker, M. R. (2021). Marine terraces of the last interglacial period along the Pacific coast of South America (1°

N–40° S). *Earth System Science Data*, *13*(6), 2487–2513. https://doi.org/10.5194/essd-13-2487-2021

Fryer, P., & Smoot, N.C. (1985). Processes of seamount subduction in the Mariana and Izu-Bonin trenches. *Marine Geology*, *64*(1-2), 77–90. https://doi.org/10.1016/0025-3227(85)90161-6

Fuenzalida, H., Cooke, R., Paskoff, R., Segerstrom, K., & Weischet, W. (1965). High Stands of Quaternary Sea Level Along the Chilean Coast. *Geological Society of America Special Papers*, *84*, 473–496.

Galbraith, R. F., Roberts, R. G., Laslett, G. M., Yoshida, H., & Olley, J. M. (1999). Optical dating of single and multiple grains of quartz from Jinmium Rock Shelter, northern Australia: Part 1, experimental design and statistical models. *Archaeometry*, *41*(2), 339–364. https://doi.org/10.1111/j.1475-4754.1999.tb00987.x

Gallen, S. F., Wegmann, K. W., Bohnenstiehl, D. R., Pazzaglia, F. J., Brandon, M. T., & Fassoulas, C. (2014). Active simultaneous uplift and margin-normal extension in a forearc high, Crete, Greece. *Earth and Planetary Science Letters*, *398*, 11–24. https://doi.org/10.1016/j.epsl.2014.04.038

Gardner, T. W., Fisher, D. M., Morell, K. D., & Cupper, M. L. (2013). Upper-plate deformation in response to flat slab subduction inboard of the aseismic Cocos Ridge, Osa Peninsula, Costa Rica. *Lithosphere*, *5*(3), 247–264. https://doi.org/10.1130/L251.1

Garreaud, R. D. (2009). The Andes climate and weather. *Advances in Geosciences*, *22*, 3–11. https://doi.org/10.5194/adgeo-22-3-2009

GEBCO Bathymetric Compilation Group. (2020). *The GEBCO_2020 Grid - a continuous terrain model of the global oceans and land*: British Oceanographic Data Centre, National Oceanography Centre, NERC, UK.

Geersen, J., Ranero, C. R., Barckhausen, U., & Reichert, C. (2015). Subducting seamounts control interplate coupling and seismic rupture in the 2014 Iquique earthquake area. *Nature Communications*, *6*, 8267. https://doi.org/10.1038/ncomms9267

German Aerospace Center, D.L.R. (2018). TanDEM-X - Digital Elevation Model (DEM) - Global, 12m.

Glodny, J., Lohrmann, J., Echtler, H., Gräfe, K., Seifert, W., Collao, S., & Figueroa, O. (2005). Internal dynamics of a paleoaccretionary wedge: insights from combined isotope tectonochronology and sandbox modelling of the South-Central Chilean forearc. *Earth and Planetary Science Letters*, *231*(1-2), 23–39. https://doi.org/10.1016/j.epsl.2004.12.014

Gomberg, J., & Sherrod, B. (2014). Crustal earthquake triggering by modern great earthquakes on subduction zone thrusts. *Journal of Geophysical Research: Solid Earth*, *119*(2), 1235–1250. https://doi.org/10.1002/2012JB009826

González, G., & Carrizo, D. (2003). Segmentación, cinemática y cronología relativa de la deformación tardía de la Falla Salar del Carmen, Sistema de Fallas de Atacama, (23°40'S), norte de Chile. *Revista Geológica De Chile*, *30*(2). https://doi.org/10.4067/S0716-02082003000200005

González-Alfaro, J., Vargas, G., Ortlieb, L., González, G., Ruiz, S., & Báez, J. C., et al. (2018). Abrupt increase in the coastal uplift and earthquake rate since ∼40 ka at the northern Chile seismic gap in the Central Andes. *Earth and Planetary Science Letters*, *502*, 32–45. https://doi.org/10.1016/j.epsl.2018.08.043

Goy, J. L., Macharé, J., Ortlieb, L., & Zazo, C. (1992). Quaternary shorelines in Southern Peru : a record of global sea-level fluctuations and tectonic uplift in Chala Bay. *Quaternary International*, *15-16*, 99–112.

Graham, S. E., Loveless, J. P., & Meade, B. J. (2018). Global Plate Motions and Earthquake Cycle Effects. *Geochemistry, Geophysics, Geosystems*, *19*(7), 2032–2048. https://doi.org/10.1029/2017GC007391

Gusman, A. R., Murotani, S., Satake, K., Heidarzadeh, M., Gunawan, E., Watada, S., & Schurr, B. (2015). Fault slip distribution of the 2014 Iquique, Chile, earthquake estimated from ocean-wide tsunami waveforms and GPS data. *Geophysical Research Letters*, *42*(4), 1053–1060. https://doi.org/10.1002/2014GL062604

Gutscher, M.-A., Malavieille, J., Lallemand, S., & Collot, J.-Y. (1999). Tectonic segmentation of the North Andean margin: impact of the Carnegie Ridge collision. *Earth and Planetary Science Letters*, *168*(3-4), 255–270. https://doi.org/10.1016/S0012-821X(99)00060-6

Gutscher, M.-A., Spakman, W., Bijwaard, H., & Engdahl, E. R. (2000). Geodynamics of flat subduction: Seismicity and tomographic constraints from the Andean margin. *Tectonics*, *19*(5), 814–833. https://doi.org/10.1029/1999TC001152

Hampel, A. (2002). The migration history of the Nazca Ridge along the Peruvian active margin: a re-evaluation. *Earth and Planetary Science Letters*, *203*(2), 665–679. https://doi.org/10.1016/S0012-821X(02)00859-2

Hasegawa, A., & Yoshida, K. (2015). Preceding seismic activity and slow slip events in the source area of the 2011 Mw 9.0 Tohoku-Oki earthquake: a review. *Geoscience Letters*, *2*(1), 615. https://doi.org/10.1186/s40562-015-0025-0

Hayes, G. P. (2017). The finite, kinematic rupture properties of great-sized earthquakes since 1990. *Earth and Planetary Science Letters*, *468*(3), 94–100. https://doi.org/10.1016/j.epsl.2017.04.003

Hayes, G. P., Moore, G. L., Portner, D. E., Hearne, M., Flamme, H., Furtney, M., & Smoczyk, G. M. (2018). Slab2, a comprehensive subduction zone geometry model. *Science (New York, N.Y.)*, *362*(6410), 58–61. https://doi.org/10.1126/science.aat4723

Hearty, P. J., Hollin, J. T., Neumann, A. C., O'Leary, M. J., & McCulloch, M. (2007). Global sea-level fluctuations during the last interglaciation (MIS 5e). *Quaternary Science Reviews*, *26*(17-18), 2090–2112. https://doi.org/10.1016/j.quascirev.2007.06.019

Heidbach, O., Rajabi, M., Cui, X., Fuchs, K., Müller, B., & Reinecker, J., et al. (2018). The World Stress Map database release 2016: Crustal stress pattern across scales. *Tectonophysics*, *744*(2131), 484–498. https://doi.org/10.1016/j.tecto.2018.07.007

Hilde, T. W.C. (1983). Sediment subduction versus accretion around the pacific. *Tectonophysics*, *99*(2-4), 381–397. https://doi.org/10.1016/0040-1951(83)90114-2

Houston, J., & Hartley, A. J. (2003). The central Andean west-slope rainshadow and its potential contribution to the origin of hyper-aridity in the Atacama Desert. *International Journal of Climatology*, *23*(12), 1453–1464. https://doi.org/10.1002/joc.938

Hsu, J. T. (1992). Quaternary uplift of the Peruvian coast related to the subduction of the Nazca Ridge: 13.5 to 15.6 degrees south latitude. *Quaternary International*, *15-16*, 87–97. https://doi.org/10.1016/1040-6182(92)90038-4

Hsu, J. T., Leonard, E. M., & Wehmiller, J. F. (1989). Aminostratigraphy of Peruvian and Chilean Quaternary marine terraces. *Quaternary Science Reviews*, *8*(3), 255–262. https://doi.org/10.1016/0277-3791(89)90040-1

Huntley, D., & Baril, M. R. (1997). The K content of the K-feldspars being measured in optical dating or in thermoluminescence dating. *Ancient TL*, *15*(1), 11–13.

Jaillard, E., Hérail, G., Monfret, T., Díaz-Martínez, E., Baby, P., Lavenu, A., & Dumont, J. F. (2000). Tectonic evolution of the Andes of Ecuador, Peru, Bolivia, and northernmost Chile. In U. G. Cordani, E. J. Milani, F. A. Thomaz, & D. A. Campos (Eds.), *Tectonic*

evolution of South America (31st ed., pp. 481–559). Rio de Janeiro: Sociedad Brasileira de Geologia.

Jara-Muñoz, J., Melnick, D., Brill, D., & Strecker, M. R. (2015). Segmentation of the 2010 Maule Chile earthquake rupture from a joint analysis of uplifted marine terraces and seismic-cycle deformation patterns. *Quaternary Science Reviews*, *113*, 171–192. https://doi.org/10.1016/j.quascirev.2015.01.005

Jara-Muñoz, J., Melnick, D., Li, S., Socquet, A., Cortés-Aranda, J., Brill, D., & Strecker, M. R. (2022). The cryptic seismic potential of the Pichilemu blind fault in Chile revealed by off-fault geomorphology. *Nature Communications*, *13*(1), 3371. https://doi.org/10.1038/s41467-022-30754-1

Jara-Muñoz, J., Melnick, D., Pedoja, K., & Strecker, M. R. (2019). TerraceM-2: A Matlab® Interface for Mapping and Modeling Marine and Lacustrine Terraces. *Frontiers in Earth Science*, *7*, 7. https://doi.org/10.3389/feart.2019.00255

Jara-Muñoz, J., Melnick, D., Socquet, A., Cortés-Aranda, J., & Strecker, M. R. (2018). Slip rate and earthquake recurrence of the Pichilemu Fault. *Congreso Geológico Chileno, 15th*.

Jara-Muñoz, J., Melnick, D., & Strecker, M. R. (2016). TerraceM: A MATLAB® tool to analyze marine and lacustrine terraces using high-resolution topography. *Geosphere*, *12*(1), 176–195. https://doi.org/10.1130/GES01208.1

Jara-Muñoz, J., Melnick, D., Zambrano, P., Rietbrock, A., González, J., Argandoña, B., & Strecker, M. R. (2017). Quantifying offshore fore-arc deformation and splay-fault slip using drowned Pleistocene shorelines, Arauco Bay, Chile. *Journal of Geophysical Research: Solid Earth*, *122*(6), 4529–4558. https://doi.org/10.1002/2016JB013339

Jolivet, R., Simons, M., Duputel, Z., Olive, J.-A., Bhat, H. S., & Bletery, Q. (2020). Interseismic loading of subduction megathrust drives long-term uplift in Northern Chile. *Geophysical Research Letters*, *47*(8), 3467. https://doi.org/10.1029/2019GL085377

Jordan, T. E., Isacks, B. L., Allmendinger, R. W., Brewer, J. A.O.N., Ramos, V. A., & Ando, C. J. (1983). Andean tectonics related to geometry of subducted Nazca plate. *Geological Society of America Bulletin*, *94*(3), 341. https://doi.org/10.1130/0016-7606(1983)94<341:ATRTGO>2.0.CO;2

Kanamori, H. (1986). Rupture Process of Subduction-Zone Earthquakes. *Annual Review of Earth and Planetary Sciences*, *14*(1), 293–322. https://doi.org/10.1146/annurev.ea.14.050186.001453

Kay, S. M., Maksaev, V., Moscoso, R., Mpodozis, C., & Nasi, C. (1987). Probing the evolving Andean Lithosphere: Mid-Late Tertiary magmatism in Chile (29°–30°30′S) over the modern zone of subhorizontal subduction. *Journal of Geophysical Research*, *92*(B7), 6173. https://doi.org/10.1029/JB092iB07p06173

Kelsey, H. M., Ticknor, R. L., Bockheim, J. G., & Mitchell, E. (1996). Quaternary upper plate deformation in coastal Oregon. *Geological Society of America Bulletin*, *108*(7), 843–860. https://doi.org/10.1130/0016-7606(1996)108<0843:QUPDIC>2.3.CO;2

Kendrick, E., Bevis, M., Smalley, R., Brooks, B., Vargas, R. B., Lauría, E., & Fortes, L. P. S. (2003). The Nazca–South America Euler vector and its rate of change. *Journal of South American Earth Sciences*, *16*(2), 125–131. https://doi.org/10.1016/S0895-9811(03)00028-2

Kley, J., Monaldi, C. R., & Salfity, J. A. (1999). Along-strike segmentation of the Andean foreland: causes and consequences. *Tectonophysics*, *301*(1-2), 75–94. https://doi.org/10.1016/S0040-1951(98)90223-2

Kopp, H., Flueh, E. R., Petersen, C. J., Weinrebe, W., Wittwer, A., & Scientists, M. (2006). The Java margin revisited: Evidence for subduction erosion off Java. *Earth and Planetary Science Letters*, *242*(1-2), 130–142. https://doi.org/10.1016/j.epsl.2005.11.036

Kreutzer, S., Schmidt, C., DeWitt, R., & Fuchs, M. (2014). The a-value of polymineral fine grain samples measured with the post-IR IRSL protocol. *Radiation Measurements*, *69*, 18–29. https://doi.org/10.1016/j.radmeas.2014.04.027

Lajoie, K. R. (1986). Coastal tectonics. In R. E. Wallace (Ed.), *Studies in geophysics. Active tectonics* (pp. 95–124). Washington D.C.: National Academics Press.

Lamb, S., & Davis, P. (2003). Cenozoic climate change as a possible cause for the rise of the Andes. *Nature*, *425*(6960), 792–797. https://doi.org/10.1038/nature02049

Lange, D., Geersen, J., Barrientos, S., Moreno, M., Grevemeyer, I., Contreras-Reyes, E., & Kopp, H. (2016). Aftershock seismicity and tectonic setting of the 2015 September 16 Mw 8.3 Illapel earthquake, Central Chile. *Geophysical Journal International*, *206*(2), 1424–1430. https://doi.org/10.1093/gji/ggw218

Lay, T., & Kanamori, H. (1981). An Asperity Model of Large Earthquake Sequences. *Earthquake Prediction: an International Review*, *41*(4), 579–592. https://doi.org/10.1029/ME004p0579

Lehner, F. K. (1986). Comments on "Noncohesive critical Coulomb wedges: An exact solution" by F. A. Dahlen. *Journal of Geophysical Research*, *91*(B1), 793. https://doi.org/10.1029/JB091iB01p00793

Leonard, E. M., & Wehmiller, J. F. (1992). Low uplift rates and terrace reoccupation inferred from mollusk aminostratigraphy, Coquimbo Bay area, Chile. *Quaternary Research*, *38*(2), 246–259. https://doi.org/10.1016/0033-5894(92)90060-V

Lohrmann, J., Kukowski, N., Adam, J., & Oncken, O. (2003). The impact of analogue material properties on the geometry, kinematics, and dynamics of convergent sand wedges. *Journal of Structural Geology*, *25*(10), 1691–1711. https://doi.org/10.1016/S0191-8141(03)00005-1

Lomnitz, C. (2004). Major Earthquakes of Chile: A Historical Survey, 1535-1960. *Seismological Research Letters*, *75*(3), 368–378. https://doi.org/10.1785/gssrl.75.3.368

Lorscheid, T., & Rovere, A. (2019). The indicative meaning calculator – quantification of paleo sea-level relationships by using global wave and tide datasets. *Open Geospatial Data, Software and Standards*, *4*(1), 591. https://doi.org/10.1186/s40965-019-0069-8

Loveless, J. P., Allmendinger, R. W., Pritchard, M. E., & González, G. (2010). Normal and reverse faulting driven by the subduction zone earthquake cycle in the northern Chilean fore arc. *Tectonics*, *29*(2), n/a-n/a. https://doi.org/10.1029/2009TC002465

Loveless, J. P., Scott, C. P., Allmendinger, R. W., & González, G. (2016). Slip distribution of the 2014 M w = 8.1 Pisagua, northern Chile, earthquake sequence estimated from coseismic fore-arc surface cracks. *Geophysical Research Letters*, *43*(19), 935. https://doi.org/10.1002/2016GL070284

Macharé, J., & Ortlieb, L. (1992). Plio-Quaternary vertical motions and the subduction of the Nazca Ridge, central coast of Peru. *Tectonophysics*, *205*(1-3), 97–108. https://doi.org/10.1016/0040-1951(92)90420-B

Madella, A., & Ehlers, T. A. (2021). Contribution of background seismicity to forearc uplift. *Nature Geoscience*, *14*(8), 620–625. https://doi.org/10.1038/s41561-021-00779-0

Maldonado, V., Contreras, M., & Melnick, D. (2021). A comprehensive database of active and potentially-active continental faults in Chile at 1:25,000 scale. *Scientific Data*, *8*(1), 20. https://doi.org/10.1038/s41597-021-00802-4

Manea, V. C., Pérez-Gussinyé, M., & Manea, M. (2012). Chilean flat slab subduction controlled by overriding plate thickness and trench rollback. *Geology*, *40*(1), 35–38. https://doi.org/10.1130/G32543.1

Mann, P., Taylor, F. W., Lagoe, M. B., Quarles, A., & Burr, G. (1998). Accelerating late Quaternary uplift of the New Georgia Island Group (Solomon island arc) in response to

subduction of the recently active Woodlark spreading center and Coleman seamount. *Tectonophysics*, *295*(3-4), 259–306. https://doi.org/10.1016/S0040-1951(98)00129-2

Marcaillou, B., Collot, J.-Y., Ribodetti, A., d'Acremont, E., Mahamat, A.-A., & Alvarado, A. (2016). Seamount subduction at the North-Ecuadorian convergent margin: Effects on structures, inter-seismic coupling and seismogenesis. *Earth and Planetary Science Letters*, *433*, 146–158. https://doi.org/10.1016/j.epsl.2015.10.043

Margirier, A., Strecker, M. R., Reiners, P. W., Thomson, S. N., Casado, I., George, S. W. M., & Alvarado, A. (2023). Late Miocene Exhumation of the Western Cordillera, Ecuador, Driven by Increased Coupling Between the Subducting Carnegie Ridge and the South American Continent. *Tectonics*, *42*(1), 157. https://doi.org/10.1029/2022TC007344

Martinod, J., Regard, V., Letourmy, Y., Henry, H., Hassani, R., Baratchart, S., & Carretier, S. (2016). How do subduction processes contribute to forearc Andean uplift? Insights from numerical models. *Journal of Geodynamics*, *96*, 6–18. https://doi.org/10.1016/j.jog.2015.04.001

Martinod, J., Regard, V., Riquelme, R., Aguilar, G., Guillaume, B., & Carretier, S., et al. (2016). Pleistocene uplift, climate and morphological segmentation of the Northern Chile coasts (24°S–32°S): Insights from cosmogenic 10Be dating of paleoshorelines. *Geomorphology*, *274*, 78–91. https://doi.org/10.1016/j.geomorph.2016.09.010

Matsu'ura, T. (2015). Late Quaternary uplift rate inferred from marine terraces, Muroto Peninsula, southwest Japan: Forearc deformation in an oblique subduction zone. *Geomorphology*, *234*(B5), 133–150. https://doi.org/10.1016/j.geomorph.2015.01.012

Matsu'ura, T., Komatsubara, J., & Wu, C. (2019). Accurate determination of the Pleistocene uplift rate of the NE Japan forearc from the buried MIS 5e marine terrace shoreline angle. *Quaternary Science Reviews*, *212*(3–4), 45–68. https://doi.org/10.1016/j.quascirev.2019.03.007

McKenzie, K. A., Kelsey, H. M., Kirby, E., Rittenour, T. M., & Furlong, K. P. (2022). Differential coastal uplift quantified by luminescence dating of marine terraces, central Cascadia forearc, Oregon. *Quaternary Science Reviews*, *298*(4), 107853. https://doi.org/10.1016/j.quascirev.2022.107853

Melet, A., Teatini, P., Le Cozannet, G., Jamet, C., Conversi, A., Benveniste, J., & Almar, R. (2020). Earth Observations for Monitoring Marine Coastal Hazards and Their Drivers. *Surveys in Geophysics*, *41*(6), 1489–1534. https://doi.org/10.1007/s10712-020-09594-5

Melnick, D. (2016). Rise of the central Andean coast by earthquakes straddling the Moho. *Nature Geoscience*, *9*(5), 401–407. https://doi.org/10.1038/ngeo2683

Melnick, D., Bookhagen, B., Echtler, H. P., & Strecker, M. R. (2006). Coastal deformation and great subduction earthquakes, Isla Santa Maria, Chile (37°S). *Geological Society of America Bulletin*, *118*(11-12), 1463–1480. https://doi.org/10.1130/B25865.1

Melnick, D., Bookhagen, B., Strecker, M. R., & Echtler, H. P. (2009). Segmentation of megathrust rupture zones from fore-arc deformation patterns over hundreds to millions of years, Arauco peninsula, Chile. *Journal of Geophysical Research: Solid Earth*, *114*(B1), 6140. https://doi.org/10.1029/2008JB005788

Melnick, D., & Echtler, H. P. (2006). Inversion of forearc basins in south-central Chile caused by rapid glacial age trench fill. *Geology*, *34*(9), 709. https://doi.org/10.1130/G22440.1

Melnick, D., Hillemann, C., Jara-Muñoz, J., Garrett, E., Cortés-Aranda, J., & Molina, D., et al. (2019). Hidden Holocene slip along the coastal El Yolki Fault in Central Chile and its possible link with megathrust earthquakes. *Journal of Geophysical Research: Solid Earth*, *124*(7), 7280–7302. https://doi.org/10.1029/2018JB017188

Melnick, D., Moreno, M., Quinteros, J., Baez, J. C., Deng, Z., Li, S., & Oncken, O. (2017). The super-interseismic phase of the megathrust earthquake cycle in Chile. *Geophysical Research Letters*, *44*(2), 784–791. https://doi.org/10.1002/2016GL071845

Melosh, H. J., & Raefsky, A. (1980). The dynamical origin of subduction zone topography. *Geophysical Journal International*, *60*(3), 333–354. https://doi.org/10.1111/j.1365-246X.1980.tb04812.x

Menant, A., Angiboust, S., Gerya, T., Lacassin, R., Simoes, M., & Grandin, R. (2020). Transient stripping of subducting slabs controls periodic forearc uplift. *Nature Communications*, *11*(1), 1823. https://doi.org/10.1038/s41467-020-15580-7

Métois, M., Vigny, C., & Socquet, A. (2016). Interseismic Coupling, Megathrust Earthquakes and Seismic Swarms Along the Chilean Subduction Zone (38°–18°S). *Pure and Applied Geophysics*, *173*(5), 1431–1449. https://doi.org/10.1007/s00024-016-1280-5

Molina, D., Tassara, A., Abarca, R., Melnick, D., & Madella, A. (2021). Frictional segmentation of the Chilean megathrust from a multivariate analysis of geophysical, geological, and geodetic data. *Journal of Geophysical Research: Solid Earth*, *126*(6), eaat4396. https://doi.org/10.1029/2020JB020647

Moreno, M., Rosenau, M., & Oncken, O. (2010). 2010 Maule earthquake slip correlates with pre-seismic locking of Andean subduction zone. *Nature*, *467*(7312), 198–202. https://doi.org/10.1038/nature09349

Moreno, M. S. (2010). Active deformation in the southern Andes from GPS and FEM models (Dissertation). Technische Universität Berlin, Berlin.

Morgan, J. K., & Bangs, N. L. (2017). Recognizing seamount-forearc collisions at accretionary margins: Insights from discrete numerical simulations. *Geology*, *45*(7), 635–638. https://doi.org/10.1130/G38923.1

Muhs, D. R. (2022). MIS 5e sea-level history along the Pacific coast of North America. *Earth System Science Data*, *14*(3), 1271–1330. https://doi.org/10.5194/essd-14-1271-2022

Muhs, D. R., Simmons, K. R., Kennedy, G. L., & Rockwell, T. K. (2002). The last interglacial period on the Pacific Coast of North America: Timing and paleoclimate. *Geological Society of America Bulletin*, *114*(5), 569–592. https://doi.org/10.1130/0016-7606(2002)114<0569:TLIPOT>2.0.CO;2

Muhs, D. R., Simmons, K. R., Schumann, R. R., Groves, L. T., DeVogel, S. B., Minor, S. A., & Laurel, D. (2014). Coastal tectonics on the eastern margin of the Pacific Rim: late Quaternary sea-level history and uplift rates, Channel Islands National Park, California, USA. *Quaternary Science Reviews*, *105*(7), 209–238. https://doi.org/10.1016/j.quascirev.2014.09.017

Müller, R. D., Sdrolias, M., Gaina, C., & Roest, W. R. (2008). Age, spreading rates, and spreading asymmetry of the world's ocean crust. *Geochemistry, Geophysics, Geosystems*, *9*(4). https://doi.org/10.1029/2007GC001743

Naranjo, J. A. (1987). Interpretacion de la actividad cenozoica superior a lo largo de la zona de Falla Atacama, Norte de Chile. *Revista Geológica De Chile*. (31), 43–55.

Ocola, L. (2008). Southern Perú coseismic subsidence: 23 June 2001 8.4-Mw earthquake. *Advances in Geosciences*, *14*, 79–83. https://doi.org/10.5194/adgeo-14-79-2008

Okada, Y. (1992). Internal deformation due to shear and tensile faults in a half-space. *Bulletin of the Seismological Society of America*, *82*(2), 1018–1040. https://doi.org/10.1785/BSSA0820021018

Ortlieb, L., & Macharé, J. (1990). Geochronologia y morfoestratigrafia de terrazas marinas del Pleistoceno superior: El caso de San Juan-Marcona, Peru. *Boletín De La Sociedad Geológica Del Perú*, *81*, 87–106.

Ortlieb, L., Zazo, C., Goy, J., Hillaire-Marcel, C., Ghaleb, B., & Cournoyer, L. (1996). Coastal deformation and sea-level changes in the northern Chile subduction area (23°S) during the last 330 ky. *Quaternary Science Reviews*, *15*(8-9), 819–831. https://doi.org/10.1016/S0277-3791(96)00066-2

Ortlieb, L., Zazo, C., Goy, J. L., Dabrio, C., & Macharé, J. (1996). Pampa del Palo: an anomalous composite marine terrace on the uprising coast of southern Peru. *Journal of South American Earth Sciences*, *9*(5-6), 367–379. https://doi.org/10.1016/S0895-9811(96)00020-X

Ota, Y., Miyauchi, T., Paskoff, R., & Koba, M. (1995). Plio-Quaternary marine terraces and their deformation along the Altos de Talinay, North-Central Chile. *Revista Geológica De Chile*, *22*(1), 89–102.

Paris, P. J., Walsh, J. P., & Corbett, D. R. (2016). Where the continent ends. *Geophysical Research Letters*, *43*(23), 12,208-12,216. https://doi.org/10.1002/2016GL071130

Pedoja, K., Dumont, J. F., Lamothe, M., Ortlieb, L., Collot, J.-Y., & Ghaleb, B., et al. (2006). Plio-Quaternary uplift of the Manta Peninsula and La Plata Island and the subduction of the Carnegie Ridge, central coast of Ecuador. *Journal of South American Earth Sciences*, *22*(1-2), 1–21. https://doi.org/10.1016/j.jsames.2006.08.003

Pedoja, K., Husson, L., Johnson, M. E., Melnick, D., Witt, C., & Pochat, S., et al. (2014). Coastal staircase sequences reflecting sea-level oscillations and tectonic uplift during the Quaternary and Neogene. *Earth-Science Reviews*, *132*, 13–38. https://doi.org/10.1016/j.earscirev.2014.01.007

Pedoja, K., Husson, L., Regard, V., Cobbold, P. R., Ostanciaux, E., & Johnson, M. E., et al. (2011). Relative sea-level fall since the last interglacial stage: Are coasts uplifting worldwide? *Earth-Science Reviews*, *108*(1-2), 1–15. https://doi.org/10.1016/j.earscirev.2011.05.002

Pedoja, K., Ortlieb, L., Dumont, J. F., Lamothe, M., Ghaleb, B., Auclair, M., & Labrousse, B. (2006). Quaternary coastal uplift along the Talara Arc (Ecuador, Northern Peru) from new marine terrace data. *Marine Geology*, *228*(1-4), 73–91. https://doi.org/10.1016/j.margeo.2006.01.004

Philibosian, B., & Meltzner, A. J. (2020). Segmentation and supercycles: A catalog of earthquake rupture patterns from the Sumatran Sunda Megathrust and other well-studied faults worldwide. *Quaternary Science Reviews*, *241*(27), 106390. https://doi.org/10.1016/j.quascirev.2020.106390

Pilger, R. H. (1981). Plate reconstructions, aseismic ridges, and low-angle subduction beneath the Andes. *Geological Society of America Bulletin*, *92*(7), 448. https://doi.org/10.1130/0016-7606(1981)92<448:PRARAL>2.0.CO;2

Prémaillon, M., Regard, V., Dewez, T. J. B., & Auda, Y. (2018). GlobR2C2 (Global Recession Rates of Coastal Cliffs): a global relational database to investigate coastal rocky cliff erosion rate variations. *Earth Surface Dynamics*, *6*(3), 651–668. https://doi.org/10.5194/esurf-6-651-2018

Prescott, J. R., & Hutton, J. T. (1994). Cosmic ray contributions to dose rates for luminescence and ESR dating: Large depths and long-term time variations. *Radiation Measurements*, *23*(2-3), 497–500. https://doi.org/10.1016/1350-4487(94)90086-8

Rabassa, J., & Clapperton, C. M. (1990). Quaternary glaciations of the southern Andes. *Quaternary Science Reviews*, *9*(2-3), 153–174. https://doi.org/10.1016/0277-3791(90)90016-4

Racano, S., Jara-Muñoz, J., Cosentino, D., & Melnick, D. (2020). Variable Quaternary Uplift Along the Southern Margin of the Central Anatolian Plateau Inferred From Modeling Marine Terrace Sequences. *Tectonics*, *39*(12), 105. https://doi.org/10.1029/2019TC005921

Radtke, U. (1987). Paleo sea levels and discrimination of the last and the penultimate interglacial fossiliferous deposits by absolute dating methods and geomorphic investigations; illustratedby marine terraces in Chile. *Berliner Geographische Studien*, *25*, 313–342.

Radtke, U. (1989). Marine Terrassen und Korallenriffe: das Problem der quartären Meeresspiegelschwankungen erläutert aus Chile, Argentinien und Barbados. *Düsseldorfer Geographische Schriften*, *27*.

Ramos, V. A., & Folguera, A. (2009). Andean flat-slab subduction through time. *Geological Society, London, Special Publications*, *327*(1), 31–54. https://doi.org/10.1144/SP327.3

Regard, V., Saillard, M., Martinod, J., Audin, L., Carretier, S., & Pedoja, K., et al. (2010). Renewed uplift of the Central Andes Forearc revealed by coastal evolution during the Quaternary. *Earth and Planetary Science Letters*, *297*(1-2), 199–210. https://doi.org/10.1016/j.epsl.2010.06.020

Rehak, K., Bookhagen, B., Strecker, M. R., & Echtler, H. P. (2010). The topographic imprint of a transient climate episode: the western Andean flank between 15.5° and 41.5°S. *Earth Surface Processes and Landforms*, *35*(13), 1516–1534. https://doi.org/10.1002/esp.1992

Reid, H. F. (1910). The Mechanics of the Earthquake, The California Earthquake of April 18, 1906: Report of the State Investigation Commission, Vol. 2. *Carnegie Institution of Washington, Washington, D.C.*

Remy, D., Perfettini, H., Cotte, N., Avouac, J. P., Chlieh, M., & Bondoux, F., et al. (2016). Postseismic relocking of the subduction megathrust following the 2007 Pisco, Peru, earthquake. *Journal of Geophysical Research: Solid Earth*, *121*(5), 3978–3995. https://doi.org/10.1002/2015JB012417

Rodríguez, M. P., Carretier, S., Charrier, R., Saillard, M., Regard, V., & Hérail, G., et al. (2013). Geochronology of pediments and marine terraces in north-central Chile and their implications for Quaternary uplift in the Western Andes. *Geomorphology*, *180-181*, 33–46. https://doi.org/10.1016/j.geomorph.2012.09.003

Rodriguez Piceda, C., Gao, Y.-J., Cacace, M., Scheck-Wenderoth, M., Bott, J., Strecker, M., & Tilmann, F. (2023). The influence of mantle hydration and flexure on slab seismicity in the southern Central Andes. *Communications Earth & Environment*, *4*(1), 492. https://doi.org/10.1038/s43247-023-00729-1

Rohling, E. J., Grant, K., Bolshaw, M., Roberts, A. P., Siddall, M., Hemleben, C., & Kucera, M. (2009). Antarctic temperature and global sea level closely coupled over the past five glacial cycles. *Nature Geoscience*, *2*(7), 500–504. https://doi.org/10.1038/ngeo557

Ruh, J. B., Sallarès, V., Ranero, C. R., & Gerya, T. (2016). Crustal deformation dynamics and stress evolution during seamount subduction: High-resolution 3-D numerical modeling. *Journal of Geophysical Research: Solid Earth*, *121*(9), 6880–6902. https://doi.org/10.1002/2016JB013250

Ruiz, S., & Madariaga, R. (2018). Historical and recent large megathrust earthquakes in Chile. *Tectonophysics*, *733*(B4), 37–56. https://doi.org/10.1016/j.tecto.2018.01.015

Saillard, M. (2008). Dynamique du soulèvement côtier Pléistocène des Andes centrales : Etude de l'évolution géomorphologique et datations (10Be) de séquences de terrasses marines (Sud Pérou - Nord Chili). Université Paul Sabatier, Toulouse.

Saillard, M., Audin, L., Rousset, B., Avouac, J.-P., Chlieh, M., & Hall, S. R., et al. (2017). From the seismic cycle to long-term deformation: linking seismic coupling and Quaternary coastal geomorphology along the Andean megathrust. *Tectonics*, *36*(2), 241–256. https://doi.org/10.1002/2016TC004156

Saillard, M., Hall, S. R., Audin, L., Farber, D. L., Hérail, G., & Martinod, J., et al. (2009). Non-steady long-term uplift rates and Pleistocene marine terrace development along the

Andean margin of Chile (31°S) inferred from 10Be dating. *Earth and Planetary Science Letters*, *277*(1-2), 50–63. https://doi.org/10.1016/j.epsl.2008.09.039

Saillard, M., Hall, S. R., Audin, L., Farber, D. L., Regard, V., & Hérail, G. (2011). Andean coastal uplift and active tectonics in southern Peru: 10Be surface exposure dating of differentially uplifted marine terrace sequences (San Juan de Marcona, ~15.4°S). *Geomorphology*, *128*(3-4), 178–190. https://doi.org/10.1016/j.geomorph.2011.01.004

Saillard, M., Riotte, J., Regard, V., Violette, A., Hérail, G., Audin, L., & Riquelme, R. (2012). Beach ridges U–Th dating in Tongoy bay and tectonic implications for a peninsula–bay system, Chile. *Journal of South American Earth Sciences*, *40*, 77–84. https://doi.org/10.1016/j.jsames.2012.09.001

Sak, P. B., Fisher, D. M., & Gardner, T. W. (2004). Effects of subducting seafloor roughness on upper plate vertical tectonism: Osa Peninsula, Costa Rica. *Tectonics*, *23*(1), n/a-n/a. https://doi.org/10.1029/2002TC001474

Sandwell, D. T., Müller, R. D., Smith, W. H. F., Garcia, E., & Francis, R. (2014). New global marine gravity model from CryoSat-2 and Jason-1 reveals buried tectonic structure. *Science*, *346*(6205), 65–67. https://doi.org/10.1126/science.1258213

Santibáñez, I., Cembrano, J., García-Pérez, T., Costa, C., Yáñez, G., & Marquardt, C., et al. (2019). Crustal faults in the Chilean Andes: geological constraints and seismic potential. *Andean Geology*, *46*(1), 32. https://doi.org/10.5027/andgeoV46n1-3067

Savage, J. C. (1983). A dislocation model of strain accumulation and release at a subduction zone. *Journal of Geophysical Research*, *88*(B6), 4984–4996. https://doi.org/10.1029/JB088iB06p04984

Sawai, Y., Namegaya, Y., Okamura, Y., Satake, K., & Shishikura, M. (2012). Challenges of anticipating the 2011 Tohoku earthquake and tsunami using coastal geology. *Geophysical Research Letters*, *39*(21), n/a-n/a. https://doi.org/10.1029/2012GL053692

Sawai, Y., Satake, K., Kamataki, T., Nasu, H., Shishikura, M., & Atwater, B. F., et al. (2004). Transient uplift after a 17th-century earthquake along the Kuril subduction zone. *Science (New York, N.Y.)*, *306*(5703), 1918–1920. https://doi.org/10.1126/science.1104895

Scholl, D. W., & von Huene, R. (2007). Crustal recycling at modern subduction zones applied to the past—Issues of growth and preservation of continental basement crust, mantle geochemistry, and supercontinent reconstruction. In *Geological Society of America Memoirs. 4-D Framework of Continental Crust* (Vol. 200, pp. 9–32). Geological Society of America. https://doi.org/10.1130/2007.1200(02)

Schurr, B., Asch, G., Hainzl, S., Bedford, J., Hoechner, A., & Palo, M., et al. (2014). Gradual unlocking of plate boundary controlled initiation of the 2014 Iquique earthquake. *Nature*, *512*(7514), 299–302. https://doi.org/10.1038/nature13681

Schurr, B., Asch, G., Rosenau, M., Wang, R., Oncken, O., & Barrientos, S., et al. (2012). The 2007 M7.7 Tocopilla northern Chile earthquake sequence: Implications for along-strike and downdip rupture segmentation and megathrust frictional behavior. *Journal of Geophysical Research: Solid Earth*, *117*(B5), n/a-n/a. https://doi.org/10.1029/2011JB009030

Schwanghart, W., & Kuhn, N. J. (2010). TopoToolbox: A set of Matlab functions for topographic analysis. *Environmental Modelling & Software*, *25*(6), 770–781. https://doi.org/10.1016/j.envsoft.2009.12.002

Schwanghart, W., & Scherler, D. (2014). Short Communication: TopoToolbox 2 – MATLAB-based software for topographic analysis and modeling in Earth surface sciences. *Earth Surface Dynamics*, *2*(1), 1–7. https://doi.org/10.5194/esurf-2-1-2014

Schweller, W. J., Kulm, L. D., & Prince, R. A. (1981). Tectonics, structure, and sedimentary framework of the Peru-Chile Trench. *Geological Society of America Memoir*, *154*, 323–350. https://doi.org/10.1130/MEM154-p323

Scott, C. P., Allmendinger, R. W., González, G., & Loveless, J. P. (2016). Coseismic extension from surface cracks reopened by the 2014 Pisagua, northern Chile, earthquake sequence. *Geology*, *44*(5), 387–390. https://doi.org/10.1130/G37662.1

Shackleton, N. J., Sánchez-Goñi, M. F., Pailler, D., & Lancelot, Y. (2003). Marine Isotope Substage 5e and the Eemian Interglacial. *Global and Planetary Change*, *36*(3), 151–155. https://doi.org/10.1016/S0921-8181(02)00181-9

Shepherd, A., & Wingham, D. (2007). Recent sea-level contributions of the Antarctic and Greenland ice sheets. *Science (New York, N.Y.)*, *315*(5818), 1529–1532. https://doi.org/10.1126/science.1136776

Shikakura, Y. (2014). Marine terraces caused by fast steady uplift and small coseismic uplift and the time-predictable model: Case of Kikai Island, Ryukyu Islands, Japan. *Earth and Planetary Science Letters*, *404*, 232–237. https://doi.org/10.1016/j.epsl.2014.08.003

Siddall, M., Chappell, J., & Potter, E.-K. (2006). Eustatic sea level during past interglacials. In F. Sirocko, T. Litt, M. Claussen, & M.-F. Sanchez-Goni (Eds.), *The climate of past interglacials.* (pp. 75–92). Amsterdam: Elsevier. https://doi.org/10.1016/S1571-0866(07)80032-7

Simms, A. R., Rood, D. H., & Rockwell, T. K. (2020). Correcting MIS5e and 5a sea-level estimates for tectonic uplift, an example from southern California. *Quaternary Science Reviews*, *248*, 106571. https://doi.org/10.1016/j.quascirev.2020.106571

Simms, A. R., Rouby, H., & Lambeck, K. (2016). Marine terraces and rates of vertical tectonic motion: The importance of glacio-isostatic adjustment along the Pacific coast of central North America. *Geological Society of America Bulletin*, B31299.1. https://doi.org/10.1130/B31299.1

Singh, S. C., Hananto, N., Mukti, M., Robinson, D. P., Das, S., & Chauhan, A., et al. (2011). Aseismic zone and earthquake segmentation associated with a deep subducted seamount in Sumatra. *Nature Geoscience*, *4*(5), 308–311. https://doi.org/10.1038/ngeo1119

Sippl, C., Schurr, B., John, T., & Hainzl, S. (2019). Filling the gap in a double seismic zone: Intraslab seismicity in Northern Chile. *Lithos*, *346-347*, 105155. https://doi.org/10.1016/j.lithos.2019.105155

Sobolev, S. V., & Babeyko, A. Y. (2005). What drives orogeny in the Andes? *Geology*, *33*(8), 617–620. https://doi.org/10.1130/G21557AR.1

Stern, C. R. (1991). Role of subduction erosion in the generation of Andean magmas. *Geology*, *19*(1), 78. https://doi.org/10.1130/0091-7613(1991)019<0078:ROSEIT>2.3.CO;2

Stewart, I. S., Sauber, J., & Rose, J. (2000). Glacio-seismotectonics: ice sheets, crustal deformation and seismicity. *Quaternary Science Reviews*, *19*(14-15), 1367–1389. https://doi.org/10.1016/S0277-3791(00)00094-9

Stirling, C.H., Esat, T.M., Lambeck, K., & McCulloch, M.T. (1998). Timing and duration of the Last Interglacial: evidence for a restricted interval of widespread coral reef growth. *Earth and Planetary Science Letters*, *160*(3-4), 745–762. https://doi.org/10.1016/S0012-821X(98)00125-3

Strecker, M. R., Alonso, R. N., Bookhagen, B., Carrapa, B., Hilley, G. E., Sobel, E. R., & Trauth, M. H. (2007). Tectonics and Climate of the Southern Central Andes. *Annual Review of Earth and Planetary Sciences*, *35*(1), 747–787. https://doi.org/10.1146/annurev.earth.35.031306.140158

Styron, R., & Pagani, M. (2020). The GEM Global Active Faults Database. *Earthquake Spectra*, *36*(1_suppl), 160–180. https://doi.org/10.1177/8755293020944182

Suárez, G., Molnar, P., & Burchfiel, B. C. (1983). Seismicity, fault plane solutions, depth of faulting, and active tectonics of the Andes of Peru, Ecuador, and southern Colombia. *Journal of Geophysical Research*, *88*(B12), 10403–10428. https://doi.org/10.1029/JB088iB12p10403

Sunamura, T. (1992). *Geomorphology of rocky coasts*. *Coastal morphology and research: Vol. 18*. Chichester: John Wiley & Sons.

Tam, E., & Yokoyama, Y. (2021). A review of MIS 5e sea-level proxies around Japan. *Earth System Science Data*, *13*(4), 1477–1497. https://doi.org/10.5194/essd-13-1477-2021

Taylor, F. W., Frohlich, C., Lecolle, J., & Strecker, M. (1987). Analysis of partially emerged corals and reef terraces in the central Vanuatu Arc: Comparison of contemporary coseismic and nonseismic with quaternary vertical movements. *Journal of Geophysical Research*, *92*(B6), 4905. https://doi.org/10.1029/JB092iB06p04905

Thatcher, W. (1990). Order and diversity in the modes of circum-Pacific earthquake recurrence. *Journal of Geophysical Research*, *95*(B3), 2609. https://doi.org/10.1029/JB095iB03p02609

Tilmann, F., Zhang, Y., Moreno, M., Saul, J., Eckelmann, F., & Palo, M., et al. (2016). The 2015 Illapel earthquake, central Chile: A type case for a characteristic earthquake? *Geophysical Research Letters*, *43*(2), 574–583. https://doi.org/10.1002/2015GL066963

Toda, S., & Tsutsumi, H. (2013). Simultaneous reactivation of two, subparallel, inland normal faults during the Mw 6.6 11 April 2011 Iwaki earthquake triggered by the Mw 9.0 Tohoku-oki, Japan, earthquake. *Bulletin of the Seismological Society of America*, *103*(2B), 1584–1602. https://doi.org/10.1785/0120120281

Trenhaile, A.S. (2002). Modeling the development of marine terraces on tectonically mobile rock coasts. *Marine Geology*, *185*(3-4), 341–361. https://doi.org/10.1016/S0025-3227(02)00187-1

Turcotte, D. L., & Schubert, G. (1982). *Geodynamics: Applications of Continuum Physics to Geological Problema*. New York (450 pp.): John Wiley.

Udias, A., Madariaga, R., Buforn, E., Munoz, D., & Ros, M. (2012). The Large Chilean Historical Earthquakes of 1647, 1657, 1730, and 1751 from Contemporary Documents. *Bulletin of the Seismological Society of America*, *102*(4), 1639–1653. https://doi.org/10.1785/0120110289

Veloza, G., Styron, R., Taylor, M., & Mora, A. (2012). Open-source archive of active faults for northwest South America. *GSA Today*, *22*(10), 4–10. https://doi.org/10.1130/GSAT-G156A.1

Venzke, E. (2013). *Volcanoes of the World, v. 4.3.4*: Global Volcanism Program.

Victor, P., Sobiesiak, M., Glodny, J., Nielsen, S. N., & Oncken, O. (2011). Long-term persistence of subduction earthquake segment boundaries: Evidence from Mejillones Peninsula, northern Chile. *Journal of Geophysical Research*, *116*(B2), 93. https://doi.org/10.1029/2010JB007771

Villegas-Lanza, J. C., Chlieh, M., Cavalié, O., Tavera, H., Baby, P., Chire-Chira, J., & Nocquet, J.-M. (2016). Active tectonics of Peru: Heterogeneous interseismic coupling along the Nazca megathrust, rigid motion of the Peruvian Sliver, and Subandean shortening accommodation. *Journal of Geophysical Research: Solid Earth*, *121*(10), 7371–7394. https://doi.org/10.1002/2016JB013080

von Huene, R., Corvalán, J., Flueh, E. R., Hinz, K., Korstgard, J., Ranero, C. R., & Weinrebe, W. (1997). Tectonic control of the subducting Juan Fernández Ridge on the Andean margin near Valparaiso, Chile. *Tectonics*, *16*(3), 474–488. https://doi.org/10.1029/96TC03703

von Huene, R., Pecher, I. A., & Gutscher, M.-A. (1996). Development of the accretionary prism along Peru and material flux after subduction of Nazca Ridge. *Tectonics*, *15*(1), 19–33. https://doi.org/10.1029/95TC02618

von Huene, R., & Ranero, C. R. (2003). Subduction erosion and basal friction along the sediment-starved convergent margin off Antofagasta, Chile. *Journal of Geophysical Research: Solid Earth*, *108*(B2), 297. https://doi.org/10.1029/2001JB001569

von Huene, R., Ranero, C. R., Weinrebe, W., & Hinz, K. (2000). Quaternary convergent margin tectonics of Costa Rica, segmentation of the Cocos Plate, and Central American volcanism. *Tectonics*, *19*(2), 314–334. https://doi.org/10.1029/1999TC001143

von Huene, R., & Scholl, D. W. (1991). Observations at convergent margins concerning sediment subduction, subduction erosion, and the growth of continental crust. *Geology*, *29*(3), 279. https://doi.org/10.1029/91RG00969

Walters, R. J., Elliott, J. R., D'Agostino, N., England, P. C., Hunstad, I., & Jackson, J. A., et al. (2009). The 2009 L'Aquila earthquake (central Italy): A source mechanism and implications for seismic hazard. *Geophysical Research Letters*, *36*(17), 187. https://doi.org/10.1029/2009GL039337

Wang, K., & Bilek, S. L. (2011). Do subducting seamounts generate or stop large earthquakes? *Geology*, *39*(9), 819–822. https://doi.org/10.1130/G31856.1

Wang, K., & Bilek, S. L. (2014). Invited review paper: Fault creep caused by subduction of rough seafloor relief. *Tectonophysics*, *610*, 1–24. https://doi.org/10.1016/j.tecto.2013.11.024

Wang, K., Hu, Y., Bevis, M., Kendrick, E., Smalley, R., Vargas, R. B., & Lauría, E. (2007). Crustal motion in the zone of the 1960 Chile earthquake: Detangling earthquake-cycle deformation and forearc-sliver translation. *Geochemistry, Geophysics, Geosystems*, *8*(10), n/a-n/a. https://doi.org/10.1029/2007GC001721

Wang, K., Wells, R., Mazzotti, S., Hyndman, R. D., & Sagiya, T. (2003). A revised dislocation model of interseismic deformation of the Cascadia subduction zone. *Journal of Geophysical Research: Solid Earth*, *108*(B1), 1085. https://doi.org/10.1029/2001JB001227

Watts, A. B., & Daly, S. F. (1981). Long Wavelength Gravity and Topography Anomalies. *Annual Review of Earth and Planetary Sciences*, *9*, 415–448.

Wesson, R. L., Melnick, D., Cisternas, M., Moreno, M., & Ely, L. L. (2015). Vertical deformation through a complete seismic cycle at Isla Santa María, Chile. *Nature Geoscience*, *8*(7), 547–551. https://doi.org/10.1038/ngeo2468

Zoback, M. L. (1992). First- and second-order patterns of stress in the lithosphere: The World Stress Map Project. *Journal of Geophysical Research*, *97*(B8), 11703. https://doi.org/10.1029/92jb00132